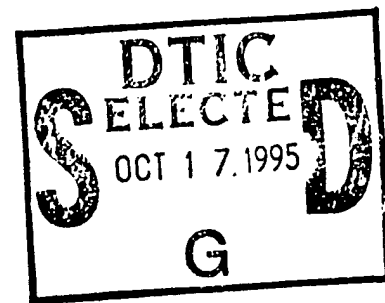




Radar Systems and
Remote Sensing Laboratory

SEA ICE RADAR BACKSCATTER MODELING,
MEASUREMENTS, AND THE FUSION OF
ACTIVE AND PASSIVE MICROWAVE DATA



19951012 050

THE UNIVERSITY OF KANSAS CENTER FOR RESEARCH, INC.

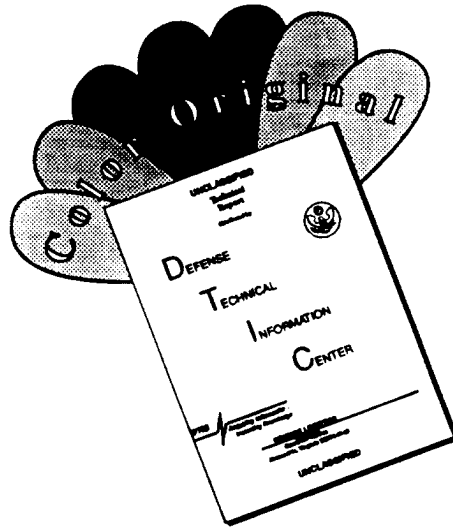
2291 Irving Hill Road
Lawrence, Kansas 66045-2969

DISTRIBUTION STATEMENT A

Approved for public release;
Distribution Unlimited

DTIC QUALITY INSPECTED 8

DISCLAIMER NOTICE



THIS DOCUMENT IS BEST QUALITY AVAILABLE. THE COPY FURNISHED TO DTIC CONTAINED A SIGNIFICANT NUMBER OF COLOR PAGES WHICH DO NOT REPRODUCE LEGIBLY ON BLACK AND WHITE MICROFICHE.

**SEA ICE RADAR BACKSCATTER MODELING,
MEASUREMENTS, AND THE FUSION OF
ACTIVE AND PASSIVE MICROWAVE DATA**

Scott Gerard Beaven

Radar Systems and Remote Sensing Laboratory
Department of Electrical Engineering and Computer Science, University of Kansas
2291 Irving Hill Road, Lawrence, Kansas 66045-2969
TEL: 913/864-4835 * FAX: 913/864-7789 * E-MAIL: graham@ardneh.rsl.ukans.edu

RSL Technical Report 8243-4

March 1995



Sponsored by

Office of Naval Research
Arlington VA 22217-5000

Grant N00014-89-J-1456

DISTRIBUTION STATEMENT A

Approved for public release;
Distribution Unlimited

TABLE OF CONTENTS

LIST OF FIGURES	viii
LIST OF TABLES	xvi
ABSTRACT	xvii
CHAPTER 1 - INTRODUCTION.....	1
1.1 Motivation.....	1
1.2 Objectives.....	3
1.3 Approach and Overview	4
CHAPTER 2 - STATUS OF MICROWAVE REMOTE SENSING	
OF SEA ICE	8
2.1 Satellite SAR and Imaging Microwave Radiometers	8
2.1.1 Spaceborne Synthetic Aperture Radars.....	8
2.1.2 Spaceborne Microwave Radiometers.....	9
2.2 Near-surface and air-based measurements.....	11
CHAPTER 3 - FM RADAR SIGNAL PROCESSING:	
COHERENT NOISE REDUCTION.....	14
3.1 FM Radar Concepts	15
3.2 Radar Systems Description	19
3.2.1 C-/X-band FM Radar System	19
3.2.2 Step Frequency Radar Systems.....	22
3.3 Coherent Noise Reduction	26
3.3.1 Theoretical Development	26
3.3.2 Results	32
3.4 Phase and Amplitude Variations and CNR.....	38
3.4.1 Effect of phase and amplitude drifts on CNR	38
3.4.2 Causes of phase variations in the IF signal	41
Effect of oscillator drift.....	42

<input checked="checked" type="checkbox"/>
<input type="checkbox"/>
<input type="checkbox"/>
ity Codes

Dist	Avail and / or Special
A-1	

3.5 Phase Correction for CNR	45
3.5.1 Phase correction	45
3.5.2 Simulation	46
3.6 Phase-Corrected Coherent Noise Reduction Results	49
3.6.1 PC-CNR for FM radar data	49
3.6.2 PC-CNR for wideband step-frequency data.....	52
3.7 Computing Backscattering Coefficients	55
3.8 Summary	56

CHAPTER 4 - RADAR BACKSCATTER MEASUREMENTS AT THE ONSET OF FREEZE-UP

4.1 IAOE Experiment Description	58
4.2 Multiyear ice signatures during freeze-up	60
4.3 Radar Backscatter from young (thin) sea ice during IAOE	62
4.4 Comparison to quasi-laboratory measurements at CRREL	66
4.4.1 CRREL overview	66
4.4.2 Comparison CRREL measurements and field measurements of thin ice.....	67
Pancake Ice	68
4.5 Implications for spaceborne SAR measurements	71
4.5.1 RADARSAT	71
4.5.2 ERS-1	73
4.6 Multipolarization classification of thin ice	75
4.7 Summary	83

CHAPTER 5 - MODELING OF SCATTEROMETER

MEASUREMENTS AT THE ONSET OF FREEZE-UP	84
5.1 Effect of snow cover on radar backscatter during freeze-up.....	86
5.1.1 Volume scattering from snow	86
5.1.2 Radar backscatter from snow-covered saline ice at CRREL	88
High-resolution measurements from snow-covered saline ice	89
CRRELEX'92 Results	91

5.1.3 Effect of wet snow loss on radar backscatter during IAOE	94
5.2 Modeling of the effects of freeze-up with surface-only and volume-only scattering models	102
5.2.1 Surface-only scatter model of sea ice prior to freeze-up	103
5.2.2 Volume scatter model of sea ice after onset of freeze-up	106
5.3 Single-layer model for radar backscatter at the onset of freeze-up	108
5.3.1 Single layer model with rough surface boundaries	108
5.3.2 Comparison of model predictions and measurements	110
Multiyear sea ice backscatter modeling after freeze-up	111
Multiyear sea ice backscatter model prior to freeze-up	115
5.4 Summary	120

CHAPTER 6 - ERS-1 SAR INTERPRETATION FROM IN SITU

MEASUREMENTS AND MODELS	122
6.1 Introduction	122
6.2 ERS-1 SAR Description	123
6.3 Computing σ^0 from ERS-1 SAR Precision Image data	125
6.4 Comparison of ERS-1 SAR images and in situ measurements	126
6.4.1 SAR-derived σ^0 variation during freeze-up	126
6.4.2 Relevant scattering model results and MY observations from SAR	132
6.5 Summary	141

CHAPTER 7 - FUSION OF ACTIVE AND PASSIVE MICROWAVE DATA FOR REMOTE SENSING OF SEA ICE DURING FREEZE-UP

7.1 Introduction	142
7.2 Observations of passive microwave signatures during freeze-up with SSM/I	144
7.2.1 The DMSP SSM/I	145
7.2.2 Computing sea ice concentration with the NASA Team algorithm	146

7.2.3 SSM/I Observations in the eastern central Arctic during freeze-up.....	146
Co-locating SSM/I and ERS-1 SAR image data.....	147
SSM/I Observations	150
7.2.4 Relationship to freeze-up detected with SAR	155
7.3 Data Fusion Background.....	155
7.3.1 Data fusion for sea ice remote sensing.....	155
7.3.2 Data Fusion Architectures.....	156
7.4 Hybrid Decision-level Fusion Approach for Sea Ice Classification.....	159
7.4.1 Architecture for hybrid fusion process.....	159
7.4.2 Determination of multiyear ice concentration from ERS-1 SAR	160
7.4.3 Modification of NASA Team algorithm for ice classification with SSM/I	162
7.4.4 Results	164
7.4.5 Implications for heat transfer	179
7.5 Summary	184
CHAPTER 8 - SUMMARY AND RECOMMENDATIONS	185
8.1 Summary	185
8.2 Recommendations for future work	189
REFERENCES.....	191
APPENDIX A	204
APPENDIX B	212
APPENDIX C	232
APPENDIX D	243

LIST OF FIGURES

Figure 3.1 FM radar signal depiction.	15
Figure 3.2 Block diagram of a typical FM radar front-end with a single- antenna configuration.	17
Figure 3.3 Block diagram of FM radar RF section design. This design was implemented at C band and X band for performing radar backscatter measurements.	21
Figure 3.4 Block diagram describing both the C-band and Ku-band step- frequency radar system.	24
Figure 3.5 Block diagram illustrating an implementation of the CNR process.	31
Figure 3.6 FM-CW radar return from sea ice before (dashed) and after (solid) coherent noise reduction is applied.	33
Figure 3.7 Ku-band step-frequency radar data with coherent noise reduction.	35
Figure 3.8 Wideband step-frequency radar return from saline ice at CRREL before (dashed) and after (solid) coherent noise reduction is applied. This measurement was obtained at normal incidence to the ice surface.	37
Figure 3.9 Wideband step-frequency radar return from saline ice at CRREL before (dashed) and after (solid) coherent noise reduction is applied. This measurement was obtained at a 15° incidence angle.	37
Figure 3.10 Effect of variation in amplitude on the cancellation effect in coherent noise reduction. This shows the residual after subtracting two sinusoids whose amplitudes are related by V_2/V_1	39
Figure 3.11 Effect of phase variation on cancellation effect in coherent noise reduction. This shows the residual error after subtracting two sinusoids whose phase differs by ϕ degrees.	40
Figure 3.12 IF spectrum for the simulated radar return signal from four coherent targets.	47
Figure 3.13 IF spectrum of the difference between two measurements when a 5 MHz drift in oscillator frequency has occurred (solid curve). The spectrum from figure 3.12 is shown to demonstrate that there is no significant cancellation of the coherent target signals.	47
Figure 3.14 Spectrum of the filter output in the phase correction algorithm. The filter is necessary to locate a reference target to which the phase from both signals can be referenced.	48

Figure 3.15 Phase-corrected difference spectrum (solid curve) and original spectrum (dashed). This demonstrates the cancellation effect after applying phase correction. The resulting difference spectrum is improved over the result shown in figure 3.13.....	48
Figure 3.16 Result of coherent noise reduction with phase correction. The corrected IF spectrum is plotted along with the original to demonstrate the suppression of unwanted coherent noise spikes.....	50
Figure 3.17 Result of CNR with phase correction, compared to CNR without phase correction. This demonstrates that while there is some suppression (4 or 5 dB) of the unwanted signals, the phase correction improves the suppression by 10 to 15 dB.	51
Figure 3.18 Result from figure 3.17, plotted on a linear scale to illustrate the suppression of coherent noise in the IF spectrum.	51
Figure 3.19 PC-CNR for wideband, step-frequency radar measurements. The antenna reflection is reduced by 50 dB, compared to 25 dB for standard CNR.	53
Figure 3.20 Results from figure 3.19, plotted on a linear scale to demonstrate the dramatic improvement in the radar return. The original return is shown in (a) and the result of PC-CNR is shown in (b). The return power is normalized to the peak in both cases. Note that the antenna reflection (located at 0 ns) is actually reduced by 50 dB as shown in figure 3.19.	54
Figure 4.1 Cruise track for USCGC Polar Star for the IAOE experiment in August-September, 1991. Radar backscatter measurements were obtained for the portion of the cruise highlighted by thicker lines.....	59
Figure 4.2 Copolarized C-band backscatter coefficients from multiyear sea ice during the freeze-up. These ship-based measurements show a general increase in the backscatter during the portion of the freeze-up studied.	61
Figure 4.3 Air temperature variation measured from aboard the Polar Star for the period in which shipborne radar measurements were obtained. The solid line indicates hourly air temperature readings from the ship's log and the x's indicate air temperatures measured at several experiment sites during the expedition.	61
Figure 4.4 C-band backscattering coefficients from young sea ice measured during IAOE as a function of polarization.	64
Figure 4.5 Measurements of C-band σ^0 versus polarization from young first-year sea ice types.....	65
Figure 4.6 Radar backscattering coefficients for thin ice in the Arctic and ice sheets grown at CRREL. The similarities between these data suggest that knowledge and models based on the CRREL data may be useful in interpreting signatures from thin Arctic sea ice.	68

Figure 4.7 Backscatter coefficient of pancake ice from IAOE (box) and CRRELEX '95 (angular response). These data show that the laboratory experiment for simulating pancake ice agrees with field measurements at 35°	70
Figure 4.8 RADARSAT noise floor in relation to backscattering coefficient measurements of thin ice.....	72
Figure 4.9 ERS-1 SAR noise floor (extrapolated to 35°) in relation to backscattering coefficient measurements of thin ice.	74
Figure 4.10 Plot of from copolarized σ^0 versus cross-polarized σ^0 for thin ice categories.	76
Figure 4.11 Dependence of ice thickness on copolarized versus cross-polarized backscatter coefficient at Ku band at 45°. Data are from table VI of Livingstone, et al., 1987 and were obtained with a C-band scatterometer in mid-October, 1980.	77
Figure 4.12 Discrimination of low-salinity sea ice types by using σ^0 from vv and hv polarization at 5.4 GHz. {from Hyypä and Hallikainen [1992]}	79
Figure 4.13 Comparison of radar backscatter from open water at cross-wind in an Arctic polynya (IAOE) and cross-wind measurements from a tower-based scatterometer in the North Sea [Nordsee data from Moore, et al., 1984].	81
Figure 4.14 Plot of σ^0 from hh polarization versus vv polarization for thin ice categories.	82
Figure 5.1 Results of Rayleigh backscatter model for snow cover situations observed during IAOE'91. The snow parameters shown in table A-2 (Appendix A) were used for these computations. These demonstrate that the backscatter from the snow does not cause the dramatic increase in σ^0 observed during this experiment.	88
Figure 5.2 Plot of the returned power versus range from the compact range antenna for snow-covered saline ice (CRRELEX'94). The return from the air/snow interface and the snow/ice interface are clearly visible.....	90
Figure 5.3 Plot of the returned power versus range from the compact range antenna for bare saline ice (CRRELEX'94). The return from the ice surface is clearly visible.	90
Figure 5.4 Backscatter coefficient versus snow depth at 13.4 GHz. Measurements were obtained at CRREL's indoor pit facility in the 1992 experiment. The backscatter does not increase significantly with increasing snow depth, indicating that the volume scatter contribution from these snow layers is not significant.	92

Figure 5.5 Radar return as a function of range for the 21-cm deep snow pile measured during CRRELEX'92. This demonstrates that the snow volume is virtually transparent at Ku-band.	93
Figure 5.6 Results from figure 5.5, normalized and plotted on a linear scale.	94
Figure 5.7 Theoretical decrease in σ^0 at 5.3 GHz, vv polarization and 23° incidence angle versus snow volumetric moisture content cause by a uniformly distributed 5-cm wet snow layer over multiyear ice. {from [Winebrenner, et al., 1994]}	99
Figure 5.8 Our computation for loss due to wet snow using Mätzler's model. This is within 1 dB of the results from Winebrenner, et al., [1994] shown in figure 5.7.	100
Figure 5.9 Measurements and surface scattering theory for multiyear sea ice just prior to freeze-up. The σ^0 measurements are averaged from multiyear floes observed from JD 234-239. Surface scattering theory accounts for the backscatter signature under summer conditions.	105
Figure 5.10 Radar backscattering coefficients under freeze-up conditions compared with volume scattering theory. The theoretical surface scattering coefficient from figure 5.9 is shown for comparison. This demonstrates that the dominant backscattering mechanism after the onset of freeze-up is volume scattering.	107
Figure 5.11 Geometry for single-layer scattering model.	109
Figure 5.12 Comparison of scattering model with measurements from multiyear sea ice after the onset of freeze-up.	113
Figure 5.13 Theoretical comparison of surface scattering contribution to the total backscatter coefficient after the onset of freeze-up using the single-layer model.	114
Figure 5.14 Comparison of scattering model with measurements from multiyear sea ice before the onset of freeze-up.	118
Figure 5.15 Offset parabolic antenna radiation pattern at C-band. The copolarized pattern is solid and the cross-polarized pattern is dashed. [Gogineni, et al. 1990]	118
Figure 5.16 Theoretical comparison of surface scattering contribution to the total backscatter coefficient prior to the onset of freeze-up using the single-layer model.	119
Figure 6.1 ERS-1 SAR image frame prior to freeze-up from 21 August 1991 (JD 233). The image shows the falloff in intensity as the incidence angle increases from the left of the image to the right of the image.	128

Figure 6.2 ERS-1 SAR image frame from 6 September 1991 (JD 249). This image was taken during the initial stages of freeze-up from the same approximate area as figure 6.1. This image shows the increase in backscatter as the freeze-up commences.	129
Figure 6.3 ERS-1 SAR image frame from 12 September 1991 (JD 255). This image was taken well into the freeze-up period in the central portion of the Arctic. For the multiyear floes, the volume scattering is dominant, resulting in backscatter values in the -7 to -8 dB range and almost no incidence angle dependence.	130
Figure 6.4 Average backscattering coefficients computed from ERS-1 SAR images of sea ice. These results are the mean σ^0 over the entire image and demonstrate the same trend as the ship-based backscatter measurements shown in figure 4.2.	131
Figure 6.5 Mean σ^0 for multiyear floes within the SAR images studied. These are divided into near and far angles, indicating multiyear floes which appear below 23° and above 23°, respectively. This figure shows the same trend as the overall mean σ^0 in figure 6.4 and the ship-based σ^0 measurements of figure 4.2.	135
Figure 6.6 Slopes of backscattering coefficients derived from ERS-1 SAR images for both the overall image and the multiyear floes within the image. The slope changes from approximately -0.4 to -0.6 dB/degree during melt conditions, to approximately -0.1 dB/degree during freeze-up.	136
Figure 6.7 Histograms from SAR σ^0 images for 21 August (JD 233) through 28 August (JD 240), 1991.	138
Figure 6.8 Histograms from SAR σ^0 images for 29 August (JD 241) through 30 August (JD 242), 1991.	139
Figure 6.9 Histograms from SAR σ^0 images for 3 September (JD 246) through 12 September (JD 255), 1991.	140
Figure 7.1 Mean values of ice type concentration, derived from the NASA Team algorithm. The averages are computed for areas enclosed by the SAR images used in chapter 6.	150
Figure 7.2 Measured spectra for vertically-polarized (solid line) and horizontally-polarized (dashed line) emissivity spectra from 6.7 GHz to 90 GHz for three sites observed during CEAREX '88. {from [Grenfell, 1992]} The x-axis is frequency on a logarithmic scale and the y-axis is emissivity	152

Figure 7.3 Comparison of mean σ^0 values computed from the ERS-1 SAR images (from chapter 6) and the first-year ice concentration obtained with the NASA Team algorithm from SSM/I data.	154
Figure 7.4 Data fusion architectures for identity declaration from multiple sensors	157
Figure 7.5 Hybrid (multi-level) architecture for data fusion.	160
Figure 7.6 Example of a local-area histogram from ERS-1 SAR frame 1719 from 12 September, 1991. This demonstrates that distributions over local areas may show separate classes of targets, although the global distribution (figure 6.9) does not.	161
Figure 7.7 ERS-1 SAR frame number 1701 from 30 August 1991 (JD 242).	165
Figure 7.8 ERS-1 SAR frame number 1719 from 6 September 1991 (JD 249).	166
Figure 7.9 ERS-1 SAR frame number 1719 from 12 September 1991 (JD 255).	167
Figure 7.10 ERS-1 SAR frame number 1737 from 22 September 1991 (JD 265).	168
Figure 7.11 Result of dynamic local-area thresholding to determine multiyear ice concentration from ERS-1 SAR frame 1701, 30 August 1991 (JD 242).	169
Figure 7.12 Result of dynamic local-area thresholding to determine multiyear ice concentration from ERS-1 SAR frame 1719, 6 September 1991 (JD 249).	170
Figure 7.13 Result of dynamic local-area thresholding to determine multiyear ice concentration from ERS-1 SAR frame 1719, 12 September 1991 (JD 255).	171
Figure 7.14 Result of dynamic local-area thresholding to determine multiyear ice concentration from ERS-1 SAR frame 1737, 22 September 1991 (JD 265).	172
Figure 7.15 First-year and multiyear ice concentration estimates from fusion of ERS-1 SAR and SSM/I data for the region corresponding to the SAR image frame 1701 from 30 August (JD 242), 1991.	175
Figure 7.16 First-year and multiyear ice concentration estimates from fusion of ERS-1 SAR and SSM/I data for the region corresponding to the SAR image frame 1719 from 6 September (JD 249), 1991.	176
Figure 7.17 First-year and multiyear ice concentration estimates from fusion of ERS-1 SAR and SSM/I data for the region corresponding to the SAR image frame 1719 from 12 September (JD 255), 1991.	177

Figure 7.18 First-year and multiyear ice concentration estimates from fusion of ERS-1 SAR and SSM/I data for the region corresponding to the SAR image frame 1737 from 22 September (JD 265), 1991.	178
Figure 7.19 Spectral response of microwave emissivity from CRREL, 1990 for several ice thicknesses at V-pol (solid curves) and H-pol (dashed curves). {from [Wensnahan, et al., 1993]}. This figure shows the rapid changes in emissivity that occur during initial saline ice growth.	179
Figure 7.20 Mean values of PR and GR for young ice types tabulated in [Eppler, et al., 1992]. The thin ice signature evolves rapidly towards the first-year ice signature as ice growth exceeds 10 cm. OW = open water, FY = first-year, MY = multiyear, Pk=consolidated pancake ice (3cm), DN = dark nilas, GN = gray nilas, LN = light nilas.....	181
Figure 7.21 Estimated heat flux over a region containing a mixture of open water, FY and MY ice for mid-September as a function of first-year ice concentration, based on the tabulated results from Maykut [1978]. The first-year ice is assumed to be composed of ice thicknesses from 5 cm to 80 cm in equal amounts, open water is assumed to comprise 10 % of the area, and MY ice comprises the remainder. The results are normalized to the case in which there is no FY ice.	183

LIST OF TABLES

Table 3.1	C/X-band FM Radar System Parameters	22
Table 5.1	Total estimated losses due to absorption of wet snow for IAOE'91	98
Table 5.2	Model parameters for post-freeze-up case	112
Table 5.3	Model parameters for prior-to-freeze-up case.....	117
Table 6.1	ERS-1 SAR image mode parameters	124
Table 6.2	Model-based parameters relevant to ERS-1 SAR for freeze-up	133
Table 7.1	SSM/I-based ice concentrations.	151
Table 7.2	Mean results from NT algorithm and hybrid fusion	174
Table A-1	IAOE'91 RSL Scatterometer Data Summary	206
Table A-2	In situ snow measurements	207

ABSTRACT

The polar oceans play a key role in our climate because of the complex interactions between sea ice, open water and the atmosphere. Because of the persistent cloud cover and darkness in the Arctic for roughly half the year, the most viable means for monitoring sea ice on a global basis is with satellite microwave remote sensing instruments. The development of techniques for utilizing microwave remote sensing data depend on our understanding of the backscatter and emission properties of sea ice. Seasonal transitions are particularly difficult for interpretation of microwave scattering and emission from sea ice, due to the rapidly changing environmental conditions.

We investigated several key issues concerning the radar backscatter signatures of Arctic sea ice during the summer-to-fall transition and examined the potential for fusing active and passive microwave data for ice type concentration estimation.

To improve measurements made with short-range FM and step-frequency radar systems we developed coherent noise reduction techniques. We have demonstrated that these techniques are useful for a number of the systems designed for exploring the backscatter properties of sea ice. These coherent noise reduction methods improve the sensitivity of single-antenna radar systems by as much as 25 dB.

We obtained C-band measurements of radar backscatter from multiyear ice during the onset of freeze-up in the Arctic. Through the use of measurements of ice and snow physical properties and electromagnetic scattering models we determined the

scattering mechanisms responsible for the observed changes in radar backscatter. The refreezing of moisture on or near the ice surface of multiyear ice causes a decrease in the lossy part of the permittivity of the ice. This allows more energy to penetrate into the sea ice volume, which results in increased volume scattering. This results in a dramatic increase in the radar backscatter from sea ice at the onset of freeze-up. We demonstrated that these changes are also observed on a large scale from satellite synthetic aperture radar (SAR) data and can be used to detect the onset of freeze-up in the Arctic.

Finally, we utilized a technique to combine active and passive microwave data for estimating ice type concentration during the freeze-up season. This technique uses multiyear ice concentrations, obtained by analysis of ERS-1 SAR data. The multiyear ice concentration, derived from the SAR data, is used to constrain a multispectral algorithm for determining ice type concentration from satellite passive microwave data. According to ship-based ice observations the "fused" estimates of first-year ice concentration appear to be more accurate than estimates based on the SSM/I data alone.

CHAPTER 1

INTRODUCTION

1.1 Motivation

The impact of humankind on our environment has sparked interest into the understanding of the earth's climate and how different components of our earth system affect it. Historically, there have been dramatic changes in our planet's climate, from rather warm periods to ice ages. The hydrosphere, cryosphere, atmosphere and geosphere interact in a complex and delicate manner to produce the state of our climate. The polar oceans, in particular, play a key role in the earth's climate due to the complex interaction between sea ice (floating, frozen ocean), open water and the atmosphere. Heat exchange between the ocean and the atmosphere is modulated by the sea ice separating them. The heat exchange also depends on the thickness and morphology of the sea ice. In the Arctic, sea ice covers approximately 14.8 million square kilometers at its average maximum extent in winter and 7.8 million square kilometers at its average minimum extent in summer [Parkinson, et al., 1987]. The change in the amount of the Arctic ocean that is covered by sea ice throughout a year is roughly the size of the contiguous 48 states of the US. So, globally, the Arctic sea ice cover is significant in determining the heat exchange at the earth's surface. Thus, climate change is influenced by the Arctic sea ice cover.

Sea ice also plays a key role in the climate because it affects the amount of short-wave radiation from the sun that is absorbed at the earth's surface. When sea ice is

present, it can reflect up to 90% of the incoming radiation [Grenfell, 1983]. When sea ice is absent the ocean absorbs most of the incoming radiation, reflecting only a small percentage of it. Therefore, one component of the net energy absorbed by the earth is controlled by the Arctic sea ice cover. In a global warming scenario the earth would be retaining more heat energy than normal. This warming may cause a significant decrease in the sea ice cover. This will in turn allow for increased absorption of short-wave radiation through the polar oceans. This positive feedback effect can enhance the heating effect in a global warming scenario. Likewise, if the earth were to be cooling, the amount of sea ice cover would likely increase. This increase in sea ice extent would not allow as much radiation to be absorbed into the polar oceans. This is also a positive feedback effect, which could enhance the cooling effect in a global cooling scenario. Thus, the interaction between the polar ocean, sea ice, and the atmosphere can cause amplification of changes in the global climate. This effect has been termed "polar amplification" of global climate change by some researchers [Houghton, et al., 1990].

In addition to playing an important role in the long-term climate of our planet, the sea ice cover is an input variable to shorter-term weather patterns, such as the production of Arctic lows due to the interaction of open ocean and atmosphere near the ice edge [Gloersen, et al., 1992]. This sharp boundary is capable of triggering harsh weather conditions, given the proper atmospheric conditions.

Sea ice also affects shipping and offshore exploration in the Polar regions. Sea ice can reach several meters in thickness, thus creating an impediment to ship traffic. The ability to explore offshore oil reserves in ice-infested oceans is also affected by

sea ice cover. Therefore monitoring and understanding of sea ice mechanics and dynamics is important in both shipping and offshore exploration.

Because of the importance of sea ice in the study of global change, both as an indicator and as an active participant through positive feedback mechanisms, the global monitoring of sea ice is vital in understanding our earth system. Its role as an impediment to ship traffic and offshore exploration also makes the observation of sea ice on a large scale important. Monitoring of sea ice on a global scale is best accomplished with satellite remote sensors. Millions of dollars have been spent on investigating properties of the Arctic through field experiments. These "point" measurements have been important in giving us knowledge on the basic understanding of Arctic processes, but do not provide the large-scale view afforded by satellite sensors.

Since the Arctic is dark for roughly half of the year and clouds are omnipresent, visible and infrared (IR) sensors are not well-suited for monitoring sea ice. Both active (radar) and passive (radiometer) microwave sensors are capable of penetrating through cloud cover and through darkness and provide the only means of monitoring sea ice in all weather conditions and in all seasons from space.

1.2 Objectives

The primary objectives of this work are: (1) to develop radar signal processing techniques, which significantly improve *in situ* measurements obtained with short-range radar systems, (2) to determine the physical mechanisms responsible for

changes in radar backscatter from sea ice observed during the transition from summer melt to fall freeze-up, (3) to extrapolate *in situ* measurements and scattering models to interpretation of satellite-based synthetic aperture radar imagery, and (4) to study the feasibility of combining active and passive microwave data for sea ice concentration estimates during the freeze-up season.

1.3 Approach and Overview

The key observational sea ice parameters for use in dynamic and thermodynamic models and in monitoring climate change include concentration, thickness, ice type, and surface properties. The key surface properties are albedo, snow cover and temperature. In addition, the kinematics of sea ice, including drift velocity are important in these models [Preller, et al., 1992]. To effectively utilize data from satellite remote sensing instruments there is a need for valid, automated algorithms to extract the geophysical parameters of sea ice. At present, image interpretation is manual and time-consuming and automated classification algorithms for SAR, based on intensity differences, have been developed for distinguishing between three basic ice classes during Arctic winter [Kwok, et al., 1992a]. There are key processes during the seasonal transitions that affect the ice-ocean brine fluxes in early winter. In addition, the amount of new ice that forms during the freeze-up period can affect the annual cycle of energy fluxes between the ocean and atmosphere in the Arctic [Gogineni, et al., 1992]. Because of the key geophysical changes that occur and the lack of algorithms for sea ice during the seasonal transitions this is a key time period for study of microwave signatures of sea ice. In this study the focus is on determining

conditions responsible for changes in backscatter during the seasonal transitions, based on *in situ* radar measurements, ice properties and satellite SAR measurements.

A combination of high-quality radar backscatter measurements, appropriate scattering models, and physical property measurements of snow and sea ice is necessary for determining the physical mechanisms responsible for active microwave signatures of sea ice. Satellite-based radars, particularly synthetic aperture radar (SAR) systems, are useful for global monitoring of sea ice. Proper interpretation of data from these sensors and the utilization of these data for extracting geophysical parameters of sea ice are dependent on understanding the physical mechanisms which govern radar backscatter. The issues we address in this work concerning sea ice remote sensing are described below.

We briefly discuss the satellite microwave instruments used for sea ice remote sensing and give an overview of previous backscatter measurements obtained in the Arctic in chapter 2.

In chapter 3 we develop coherent noise reduction techniques to improve the quality of radar backscatter measurements. These techniques are designed for short-range radar systems, particularly frequency-modulated (FM) and step-frequency radars. The sensitivity of short-range radars is limited by reflection and feedthrough signals, rather than by thermal noise. The application of these signal processing methods pushes the noise floor of FM and step-frequency radar measurements much closer to the thermal noise floor than with standard processing. The coherent noise reduction techniques we have developed do not require an independent measurement of background noise by pointing the radar at the sky. This measurement is often

difficult to obtain in field experiments because of the physical limitations of the antenna mount. Also, moving the antenna to a new position to obtain this measurement may result in flexing of the cables that couple the radar system to the antenna. This flexing introduces a degradation of the coherency of the primary antenna reflection. The techniques we developed require only the actual measurements over the target of interest.

In chapter 4 we present field measurements of radar backscatter from multiyear ice during the onset of freeze-up. To the best of our knowledge, these are the first *in situ* C-band backscatter measurements that have captured the change in backscatter that occurs at the onset of freeze-up in the deep Arctic. Also, few *in situ* measurements of Arctic sea ice in the thickness range of 1 to 15 cm appear in the literature, [Tucker, et al., 1991; Grenfell, et al., 1992;] particularly at C band. Most of our knowledge of the backscatter characteristics of thin ice is based on laboratory measurements from artificial sea ice at CRREL [Swift, et al., 1992; Gogineni, et al., 1991; Onstott, 1992b]. We obtained measurements over thin Arctic sea ice in the thickness range of 1 to 15 cm. We used these measurements to quantify the capability of existing and planned spaceborne radar systems for observing thin Arctic sea ice.

In chapter 5, the measurements from multiyear ice are used, along with appropriate scattering models, for interpreting the radar backscatter signatures of multiyear ice during the summer-to-fall transition. The change in the signature is caused by the refreezing of moisture in the upper layers of the ice, allowing for increased penetration of electromagnetic energy into the sea ice volume. Therefore, the backscatter is primarily due to surface scattering prior to freeze-up and volume scattering after the onset of freeze-up. This effect is demonstrated through the use of

scattering models, whose parameters are based on measurements of the ice and snow properties at the time of the radar measurements. These *in situ* measurements and model results are then used in the interpretation of satellite SAR imagery in chapter 6. The changes observed from *in situ* measurements are also observed in the satellite SAR data. We demonstrate that the SAR data are useful for detecting the transition from the summer melt period into the Fall freeze-up.

It has been speculated that the combination of active and passive microwave measurements should lead to improved extraction of the key sea ice parameters. In chapter 7 the fusion of satellite active and passive microwave measurements for extracting geophysical parameters of interest is investigated, with the emphasis on combining the information from the current spaceborne microwave remote sensing instruments: ERS-1 SAR and SSM/I. The key issue affecting fusion of ERS-1 SAR and SSM/I data is the vast difference in resolution between the two instruments. Standard data fusion approaches for combining multisensor information typically require data that have similar resolution characteristics. The approach used here for overcoming the resolution problem is to combine the data for a fused estimate of ice types at the knowledge or information level. We demonstrate that the data from satellite active and passive microwave instruments can be combined using a hybrid fusion technique. Our method utilizes multiyear ice concentration, derived from SAR data, to constrain an augmentation of an existing passive microwave ice classification algorithm. Our results show that the approach yields significant improvement in the estimates of ice type concentration during the freeze-up season.

CHAPTER 2

STATUS OF MICROWAVE REMOTE SENSING OF SEA ICE

2.1 Satellite SAR and Imaging Microwave Radiometers

2.1.1 Spaceborne Synthetic Aperture Radars

Currently, the synthetic aperture radar (SAR) on board the European Space Agency's Remote Sensing Satellite, ERS-1 is obtaining active microwave images over the polar regions. This SAR operates at 5.3 GHz with a single polarization (vv). This sensor has been operating since June, 1991 and will be followed-up with another satellite, ERS-2, which will carry an identical sensor. The Japanese Earth Resources Satellite (JERS-1) was launched in early 1992 and carries an L-band hh-polarized SAR. These satellite SAR systems will soon be accompanied by Canada's RADARSAT, scheduled for launch in 1995, which will also carry a SAR at 5.3 GHz, but with hh polarization. These are the only western satellite SAR systems for extensive monitoring of sea ice since the Seasat SAR, which operated for a few months in 1978. In addition to the western satellite SAR programs, the Russian satellite Okean includes an X-band real-aperture radar and the Priroda module carries an X-band SAR.

Currently, algorithms are in place for the tracking of ice motion and estimating ice types from spaceborne SAR imagery, with some limitations. A number of algorithms for tracking sea ice from limited digital SAR image data sets have been developed. Using cross-correlation of image intensities from image to image at different

resolution scales (by averaging to degrade the resolution) Fily and Rothrock [1987] and Vesecky, et al. [1988] have determined ice motion from digital Seasat SAR data. Collins and Emery [1988] have used similar techniques based on Seasat SAR imagery. An operational ice motion detection algorithm has been implemented at the Alaska SAR Facility (ASF) for use with ERS-1 SAR data. This system is described in detail by Kwok, et al. [1990] and Holt, et al. [1992].

Maps of ice type and concentration are currently being generated from ERS-1 SAR data at ASF's geophysical processor system (GPS). The algorithm is described in Kwok, et al. [1992a and 1992b] and is based on image intensities. This algorithm only works during the winter months and does not distinguish between various classes of thin sea ice. Algorithms that are valid for the seasonal transitions between summer melt and fall freeze-up are virtually non-existent.

2.1.2 Spaceborne Microwave Radiometers

While the consistent use of spaceborne SAR for monitoring sea ice has only recently come to pass, microwave radiometers for monitoring sea ice have been flying on satellites since the early 1970's. Beginning with the Electrically Scanning Microwave Radiometer (ESMR) on the NASA Nimbus 5 spacecraft there have been almost continuous satellite passive microwave measurements since 1972. ESMR was operational from 1973 to 1976. This single-frequency, single-polarization sensor was followed in 1978 by the Scanning Multichannel Microwave Radiometer (SMMR) on board the Nimbus 7 satellite. The SMMR operated from 1978 to 1987 at five different microwave frequencies (6.6, 10.7, 18, 21, 37 GHz), each with dual polarization. This sensor allowed for accurate estimates of both multiyear sea ice concentrations and physical temperatures of sea ice, as well as significant

improvement over ESMR for ice extent, and ice concentration. Since 1987 the Defense Meteorological Satellite Program (DMSP) Special Sensor Microwave/Imager (SSM/I) sensors have been providing passive-microwave images at both polarizations at three microwave frequencies, (19.4, 37.0, and 85.5 GHz) and vertical polarization at one frequency (22.2 GHz). This sensor extends the frequency range of SMMR and also has improved radiometric resolution. The resolution of the SSM/I is nominally 12.5 km to 45 km. Because of the poor resolution, most pixels from SSM/I images contain a combination of two or more ice types.

Algorithms for measuring ice concentration and ice type have been developed for ESMR data [Zwally, et al., 1983] and [Parkinson, et al. 1987]. These are based on the linear relationship between the measured brightness temperature from a mixed pixel and the brightness temperatures of the different materials weighted by their concentration. This concept has been extended for use with multichannel, multi-frequency passive microwave data (for SMMR and SSM/I) in the NASA team algorithm [Cavalieri, et al., 1984]. Both the ESMR and NASA team algorithm depend on empirical tie points, which are based on the brightness temperatures of pure sea ice types measured by the satellite radiometer through the Arctic atmosphere. Other algorithms for estimating ice concentration and surface temperature from SSM/I data include the AES-York algorithm, the NORSEX algorithm, the bootstrap algorithm, and the U-MASS algorithm [Steffen, et al., 1992].

2.2 Near-surface and air-based measurements

There have been many field experiments to study the microwave characteristics of Arctic sea ice. A comprehensive discussion of previous backscatter measurements is provided by Onstott [1992]. Here, we will briefly outline a number of experiments that have been performed over the last three decades, with emphasis on measurements during seasonal transitions.

The first measurements to investigate the radar scattering characteristics of sea ice were acquired by the Naval Research Laboratory in 1956 off the coast of Greenland with 400 MHz and 10 GHz radar [Onstott, 1992]. The first attempt to map sea ice came when Anderson [1966] determined that first-year and multiyear ice could be distinguished in side-looking radar (SLAR) images. Since these measurements, a number of campaigns have been carried out with the aim of determining the backscatter characteristics of sea ice under a variety of conditions.

Beginning in the late 1960's more quantitative data were being acquired. Rouse [1969] used a Ku-band scatterometer in the Beaufort Sea in one of the first studies of ice type identification. Parashar [1977] performed backscatter measurements at P-band and Ku-band and compared these with Ku-band images. An early combination of airborne and surface-based measurements was also carried out during the US-USSR Bering Sea Experiment in 1973. Groups from USSR, including Loshchilov and Voyevodin [1972] also used SLAR for monitoring sea ice during the early 1970's. The potential for classifying several ice types by using angular information, along with the magnitude of the radar backscatter, was suggested by Gray, et al. [1977] based on measurements at Ku band.

These early experiments were followed by studies which included the combination of radar measurements with ice characterization. Groups from The University of Kansas (KU) made measurements off Point Barrow, Alaska in 1977 and 1978. In the early 1980's the Mould Bay experiments began investigation into the seasonal effect of sea ice on radar backscatter. These measurements demonstrated that rapid fluctuations in backscatter during the melt season are governed by surface properties, especially melt water [Gogineni, 1984; Onstott and Gogineni, 1985]. Livingstone, et al. [1987] characterized the radar backscatter signatures from early melt through advanced melt. SAR and scatterometer measurements at several frequencies were made during the Marginal Ice Zone Experiment (MIZEX) in the Fram Strait during summer, 1984 [Onstott, et al., 1987]. These experiments demonstrated the difficulty in distinguishing multiyear and first-year sea ice in the summer months with SAR.

The Labrador Ice Margin Experiments in 1987 and 1989 consisted of C- and X- band SAR data, along with surface measurements. These results were similar to the Mould Bay results in that the surface properties, particularly water, controlled the signature during melt. Significant differences in the SAR signatures from Mould Bay measurements demonstrated that regional differences in Arctic sea ice play a role in the summer signature [Gogineni, et al., 1992]. More recently, the Seasonal Sea Ice Monitoring Site (SIMS) program has been aimed at examining the seasonal changes in radar backscatter from early melt onset to advanced melt [Barber, et al. 1992]. The fall freeze-up season has been studied during the Coordinated Eastern Arctic Research Experiment (CEAREX). Here C-, L-, and X-band SAR imagery, along with in situ measurements at five frequencies were acquired during September, 1988 through March, 1989 [Onstott and Shuchman, 1990]. These measurements include

the seasonal changes from late in the fall freeze-up through winter and ceased just prior to significant melt onset. Other measurements during the late summer and freeze-up have been made at C band by Ulander and Carlström [1992] and Beaven and Gogineni [1994].

CHAPTER 3

FM RADAR SIGNAL PROCESSING: COHERENT NOISE REDUCTION

We have developed new coherent noise reduction techniques for improving measurements obtained with short-range, frequency-modulated, continuous-wave (FM-CW) radar systems and step-frequency radar systems. Concepts for FM-CW radar systems, details of the systems used in this study, and advances in noise reduction techniques for data obtained with these systems are presented in this chapter. Basic FM radar concepts necessary for the signal processing and noise reduction algorithms are presented in section 3.1 and the systems used in this study are described in section 3.2. The remainder of the chapter is devoted to the development, implementation, and results of coherent noise reduction (CNR) techniques we have developed for short-range radar systems. Typically, measurements in which no target is present, or "sky" measurements, have been used to determine the coherent noise sources. These measurements often are not feasible when performing measurements in the field because of limitations in the experiment set-up. In addition, the movement of the radar system to obtain these measurements often results in flexing of the cables used to couple the radar system with the antenna. This reduces the effectiveness of noise reduction with sky measurements. The noise reduction techniques developed here do not rely on the use of "sky" measurements, and have allowed us to process data obtained from past experiments which had been previously discarded due to low signal-to-noise ratio.

3.1 FM Radar Concepts

Frequency-modulated, continuous-wave (FM-CW) radar systems are used for *in situ* scatterometer measurements, primarily because of ease in range-gating with FM-CW radars versus implementing fast switches for pulsed radar systems. Additionally, since FM radars effectively have a 100% duty cycle, one obtains more average power than in pulsed radar systems. In an FM radar the carrier is modulated over some bandwidth. Typical FM modulation signals are a triangle wave, a sawtooth wave or a sinusoid. For the systems studied here, triangular modulation was used. In an FM radar, the reflected signal is compared to a sample of the transmitted signal to obtain a beat signal. For triangular modulation, the frequency of the transmitted and received signals for a single target is depicted by the diagram of figure 3.1. Here the solid line represents the modulation waveform for the transmitted signal and the dashed line represents the instantaneous frequency of the reflected waveform. Theory for linear FM-CW radar systems is well-documented and a good description appears in [Skolnik, 1980].

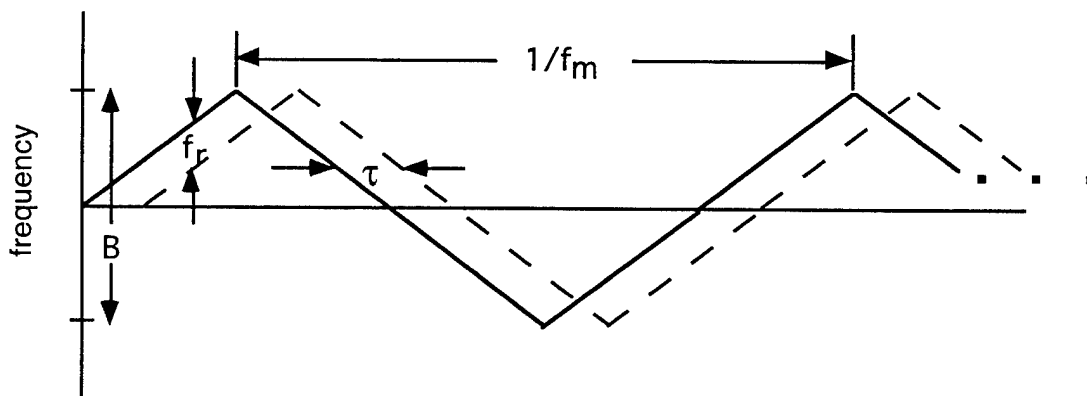


Figure 3.1 FM radar signal depiction.

The beat signal, $v(t)$, has a frequency that is equal to the difference in instantaneous frequency between the transmitted and received signals. If multiple targets are present at different ranges, the spectrum of $v(t)$ contains spectral components for each of these targets. For triangular modulation the frequency components are related to the range by

$$f_r = \frac{4Rf_m B}{c}, \quad (3-1)$$

where R is the range to the target, f_r is the beat frequency, f_m is the modulation frequency of the triangle wave, B is the bandwidth of the radio frequency (RF) signal, and c is the speed of light. The minimum range resolution, ΔR , obtained with an FM radar depends on the bandwidth transmitted,

$$\Delta R = \frac{c}{2B}. \quad (3-2)$$

By filtering the beat signal we can obtain range resolution, up to the minimum defined by equation 3-2.

Scatterometer systems may utilize single- or dual-antenna configurations. Single-antenna configurations utilize the same antenna for both transmission and reception, whereas dual-antenna systems use individual antennas for each purpose. Either configuration may be used to obtain up to four linear polarization combinations if dual-mode feeds are used. Unlike long-range and intermediate-range radar systems, the sensitivity of short-range radars are not limited by thermal noise, but rather by reflections and leakage signals from the antenna and RF section [Saunders, 1990]. These leakage signals and their sidelobes are the primary sources of unwanted signals (i.e. noise) in short-range FM radar systems. FM radars, like any band-limited radar system, suffer from range sidelobes. These range sidelobes are usually reduced by

applying a weighting (window) function to the transmitted or received signal. Typical window functions are the Hamming, Hanning, or Blackman windows.

A block diagram of a typical FM radar is shown in figure 3.2. The oscillator generates the FM radar signal according to the tune voltage applied to it, labeled FM modulation in figure 3.2. The tunable oscillator is typically a YIG-tuned oscillator or a varactor-tuned oscillator. The FM radar signal is then split using a power splitter or a directional coupler so that a portion of the signal is fed into the mixer. The rest of the signal is passed through a circulator and transmitted with an antenna. The signal is then reflected from the target(s) and received through the same antenna. The reflected signal travels through the circulator into the receive path of the RF section into the mixer. Here the reflected signal is mixed with the transmitted signal and filtered to obtain the IF signal.

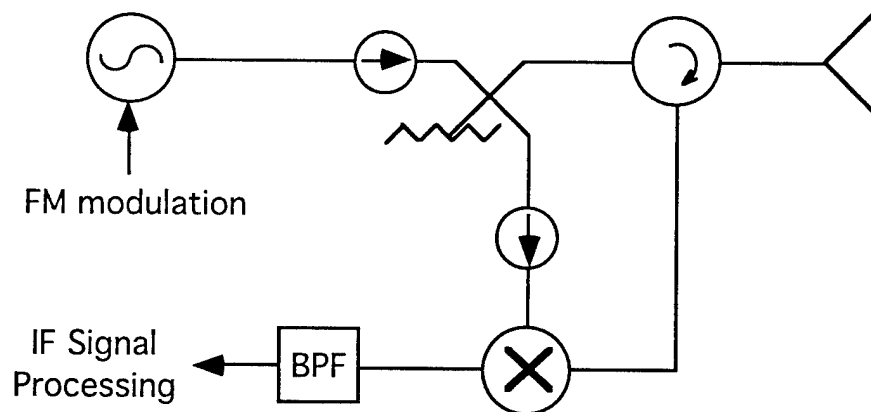


Figure 3.2 Block diagram of a typical FM radar front-end with a single-antenna configuration.

Single-antenna systems are especially vulnerable to reflections in the RF section and from the antenna feed. Even systems using antennas with 20-dB return loss have poor sensitivity due to the antenna reflection. As newer systems span ever-wider frequency ranges, matching the antenna becomes more difficult and sensitivity limitations due to the antenna reflection become even more important. Also, limited isolation of the circulator causes unwanted leakage signals as well to enter the receive path of the RF section. These leakage and reflected signals can also experience multiple reflections between various components in the RF section if not matched perfectly and cause secondary reflected signals. Even when range-gating techniques are used to suppress primary reflections, the secondary reflections may significantly reduce the sensitivity of the scatterometer system. The sensitivity of single antenna systems is limited by these reflected and leakage signals. Dual-antenna systems also are sensitivity-limited by reflections and leakage signals. The primary problem is due to leakage from the transmitting antenna into the receiving antenna. Although the magnitude of this leakage signal is considerably less than for single-antenna systems it can be several orders of magnitude larger than the returned power from the distributed target of interest.

Recently, measurements made with FM radar systems in the field and step-frequency radar systems at CRREL have been aimed at determining backscatter mechanisms from sea ice. These measurements require sensitive systems because of the low backscattering exhibited by the types of ice grown at CRREL, particularly at large incidence angles. To overcome the sensitivity limitations imposed on these scatterometer systems, various weighting techniques have been used to reduce the effect of sidelobes from these reflections on the measurement. Although windowing improves the spectrum, the sensitivity is still limited by the coherent reflections in the

system rather than the thermal noise floor. In this study, we have developed new techniques to reduce coherent reflections in FM and step frequency radar systems. These coherent noise reduction techniques improve the sensitivity of the system by approximately 10 to 20 dB, depending on the stability of the system.

3.2 Radar Systems Description

Several radar systems have been used as a part of this study for measuring backscatter from sea ice and for demonstrating various signal processing techniques. These include a triangular wave-modulated FM radar system and several implementations of step-frequency radar systems. These systems are described below.

3.2.1 C-/X-band FM Radar System

A dual-frequency FM radar system was used to perform radar backscatter measurements from Arctic sea ice during August-September 1991. This system included both a C-band and an X-band FM radar. Both systems were built with essentially identical radio frequency (RF) sections and this design is illustrated in figure 3.3.

The antenna used in this system was an offset-feed parabolic reflector antenna with two dual-polarized conical horn feeds. One feed operated at X band, the other at C band and both used ortho-mode transducers to achieve dual polarization. The YIG-tuned oscillator is used to generate the transmitter signal. It is modulated by applying a low-frequency waveform to its tuning port. A portion of the waveform is coupled into the quadrature mixer. The other portion of the RF signal is then fed to the

antennas via a series of switches and circulators. The switches are controlled by computer to switch between the different transmit and receive polarization combinations. The measurement of the radar return from all four linear polarization combinations (vv, hh, vh, hv) as well as a delay line measurement are possible with this scheme. Both the in-phase and quadrature (I and Q) signals are obtained by mixing the returned signal with the coupled portion of the transmitted signal with the quadrature mixer. The I and Q signals are fed into the IF section of the radar system, digitized, then stored onto disk. The IF section is also used to generate the triangle waveform, which drives the YIG-tuned oscillator and provides the triangular FM modulation. The characteristics of the systems are summarized in table 3.1.

The C/X-band FM radar system has been used in field experiments to measure radar backscattering coefficients from sea ice that are presented in chapter 4. The data from these systems were also used to develop, test, and demonstrate signal processing techniques developed as part of this work.

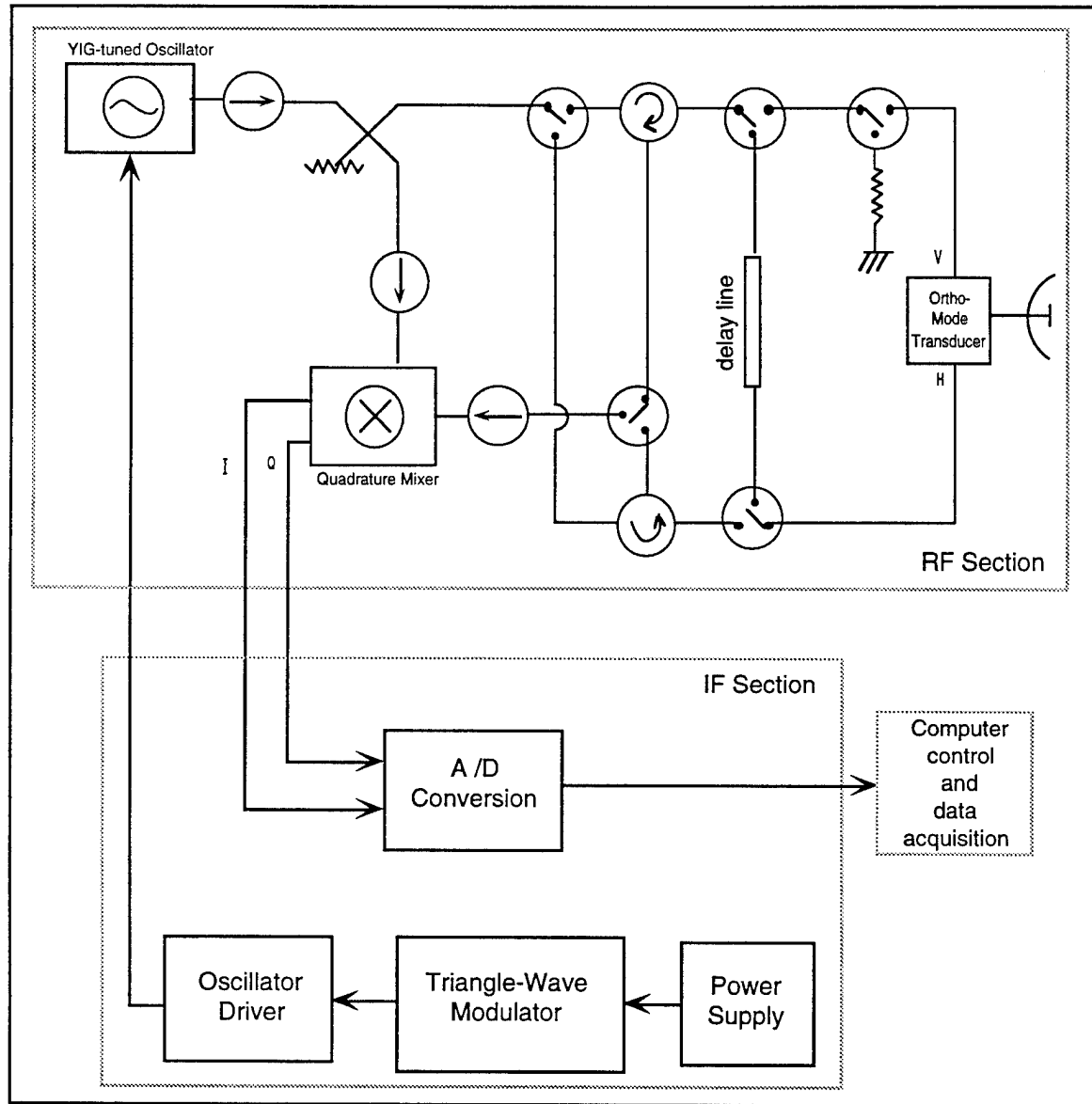


Figure 3.3 Block diagram of FM radar RF section design. This design was implemented at C band and X band for performing radar backscatter measurements.

Table 3.1 C/X-band FM Radar System Parameters		
	<u>C band</u>	<u>X band</u>
Center Frequency. (GHz)	6.2	11.3
RF Bandwidth (MHz)	300	300
Free-space Resolution (cm)	50	50
Antenna Beamwidth	6°	3°
Footprint in cm (23m range)	48 x 48	24 x 24
Transmit power (mW)	10	10

3.2.2 Step Frequency Radar Systems

Step-frequency radar systems were initially used as ground-penetrating radar systems [Iizuka, et al., 1984], and have since been used in many of the same applications as FM radars. Our step-frequency radar systems utilize network analyzers as their core, making them easy to implement. The network analyzer may be used with an appropriate antenna system and controller as a radar by itself. But, typically the network analyzer is used as a base-band radar and the actual radar signal is up-converted on transmission and down-converted on reception to the range of frequencies in which the network analyzer operates.

The principle of operation for step frequency radars has been described by [Iizuka, et al., 1984], and is summarized here. The voltage scattering coefficient from a given target can be obtained from the step-frequency radar measurement in the following manner. The amplitude and phase of the continuous wave at each of the discrete frequencies are measured by a network analyzer or similar device (either in S_{11} mode

or S21 mode, depending on the radar configuration). These measurements are usually stored on a disk to be processed as described below. The complex spectrum (usually FFT) of these data is related to the voltage scattering coefficient, s_k of a target by

$$h_k = \frac{Ns_k E_0}{z_k^2} e^{j(\frac{4\pi}{c})(kf_0 \Delta z)}, \quad (3-3)$$

where h_k is the complex spectral component of the measured data at point k , N is the total number of discrete points used over the bandwidth, E_0 is the incident electric field magnitude and z_k is the distance from the radar to the scattering point in question. The phase term is simply an unwrapping due to the propagation of the incident and reflected wave and is dependent on the specific frequency of the k^{th} measurement ($kf_0 \Delta z$). To obtain the power returned from a target the magnitude of the voltage scattering coefficients are squared. This is then used in the narrow-beam approximation to the radar equation as the returned power, from which the backscattering coefficient is computed (see section 3.6).

Several configurations of step-frequency radar systems were used in this study. Two systems used in this study, one at a center frequency of 5.3 GHz and another at a center frequency of 13.9 GHz were based on a Hewlett Packard HP8753 Vector Network Analyzer, Both systems up-converted the HP8753 output from a center frequency of 2 GHz to the appropriate frequency using an RF section described in the block diagram of figure 3.4. On receive, the signal is down-converted to the HP8753 frequency of 2 GHz. The network analyzer is typically stepped through 1 GHz of bandwidth in 2.5 MHz steps, although some C-band measurements have used only 500 MHz of bandwidth.

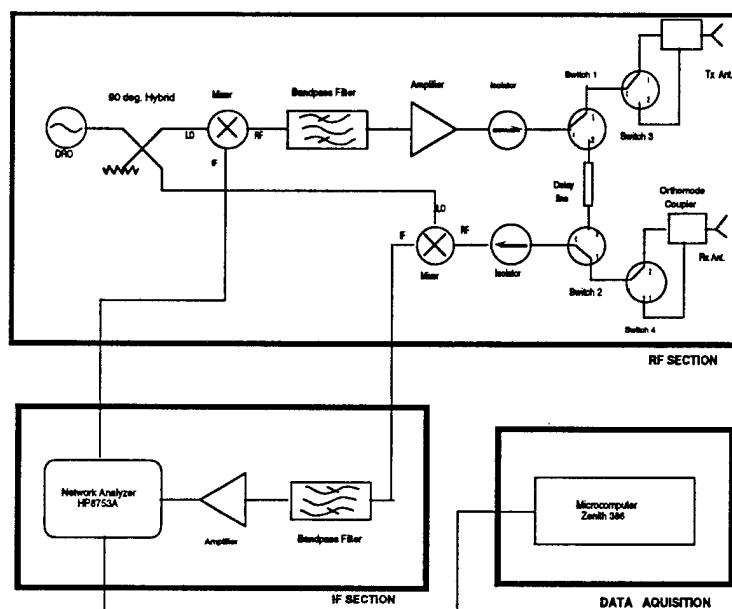


Figure 3.4 Block diagram describing both the C-band and Ku-band step-frequency radar system.

These systems have been used in conjunction with standard gain horns and diagonal horn antennas in several field and laboratory experiments [Lytle, et al., 1993; Beaven, et al., 1993]. The C-band and Ku-band step frequency systems are essentially identical. The source for each is a dielectric resonator oscillator (DRO) that operates at 11.9 GHz in the Ku-band system and 3.3 GHz in the C-band system. The output from the HP8753 is mixed with the output from the DRO in each case to up-convert to 5.3 GHz and 13.4 GHz for the C-band and Ku-band systems, respectively. After filtering and amplification, these are passed through a switching network to obtain four channels, two transmit channels and two receive channels (for vertical and horizontal polarization in each case). The reflected signal is passed through the switching network and fed into a second mixer. This mixer is also driven by a

coupled portion of the DRO output to down-convert the received signal to baseband (i.e. 1-2 GHz for the HP8753). The reflected signal is measured at baseband with the network analyzer. These measurements are controlled with a Hewlett Packard Interface Bus (HPIB) or similar expansion card (IEEE 488) and a computer program. The data are stored on disk through the HPIB for later processing.

Recently, a new technique for high-resolution, narrow beam radar measurements has been developed as a joint effort between the University of Kansas Radar Systems and Remote Sensing Laboratory (RSL), The ElectroScience Laboratory (ESL), and Byrd Polar Research Center (BPRC) at The Ohio State University. This system employs a specially-designed antenna for *in situ* radar measurements [Gogineni, et al., 1995]. The antenna operates by using the compact range concept to produce plane waves in the near field of an offset parabolic reflector antenna. The back end of this radar system is a Hewlett Packard HP8722C Vector Network Analyzer. The HP8722 is usually stepped from 2 to 18 GHz, to achieve sub-centimeter range resolution. This system uses the step frequency radar method described previously to determine scattered power as a function of range from the radar. This system has proven useful in determining primary scattering mechanisms in geophysical radar studies.

The C- and Ku-band step frequency radars, described here have been used in quasi-laboratory radar measurements of backscatter from saline ice. These measurements and their implications are described in chapter 6. Measurements obtained with the compact-range, high-resolution system are used in this chapter to demonstrate coherent noise reduction techniques. Some backscatter measurements made by this system are also presented in chapter 6.

3.3 Coherent Noise Reduction

As discussed in section 3.1, the primary limitation on the sensitivity of measurements with short-range FM radar systems is caused by range sidelobes from the antenna reflection, leakage through RF components, and multiple reflections in the RF section. These unwanted signals are much stronger than the reflections from the target(s) of interest (sometimes by 50 dB or more) and must be reduced sufficiently to attain maximum sensitivity. Weighting techniques can reduce the sidelobes (at the cost of reduced resolution and a decrease in peak signal power), but the sensitivity of the backscatter measurement is still limited by the reflection and leakage signals rather than by thermal noise. In this section, the theory and results of a coherent noise reduction (CNR) technique we developed to improve measurements obtained with short-range FM and step-frequency radar systems are presented.

3.3.1 Theoretical Development

For an FM radar, the beat signal for a single target takes the form,

$$v(t) = V \cos(2\pi f_r t + \theta), \quad (3-4)$$

where f_r is the beat frequency, defined by equation (3-1).

If multiple targets are present, the signal for multiple targets is a sum of the returns from individual targets and is given by,

$$v(t) = \sum_j V_j \cos(2\pi f_{r_j} t + \theta_j). \quad (3-5)$$

In both equation 3-4 and 3-5, the phase term accounts for a combination of scattering characteristics of the target, and systematic and random changes in phase induced by the system.

The IF signal for an FM scatterometer consists of two components: a coherent, non-random term and a random term. The coherent term comes from the antenna reflection, reflections in the system due to mismatches in the RF section, leakage signals, or reflections from unwanted target sources (e.g. nearby structures in a measurement set-up). The non-coherent, or random, term comes from the scattering from the distributed target of interest. The total signal from an individual measurement can be written as,

$$v(t) = V_0 \cos(\omega t + \theta_0) + A^n \cos(\omega t + \phi^n), \quad (3-6)$$

assuming V_0 and θ_0 are non-random (they remain constant from sample to sample), whereas A^n and ϕ^n are samples of independent random variables, A and ϕ . Here, A is normally distributed and ϕ is uniformly distributed between 0 and 2π . At any time t , the mean of the random process $v(t)$ is given by,

$$E\{v(t)\} = V_0 \cos(\omega t + \theta_0) + E\{A \cos(\omega t + \phi)\}, \quad (3-7)$$

since V_0 and θ_0 are deterministic [Gardner, 1986].

If A and ϕ are assumed to be independent and ϕ is uniformly-distributed from 0 to 2π , this reduces to

$$\begin{aligned} E\{v(t)\} &= V_0 \cos(\omega t + \theta_0) + E\{A\} \frac{1}{2\pi} \int_0^{2\pi} \cos(\omega t + \phi) d\phi \\ &= V_0 \cos(\omega t + \theta_0). \end{aligned} \quad (3-8)$$

Thus, the coherent term can be obtained by estimating the expected value of the random process $v(t)$. This is computed by coherently averaging over a set of measurements samples, which are typically obtained spatially. The coherent term estimate from equation 3-8 can be removed from the individual measurements by subtraction to obtain individual measurements containing essentially only the non-coherent term. The new signal $v_c(t)$ for the n^{th} measurement is then given by,

$$v_c(t) = v(t) - E\{v(t)\} = A^n \cos(\omega t + \phi^n), \quad (3-9)$$

which contains only the non-coherent term.

In the analysis above it was assumed that there was a single coherent term. The coherent term includes the antenna reflection and leakage signals, leakage through components in the RF section, and multiple reflections within the system. Therefore, multiple sources of coherent noise are present in a system. Also, if there is a distributed scattering target, there is a non-coherent term over some frequency band. If there are coherent and non-coherent components at a number of frequencies in the IF signal, then we can invoke superposition to show that the expected value at each frequency contains only the coherent term.

For multiple coherent terms and multiple non-coherent returns, the n^{th} radar return signal can be modeled (as in equation 3-6) as,

$$v^n(t) = \sum_j V_j \cos(\omega_j t + \theta_j) + \sum_k A_k^n \cos(\omega_k t + \phi_k^n). \quad (3-10)$$

In this case there are j frequencies containing systematic (coherent) signals and k frequencies containing the signal from a distributed target (non-coherent). The coherent noise reduction is applied by obtaining an estimate of the coherent signals. The expected value of $v(t)$ when multiple targets are present, is given by,

$$E\{v(t)\} = \sum_j V_j \cos(\omega_j t + \theta_j) + E\left\{\sum_k A_k \cos(\omega_k t + \phi_k)\right\}, \quad (3-11)$$

since the coherent terms do not vary from sample to sample. We have shown that the expected value of the non-coherent terms is zero if the phase is assumed to be uniformly distributed. Therefore, the expected value of the random process $v(t)$, which contains multiple coherent and non-coherent terms becomes,

$$E\{v(t)\} = \sum_j V_j \cos(\omega_j t + \theta_j). \quad (3-12)$$

To obtain an estimate of the coherent terms we average over a set of samples as described above. This estimate of the coherent noise is then subtracted from the individual radar measurements. This results in an estimate of the non-coherent scattering term for the n^{th} measurement,

$$v_c^n(t) = v^n(t) - E\{v(t)\} = \sum_j A_j^n \cos(\omega_j t + \phi_j^n), \quad (3-13)$$

in which systematic (coherent) effects are removed.

A block diagram describing the implementation of the CNR process is depicted in figure 3.5. Typically, we estimate the mean value (for all IF frequencies) by averaging over a number of samples (usually 4 to 10) of the IF waveforms from an FM radar system. These samples must be taken over a short enough time period such that the phase and frequency from the coherent signal sources remain invariant. The averaging process yields an estimate of the return from the coherent noise sources. This is then subtracted from each of the returns individually. Then the magnitudes of the individual non-coherent returns are averaged and used to compute the scattering coefficient as described in section 3.7.

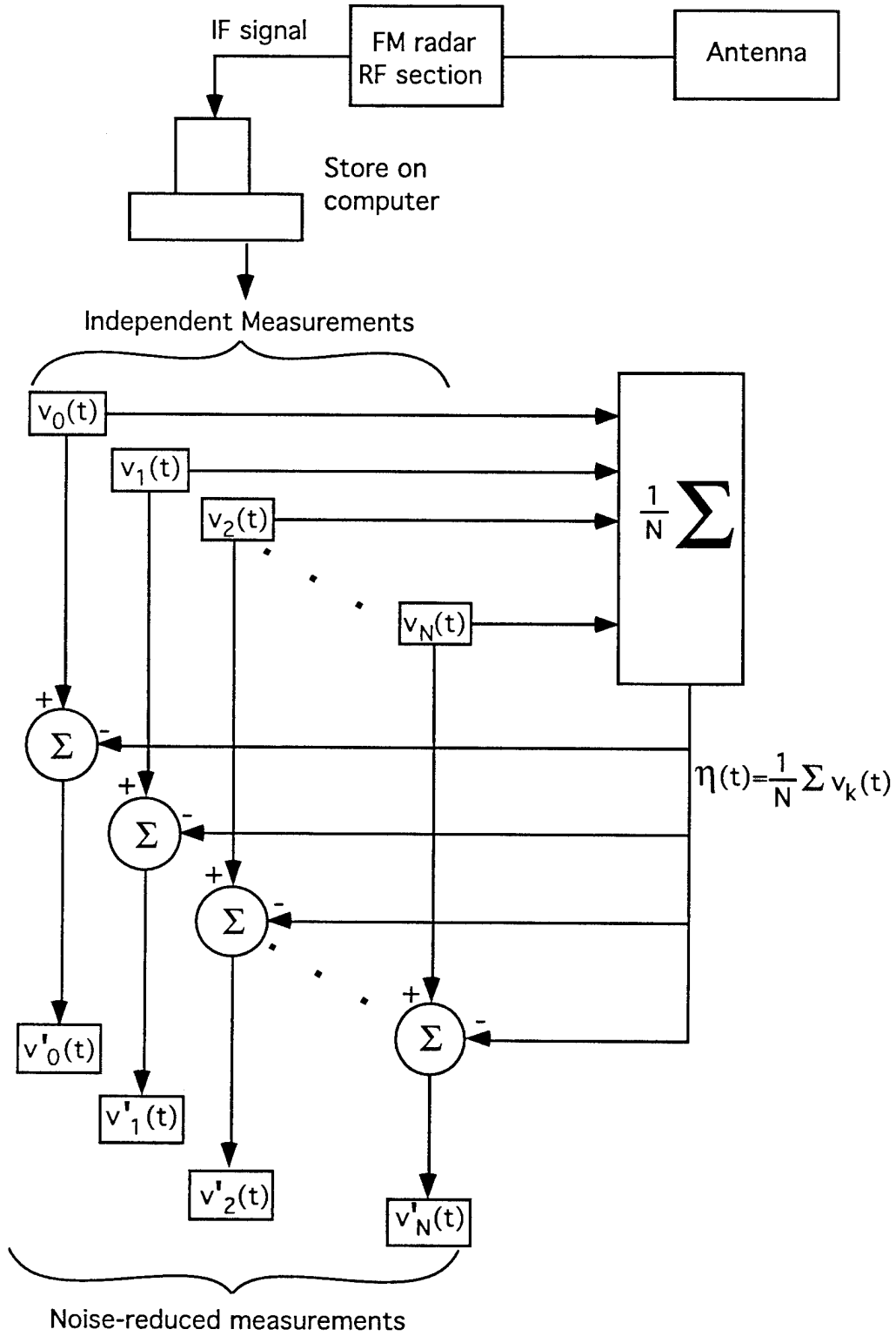


Figure 3.5 Block diagram illustrating an implementation of the CNR process.

3.3.2 Results

The CNR technique described in detail in the previous section has been applied to data from several radar systems. The C-band FM radar described in this chapter was used during IAOE to obtain radar backscatter measurements from sea ice. The IF signal for each measurement was sampled and stored on disk so that improvements in signal processing could be applied to the data after returning from the field. The coherent noise reduction technique was applied to the data obtained from this radar system and a sample of the results is shown in figure 3.6. Here, 18 radar returns were used to construct the estimate of coherent noise sources within the IF spectrum. The dashed line shows a sample of the IF spectrum before applying the CNR technique. (Since these data are from an FM radar system the frequency of the signal is proportional to range from the radar and this conversion has been used to produce this plot). Several unwanted "spikes" appear in the spectrum. These are caused by the primary antenna reflection as well as multiple reflections caused by mismatches in the RF sections. It was later discovered in the laboratory that poor cabling (i.e. "plumbing") in the RF section resulted in most of the mismatch problems. The result of applying CNR is shown in the solid line. This scheme reduces these unwanted signals by 10 to 15 dB, while retaining the return from the sea ice surface, which is located approximately 20 m from the radar antenna.

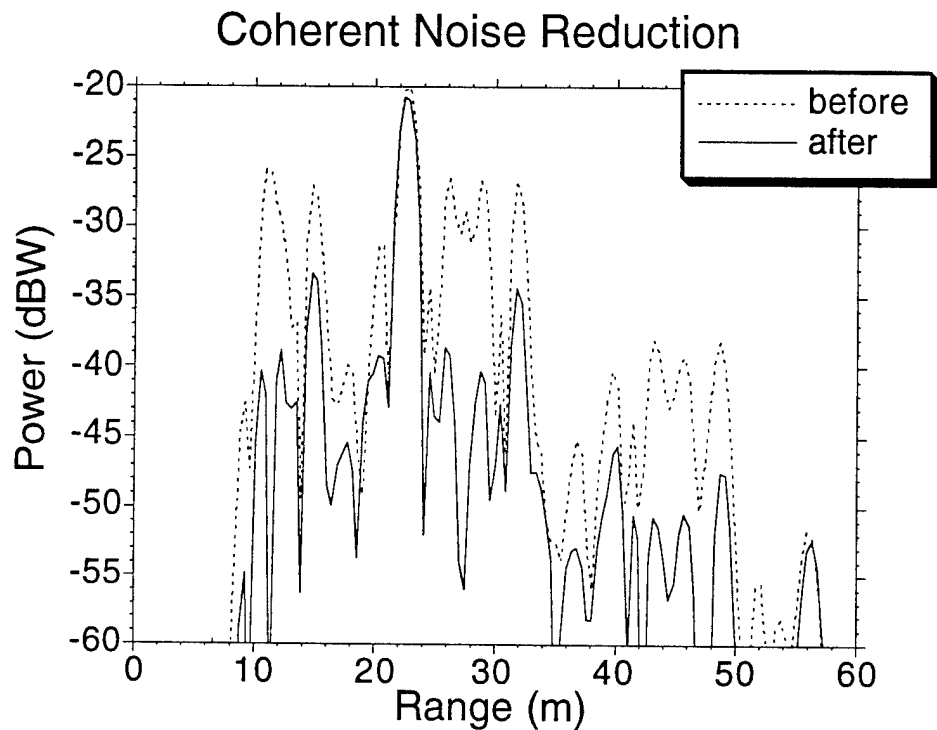


Figure 3.6 FM-CW radar return from sea ice before (dashed) and after (solid) coherent noise reduction is applied.

The CNR technique was developed for processing of FM radar data, but has also proven effective in reducing noise caused by antennas reflection and leakage signals for step-frequency radar data. As discussed in 3.3.2, step frequency radars are used in the same situations as FM radar systems and the signal processing is very similar. The primary difference is that an inverse Fourier transform is used to compute the spectrum for a step frequency radar system, rather than a forward transform. The only implication of this difference is that the spectrum is reversed when an inverse transform is used. Therefore the CNR developed for FM radar systems also may be applied to step-frequency systems. We have applied this technique to the data from

several configurations that are based on step-frequency techniques and these results are discussed below.

During experiments between 1990 and 1994, step-frequency radars were used to measure radar backscattering from saline ice sheets grown at CRREL [Beaven, et al., 1993; Kanagaratnam, et al., 1994; Beaven, et al., 1995]. These were network-analyzer-based systems that required RF sections for up- and down-conversion and one implementation is shown in figure 3.4. The CNR technique was used to reduce the effects of the reflection and leakage signals within this system. An example of the results of the CNR for step frequency data is shown in figure 3.7. Here the original spectrum is shown as a dashed curve and the result of CNR is shown as a solid curve. This demonstrates that CNR is also effective in reducing coherent noise sources inherent in step-frequency radar systems.

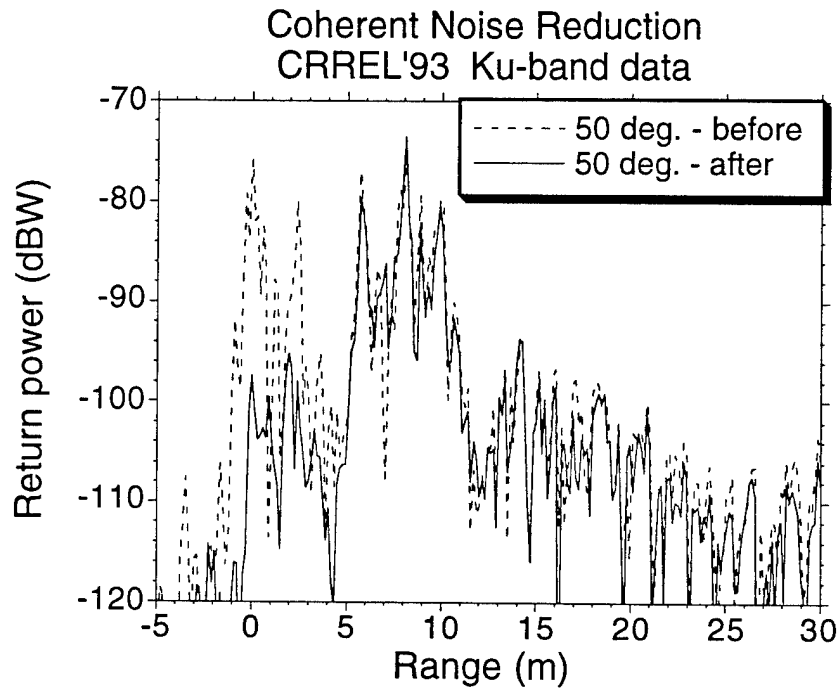


Figure 3.7 Ku-band step-frequency radar data with coherent noise reduction.

The most recent use of our CNR technique has been to reduce the systematic noise sources in the wideband measurements obtained with a new high-resolution system, based on the compact range antenna concept. Figure 3.8 shows the results of applying this scheme to measurements made in January 1994 at CRREL with the planewave, wideband system at normal incidence. Once again the spectrum prior to application of the CNR is shown as a dashed curve. The primary reflection from the antenna feed is the dominant source of unwanted signal. This is the large spike located at 0 ns (this reflection was used to calibrate to zero range). The sidelobes of this reflection are apparent throughout most of the spectrum and thus affect the measurement. The result of applying CNR to these data is shown as the solid line of figure 3.8. Here the primary reflection and its associated sidelobes are reduced

significantly. In this case the return from normal incidence (located at approximately 14 ns) is large enough that the CNR does not need to be used, but at larger incidence angles the scheme is necessary as will be demonstrated below.

Figure 3.9 shows a spectrum computed from data obtained with the wideband system at CRRELEX '94. In this case the measurements were made at 15° incidence angle, where the return from the ice is much lower than for normal incidence. Prior to applying CNR the spectrum shows a strong antenna reflection and the return from the ice is only slightly apparent above the noise level (dashed curve). Once the CNR is applied to these data the 15° return is very prominent in the spectrum (solid curve). Furthermore, the average noise level drops from approximately -75 dB to -100 dB for most of the spectrum when the CNR is used. Without this 25 dB improvement in SNR the measurement would have been useless.

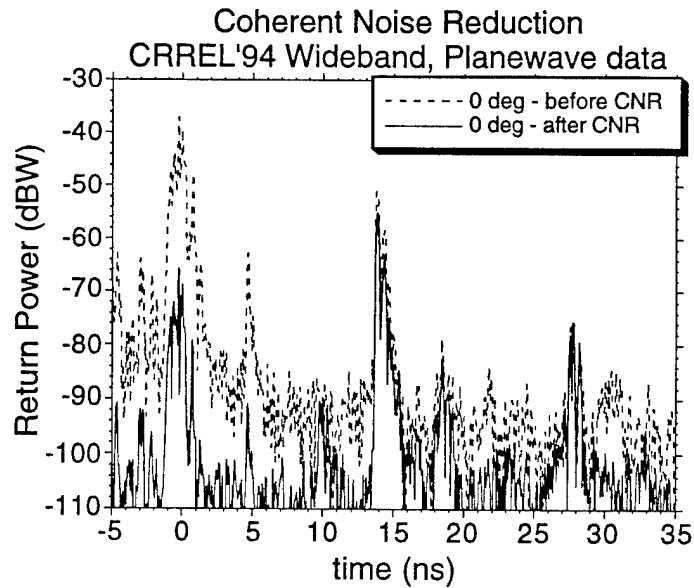


Figure 3.8 Wideband step-frequency radar return from saline ice at CRREL before (dashed) and after (solid) coherent noise reduction is applied. This measurement was obtained at normal incidence to the ice surface.

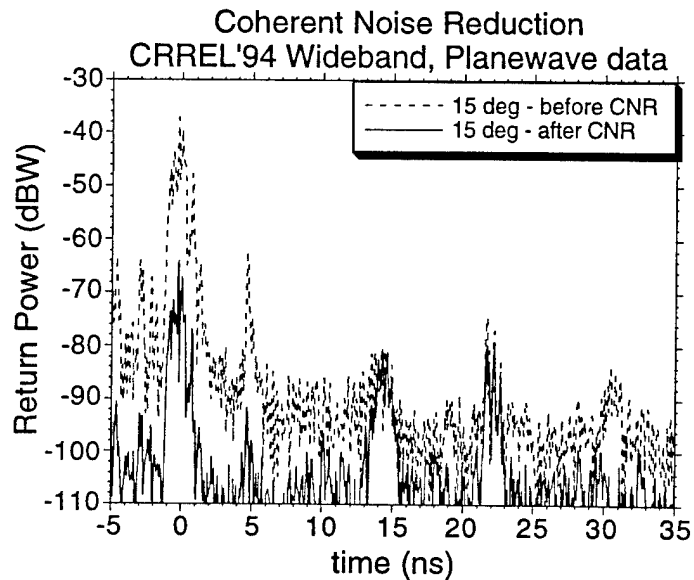


Figure 3.9 Wideband step-frequency radar return from saline ice at CRREL before (dashed) and after (solid) coherent noise reduction is applied. This measurement was obtained at a 15° incidence angle.

3.4 Phase and Amplitude Variations and CNR

The results presented thus far demonstrate that the CNR scheme is effective for reducing systematic noise sources inherent in FM and step frequency radar systems, and which limit the sensitivity of these systems. But, there are some cases when CNR is not effective for completely removing systematic noise spikes. The process works well when data are obtained over a short period of time, but degrades when data are separated by periods of time longer than several hours. Variations in amplitude and phase reduce the coherency of the noise sources, causing the degradation. If there is no variation in amplitude and phase from sample to sample, the coherent terms would be reduced to the thermal noise floor of the system. Variations in the unwanted leakage and reflected signals limit the capability of the CNR scheme. In this section the effect of phase and amplitude and phase variations on the cancellation effect of CNR is demonstrated quantitatively. Then, sources of these variations in FM radar systems are explored.

3.4.1 Effect of phase and amplitude drifts on CNR

To quantify the effect of variations in amplitude and frequency on the CNR scheme the following computation was carried out. A measure of the canceling capability of the CNR is the difference between two sinusoids when their amplitudes and/or phases vary slightly. The magnitude of the difference between two samples of a coherent signal is ideally 0 ($-\infty$ dB). Figure 3.10 shows the difference between two samples of a coherent signal as a function of the ratio of the amplitudes of the two signals. The first sample is assumed to have a magnitude of unity and the second sample has a magnitude varying from 1 to 2 in this example. This demonstrates that to achieve a

cancellation of at least 20 dB, the amplitude of the signal must not change by more than approximately 10%. In this case the phases are assumed to be equal. This implies that for ideally phase-stable systems an SNR of 10 dB is required to achieve a 20 dB cancellation of the coherent signal. The primary reflections in FM scatterometers are typically the strongest signals in the spectrum, so this is usually exceeded.

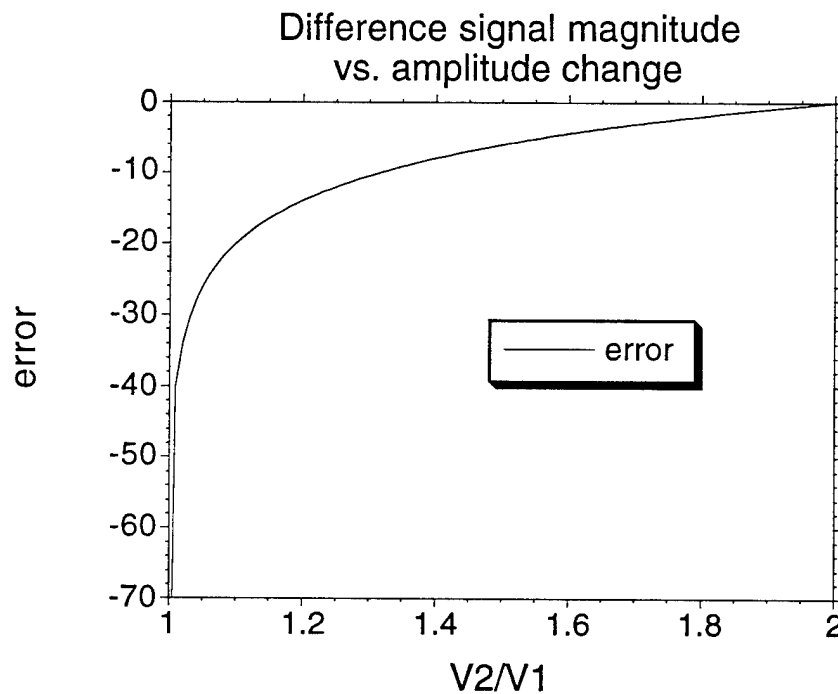


Figure 3.10 Effect of variation in amplitude on the cancellation effect in coherent noise reduction. This shows the residual after subtracting two sinusoids whose amplitudes are related by V_2/V_1 .

To investigate the effect of phase variations on the cancellation effect of CNR a similar computation was used. In this case the amplitudes were assumed to be constant and the phase difference between the signals was varied from 0 to 30° and the result is shown in figure 3.11. This demonstrates that to obtain a cancellation of at least 20 dB, the phase variation from sample to sample must be less than 6°. Therefore the system must be coherent to within this margin over the period of time in which measurements are obtained.

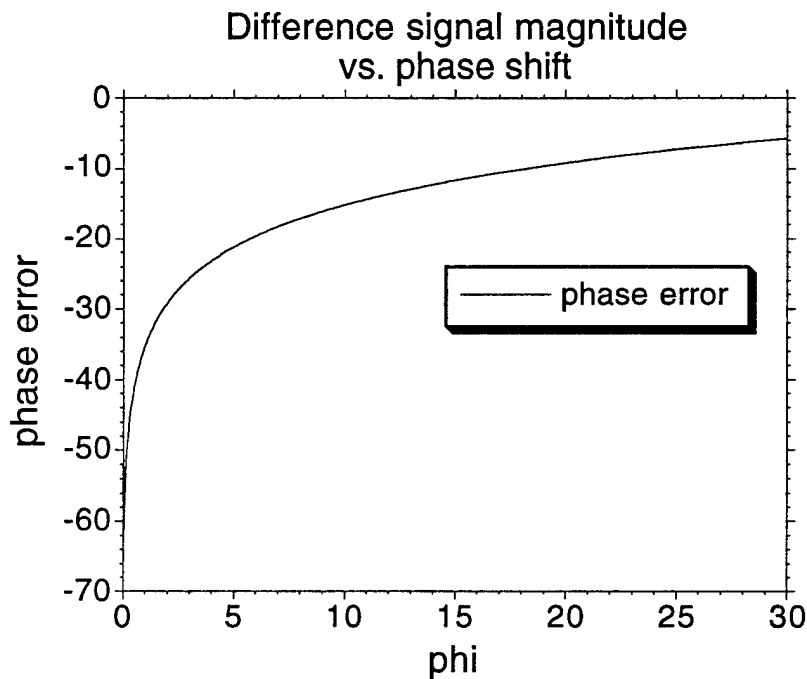


Figure 3.11 Effect of phase variation on cancellation effect in coherent noise reduction. This shows the residual error after subtracting two sinusoids whose phase differs by ϕ degrees.

3.4.2 Sources of phase variation in the IF signal

The above results demonstrate the effect of amplitude and phase changes from measurement to measurement on the cancellation effect in the CNR scheme. These show that phase variations from measurement to measurement limit the effectiveness of any coherent processing that may be performed on radar data. Phase variations from systematic sources may be caused by several sources. Variations or drift in the oscillator frequency and random noise are potential causes of phase and magnitude variations between radar measurements. Also, phase shifts through coaxial cables are highly temperature-dependent, as are many system components. Any temperature changes may result in phase variations over time in FM radar systems.

Random noise results in variations in both amplitude and phase that are dependent on the relative magnitudes of the unwanted systematic signal and the noise. When the magnitudes of the unwanted signals (i.e. coherent noise sources) are much higher than the noise level, the random noise effect on the amplitude and phase is small. The effect of SNR on magnitude variations was discussed above.

Changes in the phase through coaxial cable may be caused by temperature changes, as well as flexing of the cables. These changes in the phase shift may be significant depending on the temperature variation and the quality of the cables used. The phase shift variation of typical cables is strongly dependent on temperature. A temperature change of 5° C in 5 meters of typical semi-rigid cable results in a phase shift of nearly 10° at 10 GHz [Gore and Associates, Inc. technical note, 1990]. The phase deviation due to cable flexing may also cause an additional 2° to 3° phase deviation, even for high-quality cables [Gore and Associates, 1990]. Cable flexing and temperature

deviations are always present in field measurements and therefore their effect on CNR processing may be considerable. We have shown previously that a 10° phase shift can significantly reduce the cancellation effect in the CNR process.

Effect of oscillator drift

Oscillator drift also causes a change in the phase of the IF signal from measurement to measurement. Therefore, the capability of any coherent processing, such as CNR may be limited by the frequency stability of the oscillator. The relationship between oscillator drift and phase variation of the IF signal is explored here.

For a linear FM radar the frequency of the transmitted signal is given by,

$$\omega(t) = \omega_1 + \frac{\Delta\omega}{T} t, \quad (3-14)$$

where $T = \frac{1}{f_m}$ and ω_1 is the start frequency of the signal depicted by figure 3.1. The transmitted signal is then,

$$v_T = A_0 \cos\phi(t), \quad (3-15)$$

where,

$$\phi(t) = \int \omega(t) dt = \omega_1 t + \frac{\Delta\omega}{2T} t^2. \quad (3-16)$$

A_0 is the amplitude of the transmitted signal. The reflected signal is a time-delayed replica of the transmitted signal, modified in amplitude. The return may also be modified in phase due to the nature of the target, but in this analysis the target is the coherent scattering source.

The phase of this target is assumed to be constant. Therefore, the reflected signal is given by,

$$v_r(t) = B_0 \cos\left(\omega_1(t - \tau) + \frac{\Delta\omega}{2T}(t - \tau)^2\right). \quad (3-17)$$

After mixing the transmit and receive signal and low-pass filtering them, the beat signal, or IF (intermediate frequency) signal is given by,

$$v_{IF}(t) = \frac{A_0 B_0}{2} \cos\left(\omega_1 \tau + \Delta\omega \frac{\tau}{T} t - \frac{\Delta\omega}{2T} \tau^2\right). \quad (3-18)$$

If $\tau/T \ll 1$ this becomes,

$$v_{IF}(t) = C_0 \cos\left(\Delta\omega \frac{\tau}{T} t + \omega_1 \tau\right). \quad (3-19)$$

This IF signal serves as the reference waveform for consideration of frequency drifts in the oscillator and has a phase given by $\omega_1 \tau$.

Suppose a second measurement is made, but the oscillator frequency has changed by $\epsilon\omega_1$, so that the start frequency is given by $\omega_1 + \epsilon\omega_1$. The resulting IF signal becomes,

$$v'_{IF}(t) = C_0 \cos\left[\Delta\omega \frac{\tau}{T} t + (\omega_1 + \epsilon\omega_1)\tau\right], \quad (3-20)$$

and the phase difference between the two IF signals given by (3-19) and (3-20) is,

$$\Delta\phi = \epsilon\omega_1 \tau. \quad (3-21)$$

Therefore, a phase shift may be caused by any drift in the oscillator frequency between measurements.

The following example demonstrates the effect of a small drift on the phase difference between radar measurements. Assume that the frequency of the oscillator

in a linear FM radar changes by 1 MHz (0.02% for a 5 GHz oscillator). The primary signal that we want to remove is the antenna reflection. Assuming the antenna is at a range of 3m from the radar system, the 1 MHz frequency drift results in a phase difference of 1.15° . To obtain a phase stability of 6° as required for 20-dB suppression the CNR as demonstrated by figure 3.11 the frequency drift must be less than 5.3 MHz. Therefore, frequency stability of the local oscillator in FM radar systems is vital if coherent processes such as CNR are to be utilized. If an oscillator is used that has significant drift, its effect on coherent processing may be minimized by reducing the range to the primary coherent "noise" sources, because of the dependence on range in equation 3-22.

3.5 Phase Correction for CNR

Phase and amplitude variations can have a significant impact on the coherent noise reduction results. Therefore, a phase correction algorithm is developed here to improve coherent noise reduction when phase variations are encountered. Without correcting for phase variations we are limited to using measurements obtained over a short period of time in our estimate of the coherent noise signal from equation (3-12). Additionally, phase variations that occur over short periods of time may significantly degrade the CNR processing. Three aspects of phase correction are presented in this section. First, the algorithm for phase correction is presented, followed by a simulation to prove the concept. Then in section 3.5.3, phase correction is used to improve the CNR process with actual data obtained in the field.

3.5.1 Phase correction

The technique to correct for phase variations between measurements consists of five steps. First, one of the radar return signals is designated the "reference" signal (v_0) and subsequent return signals (v_i) are phase corrected to this. Second, a prominent coherent reflection (usually the primary antenna reflection) is located in the IF spectrum of v_0 and designated as the reference spike. Third, both the reference signal and each v_i are filtered around the reference spike. Fourth, the phase difference between the filtered signals is determined. Fifth, the return signal v_i is advanced in phase according to the phase difference measured to correct for phase errors.

3.5.2 Simulation

A simulation was carried out to demonstrate the phase correction algorithm. For this analysis, the cancellation effect was examined for four coherent "targets" when their phases change between measurements because of a change in oscillator frequency. The targets were assigned to be at ranges of 10, 23, 37, and 45 meters with various amplitudes. The FM radar system was assumed to operate at 10 GHz with 300 MHz bandwidth. The IF spectrum was computed, assuming that there were four coherent scattering targets according to equation 3-19 and again with equation 3-20, assuming a change of 5 MHz in oscillator frequency. The spectrum of the first (reference) signal is shown in figure 3.12. The IF spectrum from the second signal is identical in magnitude, but with oscillator-drift induced phase differences. The spectrum of the difference between the two IF signals is shown in figure 3.13. It is observed that because of the oscillator shift there is no significant cancellation between the two signals. Both the reference signal and the signal from the second measurement are filtered with an FIR filter and the output of the filter is shown in figure 3.14. The phase difference between the two signals is determined at the peak of the spectrum in figure 3.14. This phase shift is then applied to the second measurement and the subtraction is performed to produce the phase-corrected cancellation effect shown by figure 3.15. This demonstrates that the phase correction algorithm is useful in the CNR process to correct for the effects of oscillator drift.

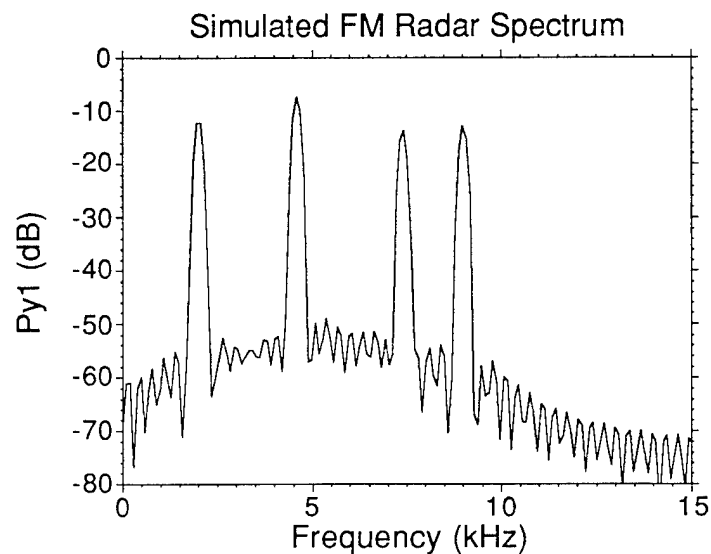


Figure 3.12 IF spectrum for the simulated radar return signal from four coherent targets.

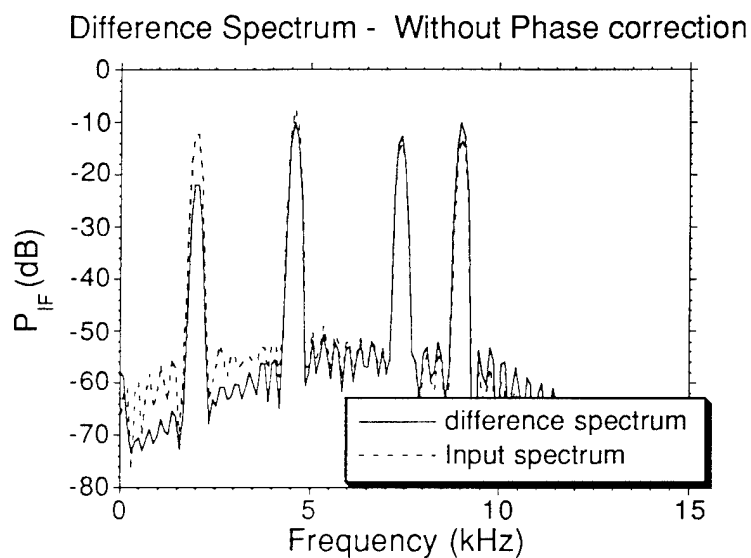


Figure 3.13 IF spectrum of the difference between two measurements when a 5 MHz drift in oscillator frequency has occurred (solid curve). The spectrum from figure 3.12 is shown to demonstrate that there is no significant cancellation of the coherent target signals.

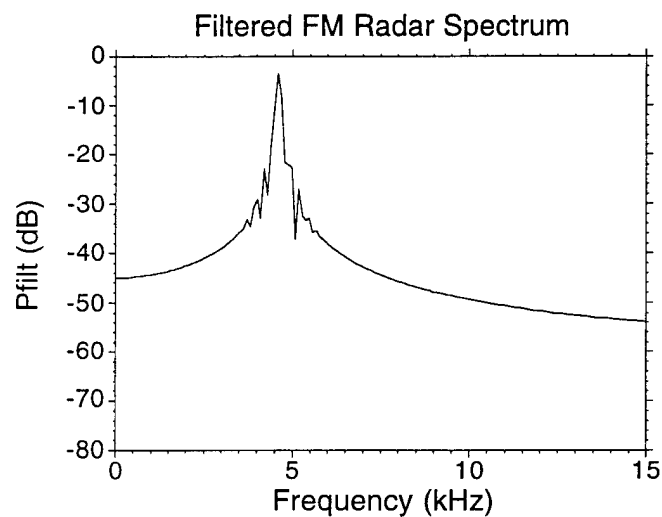


Figure 3.14 Spectrum of the filter output in the phase correction algorithm. The filter is necessary to locate a reference target to which the phase from both signals can be referenced.

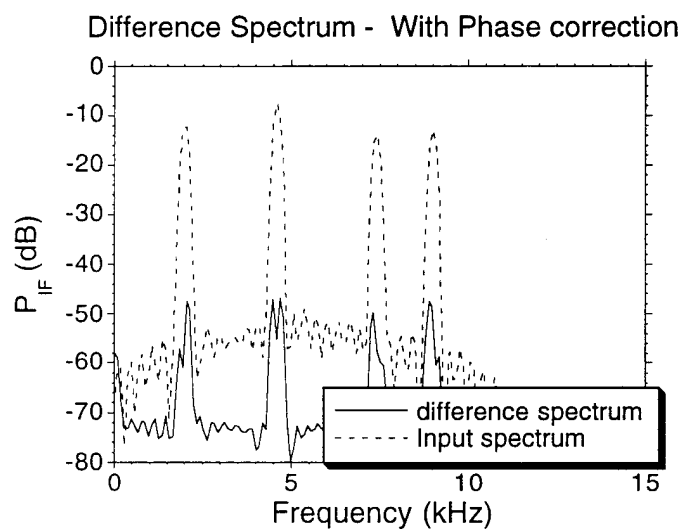


Figure 3.15 Phase-corrected difference spectrum (solid curve) and original spectrum (dashed). This demonstrates the cancellation effect after applying phase correction. The resulting difference spectrum is improved over the result shown in figure 3.13.

3.6 Phase-Corrected Coherent Noise Reduction Results

The phase-corrected coherent noise reduction (PC-CNR) process was applied to data obtained with the C-band FM radar system and the wideband, plane-wave step-frequency radar. Results of PC-CNR for both radar systems are presented below. The algorithm for the step-frequency radar is slightly modified from that used for the FM radar data. These modifications are discussed in section 3.6.2

3.6.1 PC-CNR for FM radar data

The phase-corrected coherent noise reduction process (PC-CNR) was applied to data obtained with the C-band FM radar system during the IAOE experiment. The data used to demonstrate this technique were acquired over a period of less than 24 hours from a transit segment of the expedition. Since the ship was in transit, all measurements were made at a fixed incidence angle (35°).

The original IF spectrum for one sample used in the PC-CNR process is shown as the dashed curve in figure 3.16. Several of the noise spikes are present in all of the samples used. The first strong reflection was used as the reference spike in the phase correction and is located at a range of 12 meters in figure 3.16. Each of six samples were filtered around this portion of the spectrum, using an FIR filter. The phase and amplitude differences at the peak of the filtered output for each sample were computed, with one sample arbitrarily chosen as the reference. Each sample was phase-corrected as described above and the result was used in the standard CNR process. The result for the phase-corrected, coherent noise reduction, applied to these data is shown in figure 3.16 as the solid curve. Here each of the coherent noise signals is reduced by approximately 25 dB, and the IF spectrum is clearly improved.

The true test of the improvement, though, is illustrated by a direct comparison of the PC-CNR process with the standard CNR process for these data in figure 3.17. Here we observe that the standard CNR suppresses the noise spikes by less than 5-dB. This is caused by the fact that the data were obtained over a long period of time (nearly 24 hours), and any of a number of phase errors described above have resulted in a degradation of the CNR process. However, the PC-CNR result has reduced the coherent portions of the spectrum by an additional 10 to 15 dB. The improvement of PC-CNR over standard CNR may be better illustrated on a linear scale as depicted in figure 3.18. Here it is clear that the return from the target (sea ice) at a range of approximately 23 m is the dominant return after phase-correction. The standard CNR does not significantly reduce the unwanted noise spikes for these data.

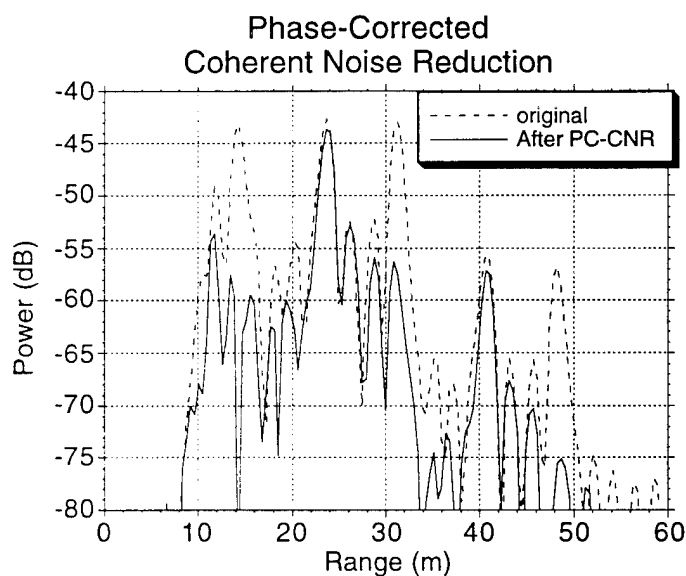


Figure 3.16 Result of coherent noise reduction with phase correction. The corrected IF spectrum is plotted along with the original to demonstrate the suppression of unwanted coherent noise spikes.

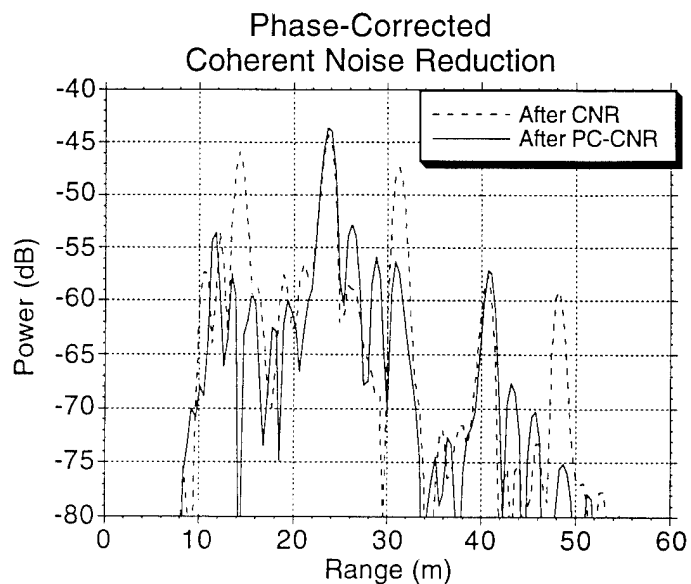


Figure 3.17 Result of CNR with phase correction, compared to CNR without phase correction. This demonstrates that while there is some suppression (4 or 5 dB) of the unwanted signals, the phase correction improves the suppression by 10 to 15 dB.

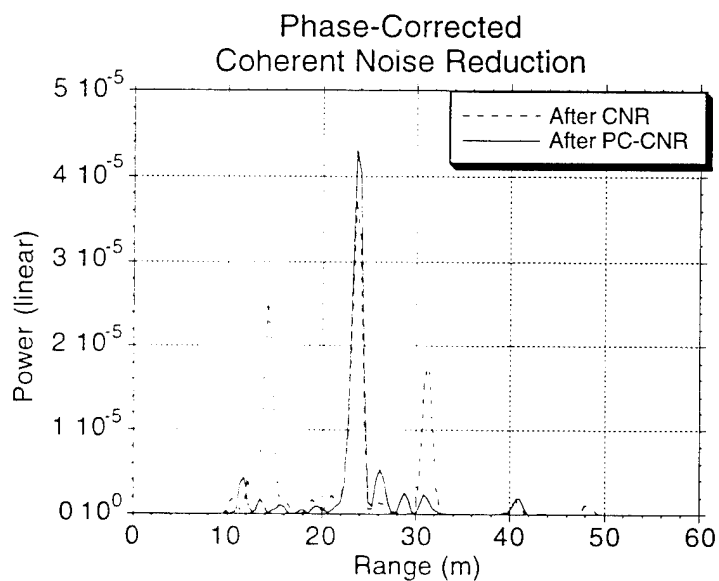


Figure 3.18 Result from figure 3.17, plotted on a linear scale to illustrate the suppression of coherent noise in the IF spectrum.

3.6.2 PC-CNR for wideband step-frequency data

The phase correction algorithm used on the FM radar data assumes that the phase errors from sample to sample are constant across the bandwidth. When ultra-wideband systems, such as the plane wave radar are used, this will not be the case. Therefore an extension of the PC-CNR algorithm was developed for wideband data. This algorithm accounts for amplitude and phase variations from sample to sample across the entire bandwidth. The process is identical to that used for the FM data above, except that instead of determining the phase shift (and amplitude difference) at the peak of the filtered systematic noise spike, the amplitude and phase are determined across the entire bandwidth used. We applied the PC-CNR process for wideband data to measurements obtained during CRRELEX '95 and the results are shown in the following figures. Figure 3.19 shows the PC-CNR for a measurement obtained at an incidence angle of 23° , along with the original measurement. These results demonstrate that the PC-CNR improves the measurement over the standard CNR (figure 3.9). The PC-CNR improves the SNR in the vicinity of the surface return by 20 to 25 dB. The result is illustrated more dramatically when displayed on a linear scale (figure 3.20). The radar return from the ice surface is not even visible due to the presence of the large reflection at the antenna, but after using PC-CNR the return from the ice surface is clearly observed.

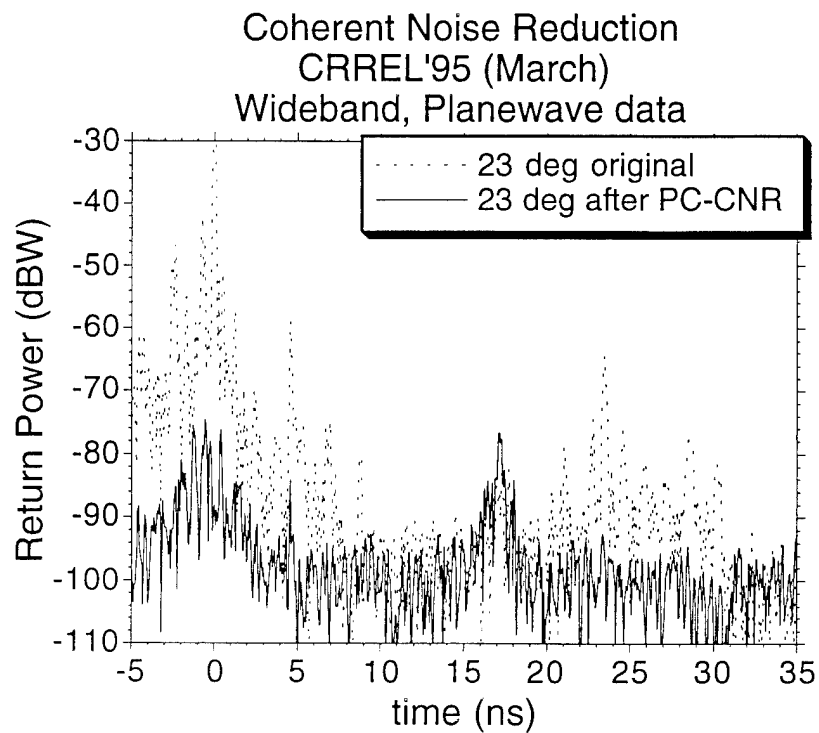


Figure 3.19 PC-CNR for wideband, step-frequency radar measurements. The antenna reflection is reduced by 50 dB, compared to 25 dB for standard CNR.

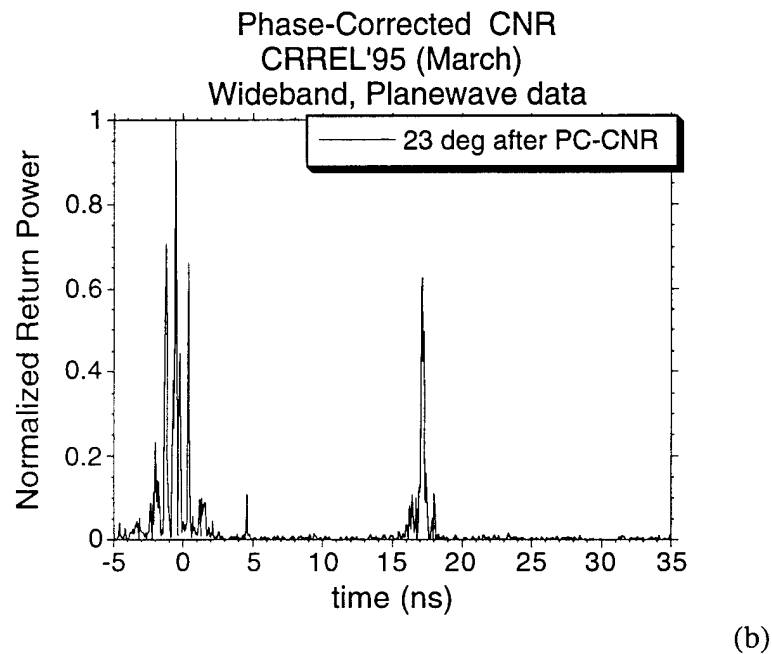
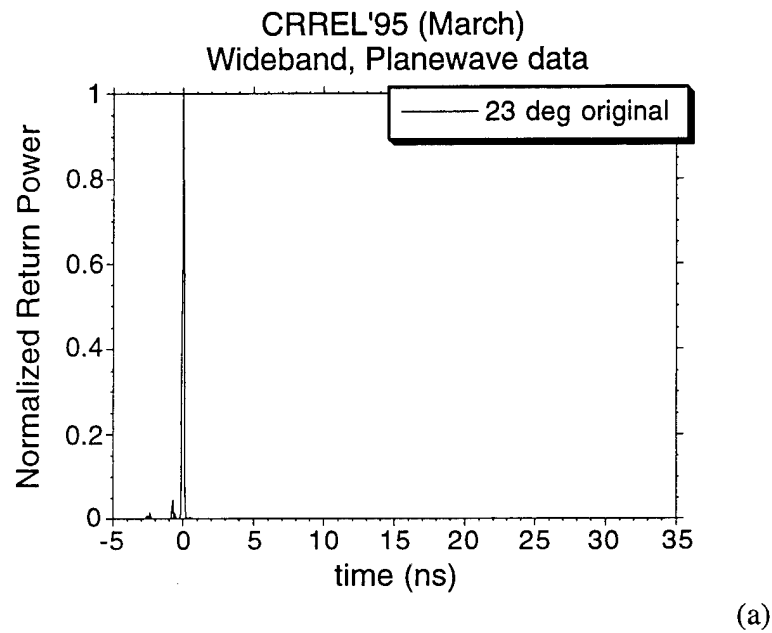


Figure 3.20 Results from figure 3.19, plotted on a linear scale to demonstrate the dramatic improvement in the radar return. The original return is shown in (a) and the result of PC-CNR is shown in (b). The return power is normalized to the peak in both cases. Note that the antenna reflection (located at 0 ns) is actually reduced by 50 dB as shown in figure 3.19.

3.7 Computing Backscattering Coefficients

Once the IF signal is processed as described previously to remove systematic effects, the power returned, P_r is estimated by filtering about the return from the distributed target. The backscatter coefficient for a calibrated radar system can be determined from the radar equation, using the narrow-beam approximation as

$$\sigma^0 = \frac{P_r \sigma_{cal} R^4 P_{dlcal}}{P_{cal} R_{cal}^4 A P_{dl}}, \quad (3-22)$$

where P_{cal} is the power returned from a calibration target of known radar cross section, σ_{cal} . The parameters P_{dlcal} and P_{dl} are the delay line readings taken at the time of calibration and the time of the field measurement, respectively. The range to the distributed target is R , A is the area illuminated by the antenna, and R_{cal} is the range to the calibration target.

The returned power is taken as the total power returned from the illuminated surface. The illuminated area is computed from [Ulaby, et al., 1982] as,

$$A_{ill} = \frac{\pi}{2} R_0^2 \cos(\theta^{inc}) \tan\left(\frac{\beta_{az}}{2}\right) \left[\tan\left(\theta^{inc} + \frac{\beta_{el}}{2}\right) - \tan\left(\theta^{inc} - \frac{\beta_{el}}{2}\right) \right], \quad (3-23)$$

where β_{az} and β_{el} are the antenna's azimuth and elevation beamwidth, respectively. The angle of incidence is denoted by θ^{inc} and the range to the surface, R_0 is calculated from the relationship in (3-1). The range is corrected for delays in the system itself by simply subtracting the system delay from the range measured. The determination of the system delay is based on knowledge of the range to the calibration target, which was measured during calibration.

3.8 Summary

We developed the coherent noise reduction (CNR) and phase-corrected coherent noise reduction (PC-CNR) techniques presented in this chapter to improve radar backscatter measurements with short-range FM and step-frequency radar systems. Short-range radar systems are not limited by thermal noise, but by the leakage and reflection signals from the antenna and RF sections. The coherent noise reduction techniques developed here reduce the effects of these leakage and reflection signals. These schemes hinge on the fact that the returns from distributed targets are non-coherent from sample to sample and that the returns from systematic sources are coherent from sample to sample. Using this basic assumption we have developed techniques which do not require "sky" measurements, which are not always feasible in field measurements due to practical physical constraints in the measurement set-up. Also, movement of the antenna to obtain sky measurements results in cable flexing, which reduces their effectiveness. Phase-correction algorithms for improving the CNR process in the presence of phase variations caused by oscillator drift, cable flexing or temperature fluctuations were also developed. These algorithms result in measurements whose sensitivity approaches the thermal noise floor, rather than being limited by systematic leakage and reflection signals.

CHAPTER 4

RADAR BACKSCATTER MEASUREMENTS AT THE ONSET OF FREEZE-UP

Freeze-up in the Arctic occurs when the temperature drops below freezing and new ice growth is initiated. The beginning of the freeze-up signals a change in the thermodynamics of sea ice/atmosphere interactions, which occurs on an annual basis. The timing and extent of the freeze-up are key functions in thermodynamic models of the Arctic [Thorndike, 1992]. Therefore, detecting the timing and extent of the onset of freeze-up are vital in understanding annual cycles of sea ice growth and decay. The extent of sea ice at the end of summer also affects the amount of new growth in the winter, which affects the annual cycle of heat flux.

The microwave backscatter characteristics of Arctic sea ice also change during seasonal transitions. To monitor these changes and to develop algorithms to exploit these changes we must first understand the nature of these microwave signatures. Radar backscatter measurement results from multiyear ice and thin sea ice during the initial stages of freeze-up are presented. These are the first *in situ* backscatter measurements that have captured the signature change during the onset of freeze-up in the deep Arctic. The measurements from thin ice also appear to be the first published C-band measurements of Arctic ice in this thickness range (< 15 cm), although there have been numerous measurements from artificial ice in this thickness range in the laboratory [Swift, et al., 1992]. These measurements are compared to previously published measurements of thin ice at Ku band and measurements from

slightly thicker ice at C band. This is followed with implications for monitoring thin sea ice and mapping thin ice thickness with present and future radar systems.

4.1 IAOE Experiment Description

We measured radar backscattering coefficients from various types of sea ice in the eastern central Arctic during the early stages of freeze-up in August and September 1991. These measurements were obtained as part of the International Arctic Ocean Expedition (IAOE) from aboard the USCGC *Polar Star*, a Coast Guard icebreaker, with an FM-CW radar system built at RSL. This experiment followed the July 1991 launch of the ERS-1 satellite, and, thus, the first field measurements of radar backscatter during the onset of freeze-up that coincide with ERS-1 SAR observations were obtained.

Using the shipborne radar system described in section 3.3.1 we measured backscattering coefficients from multiyear ice and various types of young first-year ice, including grease ice, light nilas, dark nilas, and pancake ice. These measurements were accompanied by the study of ice physical properties by the US Army Cold Regions Research and Engineering Laboratory (CRREL) and physical properties of snow by Microwave Group, Ottawa, Canada (MWG) for multiyear floes studied. The thin ice backscatter measurements were obtained while the ship was in transit. Observations of ice type and approximate thickness were made while backscatter data were acquired. The radar measurements were obtained in the eastern central Arctic and a map of the ship's cruise track is shown in figure 4.1. The ship left from Tromsø, Norway and headed North past Svalbard to approximately 85° North

latitude, before heading East and South through the eastern, central Arctic Ocean. The region is approximately from 82° to 85° N latitude and 30° to 50° E longitude. Details regarding measurement station locations, times and all radar measurement results can be found in [Beaven, 1992; and Beaven, et al., 1993a] and are tabulated in Appendix A. The *in situ* ice and snow property measurements obtained by MWG and CRREL are also given in Appendix A.

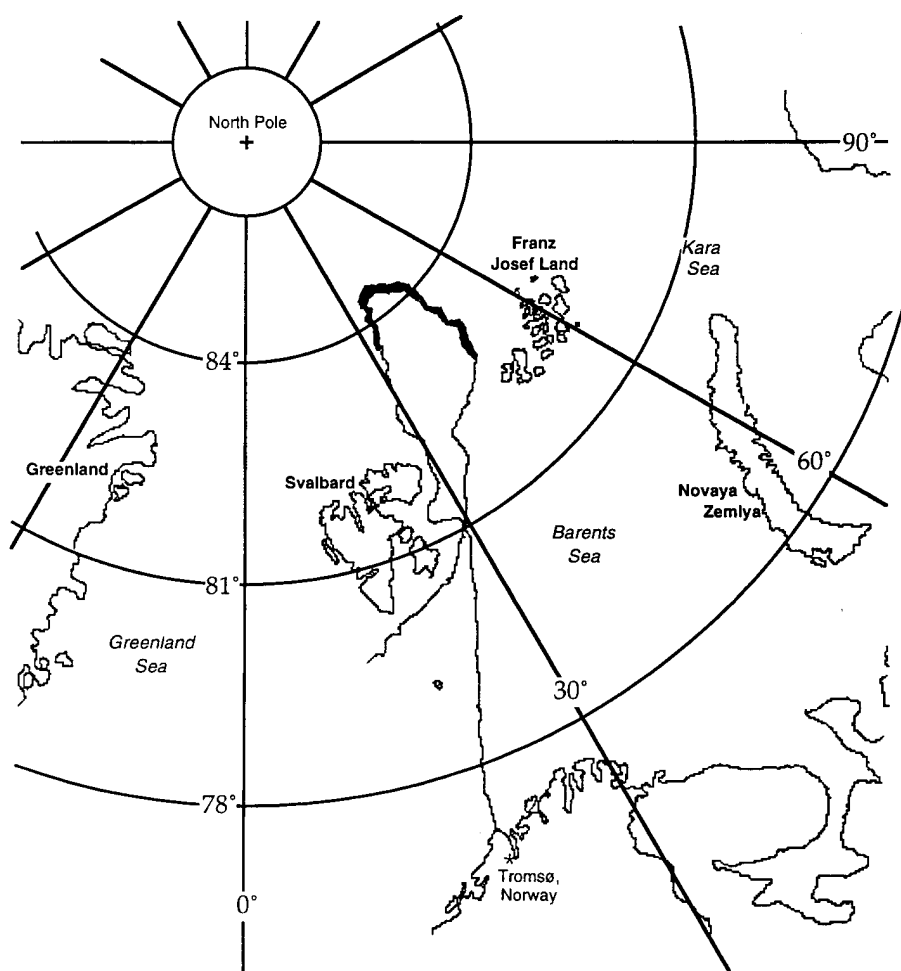


Figure 4.1 Cruise track for USCGC *Polar Star* for the IAOE experiment in August-September, 1991. Radar backscatter measurements were obtained for the portion of the cruise highlighted by thicker lines.

4.2 Multiyear ice signatures during freeze-up

The ERS-1 SAR operates with incidence angles from approximately 19° to 26° . Ideally, all of the shipborne radar measurements should be made in this range if they are to be compared to ERS-1. Unfortunately, low incidence angles were affected by the ship's movement in the ice, therefore most measurements were acquired for incidence angles of 35° and above. The data from these measurements were processed as described in chapter 3 to obtain backscatter coefficients. Figure 4.2 shows the backscatter coefficients for multiyear ice observed during IAOE as a function of Julian date (JD) for 35° incidence angle. This figure includes ice station data for which angular scans were obtained and transit data for which the incidence angle was fixed. Previously, we have shown the same trend but without including transit data to fill the gaps between station data. The transit data were only recovered because of the coherent noise reduction techniques we introduced in chapter 3. These data show a general trend of increasing backscatter at the onset of freeze-up, with two events of decreasing backscatter. Hourly temperatures were recorded on board the *Polar Star* as standard procedure throughout the experiment. These temperatures, along with "spot" temperature readings from several multiyear stations, are shown in figure 4.3. These figures depict the changes in backscatter signature that occur during the initial stages of freeze-up. The scattering mechanisms responsible for the changes observed in figure 4.2 are addressed in chapter 5.

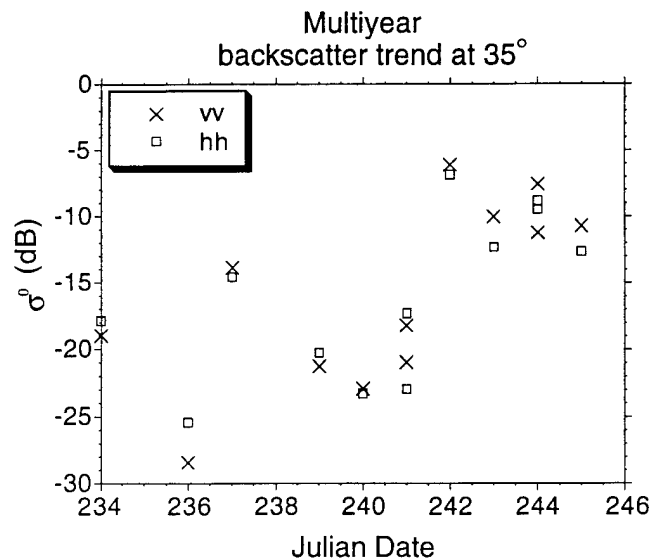


Figure 4.2 Copolarized C-band backscatter coefficients from multiyear sea ice during the freeze-up. These ship-based measurements show a general increase in the backscatter during the portion of the freeze-up studied.

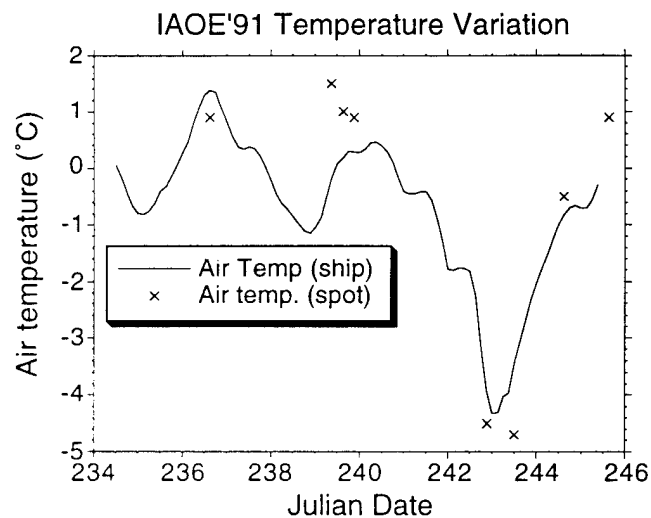


Figure 4.3 Air temperature variation measured from aboard the *Polar Star* for the period in which shipborne radar measurements were obtained. The solid line indicates hourly air temperature readings from the ship's log and the x's indicate air temperatures measured at several experiment sites during the expedition.

4.3 Radar Backscatter from young (thin) sea ice during IAOE

In addition to the changes in multiyear sea ice during freeze-up, this season initiates new ice growth in the Arctic. Ice growth injects brine into the upper layers of the ocean and causes a distinct change in the albedo of the ocean surface. Thin ice plays a key role in affecting the heat transfer between the ocean and atmosphere in the Arctic. Thin ice may be as important as thick ice (multiyear and thick first-year ice) in determining the heat transfer from ocean to atmosphere in the Arctic winter [Maykut, 1978], despite the fact that thin ice may account for only a small fraction of the total ice cover.

Few radar backscatter measurements have been reported from thin sea ice. Grenfell et al. [1992] reported the general backscatter trend for young first-year ice. These results are similar to those derived from Cosmos 1500 Real-Aperture Radar images by Nazirov [Grenfell, et al., 1992]. Tucker, et al., [1991] documented thin ice signatures at 18 and 37 GHz. Drinkwater, et al., [1991] derived backscatter signatures for thin ice from SAR images acquired over the Beaufort, Chukchi, and Bering seas in March 1988. They showed that at L band, the magnitude ratio and phase difference of the scattering coefficients for vv and hh polarizations can be used to distinguish between various types of thin ice. They also concluded that thin ice may not be easily distinguished with the ERS-1 Synthetic-Aperture Radar (SAR). Gray, et al., [1982] performed extensive measurements at Ku band over thin ice. Thin ice signatures as a function of season are explored by Livingstone, et al., [1987], based on aircraft-based, Ku-band scatterometer measurements. Numerous backscatter and emission measurements have been obtained from saline ice at CRREL [Swift, et

al., 1992]. These measurements have been designed to aid in the development and testing of scattering and emission models and few comparisons have been made with actual measurements from thin ice in the Arctic.

Recently, Ulander, et al., [1992] and Holt, et al., [1992] have determined scattering coefficients derived from ERS-1 SAR images over sea ice and open water. Both reported that backscatter from thin ice is highly variable and it may be difficult to distinguish young ice from old ice using intensity-based algorithms. They recommended that temporal and textural information, as well as context, be incorporated into algorithms.

We made radar backscatter measurements of several types of thin ice during IAOE. These include measurements from light nilas, dark nilas, grease/frazil ice, and pancake ice. Grease and frazil ice are the first stage of sea ice growth and have a thickness of less than 1 cm. Dark nilas is slightly thicker and is about 1-cm to 5-cm thick and appears dark to the eye. Light nilas appears white to the eye and ranges from about 5-cm to 10- or 15-cm thick. Pancake ice received its name from its circular pancake-like shape; individual pancakes are typically 30 to 300 cm in diameter. Pancake ice is formed in areas where there is some wave action while the ice is in its early stages of growth and can be from 10-cm to 20-cm thick. Radar measurements of thin ice were acquired while the ship was in transit, so the incidence angle was fixed at 35°. These data were processed using the CNR technique described in chapter 3. The C-band, vv polarization (the ERS-1 SAR is C-band vv) backscattering coefficient from these thin ice types varied from -40 to -14 dB. The mean values at vv polarization were as follows: -26.5 dB for grease/frazil ice, -24 dB

for dark nilas ice, -20 dB for light nilas ice, and -16 dB for pancake ice. The mean values for these ice types are plotted in figure 4.4.

The mean value of backscatter from these thin ice types is only part of the information necessary in developing algorithms for ice parameter retrieval. The variation in backscatter from thin ice may be useful for classification. The variation of the backscatter from thin ice as measured during IAOE is demonstrated in figure 4.5. Here a "box plot" is used to show the spread of the data. The center line indicates the median value. The top and bottom lines of the shaded boxes denote the $\pm 25\%$ of the distribution, meaning that half of the measurements fell in that range. Similarly, the extended lines mark the $\pm 45\%$ points of the data. These measurements show that there is generally a high variance for backscattering from young ice.

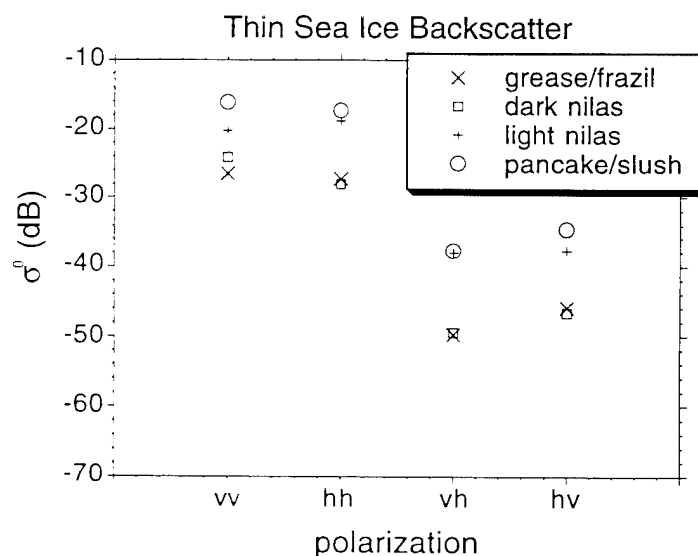
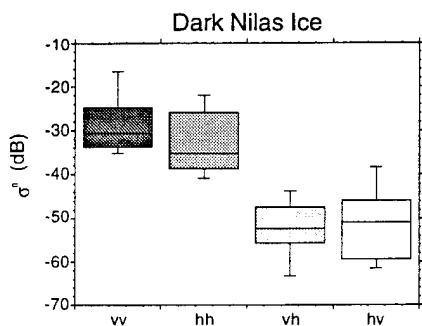
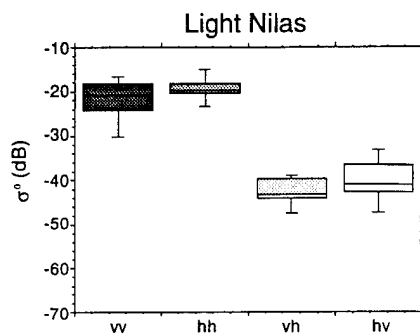


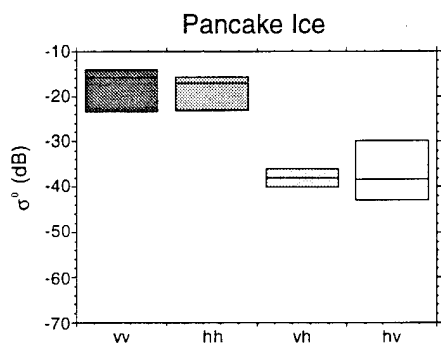
Figure 4.4 C-band backscattering coefficients from young sea ice measured during IAOE as a function of polarization.



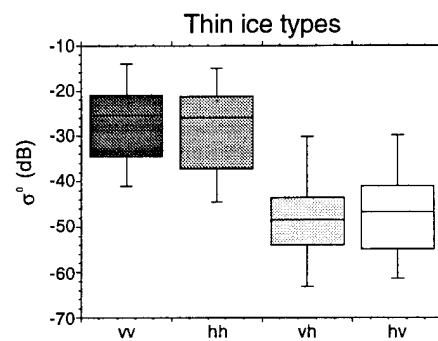
(a)



(b)



(c)



(d)

Figure 4.5 Measurements of C-band σ^0 versus polarization from young first-year sea ice types: a) dark nilas, b) light nilas, c) pancake ice, and d) all young first-year ice types combined. The center line is the median value measured. The top and bottom lines of each of the shaded boxes mark the $\pm 25\%$ points in the distribution and the extended lines (when shown) mark the $\pm 45\%$ points in the distribution.

4.4 Comparison to quasi-laboratory measurements at CRREL

In this section we compare quasi-laboratory measurements with the field measurements of this ice. This serves two purposes: (1) to utilize the information obtained from the laboratory experiments such as angular trends to interpret field measurements of radar backscatter and (2) to verify that the laboratory-grown saline ice sheets resemble those found growing in Arctic leads.

4.4.1 CRREL overview

Radar backscatter measurements from saline ice have been obtained over the last decade in a series of experiments at the US Army Cold Regions Research and Engineering Laboratory (CRREL). These experiments were designed to determine scattering properties of sea ice. Radar backscatter measurements at this facility have been used to develop and test scattering models for sea ice and to determine scattering properties at various stages of saline ice growth [Bredow, et al., 1989; Onstott, 1990; Beaven, et al., 1995]. As a part of these experiments we have obtained radar backscatter data from bare and snow-covered saline ice with several different radar systems, which were described in chapter 3. Results from these experiments are used in this section to support the field measurements and provide a measure of angular dependence for thin Arctic ice. This angular dependence is important for linking the measurements made during IAOE at 35° incidence angle to the ERS-1 SAR incidence angle (nominally 23°).

4.4.2 Comparison of laboratory and field measurements of thin ice

If CRREL measurements and subsequent modeling efforts are to be useful in Arctic research there must be some agreement between measurements from the saline ice grown at CRREL and field measurements in the Arctic. Arcone, et al. [1986], Gow [1986], and Swift, et al. [1992] have shown that the physical properties of saline ice grown at CRREL closely resemble that of young first-year sea ice in the Arctic. A direct comparison of IAOE measurements and the CRREL measurements is also informative. Figure 4.6 shows a direct comparison of C-band radar backscattering coefficients measured at CRREL's outdoor pond facility in 1990 with field measurements from IAOE for various thin ice types. There is general agreement between the two measurements that as the young ice grows the radar backscatter at 35° increases. This shows that there are similarities between the saline ice sheets grown at CRREL and real Arctic sea ice. The 1990 experiment suffered from bad weather conditions, but the data show that there is general agreement. The modeling used to fit CRREL data may be applicable to model real sea ice and aid in interpretation of radar backscatter signatures and SAR images of sea ice. In fact, we use the angular variation of the saline ice sheets observed at CRREL to extrapolate our measurements of thin ice obtained at 35° during IAOE to examine the capability of ERS-1 SAR for observing thin ice at 23° .

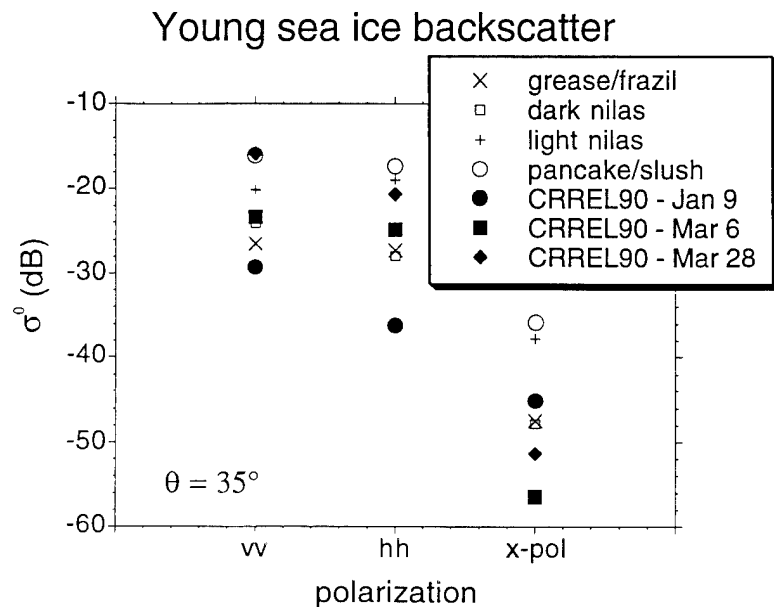


Figure 4.6 Radar backscattering coefficients for thin ice in the Arctic and ice sheets grown at CRREL. The similarities between these data suggest that knowledge and models based on the CRREL data may be useful in interpreting signatures from thin Arctic sea ice.

Pancake Ice

Pancake ice is formed in areas of the Arctic where significant wave action is present in the early stages of ice growth. The wave action does not allow columnar ice to form immediately. Instead, frazil ice forms on the ice surface and congeals into an ice layer. The wave action breaks up the ice into small individual pieces usually 30 to 300 cm in diameter, that resemble pancakes. Pancake ice thickness can range from about 3 cm up to 20 cm and is common in the marginal ice zones. We obtained backscatter measurements from pancake ice growing in leads during IAOE as shown in figure 4.3c. In January, 1995 an experiment was conducted at CRREL's GRF to produce a simulated pancake ice sheet. The pancakes were formed by using a motor-

driven paddle to produce wave action in the GRF pond as frazil ice formation commenced. The wave action and ice growth produced pancake ice up to 10-cm thick in the GRF pond. This allowed for more extensive measurements to be performed under the quasi-laboratory conditions at CRREL than were obtained in the field.

We measured radar backscatter coefficients from the pancake ice grown at CRREL with the wideband, planewave system over the 500 MHz to 16.5 GHz frequency range. Measurements were made at incidence angles from 0° to 50° at four independent spots on the pancake ice sheet. These measurements were processed using the coherent noise reduction technique in chapter 3 and calibrated to a metal sphere according to equation (3-22). The σ^0 for vv polarization and 5.5 GHz is shown in figure 4.7 as a function of incidence angle, along with the field measurements from IAOE for pancake ice. The average σ^0 from the IAOE measurements is shown as the box, with maximum and minimum measurements as the extended bars. These measurements indicate that the simulated pancake ice has backscatter characteristics that are similar (at least at 35°) to pancake ice observed in the Arctic. The slope of σ^0 for the simulated pancake ice is about 6-dB per 10° change in incidence angle for the 25° to 35° range. This is the slope chosen in the analysis of section 4.5 for determining if ERS-1 and RADARSAT are suitable for observing thin ice in the Arctic.

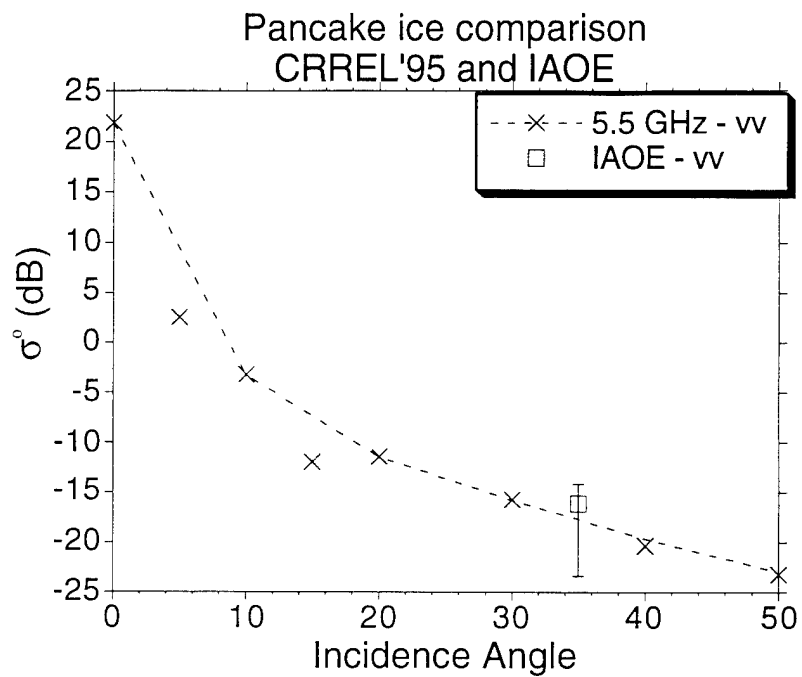


Figure 4.7 Backscatter coefficient of pancake ice from IAOE (box) and CRRELEX '95 (angular response). These data show that the laboratory experiment for simulating pancake ice agrees with field measurements at 35°.

4.5 Implications for spaceborne SAR measurements

These measurements demonstrate that backscatter from thin ice, particularly dark nilas and grease/frazil ice formations, is lower than for multiyear and thick first-year ice. These measurements may be used to establish noise floor limitations on systems that are designed to observe thin ice. Both the ERS-1 SAR and RADARSAT are to be used for sea ice remote sensing purposes, but the noise floor for each instrument is too high to effectively observe the thinner ice types. The noise-equivalent σ^0 for each instrument is used to determine whether they are capable of observing each of the four thin ice categories of figure 4.5. For ERS-1 SAR, past laboratory measurements of the angular dependence of young saline ice are used to extrapolate the measurements at 35° in figure 4.5 to the ERS-1 SAR nominal incidence angle of 23° .

4.5.1 RADARSAT

The RADARSAT SAR, scheduled for 1995 launch, will operate at 5.3 GHz with hh polarization and incidence angle from 20° to 50° . This SAR has a designed noise-equivalent σ^0 of -23 dB [Raney, et al., 1991]. This noise floor is plotted along with the results of the measurements of thin ice at hh polarization in figure 4.8. The backscatter data presented here show that at 35° incidence angle RADARSAT will not be able to observe dark nilas (mean $\sigma^0 = -24$ dB) and grease/frazil ice (mean $\sigma^0 = -27$ dB). The data also show that RADARSAT may be useful for observing light nilas and pancake ice due to their higher backscatter. This graphically demonstrates the fact that RADARSAT is not ideal for observing thin ice at angles larger than 35° , although its wide swath may be useful in exploiting the angular dependence of thin

ice. The angular dependence of thin ice was not measured during IAOE, but extensive angular responses of σ^0 for thin saline ice have been measured in laboratory experiments at CRREL.

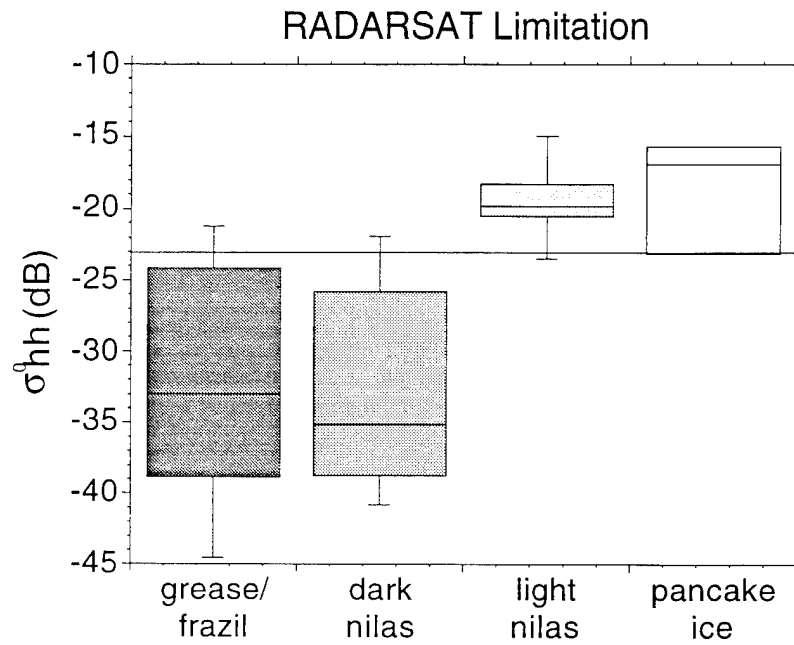


Figure 4.8 RADARSAT noise floor in relation to backscattering coefficient measurements of thin ice.

4.5.2 ERS-1

The ERS-1 SAR operates at C band with vv polarization at a nominal incidence angle of 23° and has a noise-equivalent σ^0 of -24 dB [Attema, et al., 1991]. The backscatter from dark nilas, grease, and frazil ice is between -34 and -24 dB for VV polarization, whereas the backscatter from light nilas is -18 to -22 dB at 35° . To use these data in determining the ability of the ERS-1 SAR for observing these ice types, the angular variation between 23° and 35° must be taken into account. We have performed extensive measurements of the angular variation of thin saline ice. The angular response of the young first-year ice σ^0 is similar to that of the saline ice sheets observed at CRREL. As a first-order approximation, we assume that the falloff for young sea ice is the same as that for simulated first-year sea ice at CRREL. We found that the scattering coefficient decreased by 6 dB when the incidence angle increased from 23° to 35° [Beaven, et al., 1995]. Onstott [1992] reported the rate of angular variation for first-year ice and open water in fall season was about -0.04 to -0.63 dB per degree. This implies that 0.48 to 7.6 dB must be added to extrapolate our measurements at 35° to ERS-1's measurements at 23° incidence. Since the 6-dB scaling factor falls within this range we will use the observation of angular falloff from CRREL data.

Assuming a signal-to-noise ratio of 3 dB, areas with backscatter values lower than -21 dB cannot be distinguished from noise by the ERS-1 SAR. If we assume a 6-dB factor to scale our results at 35° to ERS-1's incidence angle at 23° , any ice types with backscatter less than -27 dB measured at 35° during IAOE'91 cannot be observed by the ERS-1 SAR. This extrapolated noise floor (-27 dB) is plotted along with the results of the measurements of thin ice at vv polarization in figure 4.9. This

demonstrates that neither dark nilas nor grease/frazil ice may be observed by ERS-1 SAR, based on intensity alone. The variability of these types, however, causes a portion of the distribution to be above the -27 dB threshold. This implies that higher-order image statistics, such as variance and texture, may aid in observing thin ice with ERS-1. Both pancake and light nilas may be observable since their backscatter coefficients were measured to be at least 7 to 10 dB greater than our assumed cutoff of -27 dB.

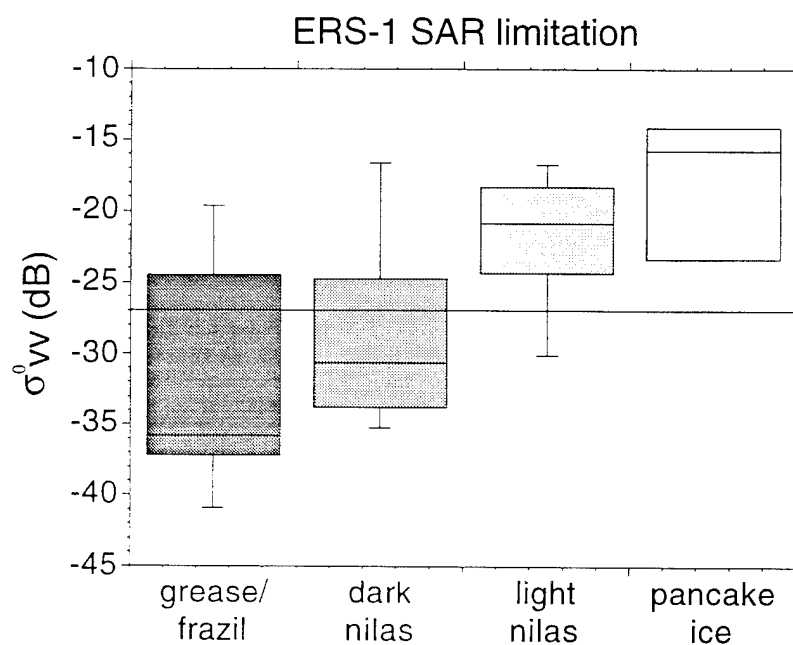


Figure 4.9 ERS-1 SAR noise floor (extrapolated to 35°) in relation to backscattering coefficient measurements of thin ice.

4.6 Multipolarization classification of thin ice

Although single-polarization synthetic aperture radars, ERS-1 and RADARSAT, are not ideal for observing thin ice, it has been speculated in the past that a combination of polarizations and/or frequencies might be useful for classifying young first-year ice into thickness categories [Livingstone, et al., 1987]. The radar backscatter measurements by Livingstone, et al., [1987] were combined with passive microwave data at 19 GHz to demonstrate that several thin ice categories can be classified. C-band and X-band measurements from thin ice have been made in the Gulf of Bothnia on low-salinity sea ice [Hyypä and Hallikainen, 1992]. During IAOE we obtained radar backscatter coefficients at all four polarizations from thin ice in the central Arctic. To determine whether multi-polarization data are useful for discriminating thin ice categories at C band, the thin ice measurements made during IAOE are analyzed here.

Figure 4.10 shows the copolarized σ^0 (average of vv and hh) versus the cross-polarized σ^0 (average of vh and hv). Here, we observe that there is a definite ice thickness trend with respect to the copolarized versus cross-polarized σ^0 . The thin ice types are indicative of their thickness as described in section 4.3. In order of increasing thickness, the ice types observed during IAOE are grease/frazil, dark nilas, light nilas, and pancake ice. As the thickness of the ice increases from < 1 cm to greater than 10 cm, we move from the lower right to the upper left portion of figure 4.10. Thus, thin ice thickness is directly related to the polarization information at C band. The additional information obtained by using two channels instead of one appears to be relatively small since the data seem to cluster around the diagonal of the

plot. However, the use of only the copolarized data would result in misclassification of some of the grease/frazil and dark nilas categories as light nilas. Some measurements from grease/frazil ice and dark nilas are comparable to light nilas in the copolarized channels, but are 5 to 10 dB lower in the cross-polarized channels. Thus, the use of both copolarized and cross-polarized backscatter information is useful. Although there is some mixing between classes, the use of dual-channel backscatter data at C band may be useful for determining thin ice thickness. However, the measurements from open water (x's in figure 4.10) have the same scattering characteristics at 35° as nilas ice. Therefore, the presence of open water will complicate an algorithm based on polarization ratio for determining thickness of thin ice, and this type of classification scheme may be limited.

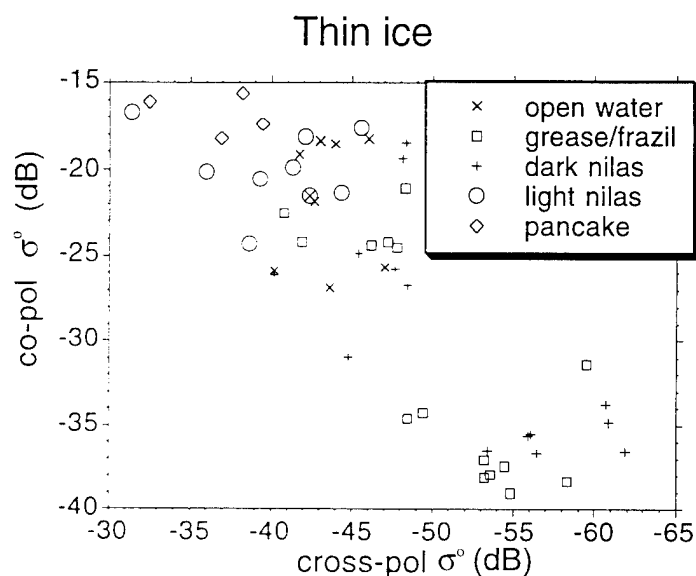


Figure 4.10 Plot of from copolarized σ^0 versus cross-polarized σ^0 for thin ice categories.

Previous measurements used to demonstrate the classification of thin ice types and open water based on the polarization comparison as well as brightness temperature measurements at 19 GHz showed that young ice, grease ice, and calm open water can be classified during the freeze-up season [Livingstone, et al., 1987]. The backscatter data from the Canadian Centre for Remote Sensing (CCRS) [Livingstone, et al., 1987] are used to show the dependence of thin ice and smooth open water to copolarized to cross-polarized σ^0 at 45° incidence angle at Ku band in figure 4.11. In their case the ice categories are grease, young broken (rafted), young, and multiyear ice; along with calm open water.

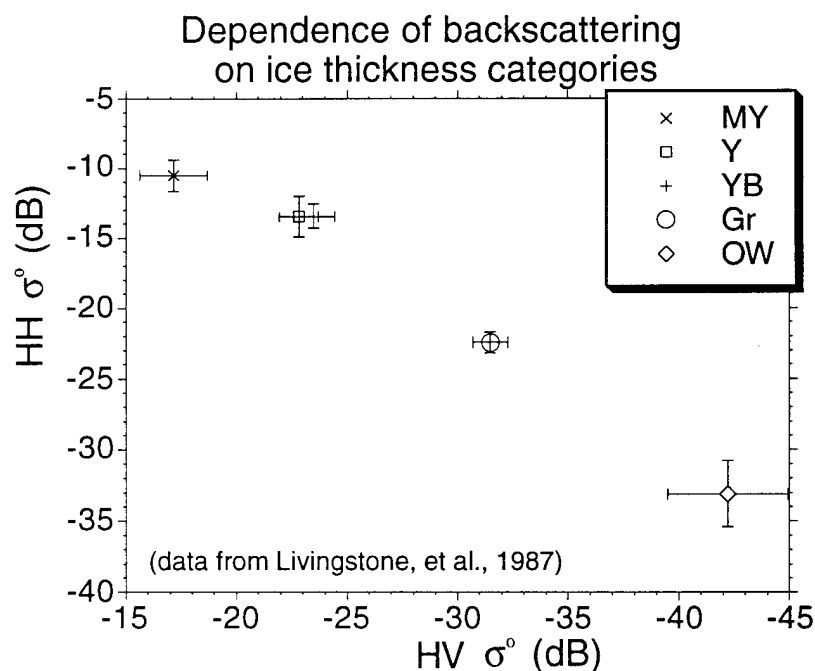
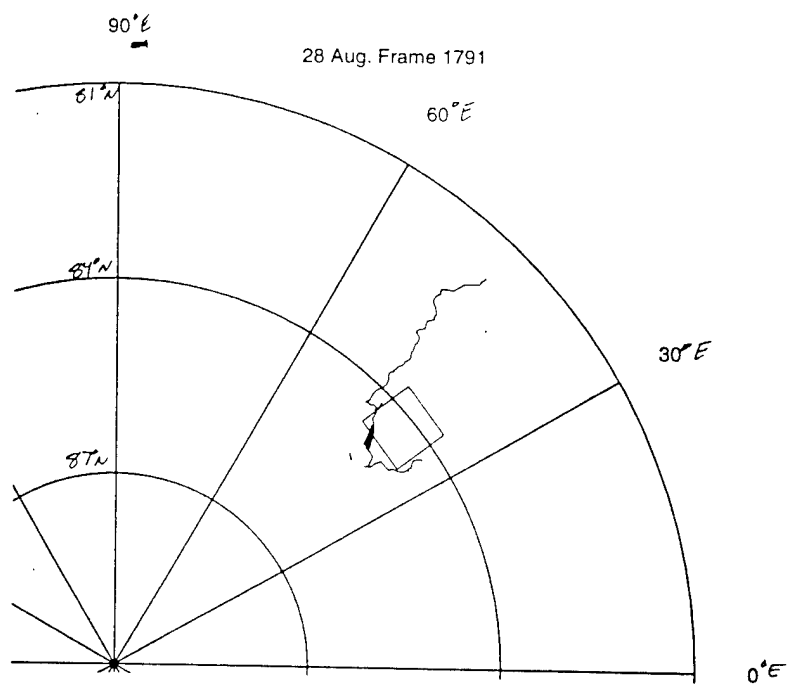
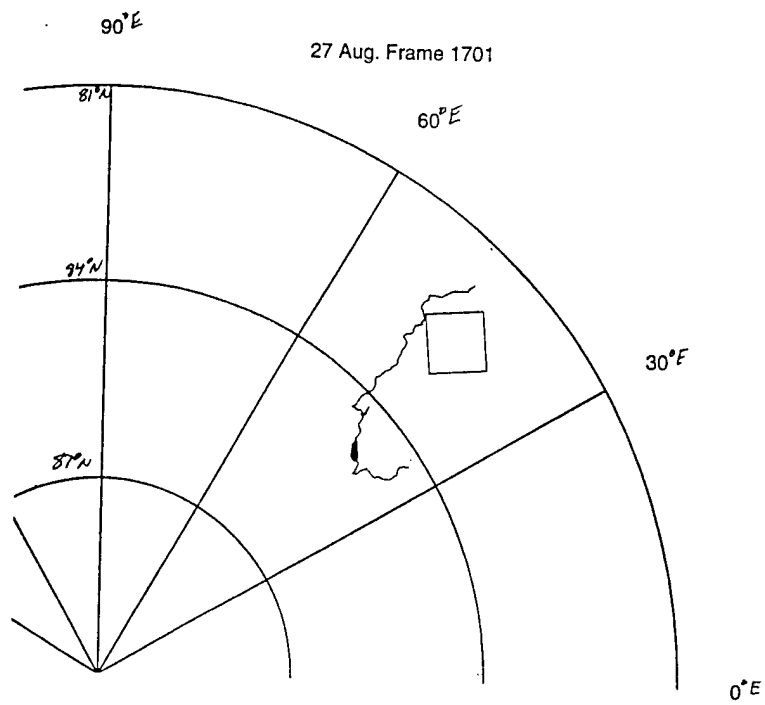


Figure 4.11 Dependence of ice thickness on copolarized versus cross-polarized backscatter coefficient at Ku band at 45° . Data are from table VI of Livingstone, et al., 1987 and were obtained with a Ku-band scatterometer in mid-October, 1980.



The CCRS results demonstrate the same general dependence of σ^0 on ice thickness categories as we have demonstrated in figure 4.10, however their measurements were obtained at Ku band. In addition, our measurements from thin ice are divided into more categories. We have light nilas and dark nilas, whereas CCRS has only separated their thinner ice into frazil and two "young" ice categories. Sea ice is classified as young ice when it reaches a thickness of about 30 cm and their measurements were obtained later in the freeze-up season (October) than the IAOE measurements. Ku-band measurements made by CCRS during advanced melt (July, 1980) show that the Ku-band hh-polarized backscatter coefficient at 45° from young ice varied between -23 dB to -16 dB depending on whether the surface was relatively wet or dry. They also showed that the cross-polarized σ^0 also varied from -32 dB to -25 dB at the same time. Our measurements fill in the gap between the advanced melt case and the late freeze-up case with ice thicknesses in the range of <1 cm to 15 cm. In addition, our measurements were acquired with a C-band system and thus have more relevance in terms of understanding radar backscatter signatures from ERS-1 or RADARSAT, since both of these systems operate at C band.

Hyypä and Hallikainen [1992] have obtained C-band backscatter data from various ice thickness categories for low salinity sea ice in the Gulf of Bothnia. They have also explored the use of copolarized versus cross-polarized σ^0 for separating ice classes. Their figure demonstrating the separation of low-salinity ice into five categories is shown in figure 4.12. They have demonstrated that new ice can be distinguished from thick ice and open water, but have not explored the possibility of mapping thin ice thickness within the new ice category.

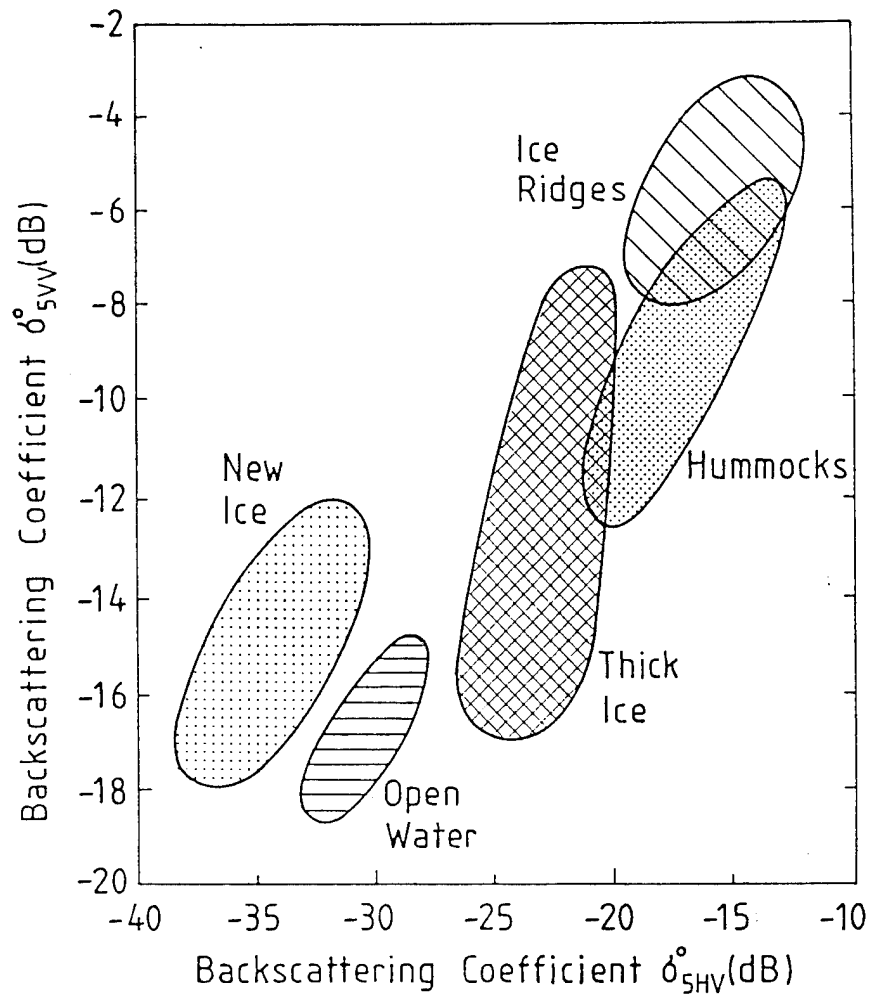


Figure 4.12 Discrimination of low-salinity sea ice types by using σ^0 from vv and hv polarization at 5.4 GHz. {from Hyyppä and Hallikainen [1992]}

Although these results show that open water can be distinguished from thin ice, the presence of wind-roughened open water presents problems when using the polarization information reflected in figure 4.10. This is generally a problem in any attempt to distinguish between open water and sea ice with radar since the backscattering coefficient of water depends on wind speed and direction. Backscatter measurements from open water were obtained on only one day during IAOE and the wind speed at the time of the measurements was 15.4 m/s. These are compared to

cross-wind measurements of radar backscatter obtained from the Nordsee tower in Germany [Moore, et al., 1984] in figure 4.13. The backscattering coefficients from the polynya in the Arctic are about 5 to 7 dB below those measured on the Nordsee platform. The primary difference between the water observed polynyas in the Arctic and the North Sea as observed during the Nordsee experiment is the presence of the pack ice. Polynyas are relatively small and so there is less fetch; the surrounding pack ice doesn't allow for the winds to have as much effect on the surface of the water as takes place in the open ocean. Although there are not enough data obtained during IAOE to fully explore these effects (measurements were obtained at only one wind speed), the fetch difference could be responsible for the discrepancy in backscatter between the Nordsee and IAOE measurements. Nonetheless, backscatter from open water in Arctic polynyas also depends on wind speed. For calm open water the backscatter is low and appears dark in SAR imagery. This has been observed in many field experiments and SAR sea ice studies [Tucker, et al., 1991; Hyypä and Hallikainen, 1992; Onstott, 1992]. The wind-induced roughness effects on open water present a challenge in distinguishing between open water and thin ice with radar.

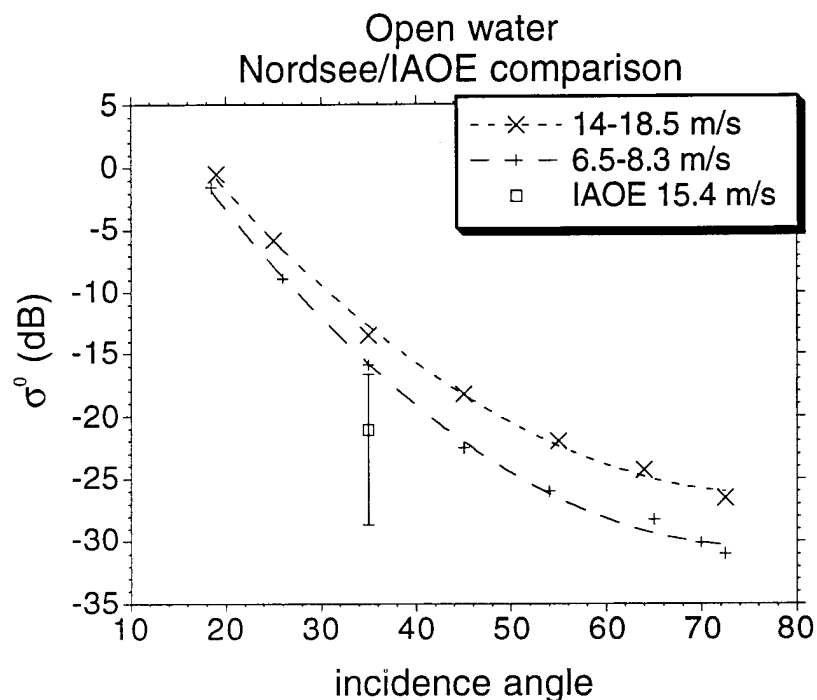


Figure 4.13 Comparison of radar backscatter from open water at cross-wind in an Arctic polynya (IAOE) and cross-wind measurements from a tower-based scatterometer in the North Sea [Nordsee data from Moore, et al., 1984].

In addition to copolarized vs. cross-polarized σ^0 for ice thickness classification, the two copolarized channels (vv and hh) have been suggested as useful in classifying thin ice categories and thin ice from open water at L band and Ku band [Drinkwater, et al., 1991; Tucker, et al., 1991]. Figure 4.14 shows the σ^0 for hh versus vv polarization at C band. Each thin ice type has a unique symbol in the figure. From these data it does not appear that thin ice thickness may be obtained by using only vv- and hh-polarized σ^0 . This also demonstrates that open water under wind-roughened conditions may not be separated from some types of thin ice based on the relative difference between vv- and hh-polarized σ^0 .

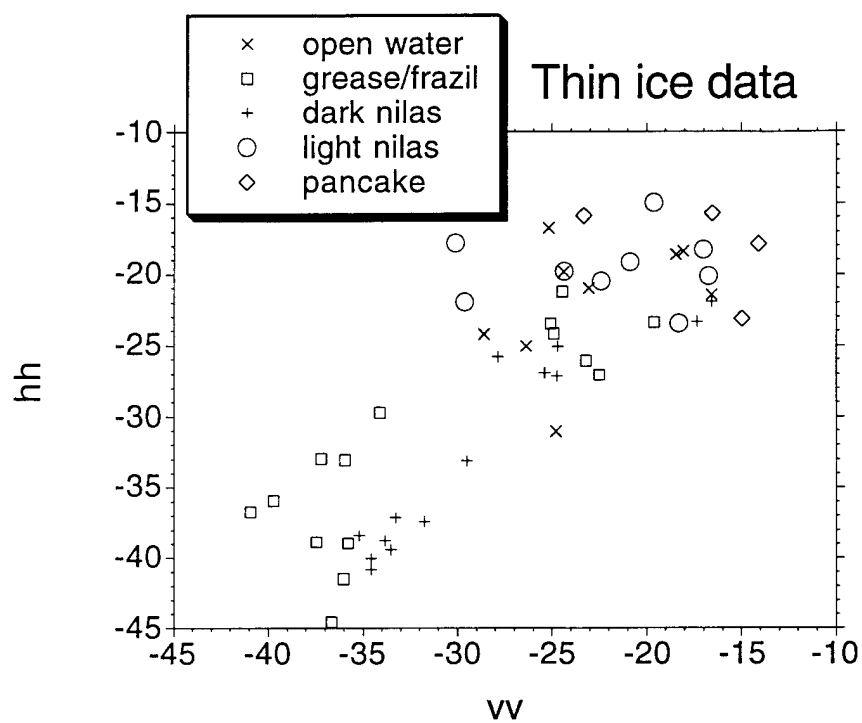


Figure 4.14 Plot of σ^0 from hh polarization versus vv polarization for thin ice categories.

4.7 Summary

Radar measurements presented here demonstrate the effect of the initial stages of freeze-up on the backscatter signature of multiyear ice in the Arctic. The σ^0 is highly dependent on the air temperature and may be used to determine the onset of freeze-up in the Arctic. These are the first *in situ* C-band backscatter measurements obtained during the transition from summer melt into the freeze-up period. The physical mechanisms responsible for these changes are explored in chapter 5. Measurements from thin ice were also obtained during the initial stages of freeze-up. These measurements indicate that neither ERS-1 nor RADARSAT is well-suited for observing grease, frazil and dark nilas ice. These ice types are in the 1-cm to 5-cm thickness range. Thicker ice, such as light nilas and pancake ice (5-cm to 15-cm thickness) can be observed with both satellite instruments, based on these field measurements. These measurements also indicate that thin ice thickness may be obtained by the combination of copolarized and cross-polarized channels at C-band, with the exception of wind-roughened open water.

CHAPTER 5

MODELING OF SCATTEROMETER MEASUREMENTS AT THE ONSET OF FREEZE-UP

Electromagnetic scattering models and measurements of ice and snow properties must be coupled with field measurements of radar backscatter to understand the physical mechanisms responsible for observed changes in radar backscatter. This study focuses on the backscatter signatures of sea ice at the onset of freeze up. Here, several approaches to modeling the radar backscatter before and after the onset of freeze-up are used to determine these backscatter mechanisms. These measurements are the first C-band *in situ* measurements in which the summer-to-fall transition is observed. The accompanying ice and snow physical properties allow us to examine the physical mechanisms responsible for the observed changes in radar backscatter during this transition.

The copolarized C-band radar backscattering coefficient prior to freeze-up is lower than after freeze-up by 4 to 12 dB at incidence angles ranging from 15° to 55°. By observation, the backscatter response prior to freeze-up appears to be primarily due to surface scattering and the response after the onset of freeze-up appears to be primarily due to volume scattering for old ice. First, we use scattering and absorption calculations to determine the effect of the snow cover. Second, we use surface-only and volume-only scattering models to determine the primary scattering mechanisms responsible for the observed changes in freeze-up at vv and hh polarizations. Finally,

we use a rigorous single layer model with rough surface boundaries to model the changes in backscatter at all four linear polarizations. This model includes the effects of surface scattering, volume scattering in the ice layer, and interactions between the two.

Through this modeling effort we have determined that the increase in backscatter during freeze-up is not caused by changes in snow wetness, but by refreezing of moisture on or near the ice surface. The permittivity of sea ice, particularly the lossy part, increases sharply as temperatures near 0° C due to this moisture. When temperatures drop, both the real and imaginary parts of the permittivity decrease. It is the decrease in the loss as temperatures drop that is responsible for the observed changes in backscatter. Loss through wet snow has been shown to be the primary factor which causes the initial decrease in σ^0 at the onset of melt in the spring [Onstott and Gogineni, 1985; Livingstone, et al., 1987; Winebrenner, et al., 1994], but this is not the case during the onset of the freeze-up period. The small amount of snow cover present during this time refreezes prior to the sharp increase in backscatter observed as air temperatures drop. Therefore, the refreezing of moisture in the upper layers of the ice itself is responsible for the change in backscatter signature.

These modeling approaches and the comparison of field measurements with these models provide an insight into the physical mechanisms responsible for backscatter changes observed during the initial stages of freeze-up in the central Arctic. We used the knowledge from these measurements and modeling in the interpretation of ERS-1 SAR data as discussed in chapter 6

5.1 Effect of snow cover on radar backscatter during freeze-up

In this section we will demonstrate that the increase in backscatter is not due to the effect of snow volume scattering or absorption effects in the snow layer. Because falling temperatures coincide with new snowfall we must consider the effect of this new snowfall on the backscatter signature. First, the Rayleigh model is used to determine the contribution to the backscatter that may be caused by volume scattering from the snow layer. Second, we quantitatively examine the effect of loss through the wet snow layer. Loss through a wet snow layer has been used previously to explain changes in backscatter signatures that take place at the onset of melt in the Arctic .

5.1.1 Volume scattering from snow

The Rayleigh model has been used effectively to model the backscatter from dry snow [Ulaby, et al., 1982]. This model assumes that the particles are spheres with radii that are small with respect to wavelength and that scattering from each sphere is independent. With these assumptions the backscatter from a snow layer can be computed as the sum of the scattering from individual spherical scatterers as,

$$\sigma_{\text{snow}}^0 = \frac{\sigma_v N_v \cos \theta}{2\kappa_e} (1 - e^{-2\kappa_e \sec \theta}), \quad (5-1)$$

where θ is the incident angle in the snow and N_v is the number density of the snow particles. The extinction coefficient consists of loss due to scattering and loss due to absorption. Since we are modeling the scattering from dry snow, the absorption term is negligible.

Therefore, the extinction coefficient, κ_e , and the scattering cross section, σ_v , are

$$\kappa_e = 2R_v r^3 k^4 \frac{|\epsilon_s - \epsilon_0|^2}{|\epsilon_s + 2\epsilon_0|^2} \quad (5-2)$$

and

$$\sigma_v = \frac{8\pi k^4 r^6 |\epsilon_s - \epsilon_0|^2}{3|\epsilon_s + 2\epsilon_0|^2}, \quad (5-3)$$

respectively. Here, ϵ_s is the permittivity of the each snow particle, k_0 is the wave number, ϵ_0 is the permittivity of free space, R_v is the volume density of the snow, and r is the radius of the snow particles.

This model was used to compute backscatter for the snow layers observed on days 241 through 245. The measured snow parameters are tabulated in Appendix A, table A-2. These are cases in which dry snow (< 1% wetness) was observed and the results are shown in figure 5.1. The stations are labeled according to the Julian Date (JD) in 1991 on which they were observed and are appended with a letter if multiple floes were observed. These model results show that the backscatter due to snow volume scattering at C band cannot account for the increase in backscatter observed during IAOE'91. In each case the measured backscatter is at least 10 dB higher than the theoretical snow volume backscatter. The primary factor for the variation among the theoretical computations is due to the snow depth measurement. The station 244 b floe had 10 cm of snow, whereas the station 245 b floe had 4 cm of snow. This results in a 10-dB difference between the computation of snow volume backscatter for these two cases even though the grain size and density are nearly the same. Even for the deepest snow cover observed during IAOE, the effect of scattering on the measured backscattering coefficient is minimal.

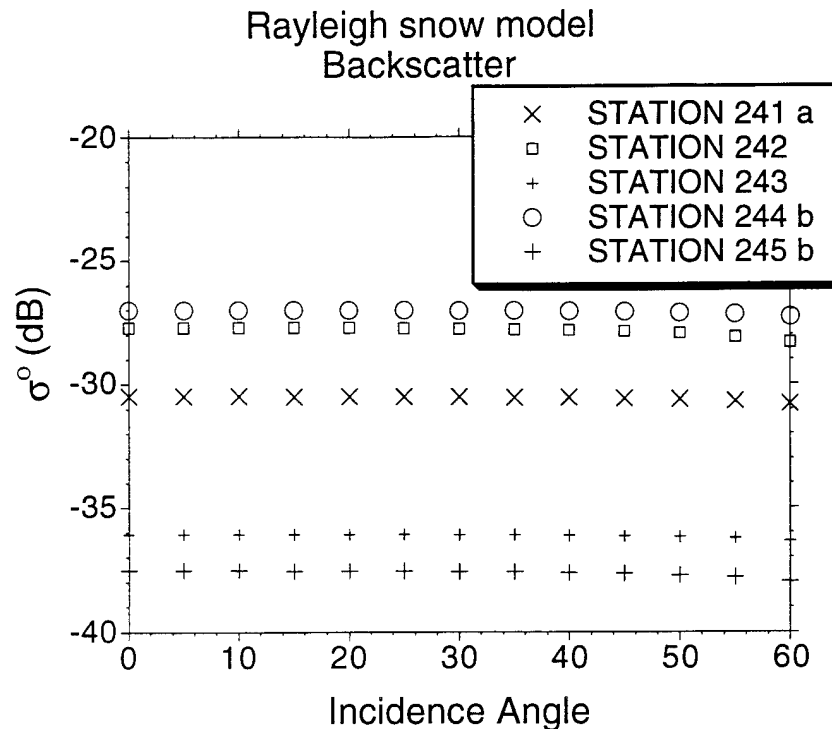


Figure 5.1 Results of Rayleigh backscatter model for snow cover situations observed during IAOE'91. The snow parameters shown in table A-2 (Appendix A) were used for these computations. These demonstrate that the backscatter from the snow does not cause the dramatic increase in σ^0 observed during this experiment.

5.1.2 Radar backscatter from snow-covered saline ice at CRREL

In addition to aiding in the development and verification of scattering models for sea ice, the CRREL measurements were designed to examine the effect of snow cover on sea ice at microwave frequencies. (A brief description of the CRREL experiments is given in chapter 3). We obtained radar backscatter measurements from bare and snow-covered saline ice during the CRREL experiments in 1992-1994. The measurements in 1992 and 1993 were obtained with the Ku-band step frequency radar system at CRREL's indoor pit facility. This system operated at 13.4 GHz, with 1

GHz bandwidth. We also obtained radar backscatter measurements from bare and snow-covered saline ice with the wideband plane wave system in January-March, 1994, and again in January 1995 at CRREL's Geophysics Research Facility (GRF). These measurements are used in the following sections to demonstrate from direct experiment that volume scattering by dry snow does not contribute significantly to the backscatter at frequencies below 13 GHz

High-resolution measurements from snow-covered saline ice

The wideband, planewave system was used to collect radar data from bare and snow-covered saline ice during CRRELEX'94. Because of the excellent range and angular resolution of this system, we are able to experimentally determine the sources of scattering within the snow-ice volume. We operated this system from 2 to 18 GHz to obtain data using the step-frequency technique. These data are inverse Fourier transformed to obtain the power return versus range from the radar as described by section 3.2.2. The power return at normal incidence from snow-covered saline ice is plotted versus range in figure 5.2. The return from the air/snow and snow/ice interface are clearly visible on this plot. The return from the air/snow interface is about 10-dB lower than from the snow/ice interface. Also, there is no significant contribution to the backscatter from within the snow volume. The return from bare saline ice was also obtained during this experiment. The power return versus range is plotted in figure 5.3 to demonstrate that for bare saline ice, the ice surface dominates the scattering return for young saline ice. This result also serves as a reference for the snow-covered saline ice measurement of figure 5.2. These results clearly demonstrate that the dry snow volume is not a significant source of scattering for the snow-covered saline ice sheet in the 2-16 GHz frequency range.

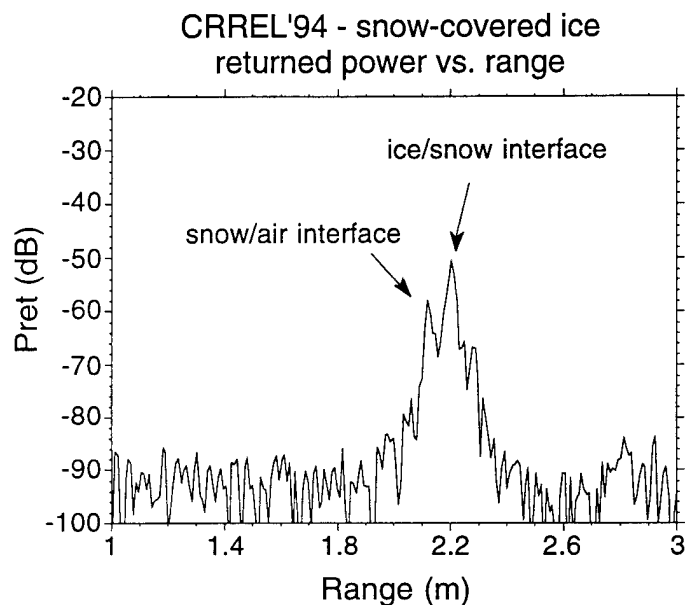


Figure 5.2 Plot of the returned power versus range from the compact range antenna for snow-covered saline ice (CRRELEX'94). The return from the air/snow interface and the snow/ice interface are clearly visible.

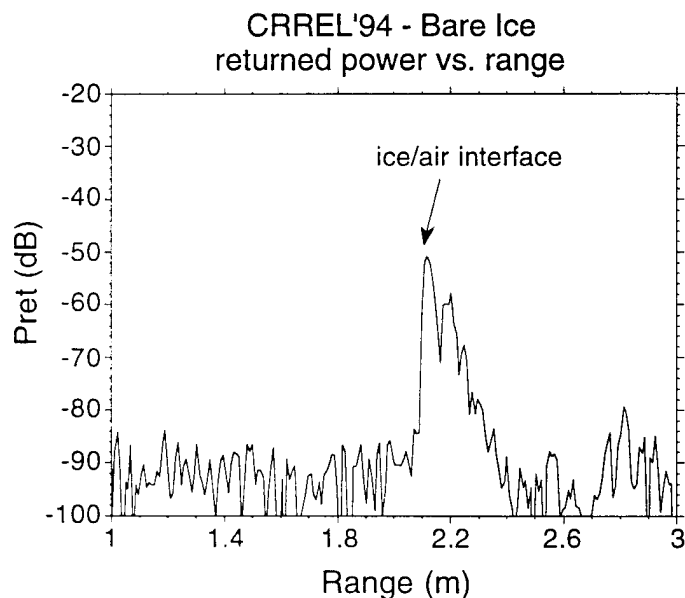


Figure 5.3 Plot of the returned power versus range from the compact range antenna for bare saline ice (CRRELEX'94). The return from the ice surface is clearly visible.

CRRELEX'92 Results

We also obtained Ku-band measurements from snow-covered saline ice at CRREL's indoor pit facility during the 1992 experiment. These measurements were performed in an indoor refrigerated facility which contains a test tank in which saline ice sheets are grown under quiescent conditions.

To quantify the effects of snow cover on the radar backscatter of sea ice, we made Ku-band radar backscatter measurements at the indoor pit facility with the step-frequency radar system described in chapter 3. After the ice sheet reached a thickness of 12 cm, four snow layers were applied on top of the ice in approximately equal increments to a height of 12 cm. These layers were made by taking newly-fallen snow from outside the CRREL facility and sifting it through a screen onto the ice to simulate a snowfall. The density for each of the four snow layers were measured to be 0.485, 0.277, 0.258, and 0.288 Mg/m³, and the grain sizes were estimated to be in the 1-3 mm range. We obtained backscatter measurements for each successive layer of snow added and the results are shown in figure 5.4 for incidence angles of 0°, 10° and 15°. These measurements show that while there is some variation in the backscatter measurements for the four snow depths, there is not a clear increase in backscatter that could be caused by volume scattering in the snow layer.

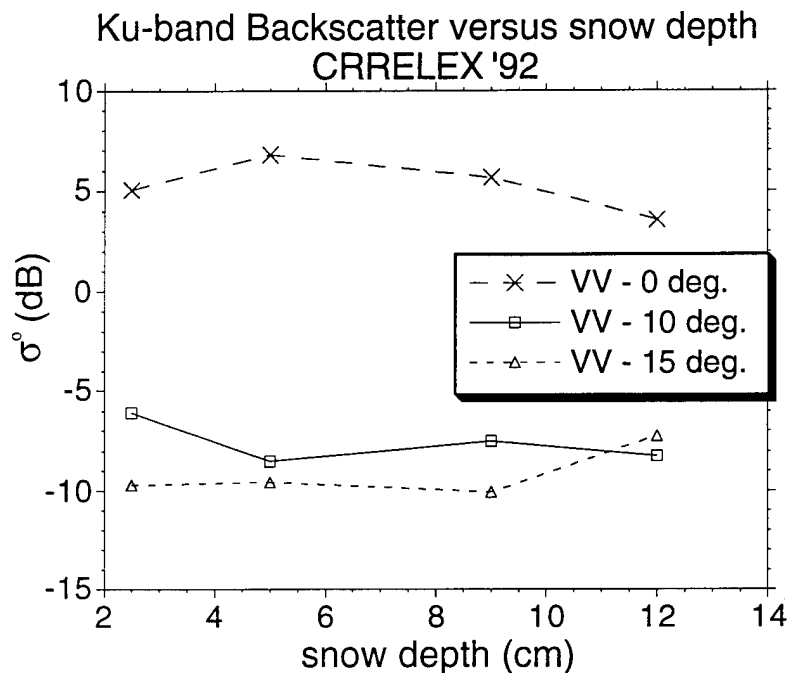


Figure 5.4 Backscatter coefficient versus snow depth at 13.4 GHz. Measurements were obtained at CRREL's indoor pit facility in the 1992 experiment. The backscatter does not increase significantly with increasing snow depth, indicating that the volume scatter contribution from these snow layers is not significant.

After completing the snow-cover experiments with a 12-cm snow layer we piled 21 cm of snow in a small area of the CRRELEX indoor pit. This snow pile was deep enough so that the return from the air-snow interface was resolvable from the snow-ice interface. The radar system has a resolution of 15 cm in free space and 11 cm in the snow, due to the higher dielectric constant, so the return from the snow-ice interface is resolvable from the air-snow interface. First, we placed a metal plate on top of the snow pile and measured the return at normal incidence. This provided a "range marker" to the snow surface. Then we removed the plate and measured the

backscatter at normal incidence from the deep snow-covered ice. The results from this experiment are shown in figure 5.5 (dB scale) and 5.6 (normalized, and plotted on a linear scale). Here we see that at the position of the metal plate return, the return from the snow-covered ice is negligible. The center of the snow-covered ice return occurs approximately 25 cm further in free-space range. Assuming the relative permittivity of snow is 1.5, this corresponds to a range separation of approximately 20 cm. This result clearly demonstrates that the return from the air-snow interface is significantly lower than the return from the snow-ice interface. A significant contribution due to snow volume scatter would cause a broadening of the returned power. We did not observe any significant broadening, therefore the snow volume scatter contribution was negligible in this case.

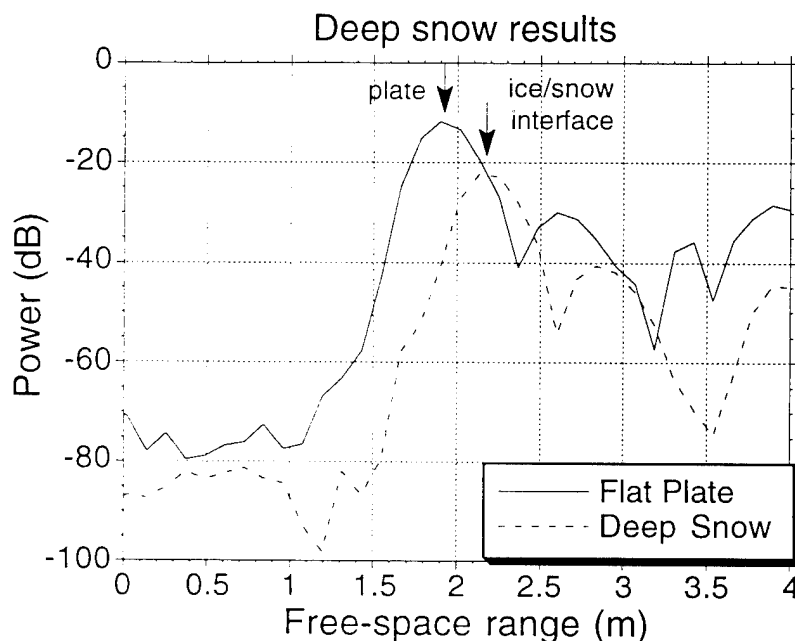


Figure 5.5 Radar return as a function of range for the 21-cm deep snow pile measured during CRRELEX'92. This demonstrates that the snow volume is virtually transparent at Ku-band.

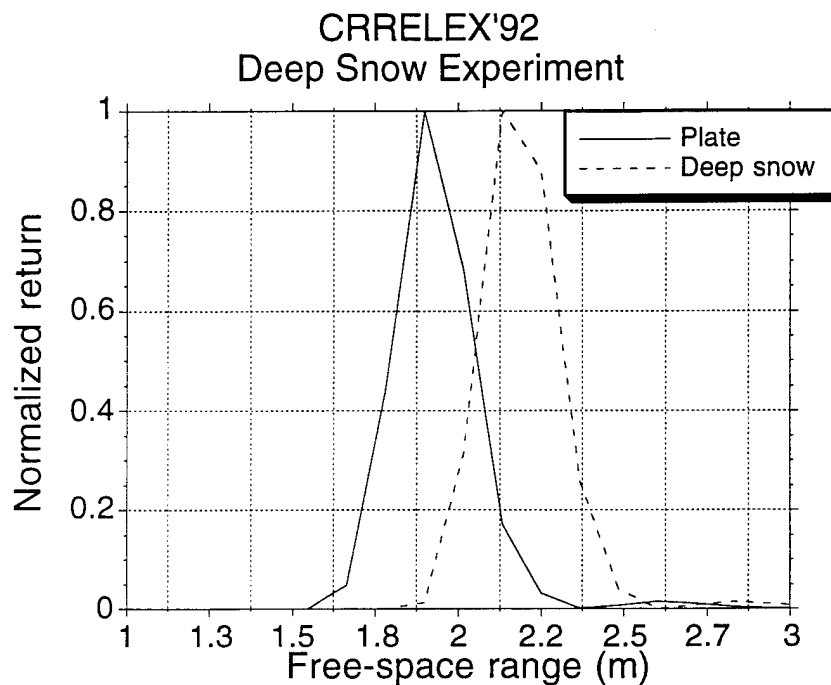


Figure 5.6 Results from figure 5.5, normalized and plotted on a linear scale.

The results from both the high-resolution measurements obtained in 1994 and the Ku-band measurements in 1992 indicate that snow volume scattering is not a significant source of backscatter for snow-covered saline ice. It should be noted that the snow cover in both cases existed under relatively dry conditions at temperatures below -3°C , and had not gone through the same metamorphosis as does snow cover on Arctic sea ice.

5.1.3 Effect of wet snow loss on radar backscatter during IAOE

It has been shown that for snow of 2% wetness by volume the loss can be as much as 10 dB/meter depending on the frequency used [Hallikainen, et al., 1986; Hallikainen, 1992]. Winebrenner, et al., [1994b] have also shown that attenuation by moisture in

the snow cover can result in a decrease in the backscatter coefficient from multiyear ice at the onset of melt. They have also shown that this decrease in σ^0 is consistent with measurements from ERS-1 SAR imagery, but these measurements lack coincident measurements of ice and snow properties to verify their claim. In this section we compute the attenuation due to wet snow based on physical property measurements obtained during IAOE to quantify its effect on the backscatter measurements during the onset of freeze-up.

The attenuation in a lossy medium in terms of its complex relative permittivity ($\epsilon_r = \epsilon' - j\epsilon''$) is,

$$\alpha = \frac{2\pi}{\lambda_0} \sqrt{\frac{1}{2} \epsilon' \left[\sqrt{1 + \left(\frac{\epsilon''}{\epsilon'} \right)^2} - 1 \right]}. \quad (5-4)$$

The power absorption coefficient is given by

$$\kappa_a = 8.686\alpha \quad (\text{dB/m}). \quad (5-5)$$

Various models for computing wet snow permittivity have been developed. The average permittivity of a heterogeneous material, such as wet snow, depends on the relative concentrations of the individual components as well as their distributions. The average electric field within a heterogeneous material must be related to the fields within the various components, or inclusions, to determine the average dielectric constant. Two models in particular have been shown to fit permittivity measurements within experimental accuracy. These are the Debye-like model [Hallikainen, et al., 1986] and the model based on the two-phase Polder-van Santen mixing formula for heterogeneous dielectric materials [Mätzler, 1992].

The Debye-like model is described by the empirical equations [Hallikainen, et al., 1986],

$$\epsilon' = A + \frac{0.073m^{1.31}}{1 + \left(\frac{f}{f_0}\right)^2} \quad (5-6)$$

and

$$\epsilon'' = \frac{0.073 \left(\frac{f}{f_0}\right) m^{1.31}}{1 + \left(\frac{f}{f_0}\right)^2}, \quad (5-7)$$

where

$$A = 1 + 1.83\rho + 0.02m^{1.015}. \quad (5-8)$$

In the above equations ρ is the dry snow density, f_0 is 9.07 GHz, m is the volume fraction of water in the mixture, and f is the frequency of interest in the calculation.

The model used by Mätzler [1987] for dielectric constant of wet snow given is,

$$\epsilon_r = 1 + \frac{1.60\rho}{1 - 0.35\rho} + \frac{23.0m}{1 - j\frac{f}{f_0}}, \quad (5-9)$$

where f_0 is 10 GHz in this case. The Mätzler model is based on the mixture of dry snow and liquid water present in the snow layer.

Either of these models for the bulk dielectric constant of wet snow may be used in (5-4) and (5-5) to obtain estimates of the power absorption due to the snow cover since both agree with experimental values for snow dielectric constant

The total loss due to absorption through the wet snow cover is then twice the path length through the snow layer times the power absorption coefficient,

$$\text{Total Loss}_{ws} = 2\kappa_a d_s \sec\theta. \quad (5-10)$$

Previously, we used the Debye-like model to compute the dielectric constant for the snow covers we observed during IAOE [Beaven and Gogineni, 1994]. These calculations showed that the loss through wet snow is not responsible for the change in backscatter that we observed during the freeze-up. However, the dielectric constant for wet snow based on Mätzler's model results in higher values for the complex relative permittivity. Therefore, we will use Mätzler's model to compute the complex permittivity of wet snow in our attenuation computation. This also will allow us to compare our simple methodology to that described by Winebrenner, et al., [1994].

The measured ρ for the various snow covers encountered in IAOE'91 (table A-2) were used to calculate estimates of relative complex permittivity from (5-9). The computed dielectric constants were used to estimate the loss due to the snow cover for the measurements taken during IAOE'91 at 25° and 35°. These results are shown in table 5.1 and are the computed absorption loss through the snow layers encountered during IAOE.

In two cases the snow wetness was too small to be measured, (table A-2), so 0.3% by volume was assumed. These data demonstrate that the absorption loss due to the snow cover was negligible for the multiyear ice floes from which backscatter data were taken. The estimated loss may be higher than the actual loss because of higher wetness used in the computation for the two cases mentioned above.

Table 5.1 Total estimated losses due to absorption of wet snow for IAOE'91 using Mätzler's model for wet snow permittivity			
Station	ϵ' , ϵ'' from (5-6)	Loss at 25° (dB)	Loss at 35° (dB)
234	1.77, 0.19	0.74	0.82
236	1.61, 0.13	1.12	1.24
239	1.59, 0.093	0.39	0.43
241 a	1.52, 0.031	1.20	1.33
242	1.51, 0.031	0.80	0.89
243	1.33, 0.015	1.71	1.89
244 b	1.31, 0.021	1.92	2.12
245 b	1.43, 0.031	1.10	1.22

Winebrenner, et al. [1994b] have demonstrated the effect of wet snow using a radiative transfer approach. They derive an expression for the theoretical decrease in 5.3 GHz, vv-polarized σ^0 caused by a layer of wet snow over multiyear ice. Their results for a uniformly-distributed 5-cm snow layer are shown here in figure 5.7. This expression is the relative difference between snow-covered multiyear ice between wet snow and dry snow conditions. The expression is of the form,

$$\Delta\sigma^0 \approx \exp[-4d\kappa], \quad (5-11)$$

where κ depends on the permittivity of the wet snow, frequency, the incidence angle and polarization.

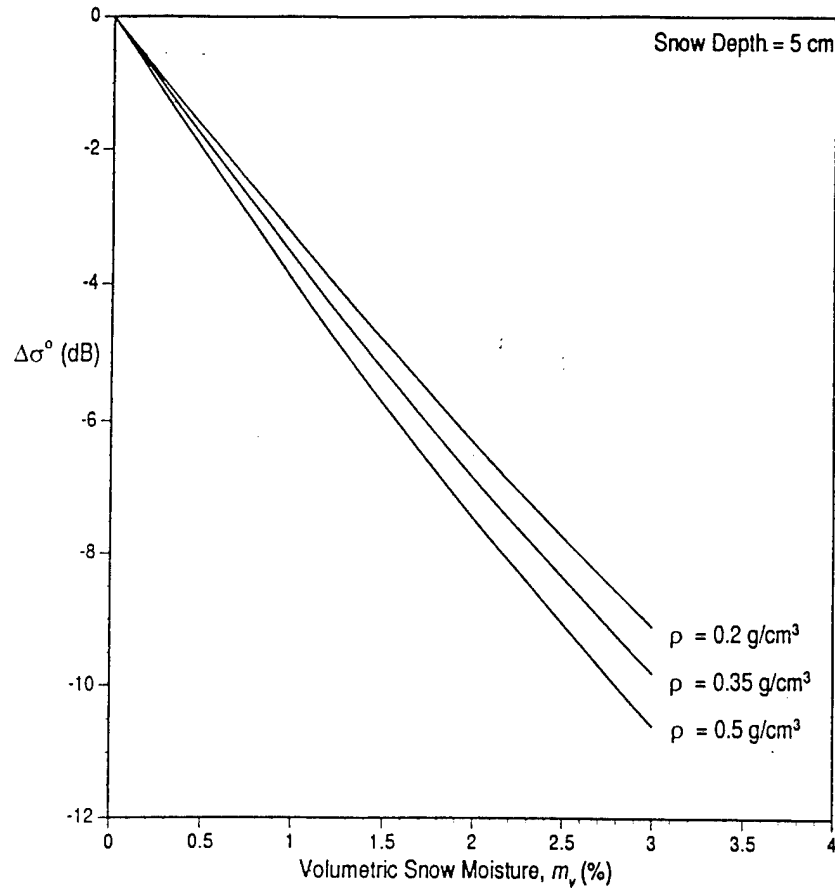


Figure 5.7 Theoretical decrease in σ^0 at 5.3 GHz, vv polarization and 23° incidence angle versus snow volumetric moisture content cause by a uniformly distributed 5-cm wet snow layer over multiyear ice. {from [Winebrenner, et al., 1994]}

For comparison to Winebrenner's calculations, we used Mätzler's model for permittivity of wet snow and our simple attenuation calculations to compute the loss due to a 5-cm snow layer with the same parameters as Winebrenner, et al., [1994], and the results are shown in figure 5.8. This comparison indicates that our simplified

analysis, based on attenuation through a lossy medium is consistent with Winebrenner's model.

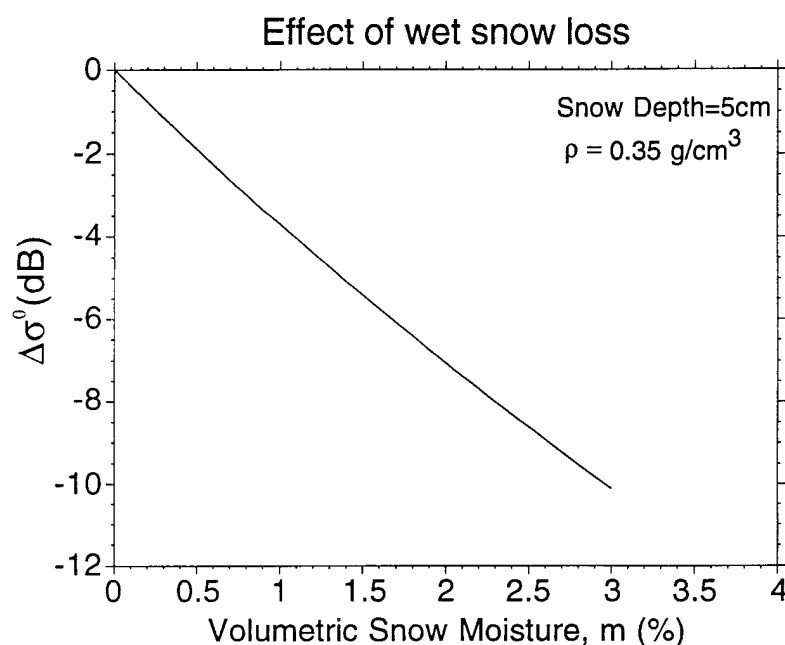


Figure 5.8 Our computation for loss due to wet snow using Mätzler's model. This is within 1 dB of the results from Winebrenner, et al., [1994] shown in figure 5.7.

We have demonstrated that the effect of scattering and absorption from the snow covers observed during IAOE have a small effect on the backscatter coefficient. The magnitude of backscattering from the snow volume was shown to be at least 10-dB lower than the measurements. The attenuation through the snow covers also causes minor (< 2 dB) changes in observed σ^0 for the snow covers observed during freeze-up. However, wet snow may play a primary role in masking the backscatter from multiyear ice during the melt season because of the larger amounts of snow present prior to the onset of melt (up to 60 cm or greater) [Gogineni, et al., 1992]. Based on

our calculations, the attenuation and scattering in the snow layer is not the primary cause for the changes in backscatter observed at the onset of freeze-up.

5.2 Modeling of the effects of freeze-up with surface-only and volume-only scattering models

The C-band radar backscatter signature of multiyear sea ice during the onset of freeze-up is characterized by a sharp increase in σ^0 and a decrease in the slope of σ^0 with incidence angle. The signature prior to the onset of freeze-up is typical of a medium in which surface scattering is the dominant backscattering mechanism. The signature after the onset of freeze-up is typical of a medium in which volume scattering dominates. The change in backscatter observed during the fall freeze-up may be caused by moisture in the ice volume or at the ice surface, which increases its permittivity, under warm conditions. This is evident when comparing the radar backscattering coefficient measurements to surface and volume scattering models. We used a surface-only scattering model to compute theoretical backscattering coefficients for the warm case (prior to freeze-up) and a volume-only model for the cold case (after onset of freeze-up). The surface-only model is based on the Kirchhoff scattering model (Physical optics approximation) for a random rough surface. The volume-only model uses Rayleigh theory and assumes that the backscatter signature observed after the onset of freeze-up is caused by volume scattering by independent spherical scatterers (air bubbles) within the multiyear ice volume. These models are described in sections 5.2.1 and 5.2.2, to follow.

5.2.1 Surface-only scatter model for sea ice prior to freeze-up

Prior to the onset of freeze-up the backscatter from multiyear ice can be modeled as surface scatter only. The penetration of electromagnetic waves into the ice volume is impeded by the high permittivity, particularly the lossy part, of sea ice under warm conditions. Here we use the Kirchhoff model under the scalar approximation with exponential correlation function [Ulaby, et al., 1986]. The backscattering from a random rough surface using this model is

$$\sigma_{ppn}^0 = 2k^2 \cos^2 \theta |R_p(\theta)|^2 e^{-(2k\sigma_h \cos(\theta))^2} \cdot \sum_{n=1}^{\infty} \left[\frac{(4k^2 \sigma_h^2 \cos^2 \theta)^n}{n!} \right] \cdot \text{INT}_n, \quad (5-12)$$

where INT_n is the integral given by

$$\text{INT}_n = \int_0^{\infty} \rho^n(\xi) J_0(2k\xi \sin \theta) \xi d\xi. \quad (5-13)$$

Here, k is the wave number, σ_h is the rms surface height, θ is the incidence angle at the ice surface, $|R_p|^2$ is the Fresnel reflection coefficient for the polarization p (v or h), and J_0 is the zeroth-order Bessel function of the first kind. The exponential correlation function is given by

$$\rho(\xi) = e^{\left(\frac{-|\xi|}{L_c}\right)}, \quad (5-14)$$

where L_c is the correlation length and ξ is the distance variable. The integral, INT_n is simplified by using the following Bessel-function identity,

$$\int_0^{\infty} x^{n+1} e^{-\alpha x} J_n(\beta x) dx = \frac{2\alpha(2\beta)^n \Gamma(n + \frac{3}{2})}{\sqrt{\pi}(\alpha^2 + \beta^2)^{n+\frac{3}{2}}}, \quad (5-15)$$

$$\text{Re}\{n\} > -1, \text{Re}\{\alpha\} > |\text{Im}\{\beta\}|$$

Thus, the integral becomes

$$\text{INT}_n = \frac{\frac{2n}{L_c} \Gamma\left(\frac{3}{2}\right)}{\sqrt{\pi} \left[\left(\frac{n}{L_c} \right)^2 + (2k \sin \theta)^2 \right]^{\frac{3}{2}}}, \quad (5-16)$$

where Γ is the gamma function defined by

$$\Gamma(\tau) = \int_0^{\infty} e^{-x} x^{\tau-1} dx, \quad \tau \geq 0. \quad (5-17)$$

The summation over n is truncated at $n=10$ and the error due to this truncation is less than 0.1 dB [Ulaby et al., 1986, pp. 1814-1815]. We also incorporate the change in incidence angle at the ice surface, caused by refraction in a snow layer, by the use of Snell's law.

Field measurements of surface roughness were obtained during the IAOE experiment over several multiyear ice floes using a wood grain gauge [Beaven et al., 1993]. The result of these measurements were a mean rms roughness of 4.2 mm and a correlation length of 4.0 cm. The autocorrelation function computed from these measurements is included in Appendix A, figure A.5. These surface parameters were used in the Kirchhoff model, and a dielectric constant of the ice was assumed to be 3.9, based on past measurements of desalinated ice at C band at temperatures around 1°C [Arcone et al., 1986]. The dielectric constant of the snow layer, which was used to account for refraction in the snow layer, was 1.7. This was based on field measurements of the snow properties by MWG during the early part of the experiment [Garrity et al., 1992]. Using these parameters, we computed the surface-only backscattering coefficients (vv polarization) and compared these to the average of multiyear results at three ice stations between JD 234 and 239, 1991. These results are shown in figure

5.9 and demonstrate that surface scattering alone accounts for the observed copolarized radar backscatter signature prior to the onset of freeze-up conditions.

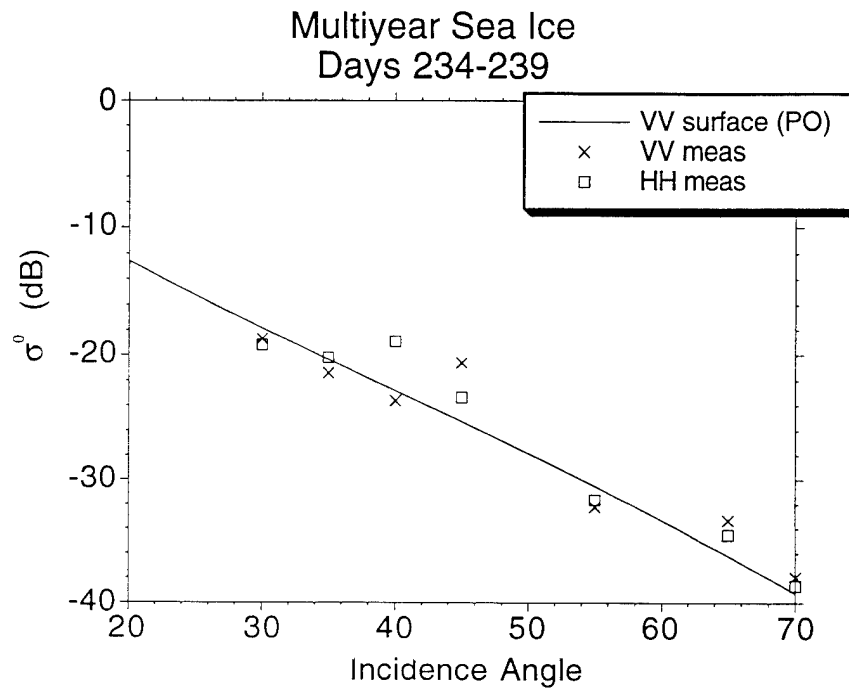


Figure 5.9 Measurements and surface scattering theory for multiyear sea ice just prior to freeze-up. The σ^0 measurements are averaged from multiyear floes observed from JD 234-239. Surface scattering theory accounts for the backscatter signature under summer conditions.

5.2.2 Volume scatter model of sea ice after onset of freeze-up

At the onset of freeze-up, the backscatter increased dramatically as shown earlier in chapter 4. To model the backscatter signature after the onset of freeze-up we used Rayleigh volume scattering theory. Although more advanced volume scattering theories have been developed, the Rayleigh model can be used to explain the change in backscatter mechanism observed here. A more rigorous analysis follows in this chapter. Assuming that the air bubbles within the ice volume are spherical and small with respect to wavelength, the backscatter from an ice layer of penetration depth d is

$$\sigma_{vol}^0 = \frac{\sigma_v N_v \cos \theta}{2\kappa_e} (1 - e^{-2d\kappa_e \sec \theta}), \quad (5-18)$$

where θ is the incident angle in the ice and N_v is the number density of the scatterers (air pockets) in the ice volume. The extinction coefficient, κ_e , and the scattering cross section, σ_v , are

$$\kappa_e = 2R_v r^3 k^4 \frac{|\epsilon - \epsilon_i|^2}{|\epsilon + 2\epsilon_i|^2} \quad (5-19)$$

and

$$\sigma_v = \frac{8\pi k^4 r^6 |\epsilon - \epsilon_i|^2}{3|\epsilon + 2\epsilon_i|^2}, \quad (5-20)$$

respectively.

To compute the volume scatter we assumed a mean air pocket radius of 1.5 mm, which was used by Ulander and Carlström [1992] to fit measurements from multiyear ice after the onset of freeze-up to a volume scattering model. We also used published measurements of a dielectric constant of 3.1 in this temperature range in the model [Arcone et al., 1986]. Drinkwater [1989] computed the penetration depth for low-salinity ice at various temperatures. Since the salinity properties of the ice we

observed were similar to those used by Drinkwater, [1989] we used his results. The penetration depth in the temperature range of -4° to -5° C for low-salinity ice is about 70 cm. We compared the theoretical volume scatter results using these parameters with the measurements from multiyear ice observed from JD 243 to 245, 1991. These results are plotted in figure 5.10 and demonstrate that volume scattering is the dominant backscatter mechanism under freeze-up conditions.

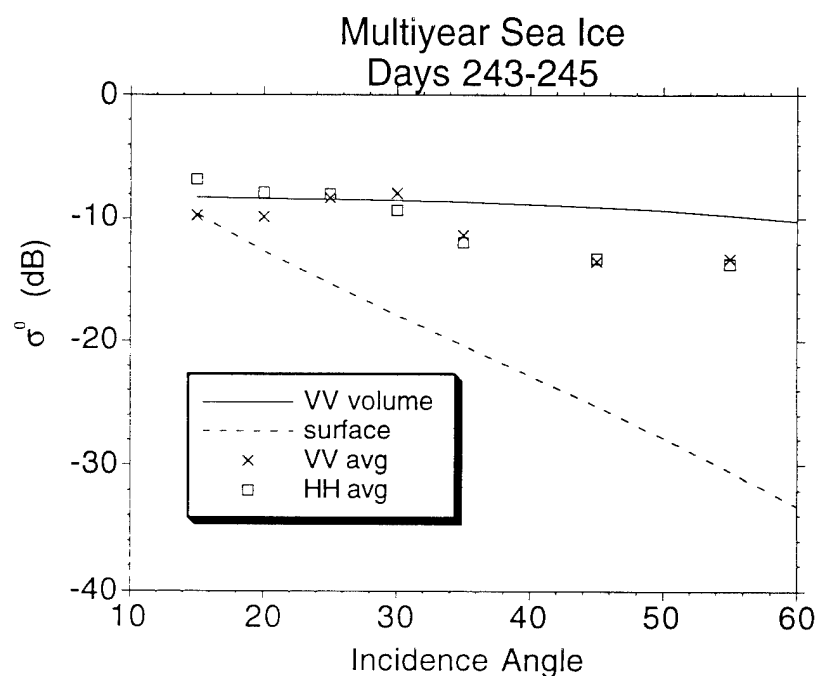


Figure 5.10 Radar backscattering coefficients under freeze-up conditions compared with volume scattering theory. The theoretical surface scattering coefficient from figure 5.9 is shown for comparison. This demonstrates that the dominant backscattering mechanism after the onset of freeze-up is volume scattering.

5.3 Single-layer model for radar backscatter at the onset of freeze-up

The surface-only and volume-only scattering models presented thus far give insight into the change in scattering mechanism responsible for observed changes in radar backscatter, although they are not the most rigorous techniques. The models used in the previous section suffer from the following deficiencies: (1) They do not include the cross-polarized radar backscattering coefficients; (2) Both volume and surface scattering are present at all times although one or the other may dominate; and (3) The volume scatter model is only valid for sparsely distributed scatterers in the Rayleigh regime. Therefore, to explore the phenomena that are responsible for changes in scattering mechanism during the freeze-up, more rigorous models are employed here. A single-layer volume scattering model with rough surface boundaries at the top and bottom is used to model the radar backscatter from multiyear sea ice. The model is based on radiative transfer theory, but accounts for scattering from closely-spaced and non-Rayleigh scatterers. The same model is used for predictions prior to freeze-up and after the onset of freeze-up, but with different parameters, based on physical differences observed in the field. The model is discussed in section 5.3.1. A comparison of model predictions with measurements, along with particulars for each case, are discussed in section 5.3.2.

5.3.1 Single-layer model with rough surface boundaries

The geometry of the single-layer model is described by figure 5.11. The model can be used for several situations involving layers of ice and snow, including bare ice and snow-covered sea ice [Tjuatja, et al., 1992 and Tjuatja, et al., 1993]. In this case the inhomogeneous layer consists of multiyear sea ice with air pockets as the scatterers.

The upper boundary is the ice surface and the lower boundary is the ice-water interface. In section 5.1 the snow layer was shown to be transparent at this frequency range and its only significant effect is to cause a slight refraction at the air-snow boundary.

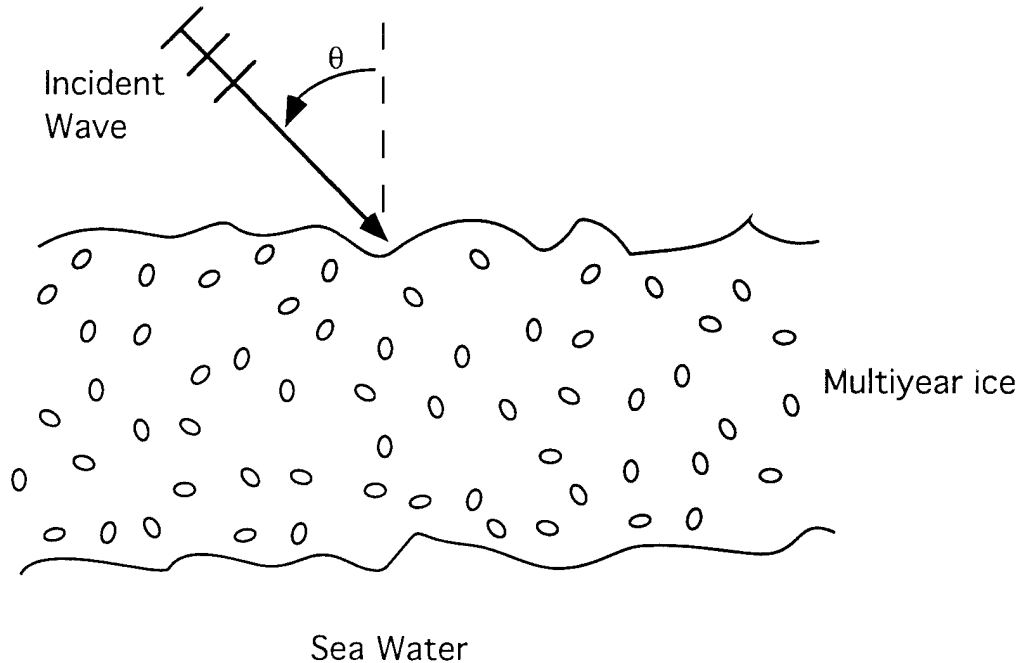


Figure 5.11 Geometry for single-layer scattering model.

This model computes the scattering coefficient of a layer that consists of spherical scatterers, embedded in a background dielectric medium. The model is based on radiative transfer theory, but it is reformulated using the matrix doubling method [Ulaby, et al., 1986, pp. 1146-1161], to obtain an exact solution when first-order approximations are not sufficient, such as when multiple-scattering effects must be taken into account. The phase matrix is developed using the scattered field of a single Mie scatterer without making far-field approximations. Therefore, closely-spaced scatterers (with respect to wavelength) may be modeled with this technique. The

layer is bounded by rough boundaries at the top and bottom, which are modeled by the integral equation (IEM) method. The surface roughness for each boundary is represented by the "natural" correlation function, given by,

$$\rho(\xi) = \left(1 + \frac{\xi^2}{L_c^2}\right)^{-1.5}. \quad (5-21)$$

This yields results that are similar to exponential correlation function estimates, except for large incidence angles [Tjuatja, personal communication]. The advantage to using this correlation function is that it requires fewer computations. A complete description of the single-layer model can be found in Tjuatja, et al., [1992] and Fung, [1994, ch. 8].

The important aspects of this model are that it includes both surface and volume scattering, as well as non-coherent interactions between the volume scatterers and each surface. Also, since the model doesn't use far-field approximations for scattering from the spherical scatterers (air pockets) within the ice volume it is capable of modeling closely spaced scatterers. The IEM is used for surface boundaries so that neither Kirchhoff rough surface nor small perturbation requirements need not be met.

5.3.2 Comparison of model predictions and measurements

The model described in section 5.3.1 was used to compute theoretical backscattering coefficients at all four linear polarizations, based on measured ice properties during IAOE. The comparison of backscatter measurements from multiyear ice just after the onset of freeze-up with the modeled results is discussed first. This is followed by the

measurements and model predictions for conditions observed just prior to the onset of freeze-up.

Multiyear sea ice backscatter modeling after freeze-up

After the onset of freeze-up, the snow layer was observed to be cold and dry (section 5.1), so loss is small and there is virtually no volume scatter contribution from the snow layer in this case. The upper surface of the model is the snow-air interface and the lower surface is the ice-water interface, with an inhomogeneous layer of multiyear ice as the scattering volume. As in the previous section, the effect of the snow layer was taken into account by modifying the local angle of incidence according to Snell's law. The ice was assumed to be 2 meters thick, although the optical depth is large enough that the model results hold for multiyear ice of any thickness greater than about 92 cm (based on 10-dB, two-way loss due to extinction in the MY ice layer). Parameters used in the model are based on the measurements in the field used for the surface-only and volume-only models of section 5.2. The only "free" parameter of consequence in both cases is the scatterer radius. The volume fraction is based on field measurements of density made by the CRREL group (density measurements are included in Appendix A, figure A.4). The dielectric constant was based on past measurements of dielectric constant of desalinated ice at -5°C [Arcone, et al. 1986]. The dielectric constant of sea ice is relatively constant at temperatures below this. The modeling parameters used to fit the post-freeze-up data are listed in table 5.2.

Table 5.2 Model parameters for post-freeze-up case

<u>Input parameters</u>	
frequency	6.2 GHz
ice thickness	2 m
air volume fraction	0.1
air bubble radius	1.35 mm
sea water ϵ_r	35 - j30
ice layer effective ϵ_r	3.15 - j0.015
top surface roughness $k_0\sigma_h$	0.5454
top surface correlation length, k_0L_c	5.194
bottom surface $k_0\sigma_h$	0.1
bottom surface k_0L_c	1.0
<u>Computed parameters</u>	
albedo	0.1186
extinction coefficient	1.246
optical thickness	2.492

Using the single-layer scattering model for multiyear ice we computed the backscattering coefficients at vv, hh, and cross-polarization versus incidence angle. The air pocket radius was adjusted to obtain the best fit, although it is only slightly lower than the radius used for the volume only scattering model of section 5.2 (1.3 mm, as opposed to 1.5 mm). These model results are plotted along with the measurements from multiyear floes in figure 5.12. These measurements are averaged

over the multiyear floes observed from JD 243 to JD 245 during IAOE. The copolarized measurements agree well with the modeling results and the level of the cross-polarized measurements matches the theory. The relative contribution of the surface scattering to the total scattering is shown in figure 5.13. Here, we observe that the volume scattering term is dominant at incidence angles larger than 20° . This agrees with the simpler scattering model approach used in section 5.2.

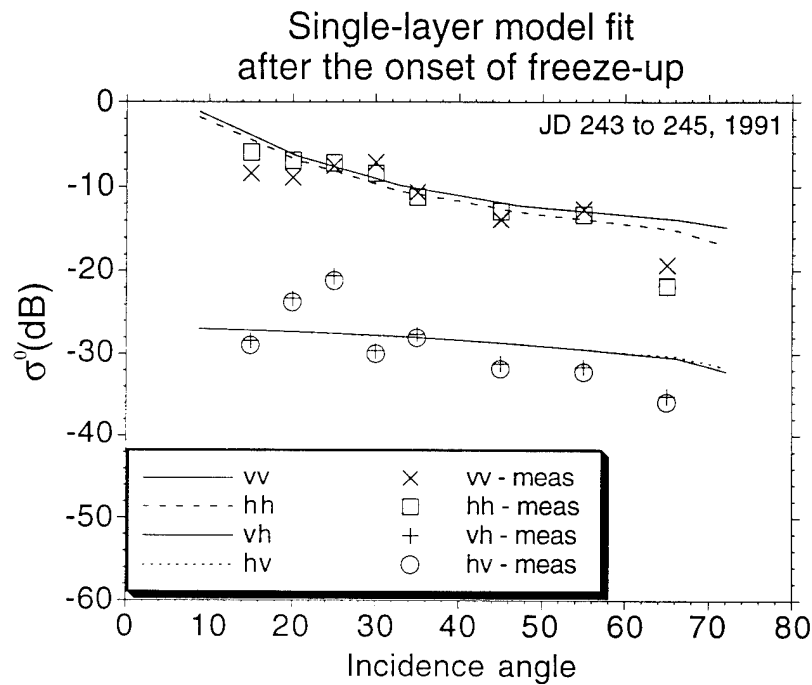


Figure 5.12 Comparison of scattering model with measurements from multiyear sea ice after the onset of freeze-up.

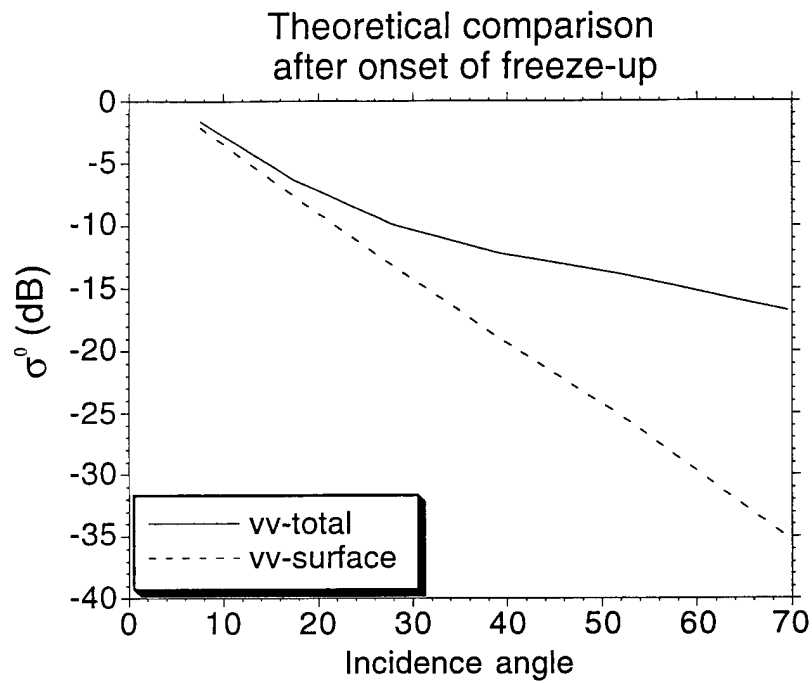


Figure 5.13 Theoretical comparison of surface scattering contribution to the total backscatter coefficient after the onset of freeze-up using the single-layer model.

Multiyear sea ice backscatter model prior to freeze-up

Prior to freeze-up, the copolarized backscattering coefficient from multiyear ice is significantly lower than after the onset of freeze-up. We modeled this previously with a surface-only scattering model. Here, we model this case as an inhomogeneous ice layer with irregular boundaries, as in figure 5.11. In this case however, we used a higher value for the effective permittivity of the multiyear ice sheet, based on past measurements of permittivity of desalinated ice around freezing [Arcone, et al., 1986]. We also reduced the rms surface roughness by less than 10% and the correlation length by less than 6% to obtain a better fit. The primary difference between the model for the post-freeze-up measurements and these measurements are that the dielectric constant is changed from $3.15 - j0.015$ to $3.9 - j0.9$. The results from the modeling are plotted along with the measurements in figure 5.14. The measurements are averaged from multiyear floes observed on JD 236 and JD 237. Once again, the copolarized measurements agree well with the theoretical calculations, except at the low incidence angles. The model parameters could be adjusted to fit these data, but we did not want to adjust any parameters by more than 10% of their initial values. Model parameters are listed in table 5.3. The cross-polarized measurements are about 5 dB higher than the predicted values. This is due to the limited polarization purity of the radar system. The copolarized to cross-polarized ratio for this antenna is between 25 and 30 dB [Gogineni, et al. 1990]. The copolarized and cross-polarized antenna patterns for this antenna are shown in figure 5.15. The polarization ratio (difference between copolarized and cross-polarized σ^0) for these measurements is about 25 dB. The modeling results predict a polarization ratio of 25 to 40 dB, depending on incidence angle. Therefore the cross-polarized

backscatter coefficients in this case are at or below their minimum measurable level, based on the theoretical results.

Table 5.3 Model parameters for prior-to-freeze-up case

<u>Input parameters</u>		
frequency		6.2 GHz
ice thickness		2 m
air volume fraction		0.10
air bubble radius		1.3 mm
sea water ϵ_r		35 - j30
ice layer effective ϵ_r		3.9 - j0.9
top surface roughness $k_0\sigma_h$		0.5
top surface correlation length, k_0L_c		5.5
bottom surface $k_0\sigma_h$		0.1
bottom surface k_0L_c		1.0
<u>Computed parameters</u>		
albedo		0.0042
extinction coefficient		59.08
optical thickness		118.2

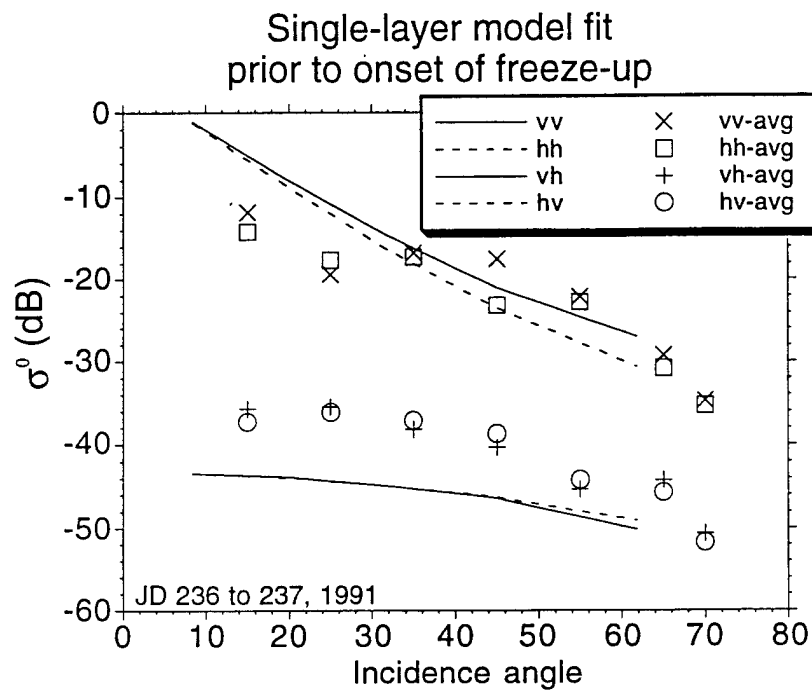


Figure 5.14 Comparison of scattering model with measurements from multiyear sea ice before the onset of freeze-up.

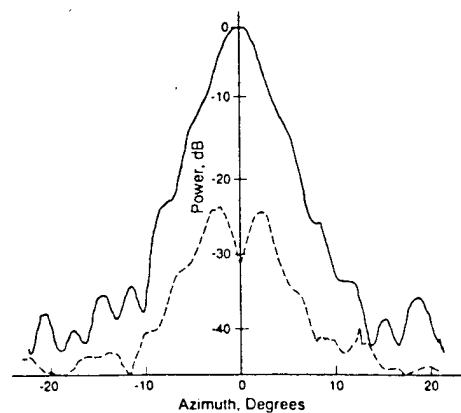


Figure 5.15 Offset parabolic antenna radiation pattern at C-band. The copolarized pattern is solid and the cross-polarized pattern is dashed. [Gogineni, et al. 1990]

The relative contribution of surface scattering as well as the total scattering for vv polarization as computed with the single-layer scattering model, is demonstrated in figure 5.16. Because of the decreased penetration caused by the moisture at or near the ice surface, the surface scattering dominates the scattering for angles up to at least 50°.

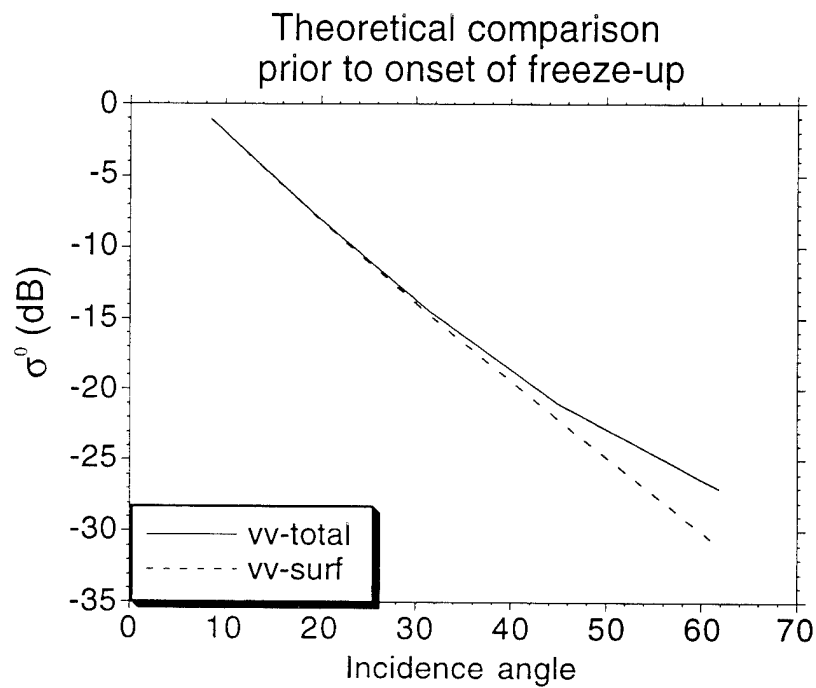


Figure 5.16 Theoretical comparison of surface scattering contribution to the total backscatter coefficient prior to the onset of freeze-up using the single-layer model.

5.4 Summary

The geophysical changes in snow-covered multiyear ice were explored in this chapter to determine the primary cause for the changes in radar backscatter coefficients that are observed during the onset of freeze-up. We examined the effect of the snow cover as well as the presence of moisture in the upper layers of multiyear ice on the backscatter.

Using Rayleigh scattering theory for a snow cover, we demonstrated that increased volume scattering caused by an increase in the snow depth does not cause the increase in observed scattering coefficient. Using a plane wave attenuation coefficient model we also demonstrated that loss through a wet snow layer is not the primary cause for the changes in backscatter that we observed. This simple model was also shown to agree to within ± 1 dB with a more complex analysis of the effect of attenuation through wet snow on multiyear ice [Winebrenner, et al., 1994]. The snow cover observed at the onset of freeze-up during IAOE have only a small effect on the observed backscatter. However, one should not generalize the effect of snow cover here to all seasons since the attenuation and scattering by snow may be a primary effect during melt onset and various stages of melt in the Arctic summer [Onstott and Gogineni, 1985; Livingstone, et al., 1987; Barber, et al., 1992].

Since the snow cover was determined to have only a small effect on the backscatter measurements made during IAOE, we examined the effect of an increase in loss caused by moisture in the upper layers of the multiyear ice floes. First, we used a surface-only scattering model to model the copolarized measurements prior to freeze-up. The Kirchhoff model for scattering from rough surfaces was used as the surface

only model. The premise for using this model is that moisture in the upper layers of the multiyear ice causes an increase in the lossy part of the permittivity of sea ice, which increases its attenuation coefficient of the ice. This does not allow for penetration of electromagnetic energy into the sea ice volume. Therefore, the scatterers present in the multiyear ice volume do not contribute significantly to the total scattering.

To model the backscatter from multiyear ice after the onset of freeze-up, we first used a volume-only scattering model, based on Rayleigh scattering theory. These results matched the measurements reasonable well for most of the incidence angle range, indicating that scattering from within the ice volume is dominant after the onset of freeze-up. Since the Rayleigh volume scattering model doesn't predict cross-polarized scattering, we used the single-layer scattering model to compare theory to measurement at all four linear polarizations [Fung, 1994 ch. 8]. These model results fit the measurements very well for both the copolarized and cross-polarized measurements. The model also demonstrates that volume scattering is the dominant scattering mechanism at angles greater than 20° after the onset of freeze-up.

The results shown from single-layer model computations for both measurements before and after the onset of freeze-up strengthens the argument that re-freezing of moisture at the ice surface or within the upper portion of multiyear ice floes is responsible for the observed change in backscatter at the onset of freeze-up. The more rigorous model results confirmed our conclusions based on the simpler models.

CHAPTER 6

ERS-1 SAR INTERPRETATION FROM IN SITU MEASUREMENTS AND MODELS

6.1 Introduction

Results from field measurements of the radar backscatter presented in chapters 4 and 5 suggest that the onset of freeze-up should be observable in ERS-1 SAR imagery. The field measurements and modeling of the freeze-up signatures were used to determine the physical mechanisms responsible for the observed change in backscatter in chapter 5. In this chapter we address the usefulness of extrapolating information based on these "point" measurements to the interpretation of SAR data. We will also demonstrate that the onset of freeze-up may be detected from SAR imagery and that the changes observed in the SAR data are comparable to that observed from *in situ* measurements. Correct interpretation of satellite SAR data is not possible without this type of ground truth information.

Detecting the onset of freeze-up may be combined with detection of the onset of melt [Winebrenner, et al., 1994] to determine the number of "melt" days during the summer. The onset of freeze-up signals a key point in the annual cycle of energy fluxes. The timing and geographic distribution of the onset of freeze-up may be important in determining the annual cycle of energy fluxes between the ocean and atmosphere. Detecting the onset of freeze-up is also important in developing algorithms to extract geophysical parameters of sea ice from satellite data. Often

algorithms are developed that work well under cold conditions in the winter months, but aren't suitable for summer months or seasonal transitions. Detection of the freeze-up may also be useful as a switch between seasonally-dependent algorithms.

A description of the ERS-1 SAR, with relevant parameters, is given in section 6.2, followed by a brief description of the radiometric corrections necessary to compute σ^0 from high-resolution ERS-1 SAR images obtained from the German processing and archive facility (D-PAF) and the United Kingdom processing and archive facility (UK-PAF) in section 6.3. Field measurements presented in chapter 4 and models derived from these measurements in chapter 5 are used to interpret the variation of SAR-derived backscattering coefficients during the initial stages of freeze-up in the eastern, central Arctic in the remainder of this chapter.

6.2 ERS-1 SAR Description

The European Space Agency (ESA) launched the ERS-1 in July 1991. This satellite carries a number of instruments, designed primarily for the study of the Earth's oceans, ice, and meteorology and is the first in a series of environmental systems planned by ESA. The Active Microwave Instrument (AMI) on ERS-1 can be operated as either a SAR or a wind scatterometer. The SAR provides the best opportunity to date for monitoring sea ice in the polar regions on a routine basis. The essential parameters of the ERS-1 SAR data used in this study are summarized in this section.

The ERS-1 mission has been divided into several phases which impact the nature of the SAR data available. Of primary interest in Arctic research are the ice phases, in

which a three-day repeat cycle was used. ERS-1 was operated with a three-day repeat cycle from initial switch-on until around 30 March 1992. The first part of this three-day orbit phase was the commissioning phase, in which calibration and geophysical validation tasks were given priority. This phase lasted until mid-December, when the first ice phase was initiated. The data obtained in this study were acquired from the commissioning phase of the satellite. The multi-disciplinary phase and geodetic phase are designed for 35-day and 176-day repeat cycles, primarily for studies involving radar altimeter data and land and ocean studies.

The design of the AMI is described by Attema [1991] and in the ESA literature [Vass and Battick, 1992]. The operational parameters of importance in this study of the SAR, when operating in image mode are given in table 6.1.

Table 6.1 ERS-1 SAR image mode parameters	
Center frequency	5.3 GHz
polarization	vv
spatial resolution	along track: ≤ 30 m; across track: ≤ 26.3 m
Radiometric resolution	≤ 2.5 dB at $\sigma^0 = -18$ dB
Dynamic range	≥ 21 dB
Swath Width	102.5 km (telemetered); 80.4 km (full performance)

6.3 Computing σ^0 from ERS-1 SAR Precision Image data

Computing σ^0 from the ERS-1 SAR precision image (PRI) product is described in Laur [1992]. The computation is a straightforward process because of the high radiometric stability of the instrument and the radiometric corrections that are performed at the processing and archive facilities (PAFs). Data processed after 1 September 1992 at D-PAF and UK-PAF are corrected for the in-flight antenna pattern and compensated for range spreading loss. Therefore, to compute σ^0 from PRI data a calibration constant, which depends on incidence angle, needs to be applied to the data. The calibration constant depends on the PAF at which the data were processed. The backscatter coefficient may be obtained from the raw image data by,

$$\sigma^0 = \frac{\langle I \rangle \sin \alpha}{K_{\text{ref}} \sin \alpha_{\text{ref}}}, \quad (7-1)$$

where K_{ref} is the calibration constant at the nominal incidence angle of 23° and α is the local incidence angle of the image (19.5° to 26.6°). The image intensity $\langle I \rangle$ is the locally-averaged image intensity, which is given in terms of the raw PRI data as

$$\langle I \rangle = \frac{1}{N} \sum_{i=1}^N \text{DN}_i^2, \quad (7-2)$$

where DN is the raw numerical image value. The number of pixels used to compute $\langle I \rangle$, and thus σ^0 , must be large enough to be considered an accurate estimate of the mean. The corrections for data processed prior to 1 September 1992 include simple expressions to compensate for range spreading loss and the antenna pattern correction [Laur, 1992].

6.4 Comparison of ERS-1 SAR images and in situ measurements

The radar backscatter signature of multiyear ice experiences dramatic changes during the fall freeze-up as demonstrated from the IAOE measurements presented in chapters 4 and 5. ERS-1 SAR images of Arctic sea ice from the same area and time frame as the IAOE experiment also show dramatic changes at the onset of freeze-up. We have analyzed 18 SAR frames from this area and time frame. Image intensities were averaged over 8x8 pixels and the backscatter coefficients for each image were computed according to the procedures outlined in section 6.3. All of the σ^0 images used in this study are included in Appendix B, along with ancillary information regarding image location, time, and identification numbers. The borders of each SAR image frame used in the study are plotted along with the IAOE cruise track in polar coordinates in Appendix C.

6.4.1 SAR-derived σ^0 variation during freeze-up

Figures 6.1 and 6.2 show two images of the same region just prior to freeze-up (figure 6.1) and after the onset of freeze-up (figure 6.2). Figure 6.1 is an ERS-1 SAR frame of sea ice from 21 August (JD 233). This image demonstrates the difficulty in interpreting SAR images under melt conditions because of the low backscattering coefficient and the falloff with incidence angle. The left side of the image is the minimum incidence angle and the right side is the maximum. The falloff with incidence angle indicates that surface scattering is the dominant backscatter mechanism. The SAR image from 6 September (JD 249) demonstrates that the

backscatter level increases and the angular falloff becomes relatively flat under freeze-up conditions. As time progresses and temperatures remain cold for a period of time, SAR images of sea ice obtain their "winter" signature. This is demonstrated by figure 6.3, an ERS-1 SAR frame from 12 September (JD 255) 1991. Here the multiyear floes are clearly visible, with young first-year ice and possibly open water between the floes.

21 August Frame 1827

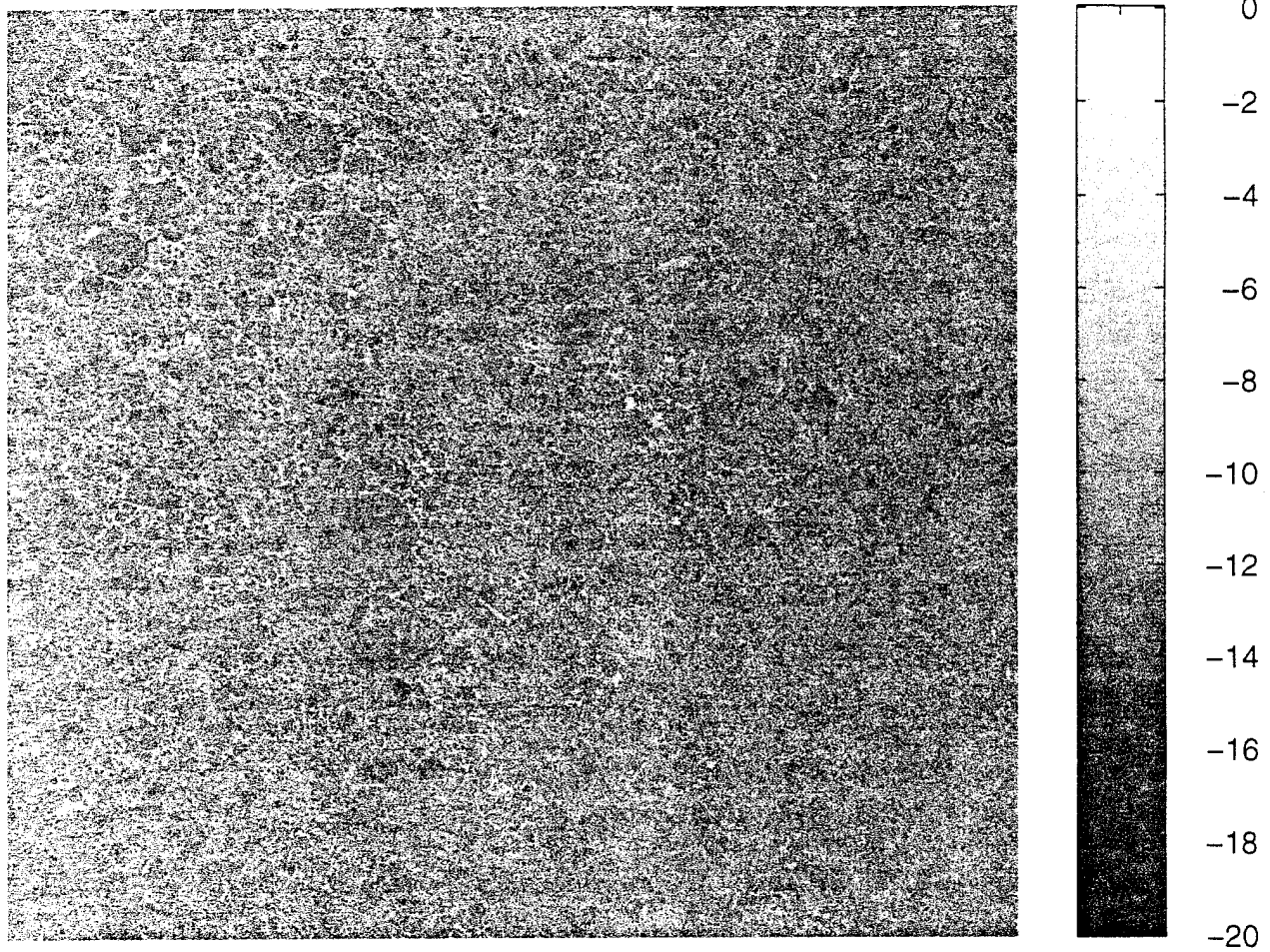


Figure 6.1 ERS-1 SAR image frame prior to freeze-up from 21 August 1991 (JD 233). The image shows the falloff in intensity as the incidence angle increases from the left of the image to the right of the image. (Copyright ESA, 1991)

6 September Frame 1827

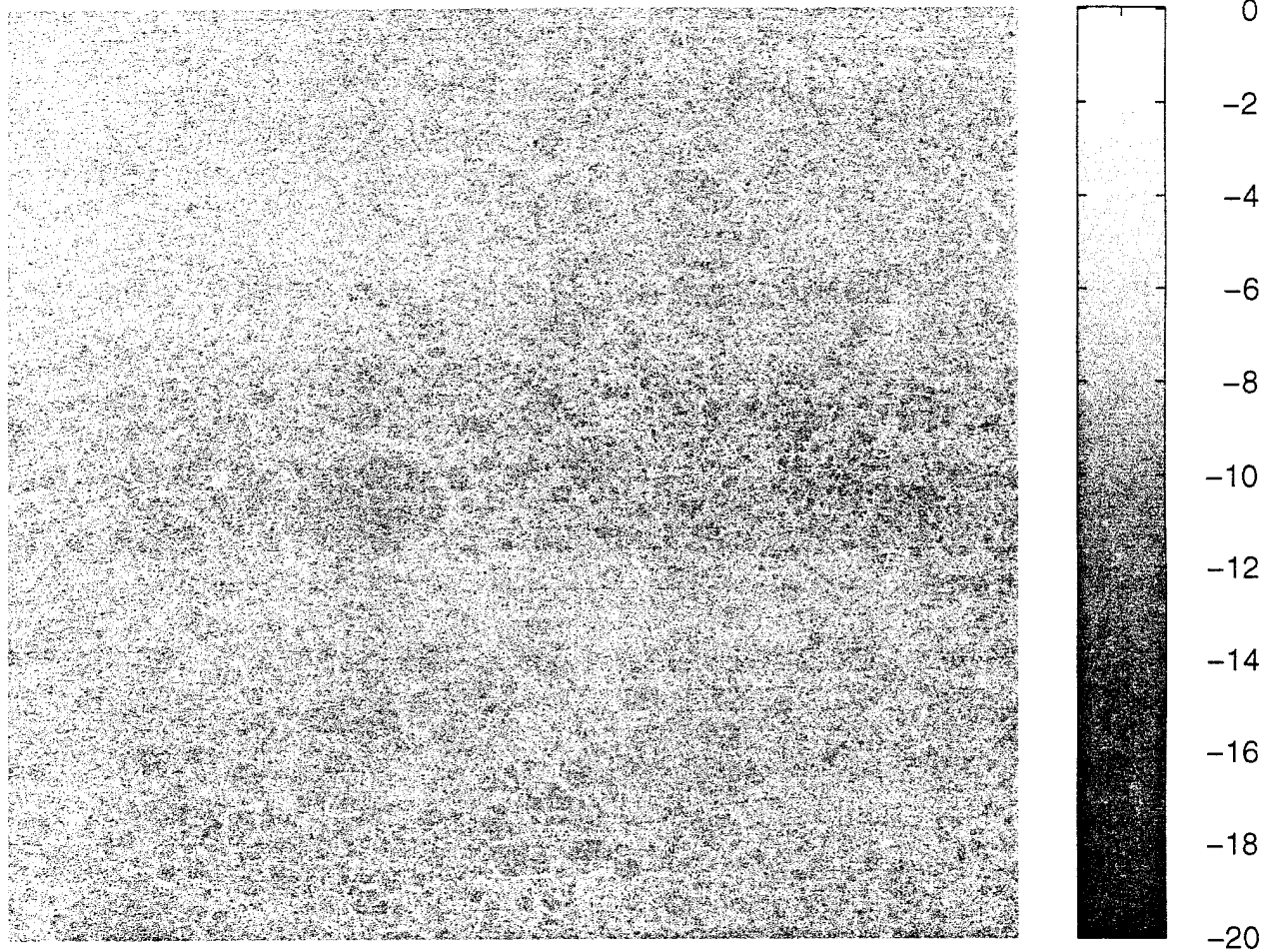


Figure 6.2 ERS-1 SAR image frame from 6 September 1991 (JD 249). This image was taken during the initial stages of freeze-up from the same approximate area as figure 6.1. This image shows the increase in backscatter as the freeze-up commences. (Copyright ESA, 1991)

12 September Frame 1719

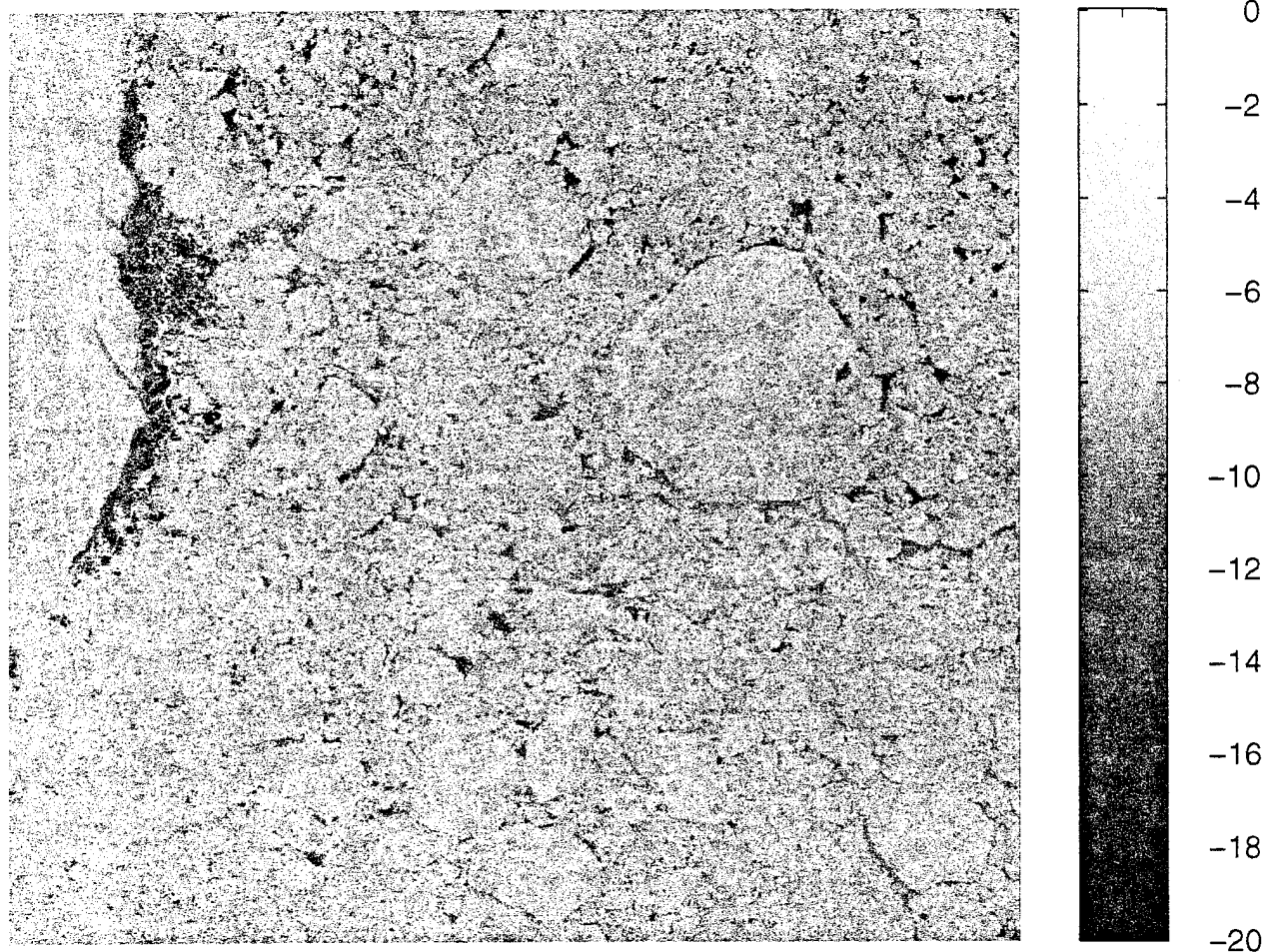


Figure 6.3 ERS-1 SAR image frame from 12 September 1991 (JD 255). This image was taken well into the freeze-up period in the central portion of the Arctic. For the multiyear floes, the volume scattering is dominant, resulting in backscatter values in the -7 to -8 dB range and almost no incidence angle dependence. (Copyright ESA, 1991)

Calibrated backscattering coefficients were computed from all the SAR images obtained from this region to determine if the changes are consistent with the shipborne measurements and the scattering models used to explain them. First, we computed the average backscattering coefficient, σ^0 , across each entire image and plotted the result versus JD in figure 6.4. This shows the same trend of increasing backscatter as observed during IAOE. Also, the drop in backscatter on days 239-240 is observed in both the SAR-derived backscatter data and the shipborne scatterometer data. The results in figure 6.4, however include all of the ice types and open water present within each SAR frame, not just the multiyear ice data.

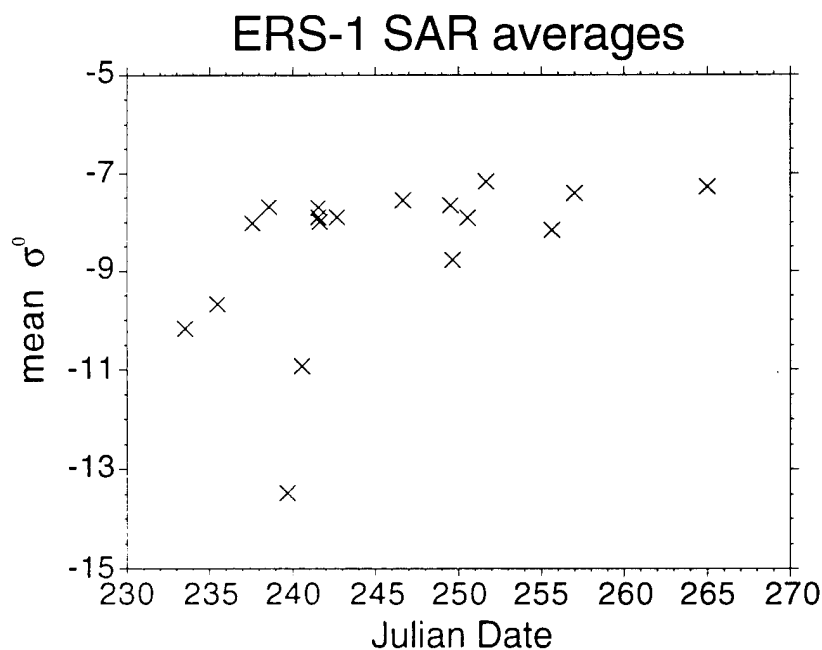


Figure 6.4 Average backscattering coefficients computed from ERS-1 SAR images of sea ice. These results are the mean σ^0 over the entire image and demonstrate the same trend as the ship-based backscatter measurements shown in figure 4.2.

The magnitude of the increase from the SAR data is different from the shipborne data. There are two reasons for this: (1) the shipborne measurements were made primarily at 35° and ERS-1 operates at a nominal incidence angle of 23° , and (2) the SAR σ° averages include all types of ice (and possibly open water) whereas the shipborne measurements include only multiyear ice. To resolve the incidence angle problem we must compare the mean σ° values from the SAR data to the values predicted by the models. The second problem can be resolved by finding the mean σ° for multiyear floes within each image. In the next section we compare the scattering model results with average multiyear ice backscatter coefficients computed from the ERS-1 SAR images.

6.4.2 Relevant scattering model results and MY observations from SAR

The scattering models described in chapter 5 were shown to accurately describe the observed changes in radar backscatter at C band during the initial stages of freeze-up in the Arctic. The vv-polarized data in the incidence angle range of 19° to 27° correspond to what should be observed from ERS-1 SAR. From these models, changes expected in ERS-1 SAR images due to the change in scattering mechanisms at the onset of freeze-up can be computed. Both the 23° value and the slope of σ^0 are computed from the backscatter model results in chapter 5. The characteristics that should be observed in ERS-1 SAR are listed in table 6.2. These are based on both the single-layer model results and the simpler volume- and surface-only models (Rayleigh and Kirchhoff, respectively).

Table 6.2 Model-based parameters relevant to ERS-1 SAR for freeze-up		
	σ^0 at 23°(dB)	slope σ^0 (dB/degree)
<u>Prior to freeze-up</u>		
Kirchhoff	-14	-0.57
Single-layer	-11	-0.56
<u>Post-freeze-up</u>		
Rayleigh	-8	≈ 0
Single-layer	-8	-0.24

Using the scattering models of chapter 5, the difference between the σ^0 just prior to freeze-up and the σ^0 just after freeze-up at 23° is 3 to 6 dB. Therefore we should expect to observe a 3- to 6-dB increase in the average backscatter coefficient from multiyear ice from ERS-1 SAR images during the freeze-up. In addition, there should be a measurable difference in the backscatter from multiyear ice as a function of incidence angle within the ERS-1 SAR image frame under melt conditions. Both models used for computing the backscatter from multiyear ice prior to freeze-up indicate that surface scattering dominates and the slope of σ^0 is around -0.56 to -0.57 dB/degree. This should be observed with ERS-1, excluding the effects of large-scale features such as ridges and floe boundaries, which may decrease the angular dependence. The volume-only model (Rayleigh) indicates that after the onset of freeze-up the slope should become nearly 0 dB/degree. The single-layer model predicts a slope of -0.25 dB/degree. This modest slope is also observed in the backscatter measurements (chapter 5) during freeze-up, rather than a flat response,

indicating that while volume scattering dominates the radar backscatter from multiyear ice after freeze-up, the surface also contributes at the lower incidence angles ($< 20^\circ$).

We computed the mean σ° for multiyear floes from ERS-1 SAR images and divided these into two categories: (1) multiyear floes at near angles ($< 23^\circ$) and (2) multiyear floes at far angles ($> 23^\circ$). The results are shown in figure 6.5. Here we observe that at the far angles the multiyear σ° increases by 5 to 8 dB during the time frame studied. The minimum backscatter was approximately -12 dB on JD 233 and -15 dB on JD 239. The maximum settled around -8 to -7 dB for multiyear floes observed from JD 246 to the end of the study. The near-angle σ° showed a less dramatic increase. At lesser incidence angles the difference between multiyear backscattering increased by 4 to 7 dB. This is due to the incidence angle dependence of surface scattering, predicted by both modeling approaches.

As we stated above, the slope of the radar backscatter as a function of incidence angle should also change from approximately -0.57 dB/degree to the range of -0.25 to 0 dB/degree as the dominant backscattering mechanism changes from that of surface scattering to volume scattering. To investigate this we computed the average slope for each entire image, using approximately 1° intervals. We have also computed approximate slopes for multiyear floes, based on the average backscattering coefficients of figure 6.5. The results of these calculations are shown in figure 6.6. Note that the slope estimates for multiyear floes are underestimated because we assumed 7° difference between near-angle multiyear floes and far-angle multiyear floes, and these categories were based on a cutoff at approximately 23° . Nonetheless,

the trend of the slopes shows that as σ^0 increases, the slope of the backscatter decreases, which is predicted by both scattering models and shipborne measurements.

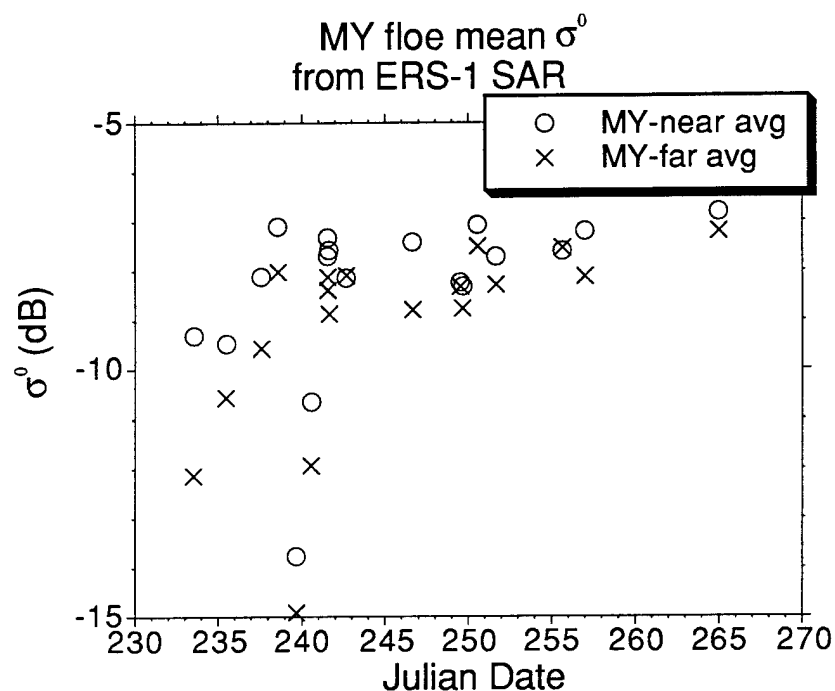


Figure 6.5 Mean σ^0 for multiyear floes within the SAR images studied. These are divided into near and far angles, indicating multiyear floes which appear below 23° and above 23° , respectively. This figure shows the same trend as the overall mean σ^0 in figure 6.4 and the ship-based σ^0 measurements of figure 4.2.

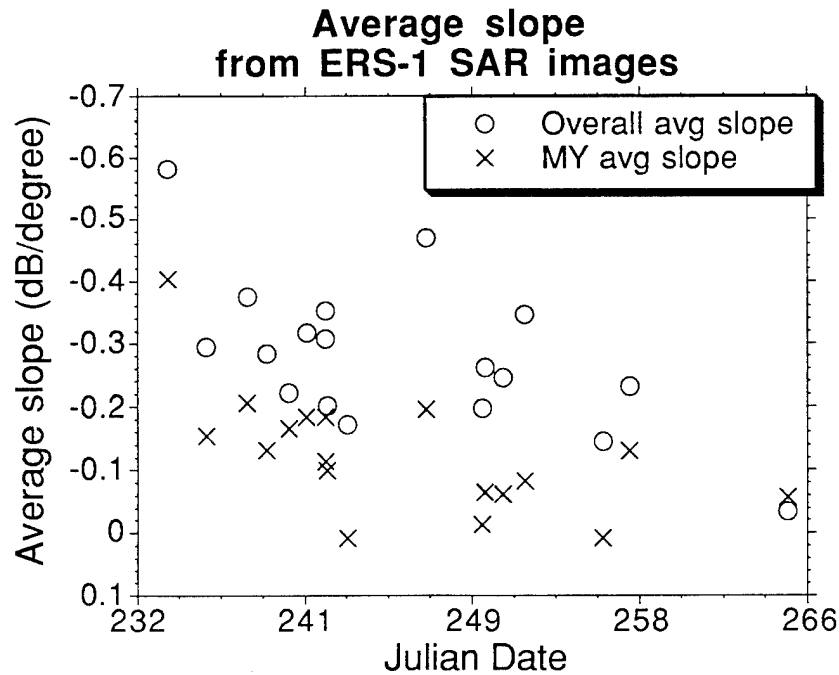


Figure 6.6 Slopes of backscattering coefficients derived from ERS-1 SAR images for both the overall image and the multiyear floes within the image. The slope changes from approximately -0.2 to -0.4 dB/degree during melt conditions, to approximately -0.1 dB/degree during freeze-up.

These comparisons demonstrate that the ERS-1 SAR is sensitive to the increase in backscatter caused by the refreezing of moisture on or near the ice surface during the summer-to-fall transition. The SAR results also demonstrate that the effect observed from ship-based measurements is responsible for large-scale variations in scattering. The SAR data may thus be exploited for mapping the freeze-up in the Arctic. Winebrenner, et al., [1994] and Schwartz, et al., [1994] have recently shown that the onset of melt can be detected from ERS-1 SAR. The results presented here demonstrate that the onset of freeze-up can be detected from ERS-1 SAR imagery,

based solely on average image statistics from multiyear floes, or from images in which multiyear ice is the dominant ice type. The slope of the backscattering coefficient also may be used, along with the mean value to detect freeze-up in the Arctic. The slope change appears to be a secondary effect, though, and should be used as a secondary measure in this case. However, the slope change should be more important for RADARSAT data since it will cover a larger range of incidence angles (20° to 50°). We have also demonstrated the primary cause for the observed effects during freeze-up, based on extensive modeling and *in situ* measurements of radar backscatter and geophysical properties of multiyear ice (chapter 5). The increase in backscatter occurs when moisture on the ice surface refreezes, allowing for penetration into the ice volume.

In Winebrenner, et al., [1994] an algorithm for detecting the onset of melt is based on the peak values of the histogram for SAR images which contain at least 50% multiyear ice. To demonstrate that the freeze-up may be detected in a similar fashion, we computed histograms for the σ^0 SAR images obtained in our study area from 21 August 1991 to 12 September 1991. These histograms are computed from the low-resolution (after 8x8 averaging) σ^0 images used above are shown in figures 6.7, 6.8, and 6.9 in chronological order. The time-series of histograms from the IAOE study area also indicate that the onset of freeze-up may be inferred by observing the peak of the histogram and determining when it exceeds some predetermined "freeze-up threshold" (possibly around -9 dB). The initial increase around JD 238-239 may be interpreted as the onset of freeze-up, when actually it is just the last of many large swings in backscatter during the late summer season, due to temperature fluctuations around freezing. The final steep increase on JD 241, followed by a stable signature actually signals the onset of freeze-up.

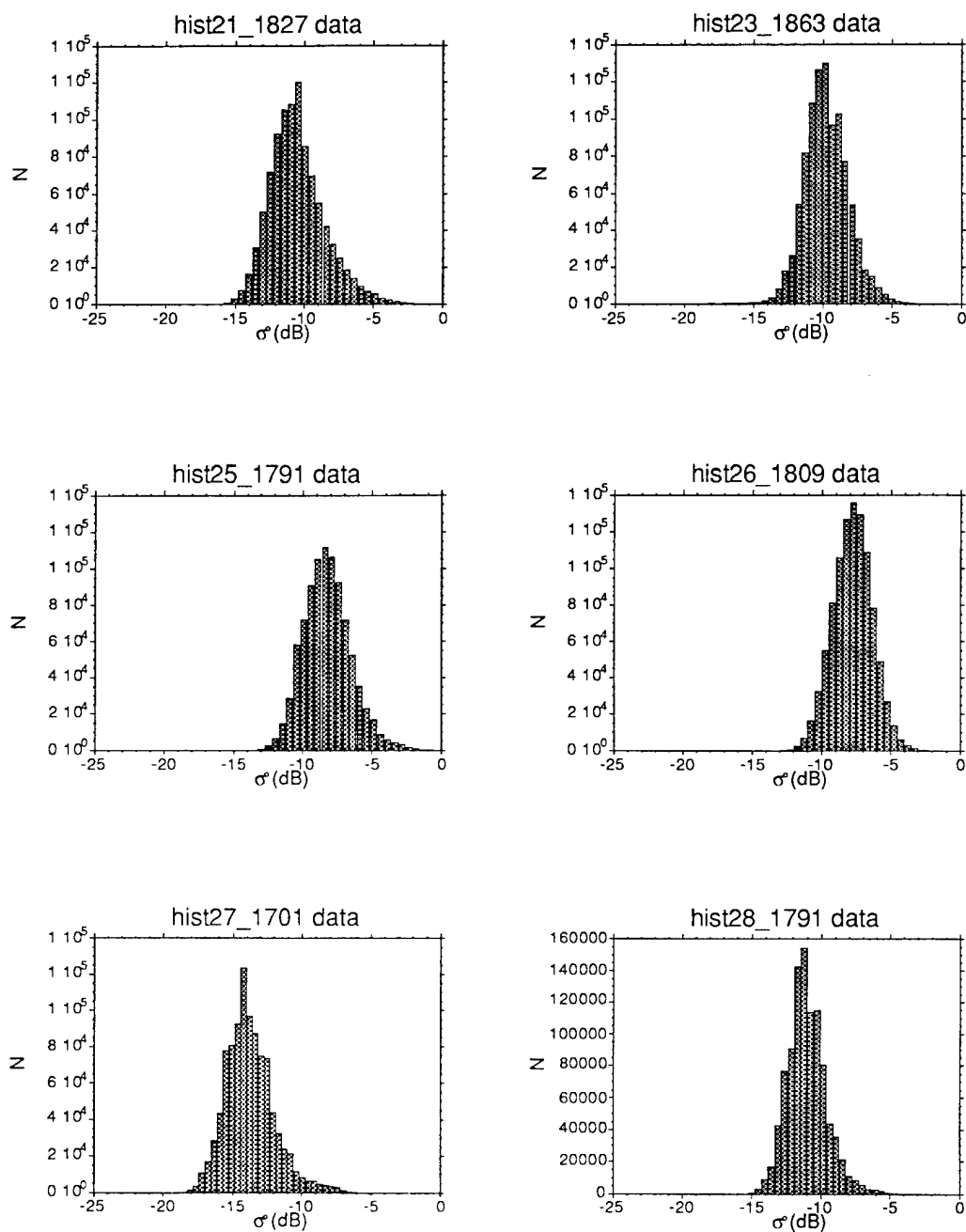


Figure 6.7 Histograms from SAR σ^0 images for 21 August (JD 233) through 28 August (JD 240), 1991.

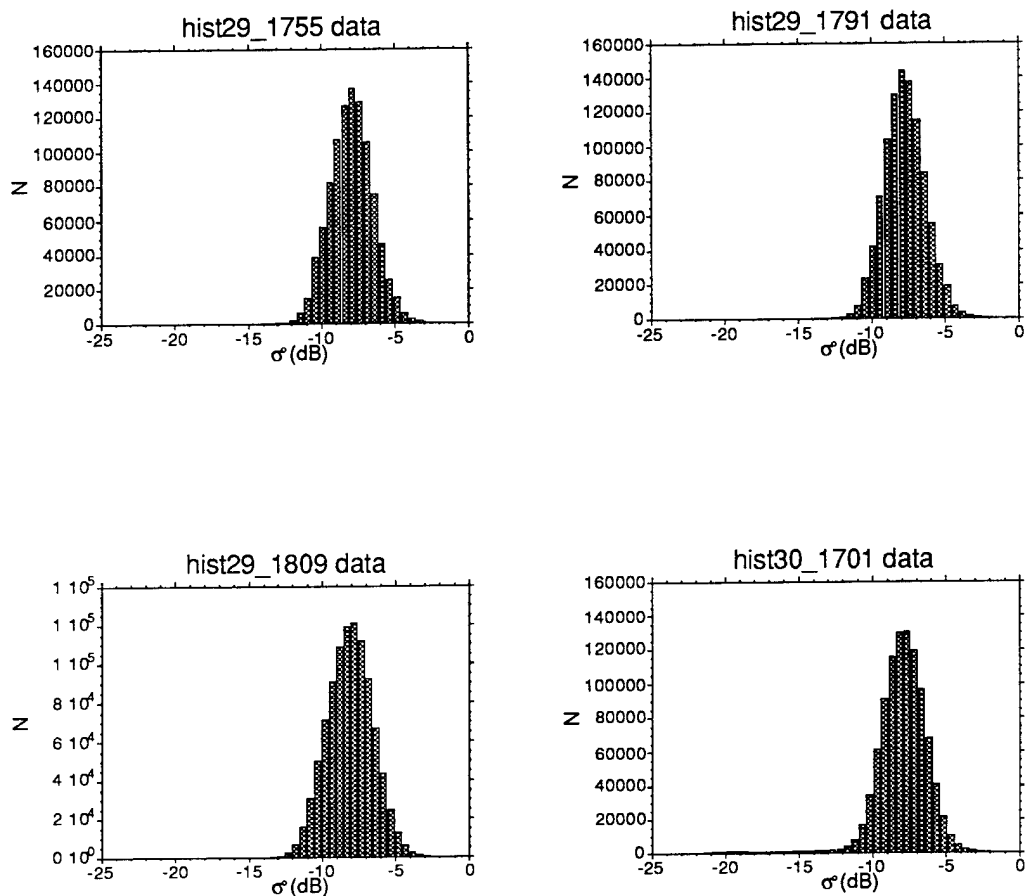


Figure 6.8 Histograms from SAR σ^0 images for 29 August (JD 241) through 30 August (JD 242), 1991.

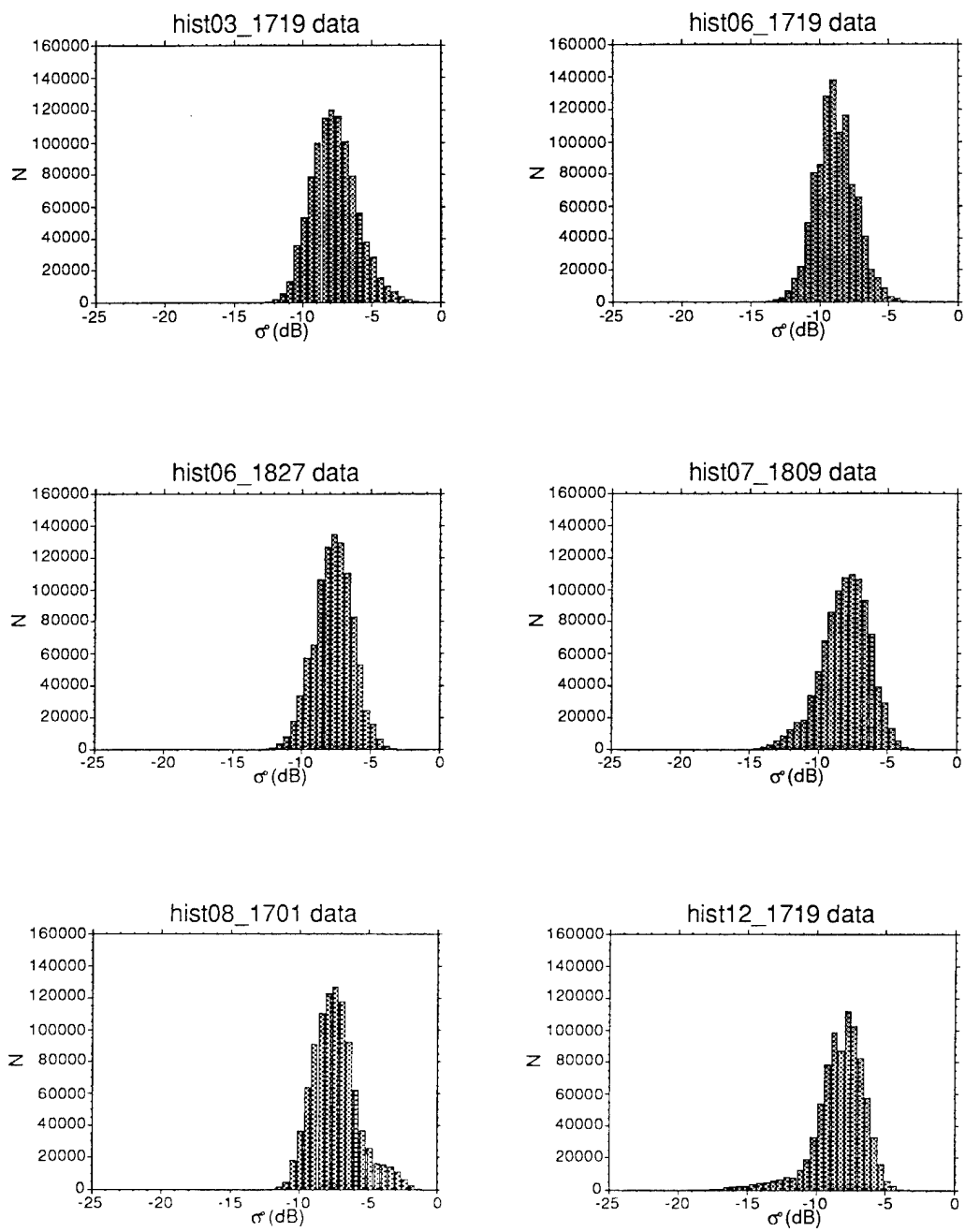


Figure 6.9 Histograms from SAR σ^0 images for 3 September (JD 246) through 12 September (JD 255), 1991.

6.5 Summary

The results presented above demonstrate that "point" measurements of radar backscatter obtained during field experiments can contribute to interpretation of satellite SAR imagery. Knowledge gained from the modeling of these field measurements is also useful in the interpretation of satellite SAR data. Determining the exact physical mechanisms responsible for observed radar backscatter variations is key in investigating the use of SAR data for the extraction of geophysical parameters. In chapter 5 we showed that the refreezing of moisture on or near the multiyear ice surface is responsible for the observed backscatter increase at the onset of freeze-up from *in situ* measurements and modeling. In this chapter we have shown that the same effect is observed from ERS-1 SAR imagery. The magnitude of the increase in backscatter from multiyear ice at the onset of freeze-up from ERS-1 SAR is comparable to the change observed from the field measurements of radar backscatter. The slope change at the onset of freeze-up is less in the SAR data than for the field measurements. The effects of large-scale features, such as ridging and floe edges, appear to dampen the effect of the change in slope in the SAR data during freeze-up.

We have also demonstrated that ERS-1 data may be used for the detection of the onset of freeze-up in the Arctic. This information will be useful in defining the duration of summer melt when combined with detection of the onset of melt in the spring. The behavior of the radar backscatter during this period, along with the knowledge of the physical mechanisms responsible, will aid in the development of algorithms for ice classification.

CHAPTER 7

FUSION OF ACTIVE AND PASSIVE MICROWAVE DATA FOR REMOTE SENSING OF SEA ICE DURING FALL FREEZE-UP

7.1 Introduction

In this chapter we examine the summer-to-fall transition of sea ice from satellite passive microwave measurements and investigate the use of a hybrid fusion algorithm for improving estimates of ice type concentration during this season. Young first-year ice may be as important as multiyear ice and open water in modulating the heat flux between the ocean and atmosphere in the central Arctic. Just after the onset of freeze-up, first-year ice will be in the early stages of growth and will consist of young first-year and thin ice. Improving the estimates of ice concentrations in this thickness range has an impact on heat transfer in the Arctic.

This is an extension of the work in previous chapters devoted to examining this season with *in situ* and satellite SAR measurements. Daily-averaged brightness temperatures over the Arctic region obtained with the DMSP SSM/I are used with an existing algorithm (NASA Team algorithm, [Cavalieri, et al., 1984]) to compute ice concentration estimates to demonstrate the difficulty in estimating concentration of ice types during this period. The NASA Team (NT) algorithm was developed primarily for cold conditions. Validation efforts have demonstrated that the mean difference between NT algorithm estimates and estimates from Landsat imagery of total ice concentration during fall (late September through November) is less than 1%,

with a standard deviation of $\pm 7.4\%$ [Steffen and Schweiger, 1991]. The results for fall are expected to be indicative of the performance of the algorithm in winter because the ice conditions are similar. Steffen and Schweiger [1991] have also shown that mean difference between NT and Landsat-based estimates of total ice concentration is 2.4% during spring, with a standard deviation of $\pm 5.9\%$. These results are obtained using hemispheric tie points as described below and they have shown that some improvements can be made through the use of local tie points. During the summer melt period, however, ice concentration estimates from the NT algorithm differ from Landsat estimates by as much as 46% , with a mean difference of 11% [Steffen and Schweiger, 1991]. In addition, estimates of multiyear ice concentration appear to be underestimated by the NT algorithm during fall and through the early winter. This appears to be associated with the use of constants as tie points for defining each of the surface types: multiyear ice, first-year ice, and open water [Thomas, 1993].

Ice type concentration estimates, based on the NASA Team (NT) algorithm, are inaccurate during the melt and early freeze-up season because they misclassify multiyear ice as first-year ice. This has been observed in past validation studies of the algorithm [Cavalieri, et al., 1984; Grenfell and Lohanick, 1985; Carsey, 1985]. A hybrid fusion technique is developed here to improve the classification of first-year ice for the period following the onset of freeze-up. The hybrid fusion technique uses information extracted from ERS-1 SAR data, namely the multiyear ice concentration, as an input to a modified version of the NASA Team algorithm. The multiyear ice concentration, derived from SAR, is used to constrain the multispectral inversion process. The "fused" estimates of first-year ice concentration appear to be more

accurate than NT estimates, based on ice observations which were logged aboard the *Polar Star* in the study area during 1991.

7.2 Observations of passive microwave signatures during freeze-up with SSM/I

We have shown in chapter 5 and 6 that the effects of refreezing of moisture on the ice surface causes a dramatic change in the radar backscatter characteristics of multiyear ice. This may be used to detect the onset of freeze-up in the Arctic. In the past, the minimum extent of sea ice from satellite passive microwave imagery has also been used as an indication of the end of the summer melt period [Gloersen, et al., 1992]. Passive microwave algorithms for determining ice concentration and for computing multiyear, first-year and open water concentrations have been used for a number of years in Arctic sea ice studies, including the NASA Team algorithm [Cavalieri, et al., 1984; Gloersen and Cavalieri, 1986] and the "bootstrap" algorithm [Comiso, 1986]. The NASA Team (NT) algorithm is based on the differences in the emission characteristics of multiyear ice, first-year ice and open water at 37 GHz and 19 GHz and the difference between vertically- and horizontally-polarized emission at 19 GHz. These algorithms suffer during summer months because of moisture in the snow cover and within the ice itself, which affects the penetration depth., causing errors in the estimation of first-year and multiyear ice [Cavalieri, et al. 1990].

Here, we compute first-year and multiyear ice concentrations using the NT algorithm for the same areas for which the SAR images and *in situ* radar backscatter measurements were obtained (chapters 4 and 6). These are used to demonstrate the improper estimation of first-year and multiyear ice at the end of summer and into the

initial stages of freeze-up. First, the DMSP SSM/I instrument is described in section 7.2.1, followed by a description of the NT algorithm for estimating ice concentration from SSM/I data in section 7.2.2. In section 7.2.3 and 7.2.4 we show the results of the NT calculations for the IAOE study area and the relationship to freeze-up detection with SAR.

7.2.1 The DMSP SSM/I

The SSM/I is one of several instruments on board the DMSP F-series of satellites. This satellite program is designed to provide meteorological, oceanographic, and solar-geophysical data to support defense and other operations. Other sensors on these satellites include the Operational Linescan System for visible and infrared imaging of clouds; and the Special Sensor Microwave/Temperature for determining vertical moisture and temperature profiles and surface temperature.

The SSM/I is a seven-channel microwave radiometer, which operates with dual-polarization at three frequencies, (19.3 GHz, 37 GHz and 85.5 GHz) and vertical polarization at one frequency (22.2 GHz). The resolution of the sensor depends on frequency since a single reflector antenna with multiple feeds is used. The instrument has beamwidths ranging from 1.87° at 19.3 GHz to 0.42° at 85 GHz. These beamwidths are reduced in the H-plane, (or cross-track direction), by the integration time. The effect varies from about a 3% degradation in resolution at 19.3 GHz to a 30% degradation at 85.5 GHz. When projected onto the Earth, the approximate fields of view for SSM/I are 69 by 43 km, 37 by 28 km, and 15 by 13 km at 19.3, 37, and 85.5 GHz, respectively. The imager uses a rotation of the feed assembly to scan the antenna beam in a circular fashion. The antenna rotation results in a conical scan on the Earth's surface at an incidence angle of 53.1° . Data are obtained during a portion

of this scan while calibration is obtained in the remainder of the scan to a hot reference absorber and a mirror which reflects sky radiation, as a cold reference is obtained in another portion of the scan. The data are acquired by integrating for 7.95 ms for the lower three frequencies and 3.89 ms for the 85.5 GHz channel, and are sampled at approximately 25 km spacing for the lower channels and 12.5 km spacing for the 85.5 GHz channel.

7.2.2 Computing sea ice concentration with the NASA Team algorithm

DMSP SSM/I brightness temperature grids, obtained from the National Snow and Ice Data Center (NSIDC), Boulder, Colorado, contain daily-averaged brightness temperatures from the SSM/I instruments for the Polar regions. These brightness temperature grids are used in this study to examine the effects of freeze-up on the NT algorithm for sea ice classification. The NASA Team algorithm is based on the algorithm developed for the SMMR, by Cavalieri, et al., [1984]. A summary of the performance of the algorithm and the validation of derived ice classification for SSM/I data are given in Cavalieri, et al., [1991] and Steffen and Schweiger, [1991]. The 25-km ice concentration algorithm is also described in detail in the SSM/I brightness temperature grid user's guide [NSIDC, 1992]. Since the algorithm has been described in detail in several of the references above, the basic development of the algorithm is described in Appendix D.

7.2.3 SSM/I Observations in the eastern central Arctic during freeze-up

The effect of melt on the surface of ice has been shown to cause confusion in the NASA Team algorithm [Cavalieri, et al., 1990]. When air temperatures are around 0° C first-year ice concentrations are over-estimated and multiyear ice concentrations are underestimated [Cavalieri, et al., 1990]. This effect continues into the onset of freeze-

up period, i.e. the time frame of the IAOE field measurements. Using SMMR data, Rothrock and Thomas [1992] have shown that the NT algorithm underestimates the multiyear ice concentration in the central Arctic just after freeze-up. The NT algorithm yields a multiyear concentration of approximately 0.4 in the central Arctic, whereas the total ice concentration at the end of summer was estimated at about 0.7. Thomas [1993] has shown that the multiyear concentration estimates from the NT algorithm reach a minimum during September, and this minimum is not believed to be caused by a real decrease in multiyear ice concentration, but by changes in the signature of multiyear ice. The underestimation of multiyear ice concentration has been attributed to the use of constant pure ice type signatures in the NT algorithm [Thomas, 1993]. He has shown that by accounting for this variability through the use of daily mean signatures, estimates of multiyear concentration may be improved. In this section we compute estimates of multiyear and first-year ice concentration using the NT algorithm for the study area in which SAR images were obtained and examine the reliability of these estimates.

Co-locating SSM/I and ERS-1 SAR image data

To compare passive microwave data over the same region and time frame of the SAR and *in situ* measurements in this study we first had to map them to the same set of coordinates. When the two sensors have drastically different resolution, this is best accomplished by mapping the low-resolution data to the same coordinates as the high-resolution data. The process we used for mapping the SSM/I images to the same coordinates consists of two parts. First, the latitude/longitude pairs for each pixel in the low-resolution SAR image are computed. These pairs are then used to find the corresponding pixel location within the SSM/I grids for the Arctic. The

corresponding pixel values are stored in "look-up" files that can be used to map the SSM/I grid locations to the SAR image. A summary of both steps are given below.

The geographic locations of the corner points of each SAR image frame are supplied by the PAFs in the header file for each ERS-1 SAR image. These corner points can be used to derive the latitude and longitude coordinates for each pixel within the image using the algorithm given by [Li, 1993]. This algorithm uses the fact that ERS-1 SAR imagery covers a small spatial area, eliminating the need for using the more general formulation given by Curlander and McDonough [1991]. The transformation from ERS-1 SAR image coordinates to geographical coordinates is based on the assumption that the boundaries of the image follow the great circle on the Earth. This assumption results in a maximum error of about 10 meters for SAR frames of 100 by 100 km. Image coordinates along each side of the image frame are first computed by interpolation from the end points using a bilinear interpolation in Cartesian coordinates. The corner points must first be converted to three-dimensional Cartesian coordinates, using the local Earth radius. This radius is computed, based on an elliptical model of the Earth and the center latitude and longitude coordinates of the image. Once the corner points are converted to Cartesian coordinates, the coordinates along any line are computed using the bilinear interpolation,

$$X' = X_1 \frac{d_2}{d_1 + d_2} + X_2 \frac{d_1}{d_1 + d_2} \quad (7-1)$$

for each of the coordinates, where X' is any point between the end points X_1 and X_2 , and the distance from X' to the end points are given by d_1 and d_2 . Equations for the other two coordinates, Y' and Z' , are similar to (7-1). In practice, the interpolation is first performed along two opposite sides of the image. Then each row or column utilizes the interpolated edges as end points. The final step involves transforming

from Cartesian coordinates into spherical coordinates to obtain the latitude and longitude for each pixel within the SAR image.

The SSM/I data, obtained from NSIDC, is mapped to polar stereographic coordinates and the brightness temperature data are stored on a rectangular grid. Latitude and longitude coordinates for each pixel of the SSM/I data can be obtained with a conversion program supplied by NSIDC. The reported accuracy of these location programs is less than 1 km, which is approximately the same accuracy of the SSM/I sensor data record geographic location values [NSIDC, 1992]. The conversion from latitude/longitude values to image pixel locations is performed in two steps. First, the latitude/longitude values are transformed into polar stereographic coordinates for the polar regions. These are then used to find the row and column values for the particular pixel in which the latitude/longitude point is located. The algorithm is described in detail in the NSIDC report [1992].

Using the two-step process for obtaining the SSM/I grid locations for each SAR image pixel we generated SSM/I gridded brightness temperature images that are mapped to the coordinates of each SAR image frame used in this study. These pixel values are then used to find the brightness temperature that corresponds to each ERS-1 SAR pixel and a re-sampled SSM/I brightness temperature image is obtained. The brightness temperatures from these resampled images may then be used in the NT algorithm to determine estimates of first-year, multiyear and open water concentration.

SSM/I Observations

The NT algorithm, described in section 7.2.2 and Appendix D, was used to compute sea ice type concentrations on the resampled SSM/I image data using hemispheric tie points. The results of the NT classification for each resampled image are shown in Appendix D. We computed the mean and standard deviation of the concentrations of first-year ice, multiyear ice and open water for each resampled image. The mean values are plotted in figure 7.1 to demonstrate the changes in relative concentrations of first-year and multiyear ice that are estimated by the NT algorithm during this time frame. The mean and standard deviation for SSM/I pixels located within the SAR frame are listed in table 7.1. The estimated changes in first-year and multiyear ice concentration are the result of misclassification of some multiyear ice as first-year ice, as is explained below.

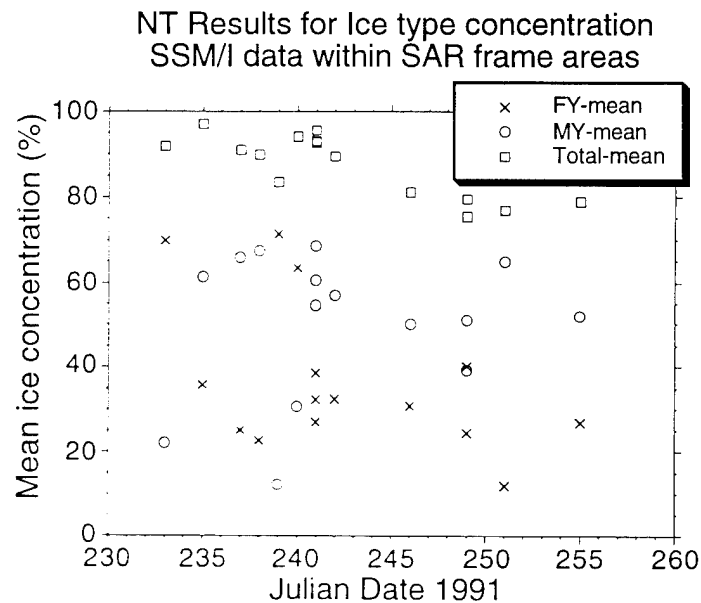


Figure 7.1 Mean values of ice type concentration, derived from the NASA Team algorithm. The averages are computed for areas enclosed by the SAR images used in chapter 6.

Table 7.1 SSM/I-based ice concentrations. Concentrations from SSM/I were computed for areas corresponding to the SAR image frames used in chapter 6.

Date and Corresponding SAR Frame Numbers		Ice Concentration		
JD	SAR frame	MY \pm std. dev.	FY \pm std. dev.	Total \pm std. dev.
233	1827	22.0 \pm 10.0	69.8 \pm 8.7	91.8 \pm 1.6
235	1863	61.3 \pm 7.4	35.8 \pm 6.8	97.1 \pm 1.3
237	1791	65.8 \pm 7.9	25.1 \pm 8.2	91.0 \pm 2.1
238	1809	67.3 \pm 10.9	22.6 \pm 11.5	89.9 \pm 1.3
239	1701	12.1 \pm 6.8	71.3 \pm 7.6	83.4 \pm 4.0
240	1791	30.7 \pm 6.6	63.4 \pm 7.9	94.1 \pm 2.3
241	1755	60.4 \pm 10.1	32.3 \pm 9.1	92.7 \pm 1.7
241	1791	68.5 \pm 5.6	27.0 \pm 5.6	95.6 \pm 1.1
241	1809	54.5 \pm 8.2	38.6 \pm 7.7	93.1 \pm 1.8
242	1701	56.9 \pm 7.1	32.5 \pm 5.9	89.4 \pm 2.6
246	1719	50.2 \pm 5.4	30.9 \pm 6.5	81.0 \pm 4.0
249	1719	39.3 \pm 7.0	40.2 \pm 9.4	79.5 \pm 3.4
249	1827	51.0 \pm 13.3	24.4 \pm 15.0	75.4 \pm 6.7
251	1701	65.0 \pm 8.9	11.9 \pm 7.3	76.9 \pm 3.3
255	1719	52.0 \pm 7.3	26.9 \pm 10.4	78.9 \pm 4.6

It is well known in the sea ice passive microwave community that under summer melt conditions the frequency dependence of emissivity of multiyear ice becomes similar to that of first-year ice [Cavalieri, et al., 1984]. Field measurements of emissivity of multiyear ice during the same season as the IAOE measurements were obtained by Grenfell [1992a] during the CEAREX campaign in 1988. These measurements demonstrate the change in spectral response of emissivity as the temperature drops during the early stages of the freeze-up season. Figure 7.2 shows the progression of vertically and horizontally-polarized emissivity as a function of frequency as the freeze-up season commences. These measurements clearly show that variations in emissivity from multiyear ice during this season can lie anywhere between the first-year and multiyear tie points of figure D.1.

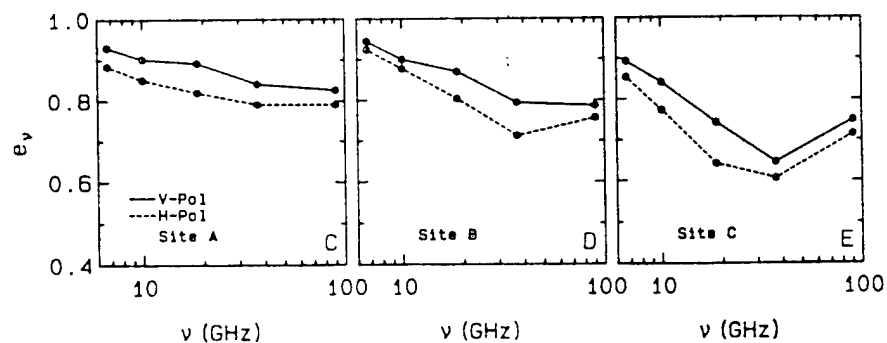


Figure 7.2 Measured spectra for vertically-polarized (solid line) and horizontally-polarized (dashed line) emissivity spectra from 6.7 GHz to 90 GHz for three sites observed during CEAREX '88. {from [Grenfell, 1992]} The x-axis is frequency on a logarithmic scale and the y-axis is emissivity.

7.2.4 Relationship to freeze-up detected with SAR

The largest values of first-year ice concentration appear on the same days as the dips in the ERS-1 SAR average σ^0 results shown in chapter 6. This is clearly evident from figure 7.3, in which we have plotted the mean σ^0 with the NT estimate of first-year ice concentration. The changes in the radar backscatter signatures were shown to be caused by the effects of moisture on or near the ice surface. Changes in temperature around 0° C cause both the real and imaginary parts of the dielectric constant of sea ice to increase dramatically, resulting in a decrease in penetration depth. This decrease in penetration depth is responsible for both the decrease in backscatter and the increase in emissivity under warm conditions. However, when fluctuations on the order of 2 dB are observed in σ^0 the change in first-year ice concentration changes between values of 10% and 40%. This may be caused by the fact that attenuation is directly proportional to frequency (see equation 5.4) and the higher frequencies of the SSM/I are more sensitive to small changes in the lossy part of the dielectric constant.

However from observations of radar backscatter shown previously it may be feasible to estimate multiyear ice fraction with SAR to augment the passive microwave algorithms for ice classification during the early freeze-up period. If the multiyear ice concentration can be computed from SAR imagery, the ambiguity between first-year and multiyear ice during this time frame may be resolved. In section 7.4 a solution to resolving this ambiguity is presented. This solution uses a hybrid data fusion solution and the background for data fusion is presented in the next section.

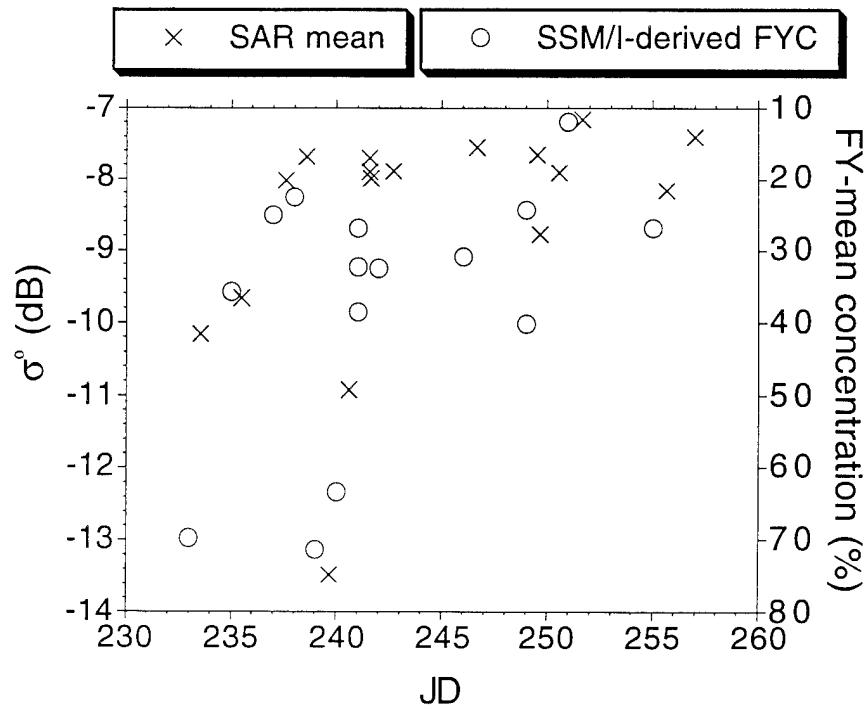


Figure 7.3 Comparison of mean σ^0 values computed from the ERS-1 SAR images (from chapter 6) and the first-year ice concentration obtained with the NASA Team algorithm from SSM/I data.

7.3 Data Fusion Background

7.3.1 Data fusion for sea ice remote sensing

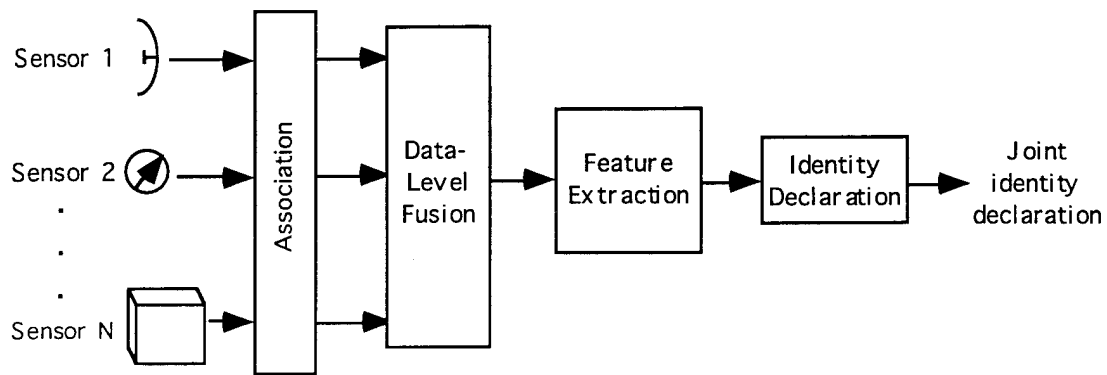
It has been speculated that a combination of active and passive microwave measurements will be important in sea ice remote sensing, particularly using SAR to improve passive microwave algorithms [Cavalieri, et al., 1990]. Studies of the microwave properties of sea ice with active and passive sensors have been carried out since the 1960's. Many of these studies have been designed to study the possibility of using the information from a variety of sensors to classify sea ice, but the current techniques used to map Arctic conditions use single-sensor information. The use of single-sensor data results in ambiguities in the estimations of geophysical parameters. For these reasons, the fusion of data from satellite microwave sensors may improve estimates of geophysical parameters. Spaceborne SARs are capable of spatial resolution on the order of tens of meters, whereas spaceborne passive microwave imagers have spatial resolution on the order of tens of kilometers. Therefore, the most fundamental issue in the fusion of these data is the disparity in resolution between SAR and passive microwave imagery. A solution to combining data from SAR and SSM/I that overcomes the vast difference in resolution is explored in this chapter.

Combining active and passive microwave imagery has been suggested as an approach to improve estimates of key parameters, including thickness, mass distribution, and extent [Collins, 1992; Livingstone, et al., 1987; Grenfell, et al., 1992; Drinkwater, et al., 1991; Burns, et al., 1987]. However, a data fusion approach has not yet been applied to this problem. When sensors differ widely in resolution it is impossible to

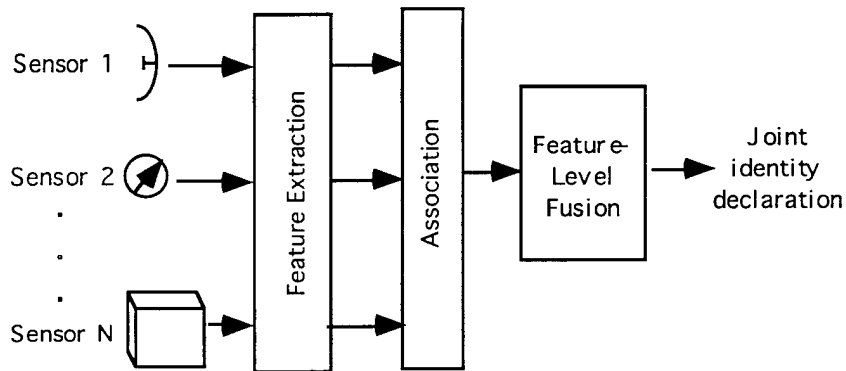
merge the data at the pixel level. In this case the most likely level to merge the data is at the decision level [Collins, 1992; Waltz and Llinas, 1990]. By first extracting information from the SAR and then using the extracted information in the passive microwave algorithms, the resolution problem may be overcome. A solution to the problem of merging of these data sets is explored here. This solution uses a multi-level, or hybrid fusion approach and simple models to combine active and passive microwave measurements for sea ice classification.

7.3.2 Data Fusion Architectures

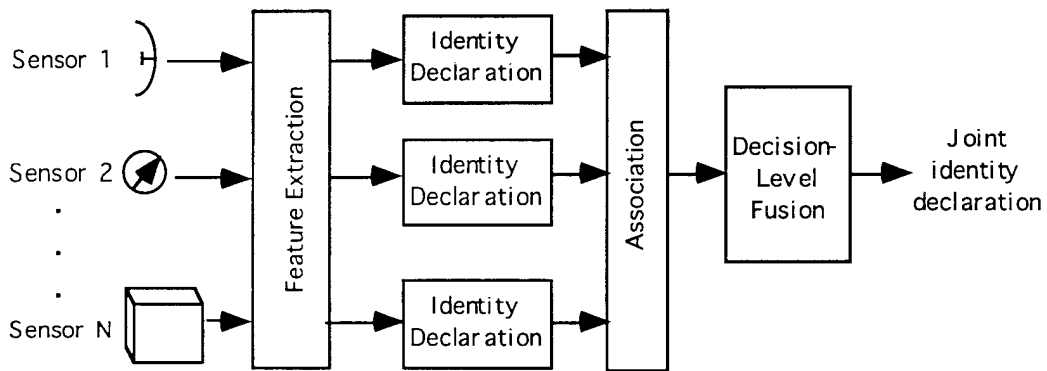
The desired result of fusing multisensor data is to obtain better estimates of geophysical parameters, or new information that could not be obtained with any single sensor. Three basic architectures are used to classify multisensor data fusion processes. These are characterized by the level at which the data are combined or fused. The three architectures are data-level, feature-level and decision-level fusion [Waltz and Llinas, 1990]. These architectures are shown in block diagram form in figure 7.4 for an identity declaration process requiring fusion of multisensor data. Although multisensor fusion problems may not necessarily fall into the identity declaration category, any fusion process will fall into one of these three categories, or a hybrid of these.



a) Data-level fusion



b) Feature-level fusion



c) Decision-level fusion

Figure 7.4 Data fusion architectures for identity declaration from multiple sensors: a) Data-level fusion, b) feature-level fusion, and c) decision-level fusion. (Adapted from Waltz and Llinas, 1990)

Data-level fusion includes techniques in which the raw data or pixels from different sensors are fused prior to any feature extraction or association operations. There is usually limited pre-processing required for data from each source, but most of the extensive processing follows the fusion of the data. This architecture is limited to sensors which are identical or very similar.

If the feature extraction process is applied to the data before combining them, but individual identity declaration is not performed separately on each sensor's data, then the process is considered a feature-level fusion process.

Decision-level fusion includes techniques in which the data are merged after products are derived from each of the sensors and the results are combined and a joint declaration of identity is made. This architecture differs from the feature-level fusion because identity declaration is obtained on each sensor individually before being combined for a joint identity declaration. Decision-level fusion is used when quite different sensors are to be employed in the process.

In addition to the basic architectures outline above, it is possible to develop a technique that is actually a hybrid of two (or possibly three) of these. Data fusion is thought to be most beneficial if it is performed "as close to the sensor as possible", although the level at which fusion is performed depends on the nature of the problem and the characteristics of the sensors to be used or developed.

7.4 Hybrid Fusion Approach for Sea Ice Classification

As discussed previously, one approach that may allow for fusing two data sets with disparate resolution is to enhance or improve the resolution of the lower-resolution sensor. An alternative is to develop a fusion technique which uses features or products derived from the high-resolution sensor data with the data from the low-resolution sensor. The second approach is used here in the development of a hybrid-level fusion of active and passive microwave data.

The problems in classification of sea ice during the freeze-up season with passive microwave measurements has been demonstrated in section 7.2. Here a hybrid fusion process is developed to remove the ambiguity between multiyear and first-year ice during this season. We first compute the multiyear ice concentration from SAR imagery and use this information to improve the estimates of first-year ice and open water by modifying the NASA team algorithm for ice concentration from SSM/I.

7.4.1 Architecture for hybrid fusion process

The fusion process developed as part of this work involves two major components: (1) deriving the multiyear ice concentration from ERS-1 SAR imagery, and (2) using this concentration as a constraint in existing passive microwave algorithms (namely, the NT algorithm). The SAR data are used at the decision level and the SSM/I data are used at the data level, so this is considered a multi-level (or hybrid) fusion approach for sea ice classification. A simplified block diagram of the architecture for this process is shown in figure 7.5.

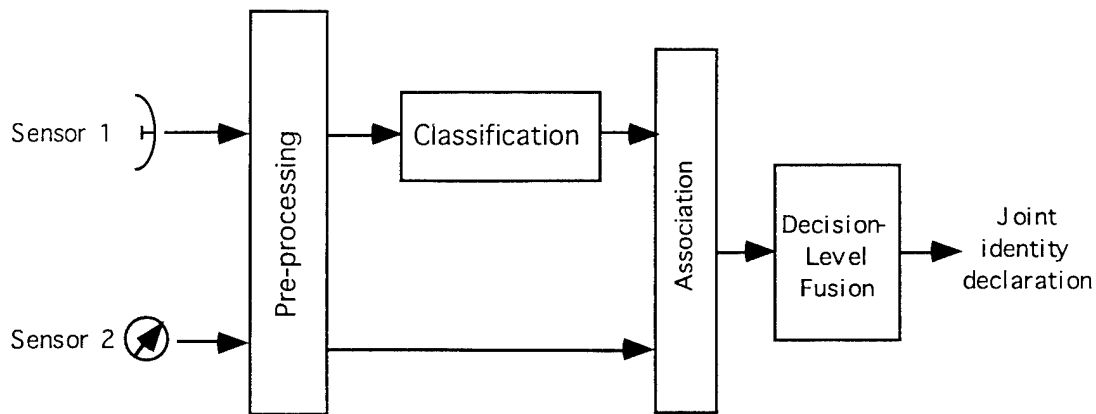


Figure 7.5 Hybrid (multi-level) architecture for data fusion.

7.4.2 Determination of multiyear ice concentration from ERS-1 SAR

The first step in the fusion process described above is to derive multiyear ice concentrations from ERS-1 SAR imagery. This is performed after the SAR data have been processed on-site at the PAFs and the radiometric corrections and calibrations described in chapter 6 have been computed. There are several algorithms for determining multiyear ice concentration from SAR imagery in the literature [Kwok, et al., 1992a; Haverkamp, et al., 1995; Haverkamp, et al., 1993]. The technique based on dynamic thresholding appears to have some advantages for ice classification during seasonal transitions because it does not depend on absolute image levels and predetermined thresholds. The dynamic local-area threshold (DLT) is used in this study for two reasons: (1) it may be more accurate under seasonal variations, and (2) it was developed at KU and is easily accessible.

The DLT algorithm is explained in detail by Haverkamp, et al., [1995], as a necessary first step in their heuristic, knowledge-based method for categorizing sea ice thickness. The DLT technique is based on computation of histograms over small,

overlapping regions which are assumed to be small enough to contain only two distinct classes of ice, based on image intensity. The subregions used in this study were 32 by 32 low-resolution image pixels, and the overlap between subregions is 50%. Thresholds based on local area statistics are used since local changes in gray level are often not distinguished when using global thresholding techniques. The histograms computed in chapter 6 do not appear to be bimodal over the entire image, but subregions of these same images yield histograms with two distinct peaks. The DLT algorithm is used to obtain thresholds for different parts of the image. An example of a bimodal histogram for a portion of the ERS-1 SAR image frame 1719 from 12 September, 1991 (JD 255) is shown in figure 7.6. The global histogram for this image frame is shown in figure 6.9. This demonstrates that although no clear threshold may be obtained from a global distribution of SAR data, local distributions can show distinct classes. This is the premise on which dynamic thresholding is based.

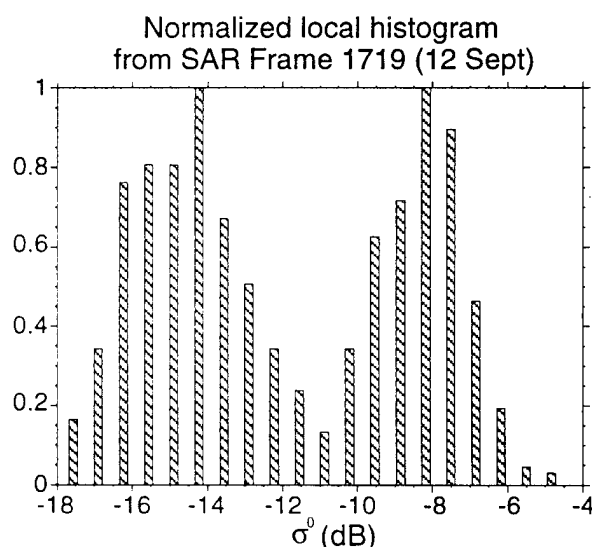


Figure 7.6 Example of a local-area histogram from ERS-1 SAR frame 1719 from 12 September, 1991. This demonstrates that distributions over local areas may show separate classes of targets, although the global distribution (figure 6.9) does not.

The result of the DLT algorithm is an image which has been divided into three categories. These three categories are not defined by the DLT algorithm and the category for each of the three solutions must be determined either by some automated means or by inspection. Here we simply identified which category corresponds to multiyear ice by visually identifying rounded floes. The multiyear ice concentration was obtained by computing the percentage of pixels that were classified as multiyear. The areas over which these percentages were computed were defined by the SSM/I grid boundaries and these boundaries were determined by the co-location methods discussed in section 7.2.3. The images used and the results of multiyear ice concentration using this method are shown in section 7.4.4

7.4.3 Modification of NASA Team algorithm for ice classification with SSM/I

To fuse the SSM/I and ERS-1 SAR data using the hybrid algorithm outlined above, the passive microwave algorithm for ice concentration estimates must be modified to utilize information obtained from SAR imagery. The multiyear ice concentration from ERS-1 SAR data is used to constrain the NT algorithm.

If the multiyear ice concentration (C_M) is known, the two equations in the NT solution can be solved for the first-year ice concentration (C_F).

These solutions can be expressed in matrix form as,

$$\begin{bmatrix} a_1 \\ a_2 \end{bmatrix} \cdot C_F = \begin{bmatrix} g_1 \\ g_2 \end{bmatrix}, \quad (7-9)$$

where a_1 and a_2 are given by,

$$a_1 = \{PR[SF_1 - SW_2] - [DF_1 - DW_2]\} \quad (7-10 a)$$

and

$$a_2 = \{GR[SF_2 - SW_2] - [DF_2 - DW_2]\}. \quad (7-10 b)$$

The SF_i , SW_i , DF_i , and DW_i terms are functions of the tie points and are defined in Appendix D. The values in the vector on the right-hand side of equation (7-9) are

$$g_1 = DW_1 - PR \cdot SW_1 - C_M \{PR[SM_1 - SW_1] - [DM_1 - DW_1]\} \quad (7-11 a)$$

and

$$g_2 = DW_2 - GR \cdot SW_2 - C_M \{GR[SM_2 - SW_2] - [DM_2 - DW_2]\}. \quad (7-11 b)$$

The value of the multiyear ice concentration (C_M) is computed from SAR imagery and is used as a constraint in this formulation. Equation (7-9) is an over-determined system of equations, which may be handled by obtaining a least-squares solution [Twomey, 1977]. The solution that minimizes the norm of the residual,

$$\begin{bmatrix} a_1 \\ a_2 \end{bmatrix} \cdot C_F - \begin{bmatrix} g_1 \\ g_2 \end{bmatrix},$$

is the least-squares solution. For this case, the least-squares estimate, which is constrained by the multiyear ice concentration, derived from SAR data is,

$$C_F = \frac{a_1 g_1 + a_2 g_2}{a_1^2 + a_2^2}. \quad (7-12)$$

This gives an updated first-year ice concentration from the modified NT algorithm.

7.4.4 Results

To demonstrate the algorithm we used the SAR images obtained from 30 August through 22 September, in which the DLT algorithm worked well for separating the multiyear ice from the remainder (presumably young or thin first-year ice and open water). The images used are shown in figures 7.7, 7.8, 7.9, and 7.10. The IAOE cruise track passed almost exactly through the center of image frame 1719 obtained on 6 September (JD 249) and 12 September (JD 255). These are shown in figure 7.8 and 7.9. The *Polar Star* passed through this region during JD 242 through JD 243 and based on observation of large features in these SAR frames there is less than a 25-km movement of large features from 6 September through 12 September. Although the use of ship-based observations may not reflect the ice characteristics across the entire SAR frame we will use ice observation recorded aboard the *Polar Star* for semi-quantitative judgement of the combined active and passive estimates of ice concentration. We also used SAR images from 30 August (JD 242, frame 1701) and 22 September (JD 265, frame 1737), figures 7.7 and 7.10, respectively, to test the hybrid fusion technique. The image obtained from 22 September has about 30% overlap with frame 1719 from 6 and 12 September, and the image from 30 August is just south and west of these frames, within 50 km of the IAOE cruise track.

30 August Frame 1701

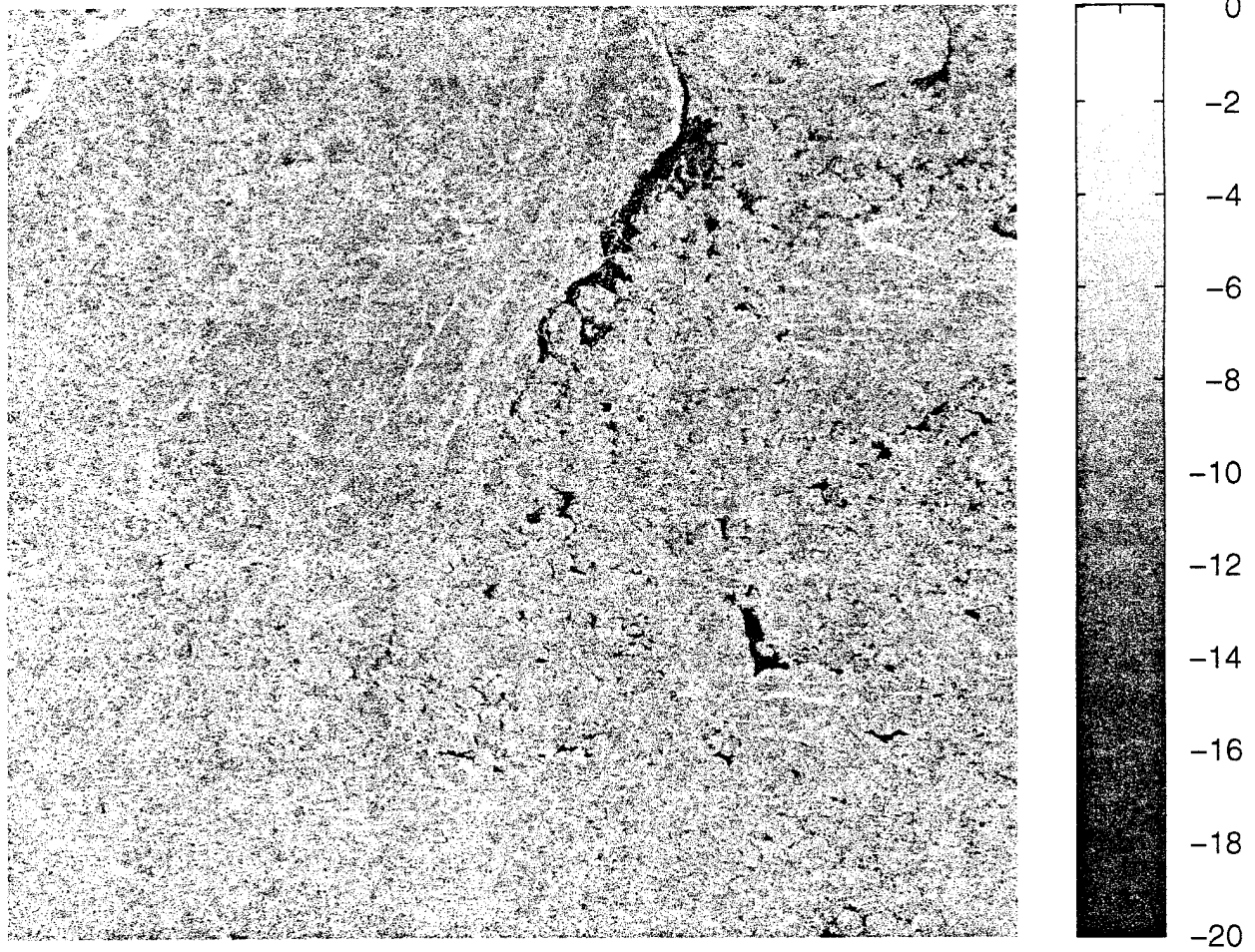


Figure 7.7 ERS-1 SAR frame number 1701 from 30 August (JD 242) 1991.

(Copyright ESA, 1991)

6 September Frame 1719

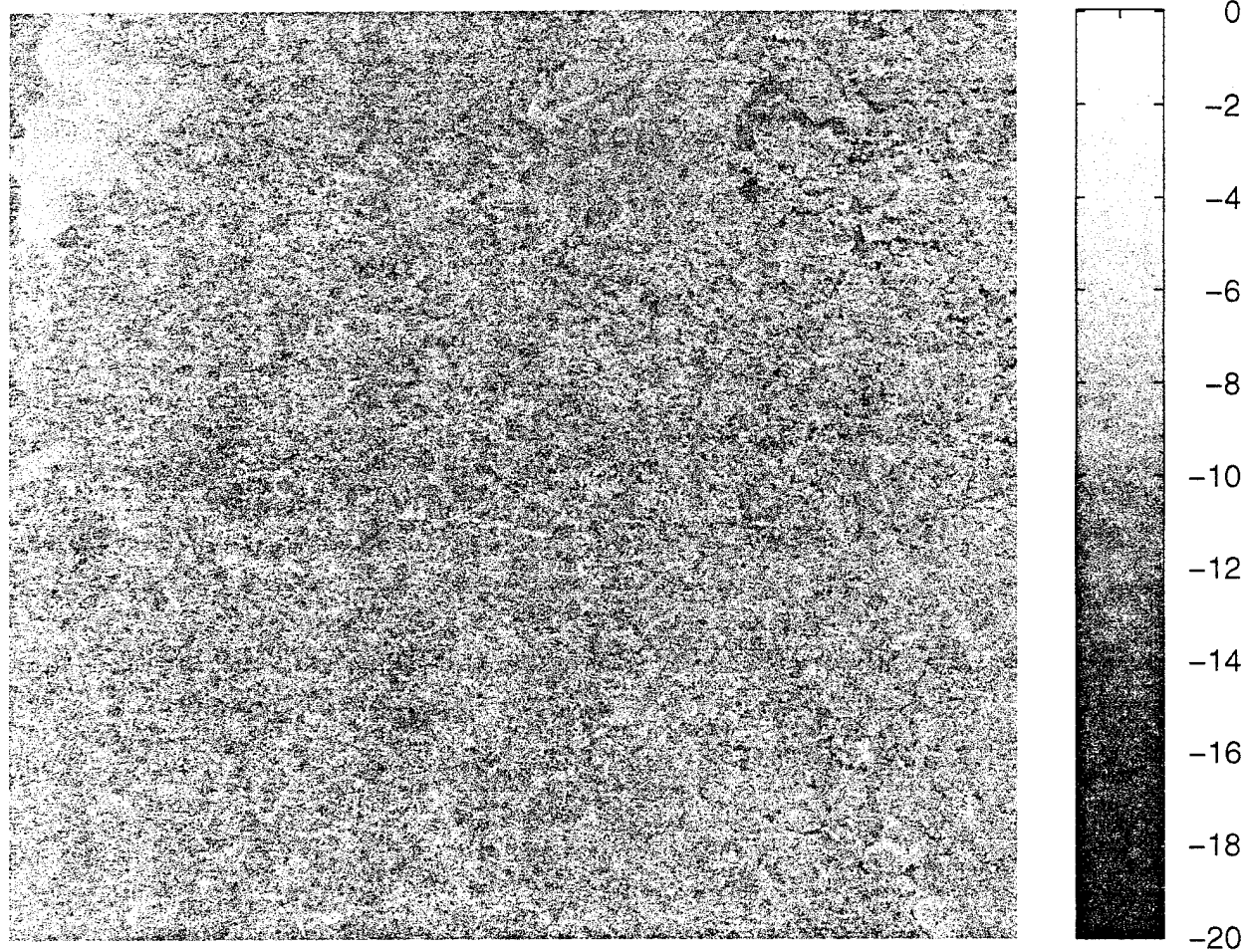


Figure 7.8 ERS-1 SAR frame number 1719 from 6 September (JD 249) 1991.

(Copyright ESA, 1991)

12 September Frame 1719

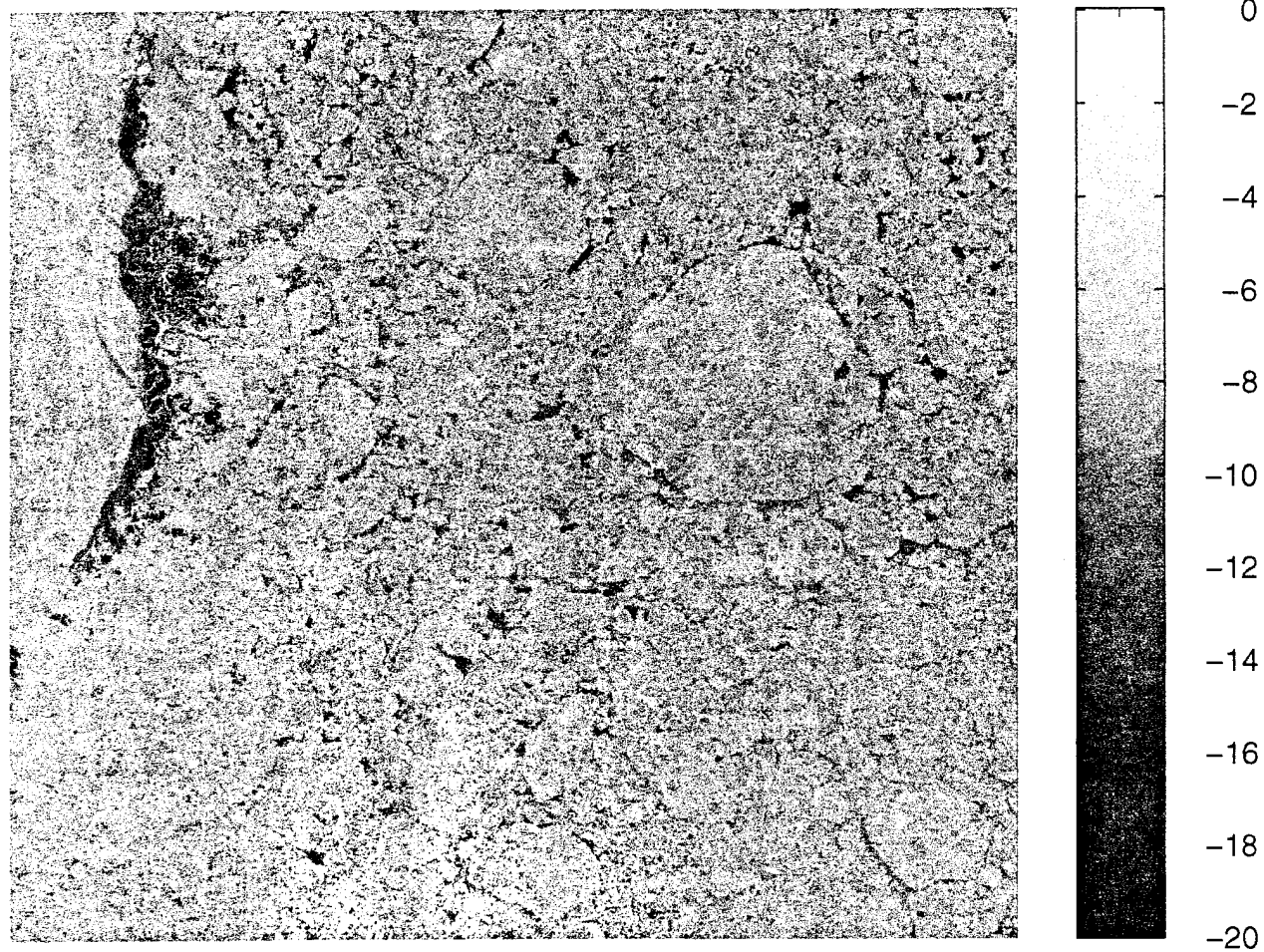


Figure 7.9 ERS-1 SAR frame number 1719 from 12 September (JD 255) 1991.

(Copyright ESA, 1991)

22 September Frame 1737

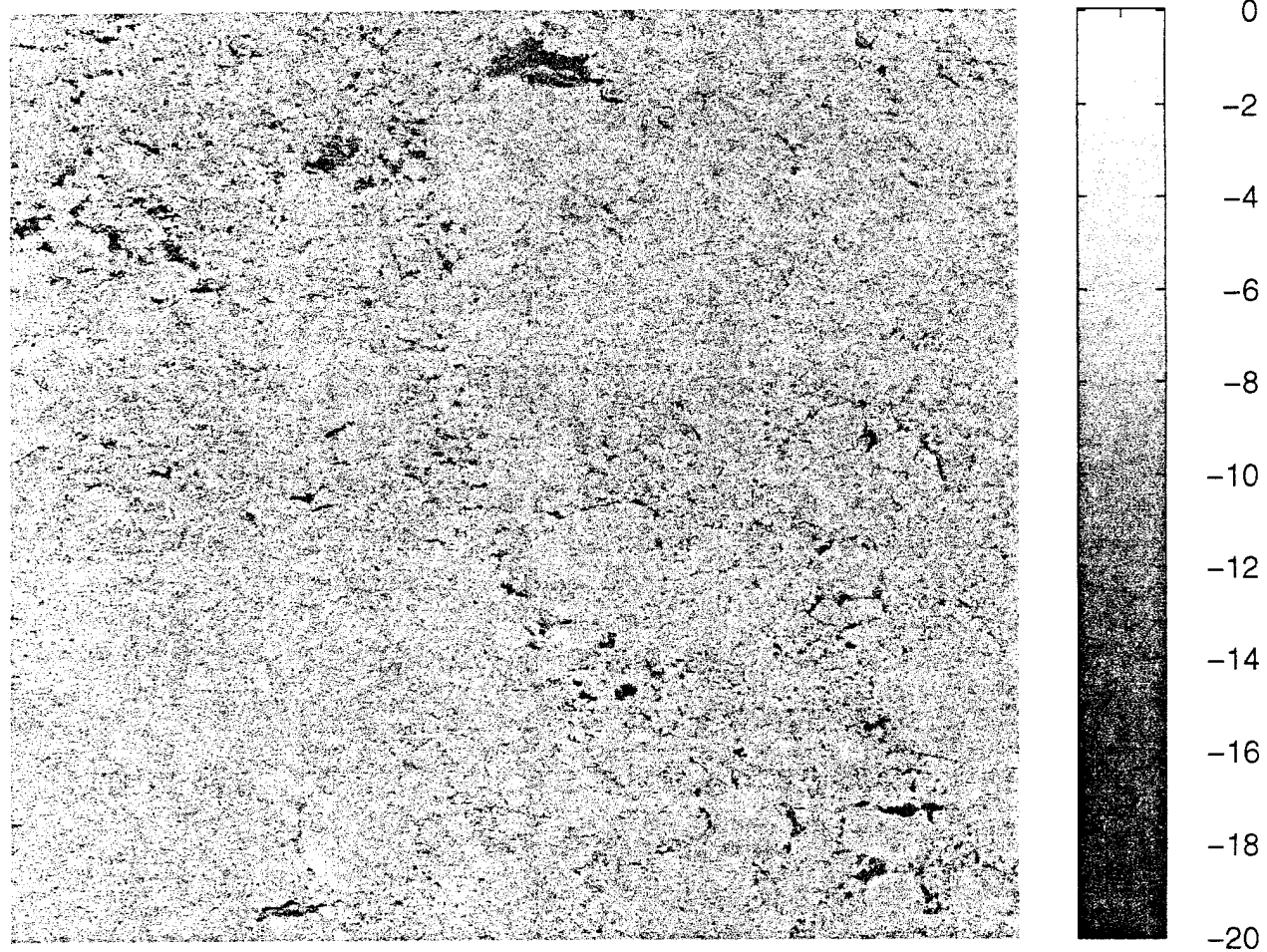


Figure 7.10 ERS-1 SAR frame number 1737 from 22 September (JD 265) 1991.

(Copyright ESA, 1991)

30 August 1701 Result of LAT

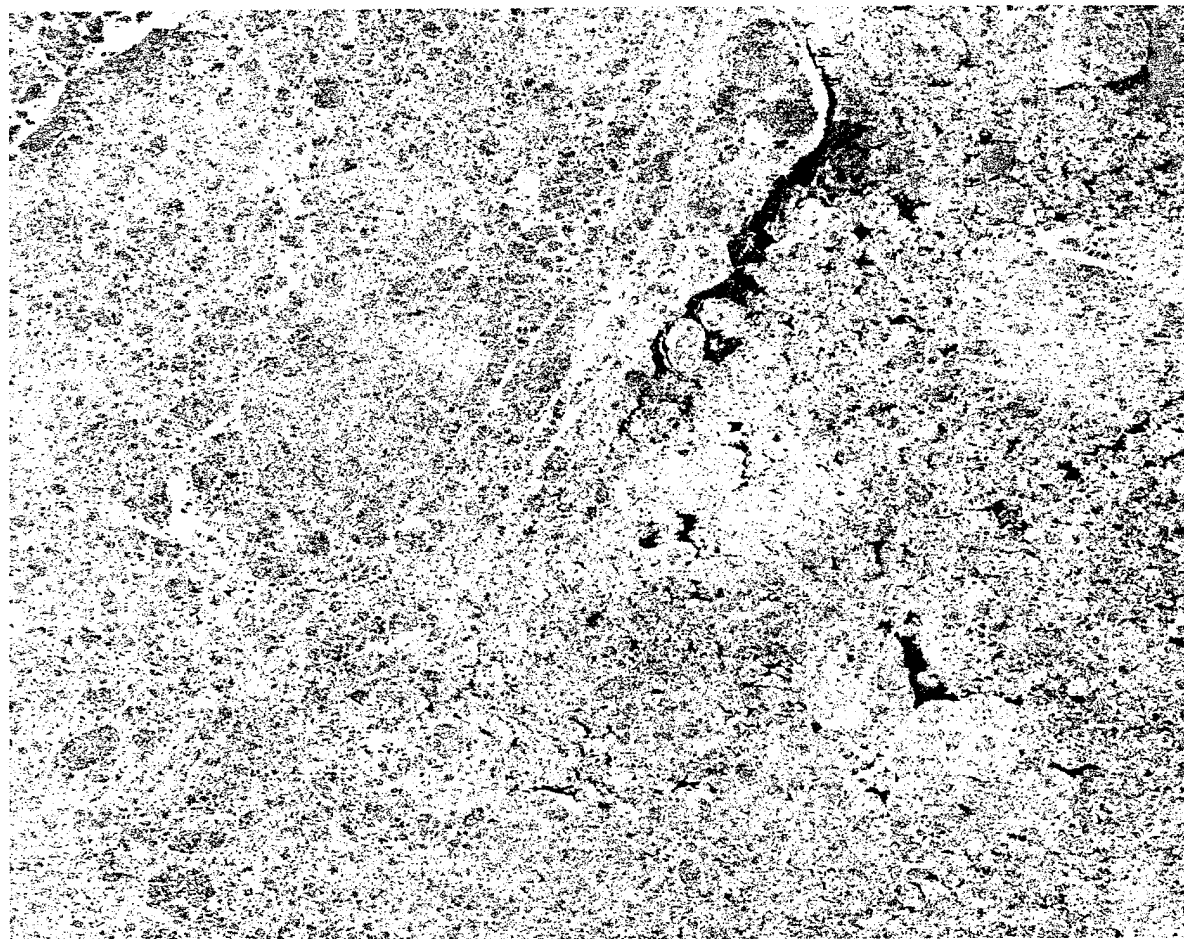


Figure 7.11 Result of dynamic local-area thresholding to determine multiyear ice concentration from ERS-1 SAR frame 1701, 30 August 1991 (JD 242).

06 September 1719 Result of LAT

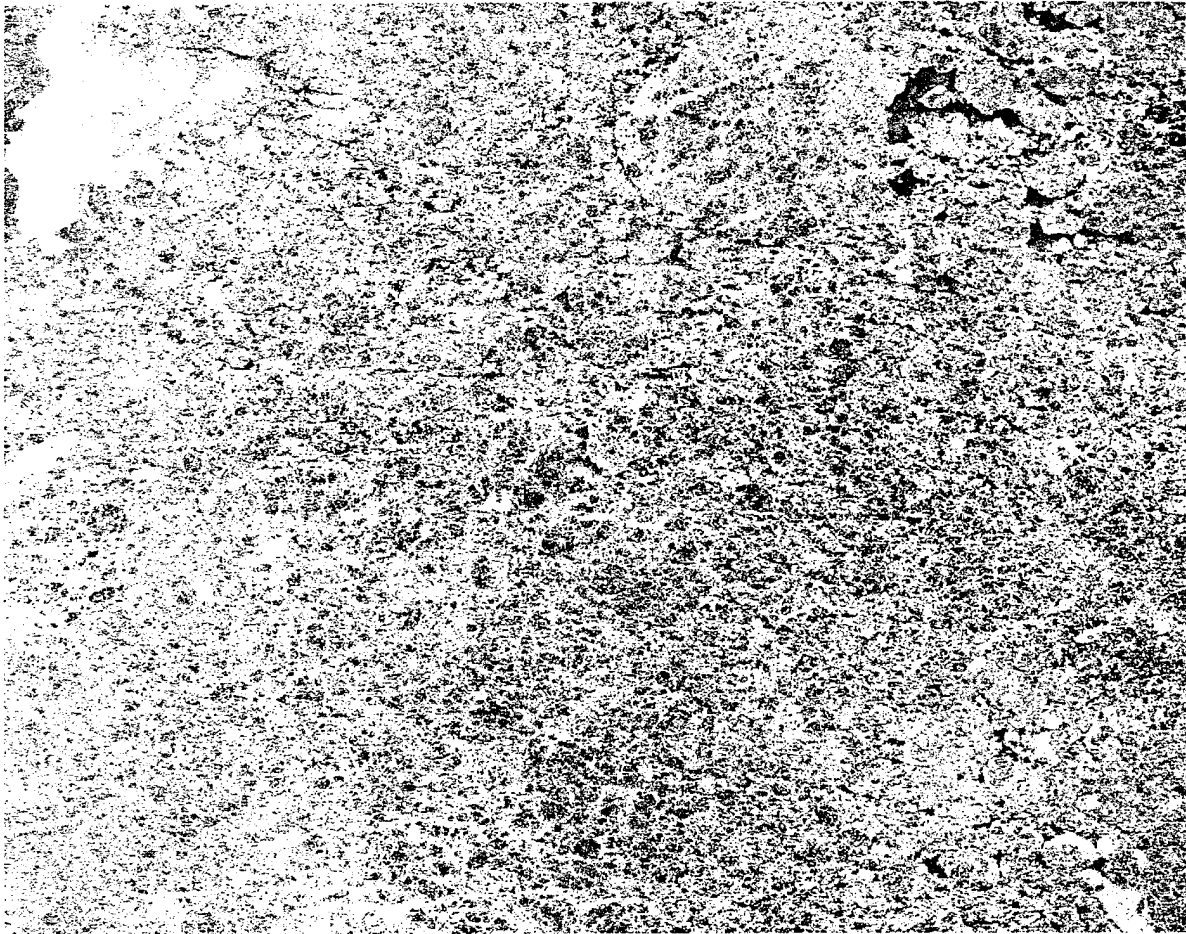


Figure 7.12 Result of dynamic local-area thresholding to determine multiyear ice concentration from ERS-1 SAR frame 1719, 6 September 1991 (JD 249).

12 September 1719 Result of LAT

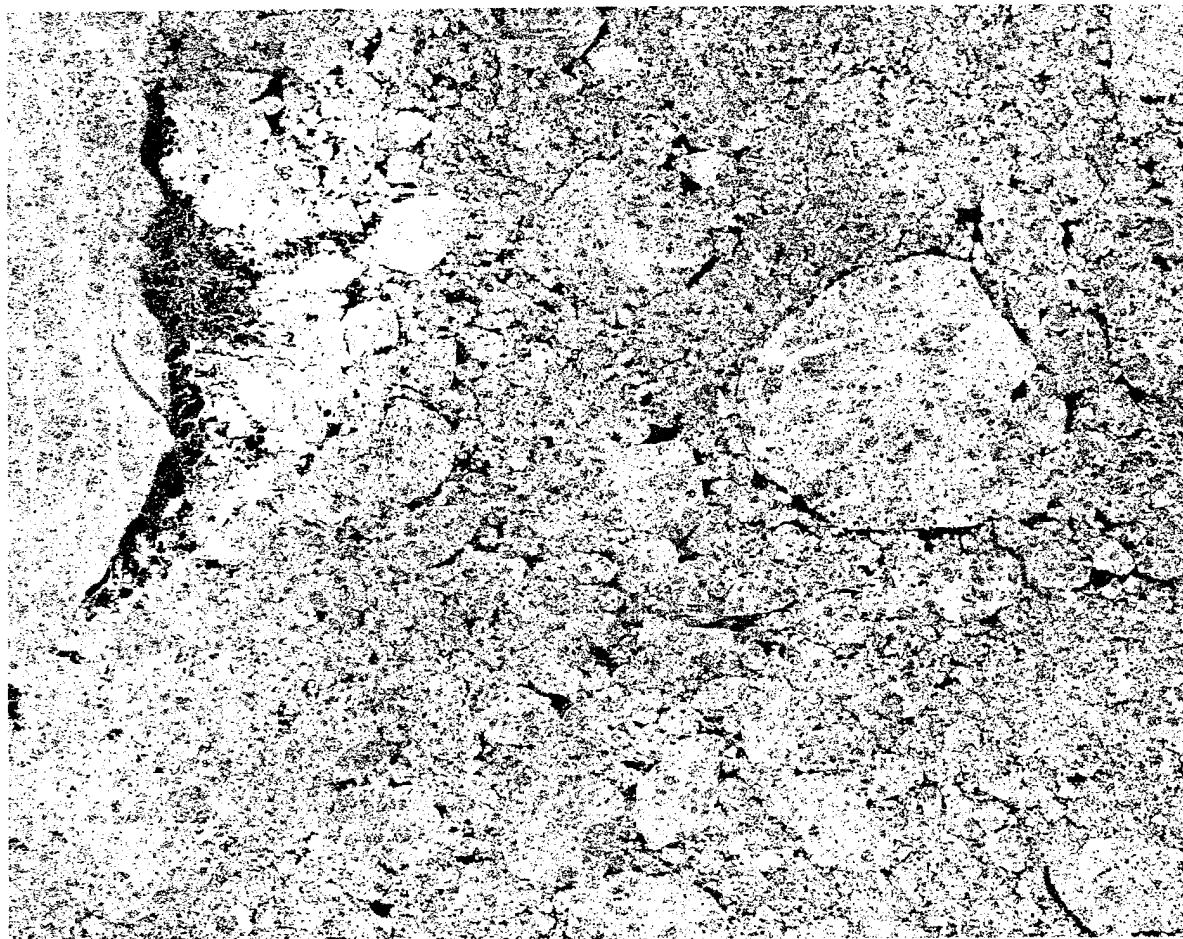


Figure 7.13 Result of dynamic local-area thresholding to determine multiyear ice concentration from ERS-1 SAR frame 1719, 12 September 1991 (JD 255).

22 September 1737 Result of LAT

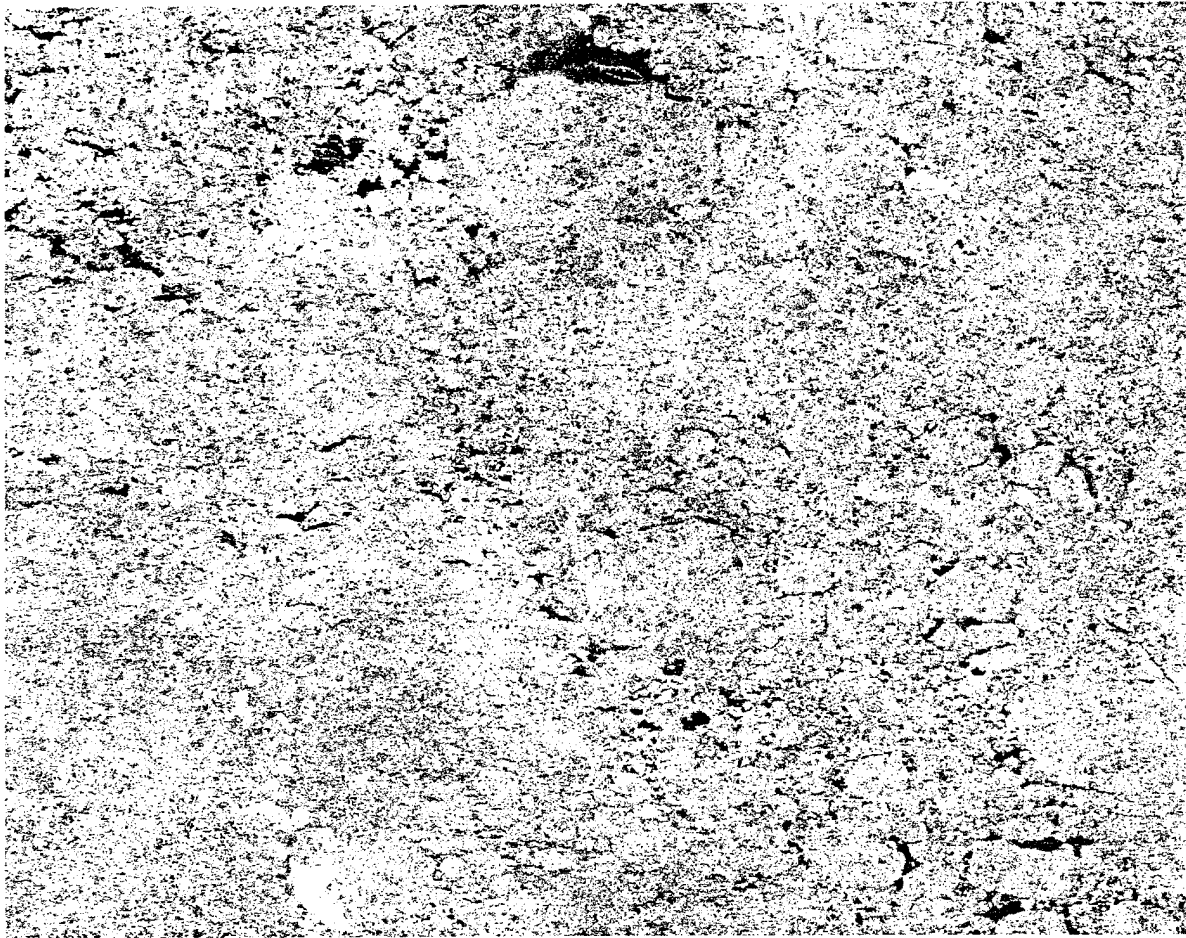


Figure 7.14 Result of dynamic local-area thresholding to determine multiyear ice concentration from ERS-1 SAR frame 1737, 22 September 1991 (JD 265).

These images were thresholded using the DLT algorithm and the results are shown in figures 7.11 through 7.14. Of the three classes separated by the thresholding technique we determined which type is most likely multiyear ice by examining the shapes of individual floes. The multiyear ice should also be the dominant ice type for this region and time frame, based on ship observations. There are some problems with our SAR classification, however. The bright, irregular features in the upper left corners for the images from 30 August and 6 September are classified as multiyear ice. The estimates of multiyear ice concentration may be improved with the use of feature extraction and/or heuristic techniques [Haverkamp, et al., 1995]. Our purpose here, however is to examine the potential for fusion of information from these two sensors, and improvements in various aspects of the technique is a topic for future work.

Assuming that multiyear is the dominant ice type in each image we computed the multiyear ice concentration from these classified SAR images for each SSM/I pixel region within the SAR frame. These estimates were used to constrain the NT algorithm to determine a revised estimate of the first-year ice concentration for each of these images. The ice concentration results averaged over each entire image frame are shown in table 7.2, along with results from strictly using the NT algorithm (without SAR input). The hybrid fusion algorithm results in an estimate of first-year ice concentration that is reduced by between 3 and 21%. The most marked differences are for the frame areas obtained on 12 and 6 September. The ice concentration results from the NT algorithm for the region covering the ERS-1 SAR frames were computed as described in section 7.2.3 above and the mean values are shown in table 7.1 and figure 7.2. These results are obtained over the region of the

SSM/I grid in which the SAR image was used for the multiyear ice concentration estimates in the fusion process. The results are shown in figure 7.15, 7.16, 7.17, and 7.18 as gray-scale images. The first-year ice concentration is scaled from 0 to 30% and the multiyear ice concentration is scaled from 50 to 75%, as indicated by the colorbars on the right side of each figure.

Table 7.2 Mean results from NT algorithm and hybrid fusion					
JD	SAR Frame	NT Results		Hybrid Fusion Results	
		FYC (%)	MYC (%)	FYC (%)	MYC (%)
242	1701	32.5	56.9	23.0	65.7
249	1719	40.2	39.3	18.7	62.3
255	1719	26.9	52.0	14.5	63.7
265	1737	11.3	62.5	8.0	65.5

For the region observed in SAR frame 1719, the ice observations logged during the IAOE field experiment aboard the *Polar Star* were used to compute average multiyear and average first-year/new ice concentrations for this region. The ice observations were obtained in this region over a period of three days from JD 243-245. The average multiyear ice concentration for this region, from the ship-based observations was about 70% and the first-year plus new ice concentration was about 14%, for a total ice concentration of approximately 84%. The ice observations for the young ice categories were approximately 10%. The hybrid fusion estimates are closer to the ship-based estimates than the NT algorithm alone.

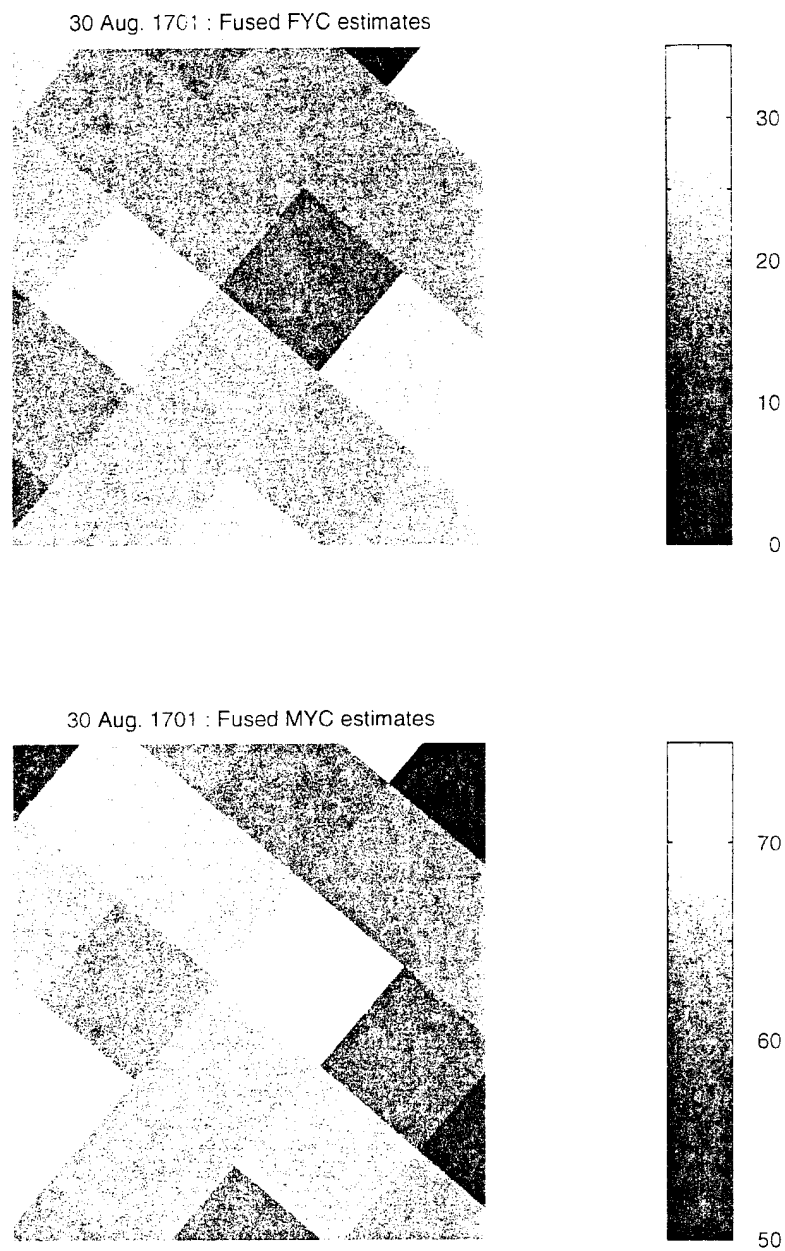
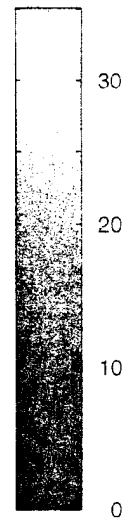
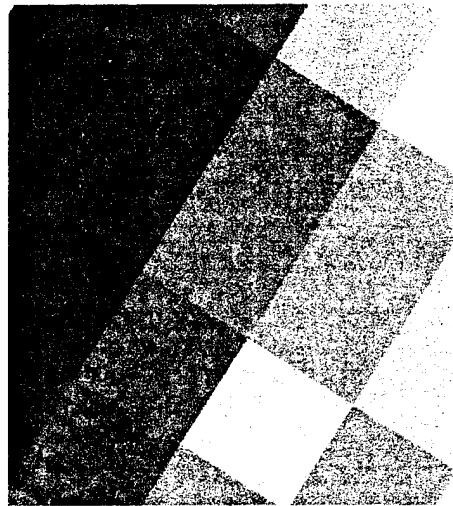


Figure 7.15 First-year and multiyear ice concentration estimates from fusion of ERS-1 SAR and SSM/I data for the region corresponding to the SAR image frame 1701 from 30 August (JD 242), 1991.

6 Sept. Frame 1719 : Fused FYC estimates



6 Sept. Frame 1719 : Fused MYC estimates

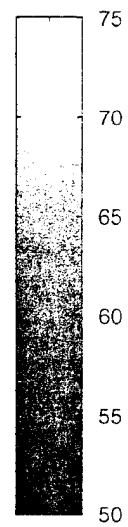
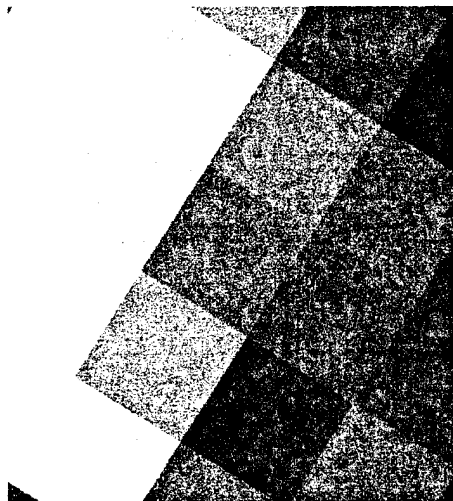


Figure 7.16 First-year and multiyear ice concentration estimates from fusion of ERS-1 SAR and SSM/I data for the region corresponding to the SAR image frame 1719 from 6 September (JD 249), 1991.

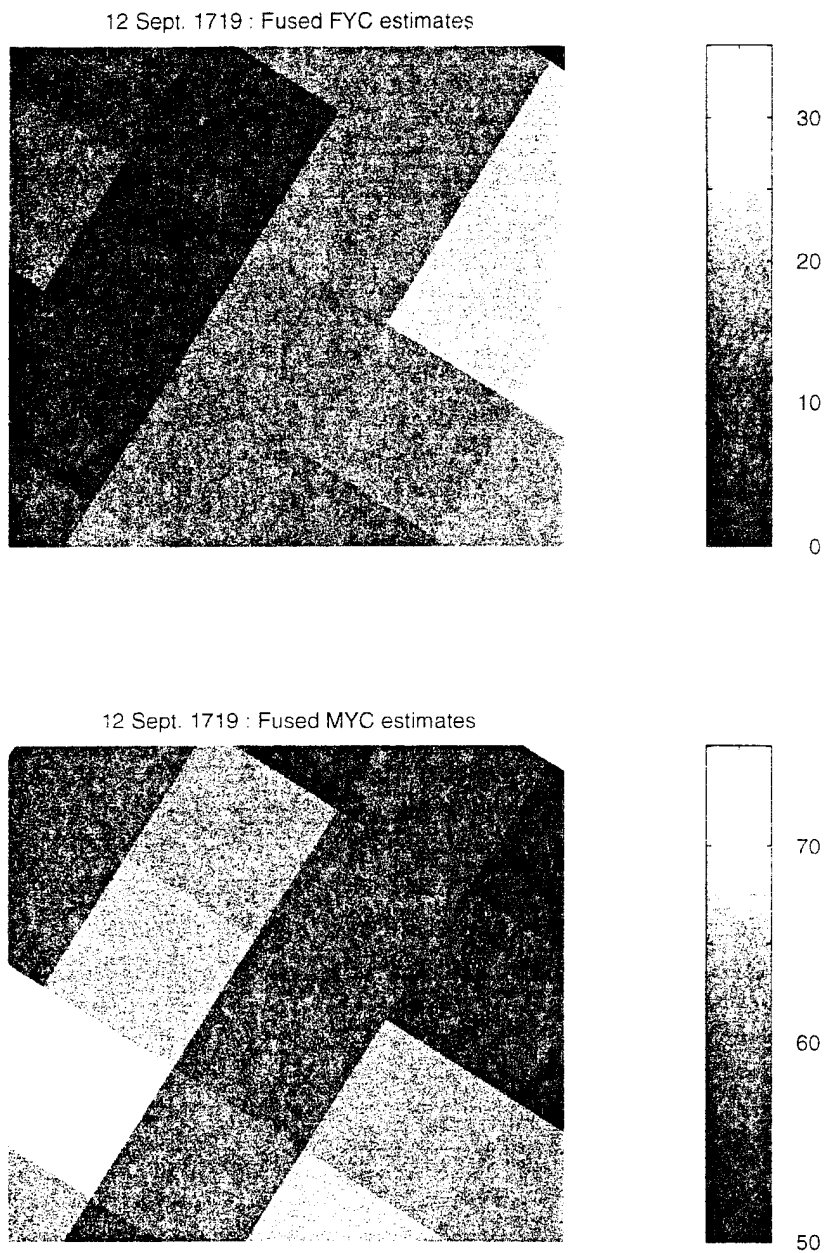


Figure 7.17 First-year and multiyear ice concentration estimates from fusion of ERS-1 SAR and SSM/I data for the region corresponding to the SAR image frame 1719 from 12 September (JD 255), 1991.

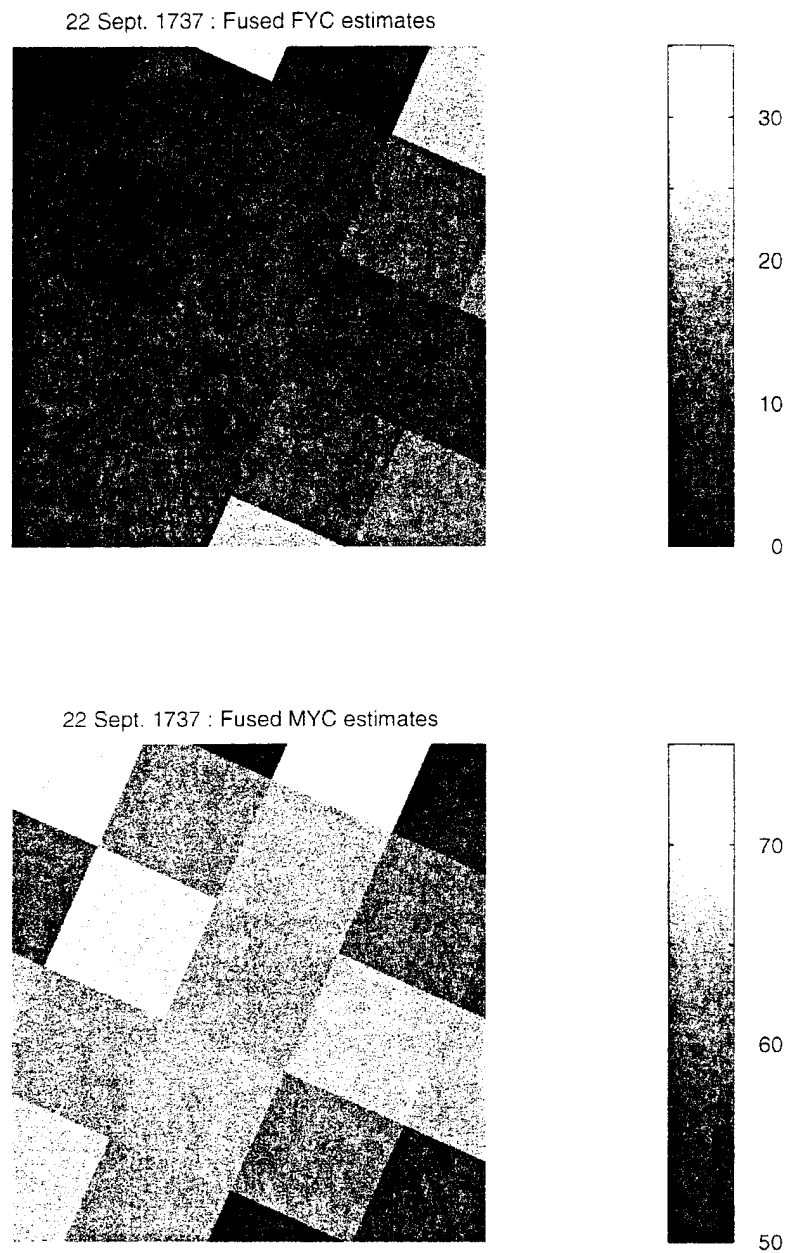


Figure 7.18 First-year and multiyear ice concentration estimates from fusion of ERS-1 SAR and SSM/I data for the region corresponding to the SAR image frame 1737 from 22 September (JD 265), 1991.

7.4.5 Implications for heat transfer

The onset of freeze-up in the Arctic signals the widespread initiation of new sea ice growth. Significant amounts of thin ice in the range of 1 cm to 10 cm were observed growing in leads during the IAOE experiment, beginning on 30 August (JD 242). The brightness temperature of thin ice goes through a series of rapid changes in its initial growth phase. This has been examined by Wensnahan, et al. [1993], who determined that these changes in emissivity are caused by salinity enhancement of the ice surface, possibly caused by brine expulsion as the ice grows. These changes occur in the initial growth phase, and settle out by the time new ice growth reaches approximately 10 cm in thickness. The spectral response reported by Wensnahan, et al., [1993] for thin ice growth measured at CRREL is shown in figure 7.19.

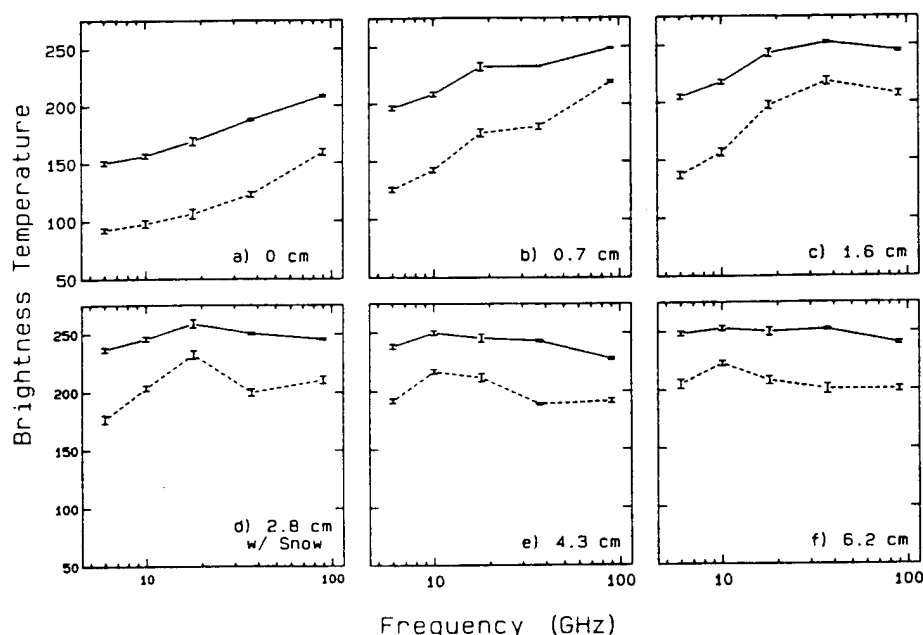


Figure 7.19 Spectral response of microwave emissivity from CRREL, 1990 for several ice thicknesses at V-pol (solid curves) and H-pol (dashed curves). {from [Wensnahan, et al., 1993]}. This figure shows the rapid changes in emissivity that occur during initial saline ice growth.

Beyond the initial stages of growth, the passive microwave signatures of young first-year ice as gradually evolve towards the first-year ice signature [Steffen and Maslanik, 1988; Eppler, et al., 1992]. Figure 7.20 shows the GR versus PR for various types of thin ice, as well as first-year ice, multiyear ice, and open water. The polarization and gradient ratios for this plot were computed from table 4-1 of Eppler, et al., [1992]. The table is a compilation of mean values for a number of measurements reported in the literature for the emissivity of different types of sea ice. This demonstrates that at approximately 10-cm thickness, new ice appears very similar to first-year ice in terms of the NT algorithm tie points. Furthermore, the thinner ice types, including dark nilas, which is typically around 5 cm thick, also have signatures that are between first-year ice and open water. First-year ice concentration estimates from the NT algorithm, then include some contribution from the thinner ice types. During the initial portion of the freeze-up season, any accurate first-year ice concentration should include thin and young first-year ice in the 10- to 50-cm range of thickness. The first-year ice concentrations obtained using our hybrid fusion technique may provide an estimate of the amount of new first-year ice during this time of the year.

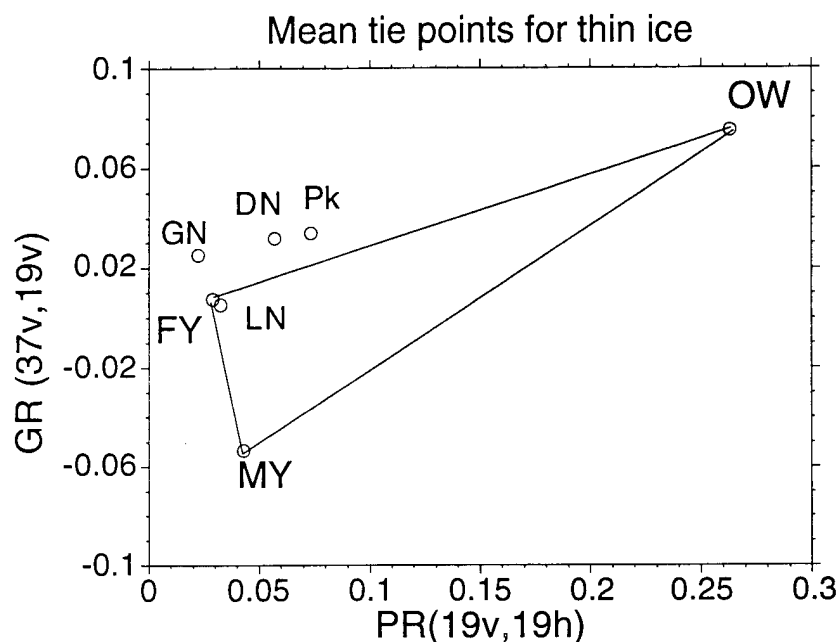


Figure 7.20 Mean values of PR and GR for young ice types tabulated in [Eppler, et al., 1992]. The thin ice signature evolves rapidly towards the first-year ice signature as ice growth exceeds 10 cm. OW = open water, FY = first-year, MY = multiyear, Pk=consolidated pancake ice (3 cm), DN = dark nilas, GN = gray nilas, LN = light nilas.

Calculations of heat transfer through ice of various thickness and as a function of season has been examined in the classic paper by Maykut [1978]. In this work, estimates of heat flux, as a function of ice thickness demonstrate that thin ice may be as important as multiyear ice and open water in determining the heat flux between the ocean and atmosphere. Therefore, misclassifying multiyear ice as first-year ice, may result in significant errors in the resulting heat flux estimates, particularly if the first-year ice is in its early stages of growth. To illustrate this point, we examined the net

heat loss over a region as a function of different percentages of young first-year and multi-year ice, based on the tabulated results from Maykut [1978]. We interpolated his tabulated results from 1 September and 1 October to obtain estimates of heat flux from the various thicknesses of young ice for mid-September. Assuming that first-year ice exists in equal amounts in the 5-cm to 80-cm range, we computed the net heat loss over a region that contains 90% ice cover. We varied the concentration of first-year ice from 0 to 90%, so the multiyear ice concentration varied from 90% to 0%, accordingly. The results are shown in figure 7.21 and are normalized to the case in which no FY ice is present (90% MY ice). These results demonstrate that errors in the estimate of first-year ice concentration have a direct effect on the heat flux estimates that might be made based on these concentration estimates.

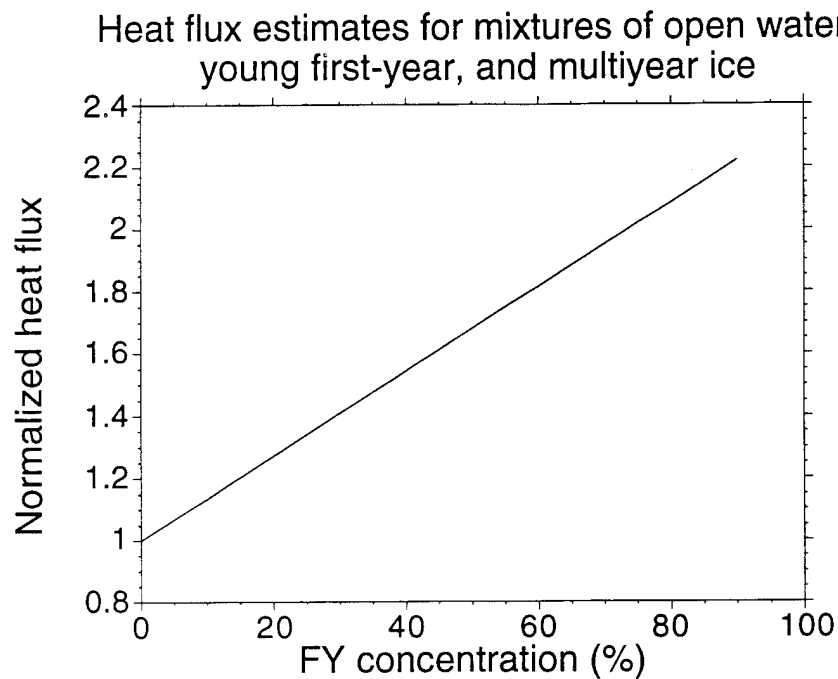


Figure 7.21 Estimated heat flux over a region containing a mixture of open water, FY and MY ice for mid-September as a function of first-year ice concentration, based on the tabulated results from Maykut [1978]. The first-year ice is assumed to be composed of ice thicknesses from 5 cm to 80 cm in equal amounts, open water is assumed to comprise 10 % of the area, and MY ice comprises the remainder. The results are normalized to the case in which there is no FY ice.

7.5 Summary

The concentrations of first-year and multiyear ice, derived from multispectral satellite radiometer data, are not accurate during the early freeze-up season in the Arctic. We utilized a hybrid fusion technique to obtain a better estimate of first-year ice concentration from passive data. First, we derived the multiyear ice concentration from ERS-1 SAR using a local-area threshold method. We then used the information derived from SAR as a constraint in a modification of an existing satellite passive microwave algorithm. The estimate of first-year ice concentration obtained from the fused result is between 15 and 19% for the area in which ship observations are available. The ship-based observations from the week prior to the satellite measurements show that approximately 10 to 15% of the ice is young first-year ice. The estimated concentration from the satellite passive microwave data alone yields 27 to 40% first-year ice concentrations. These results demonstrate that an improved estimate of first-year ice concentration during the freeze-up season may be obtained by fusing of active and passive satellite data. We have also demonstrated that errors in first-year ice concentration during this time of year have a direct impact on heat flux estimates. Combining SAR and passive microwave data has been demonstrated here and shows great potential, although some improvements may need to be implemented to improve the technique (see section 8.2). RADARSAT, to be launched later this year, will soon provide wide-swath data so that the coverage of the Arctic will be greatly increased. This increased coverage affords an opportunity for improvements in this approach since there will be a greater amount of passive microwave data available within the SAR swath.

CHAPTER 8

SUMMARY AND RECOMMENDATIONS

8.1 Summary

Sea ice is an important component in the ocean-atmosphere interactions which affect our climate. Studies of the effects of carbon-dioxide doubling on our climate predict that the most significant warming may occur in the Polar regions. Therefore, long-term changes in the sea ice cover in the polar regions may be an indicator of global change. Sea ice also plays an active role in the heat exchange between the ocean and atmosphere in the Arctic. Because of the importance of sea ice in the study of global change, monitoring of sea ice on a global scale is vital in understanding our planet. Cloud cover is persistent in the Arctic and darkness blankets the region for roughly half the year. Therefore, monitoring of sea ice on a global scale is best accomplished with satellite microwave remote sensing devices. Two of the primary instruments for microwave remote sensing of sea ice include synthetic aperture radars and passive microwave radiometers.

Understanding the basic physics of scattering from sea ice is vital in interpreting satellite microwave data. Algorithms have been developed for exploiting SAR data for ice classification, but these are primarily for use during the winter season, when signatures are relatively stable. Seasonal transitions, however are particularly difficult for interpretation of microwave scattering and emission from sea ice, due to

the rapidly varying environmental conditions. Because of these reasons, we investigated several key issues regarding backscatter signatures of Arctic sea ice and the potential for fusion with passive microwave data.

The focus of this study is on: (1) developing noise reduction methods to improve measurements from short-range scatterometers, (2) expanding our understanding of the backscatter signatures of sea ice during the summer-to-fall seasonal transition with *in situ* measurements, (3) determining the physical mechanisms responsible for the observed changes in backscatter during freeze-up, and (4) the development of a technique for extracting information from a combination of active and passive microwave sensors during this period.

In chapter 3 we discussed some of the issues affecting short-range scatterometer measurements and developed noise reduction techniques to improve these measurements. The sensitivity of short-range radar systems is not limited by thermal noise, but by reflection and leakage signals from the RF section and the antenna. These reflection and leakage signals, and their sidelobes are the primary sources of unwanted signals in short-range FM and step-frequency radar systems. We developed coherent noise reduction (CNR) techniques to improve the measurements obtained with these systems. These techniques are based on the fact that the reflection and leakage signals are coherent from sample to sample and the return from distributed targets (such as sea ice) are not coherent from sample to sample. These CNR methods improve the sensitivity of our radar systems by as much as 25-dB over conventional processing techniques. Amplitude and phase drifts inherent in FM and step-frequency radar systems can degrade the performance of the CNR. These drifts can be caused by changes in the oscillator operating frequency, temperature

fluctuations, and cable flexing. We extended our technique by developing a phase-corrected coherent noise reduction (PC-CNR) algorithm to account for these phase and amplitude fluctuations. The PC-CNR technique allows us to obtain measurements with short-range radar systems whose sensitivity approaches the thermal noise floor, rather than being limited by the leakage and reflection signals. The development of these signal processing algorithms have enabled us to obtain high quality radar backscatter measurements from natural and artificial sea ice. These techniques are presently being used in the processing of data from recent experiments as well as data from past measurements that were previously discarded because of low signal-to-noise ratio.

In chapter 4 we presented ship-based radar backscatter measurements of sea ice, obtained during the early stages of freeze-up in the Arctic. These measurements are the first published *in situ* backscatter measurements in which the transition from summer into freeze-up is observed in the deep Arctic. Radar backscatter from multiyear ice was shown to be strongly dependent on the temperature during this period. The physical mechanisms responsible for this are discussed in chapter 5 and summarized below. In chapter 4 we also reported radar backscatter measurements from thin ice and demonstrated that ERS-1 SAR and RADARSAT are not suitable for observing the initial 5-cm of ice growth, but may have enough sensitivity to observe thin sea ice that is greater than 5 cm thick. We also demonstrated that a combination of copolarized and cross-polarized σ^0 may be used to distinguish between the four categories of thin ice, which are roughly defined by their thickness.

In chapter 5 we examined the physical mechanisms responsible for changes in radar backscatter from multiyear ice during the summer-to-fall transition. The

backscattering coefficient increases by approximately 7 dB at 25° incidence at the onset of freeze-up. First, we examined the effect of the snow layer on the backscatter from snow-covered ice. We computed the attenuation through the snow layer, based on measurements of snow physical properties and permittivity models for wet snow. We also computed the volume scattering contribution of the snow layer. Neither of these effects is large enough in magnitude to explain the observed changes in the backscatter from multiyear ice. Second, we compared radar backscatter measurements obtained prior to freeze-up to predictions from a surface-only scattering model and measurements obtained after freeze-up to a volume-only scattering model. The backscatter signature prior to freeze-up is primarily caused by surface scatter, since moisture on or near the ice surface reduces penetration of electromagnetic energy into the sea ice volume. As temperatures drop there is more penetration into the sea ice volume, causing the volume scatter contribution to overcome the surface scatter contribution. The change in backscatter observed during the onset of freeze-up is caused by the refreezing of moisture on or near the surface of the multiyear ice as temperatures drop below freezing. This interpretation, based on relatively simple scattering models, is verified through comparison with the more complicated single-layer scattering models of Fung [1994] and Tjuatja, et al., [1992].

In chapter 6 we demonstrated that the changes in backscatter observed in the field measurements are also observable in ERS-1 SAR images. The mean backscattering coefficients obtained from ERS-1 SAR data also increase by 5 to 7 dB at the onset of freeze-up. This indicates that the same physical mechanisms observed on a small scale from the ship-based measurements are the primary mechanisms for the changes observed on a large scale from SAR data. We have also demonstrated that since the ERS-1 SAR is sensitive to this change in backscatter it can be used to detect the onset

of freeze-up in the Arctic. This may be useful as a switch for algorithms whose parameters change as the seasons change in the Arctic. It can also be used as a measure of the duration of the summer melt, when combined with a detection of the onset of melt in the spring.

In chapter 7 we demonstrated that SSM/I-derived concentrations of multiyear ice are underestimated during the freeze-up season. The misclassification of multiyear ice as first-year ice under warm conditions has been observed in past studies. It also appears that the misclassification of multiyear ice as first-year ice from passive microwave data continues beyond the onset of freeze-up. We used a hybrid fusion technique to obtain an improved estimate of the first-year and multiyear ice concentration during the freeze-up season. The algorithm uses multiyear ice concentration estimates from ERS-1 SAR data to constrain a modified version of the NASA Team algorithm. Based on ice observations which were logged on board the *Polar Star* in the region studied, estimates of first-year ice concentration obtained with this technique appear to be more accurate than estimates obtained using only the SSM/I data.

8.2 Recommendations for future work

The hybrid fusion technique in chapter 7 demonstrates that satellite SAR and passive microwave data may be combined for improved estimates of ice type concentration during the freeze-up season. To the best of our knowledge, this is the first time such a technique has been applied for improvement of ice type concentration estimates. We believe that this is only the first step in exploiting information from these sensors in a

fusion process and there is significant room for improvement of the algorithm. Improvements may be made in both the SAR multiyear ice concentration estimates and in the resolution of the SSM/I data.

The multiyear ice concentration is presently estimated by using the dynamic thresholding technique. Although this appears to work well for the images in figure 7.9 and 7.10, it may not be accurate in all cases. For example, consider the bright feature in the upper-left corner of the SAR image in figure 7.8. Based on the shape of this region, we believe that this is most likely wind-roughened open water, but it is classified as primarily consisting of multiyear ice in our computation. The multiyear ice concentration estimate may be improved through the use of feature extraction and knowledge-based methods.

Our results from chapter 7 indicate that improved estimates of ice type concentration may be obtained over areas covered by an entire SAR frame. However, because of the resolution difference between the sensors it is difficult to incorporate the fused results back into the SAR image. We believe that further improvements in SAR interpretation may be obtained by "closing the loop" or using fused results with the original SAR data to improve ice concentration estimates and to identify areas of thin ice or open water in the SAR image. At present we are using SSM/I data that are daily-averaged and gridded to 25 km cells for the Arctic region. At this scale, the SAR-derived estimates of multiyear concentration are computed over very large areas, and fine-scale information is lost. Recently, a technique for improving the resolution of SSM/I data has been developed [Sethmann, et al., 1994]. We believe that the use of this or a similar image reconstruction approach may be useful in enhancing the hybrid fusion algorithm developed in chapter 7.

REFERENCES

- Askne, J., L.M.H. Ulander, and D. Birkeland, ERS-1 SAR Analysis of Arctic Ice Concentration During the Melt Season, *Digest IGARSS '93*, pp. 431-433, Tokyo, Japan, August, 1993.
- Askne, J, A. Carlström, W. Dierking, and L. Ulander, ERS-1 SAR Modeling and Interpretation of Sea Ice Signatures, *Digest IGARSS '94*, pp. 162-164, Pasadena, CA, August, 1994.
- Attema, E.P.W., The active microwave instrument on-board the ERS-1 satellite. *Proceedings of the IEEE*, vol. 79, 791-799, 1991.
- Arcone, S.A., A.J. Gow, and S. McGrew, Microwave Dielectric, Structural and Salinity Properties of Simulated Sea Ice, *IEEE Transactions on Geoscience and Remote Sensing*, vol. 24, no.6, 832-839, 1986.
- Barber, D.G., E.F. LeDrew, D.G. Flett, M. Shokr, and J. Falkingham, Seasonal and Diurnal Variations in SAR Signatures of Sea Ice, *IEEE Transactions on Geoscience and Remote Sensing*, vol. 30, no. 3, pp. 638-642, 1992.
- Beaven, S. Radar Backscatter Measurements from Simulated Sea Ice and Arctic Sea Ice during the Fall Freeze-up, MS Thesis, University of Kansas, 1992.
- Beaven, S., S.P. Gogineni, M. Shanableh, A. Gow, W. Tucker, and K. Jezek, Radar Backscatter Measurements from Arctic Sea Ice during the Fall freeze-up, *RSL Technical Report 8243-1/8241-1*, February 1993a.
- Beaven, S.G., S.P. Gogineni, A. Gow, A. Lohanick, and K. Jezek, Radar Backscatter Measurements from Simulated Sea Ice During CRRELEX'90, *RSL Technical Report 8243-2*, June 1993b.

- Beaven, S., and S.P. Gogineni, Shipborne Radar Backscatter Measurements from Arctic Sea Ice During the Fall Freeze-Up, *Remote Sensing Reviews*, vol. 9, nos. 1-2, pp. 3-25, 1994.
- Beaven, S.G., G.L. Lockhart, S.P. Gogineni, K. Jezek, A.R. Hosseinmostafa, A.J. Gow, D.K. Perovich, A.K. Fung, and S. Tjuatja, Laboratory Measurements of Radar Backscatter From Bare and Snow-Covered Saline Ice Sheets, accepted for publication, in *International Journal of Remote Sensing*, 1995.
- Bredow, J., S.P. Gogineni, A.J. Gow, P.F. Blanchard, and R.K. Moore, Radar backscattering from artificially grown sea ice, *Journal of Oceanic Engineering*, vol. 14, no. 3, pp. 259-264, 1989.
- Burns, B.A., D.J. Cavalieri, M.R. Keller, W.J. Campbell, T.C. Grenfell, G.A. Maykut, and P. Gloersen, Multisensor Comparison of Ice Concentration Estimates in the Marginal Ice Zone, *Journal of Geophysical Research*, vol. 92, no. C7, pp. 6843-6856, 1987.
- Carsey, F.D., Summer Arctic sea ice character from satellite microwave data, *Journal of Geophysical Research*, vol. 90, no. C3, pp. 5015-5034, 1985.
- Carsey, F.D., R.G. Barry, and W.W. Weeks, Introduction, in *Microwave Remote Sensing of Sea Ice*, edited by F.D. Carsey (Washington D.C.:American Geophysical Union), Geophysical Monograph, vol. 68, 1-7, 1992.
- Cavalieri, D.J., P. Gloersen, and W.J. Campbell, Determination of sea ice parameters with the Nimbus 7 SMMR, *Journal of Geophysical Research*, vol. 89, no. D4, pp. 5355-5369, 1984.
- Cavalieri, D.J., B.A. Burns, and R.G. Onstott, Investigation of the Effects of Summer Melt on the Calculation of Sea Ice Concentration Using Active and Passive Microwave Data, *Journal of Geophysical Research*, vol. 95, no. C4, pp. 5359-5369, 1990.

- Cavalieri, D.J., J.P. Crawford, M.R. Drinkwater, D.T. Eppler, L.D. Farmer, R.R. Jentz, and C.C. Wackerman, Aircraft Active and Passive Microwave Validation of Sea Ice Concentration from the Defense Meteorological Satellite Program Special Sensor Microwave Imager, *Journal of Geophysical Research*, vol. 96, no. C12, pp. 21,989-22,008, 1991.
- Collins, M.J., and W.J. Emery, A computational method for estimating sea ice motion in sequential Seasat synthetic aperture radar imagery by matched filtering, *Journal of Geophysical Research*, vol 93, no. C8, pp. 9241-9251, 1988.
- Collins, M.J., Information Fusion in Sea Ice Remote Sensing, in *Microwave Remote Sensing of Sea Ice*, edited by F.D. Carsey (Washington D.C.:American Geophysical Union), Geophysical Monograph, vol. 68, 431-441, 1992.
- Comiso, J.C., Characteristics of Arctic winter sea ice from satellite multispectral microwave observations, *Journal of Geophysical Research*, vol 91, no. C1, pp. 975-994, 1986.
- Curlander, J.C., and R.N. McDonough, Synthetic Aperture Radar: Systems and Signal Processing, New York: John Wiley & Sons, 1992.
- Drinkwater, M.R., LIMEX'87 Ice Surface Characteristics: Implications for C-Band SAR Backscatter Signatures, *IEEE Trans. Geosc. and Remote Sensing*, 27(5), 501-513, 1989.
- Drinkwater, M.R., J.P. Crawford, and D.J. Cavalieri, Multifrequency, multipolarization SAR and radiometer sea ice classification, *Proceedings of the IGARSS '91 Symposium*, vol. 2, IEEE cat. no. 91CH2971-0, pp. 107-111, IEEE, New York, 1991.
- Drinkwater, M.R., R. Kwok, D.P. Winebrenner, E. Rignot, Multifrequency polarimetric synthetic aperture radar observations of sea ice, *Journal of Geophysical Research*, vol 96, no. C11, pp. 20,679-20,698, 1991.

- Eppler, D.T., L.D. Farmer, A.W. Lohanick, M.R. Anderson, D.J. Cavalieri, J. Comiso, P. Gloersen, C. Garrity, T.C. Grenfell, M. Hallikainen, J.A. Maslanik, C. Mätzler, R.A. Melloh, I. Rubenstein, C.T. Swift, Passive Microwave Signatures of Sea Ice, in *Microwave Remote Sensing of Sea Ice*, edited by F.D. Carsey (Washington D.C.:American Geophysical Union), Geophysical Monograph, vol. 68, 47-71, 1992.
- Fily, M. and D.A. Rothrock, Sea ice tracking by nested correlations, *IEEE Transactions on Geoscience and Remote Sensing*, vol. GE-25, no. 5, pp. 570-580, 1987.
- Fung, A.K., Microwave Scattering and Emission Models and Their Applications, Boston:Artech House, pp. 121, 1994.
- Fung, A.K., S. Tjuatja, S. Beaven, S.P. Gogineni, K. Jezek, A.J. Gow, and D.K. Perovich, Modeling Interpretation of Scattering From Snow-Covered Sea Ice, *Digest IGARSS '94*, pp. 617-619, 8-12 August, Pasadena, CA, 1994.
- Gardner, W.A., Introduction to Random Processes, New York:Macmillan Publishing Company, 1986.
- Garrity, C., K.W. Asmus, and R.O. Ramseier, International Arctic Ocean Experiment 1991: Summer Passive Microwave Ice Conditions, MWG Technical Report 92-1, Microwave Group - Ottawa River, Dunrobin, Ontario, Canada, December 1992.
- Gloersen, P., and D.J. Cavalieri, Reduction of weather effects in the calculation of sea ice concentration from microwave radiances, *Journal of Geophysical Research*, vol. 91, no. C3, pp. 3913-3919, 1986.
- Gloersen, P., W.J. Campbell, D.J. Cavalieri, J.C. Comiso, C.L. Parkinson, and H.J. Zwally, *Arctic and Antarctic Sea Ice, 1978-1987: Satellite Passive-Microwave Observations and Analysis*, NASA SP-511, Washington, D.C., 1992.

- Gogineni, S.P., Radar Backscatter from Summer and Ridged Sea Ice, and the Design of Short-range Radars, Ph.D. Dissertation, University of Kansas, 1984.
- Gogineni, S., F.A. Hoover, and J.W. Bredow, High-Performance, Inexpensive Polarimetric Radar for *In Situ* Measurements, *IEEE Transaction on Geoscience and Remote Sensing*, vol. 28, no. 4, pp. 450-455, 1990.
- Gogineni, S.P., R.K. Moore, P. Wang, A.J. Gow, and R.G. Onstott, Radar backscatter over saline ice, *International Journal of Remote Sensing*, vol. 11, no. 4, pp. 603-615, 1990.
- Gogineni, S.P., R.K. Moore, T.C. Grenfell, D.G. Barber, S. Digby, and M. Drinkwater, The effects of freeze-up and melt processes on microwave signatures. In *Microwave Remote Sensing of Sea Ice*, edited by F.D. Carsey (Washington D.C.:American Geophysical Union), Geophysical Monograph, vol. 68, 329-341, 1992.
- Gogineni, S.P., K. Jezek, L. Peters, J. Young, S. Beaven, and E. Nassar, Application of plane waves for accurate measurement of microwave scattering from geophysical surfaces, *IEEE Transactions on Geoscience and Remote Sensing*, accepted for publication, 1995.
- Gore-Tex Microwave Coaxial Assemblies, catalog and technical notes, issue no. 0190, W.L. Gore and Associates, Inc., Phoenix, Arizona, 1990.
- Gow, A.J., Optical Characterization of Sea Ice Structure using Polarized Light Techniques, *Proc. of the Informational Society of Optical Engineering*, vol. 637, pp. 264-271, 1986.
- Gray, A.L., R.O. Ramseier, and W.J. Campbell, Scatterometer and SLAR results obtained over Arctic sea ice and their relevance to the problem of Arctic ice reconnaissance, *Proceedings of the Fourth Canadian Symposium on Remote Sensing*, pp. 424-443, 1977.

- Gray, A.L., Hawkins, R.K., Livingstone, C.E., Arsenault, L.D., and Johnstone, W.M., 1982, Simultaneous scatterometer and radiometer measurements of sea-ice microwave signatures. *IEEE Journal of Oceanic Engineering*, vol. OE-7, 20-32.
- Grenfell, T.C., A theoretical model of the optical properties of sea ice in the visible and near infrared, *J. Geophys. Research*, vol. 88, 9723-9735, 1983.
- Grenfell, T.C., and A.W. Lohanick, Temporal variations of the microwave signatures of sea ice during the late spring and early summer near Mould Bay NWT, *Journal of Geophysical Research*, vol. 90, no C3, pp. 5063-5074, 1985.
- Grenfell, T.C., Surface-Based Passive Microwave Studies of Multiyear Sea Ice, *Journal of Geophysical Research*, vol. 97, no. C3, pp. 3485-3501, 1992.
- Grenfell, T.C., D.J. Cavalieri, J.C. Comiso, M.R. Drinkwater, R.G. Onstott, I. Rubenstein, K. Steffen, D.P. Winebrenner, Considerations for Microwave Remote Sensing of Thin Sea Ice, in *Microwave Remote Sensing of Sea Ice*, edited by F.D. Carsey (Washington D.C.:American Geophysical Union), Geophysical Monograph, vol. 68, 291-301, 1992.
- Hall, D.L., *Mathematical Techniques in Multisensor Data Fusion*, Artech House, Norwood, MA, 1992.
- Hallikainen, M.T., F.T. Ulaby, and M. Abdelrazik, Dielectric Properties of Snow in the 3 to 37 GHz Range, *IEEE Transactions on Antennas and Propagation*, vol. AP-34, no. 11, pp. 1329-1339, 1986.
- Hallikainen, M.T., Review of the Microwave Dielectric and Extinction Properties of Sea Ice and Snow, *Digest IGARSS'92*, pp. 961-965, 1992.
- Havercamp, D., L.K. Soh, and C. Tsatsoulis, A dynamic local thresholding technique for sea ice classification, *Digest IGARSS'93*, pp. 638-640, 1993.

- Havercamp, D., L.K. Soh, and C. Tsatsoulis, A comprehensive, automated approach to determining sea ice thickness from SAR data, *IEEE Transactions on Geoscience and Remote Sensing*, vol. 33, no. 1, pp. 46-57, 1995.
- Holt, B., A.A. Rothrock, and R. Kwok, Determination of Sea Ice Motion from Satellite Images, in *Microwave Remote Sensing of Sea Ice*, edited by F.D. Carsey (Washington D.C.:American Geophysical Union), Geophysical Monograph, vol. 68, pp. 343-353, 1992.
- Holt, B., Cunningham, G., and Kwok, R., Sea ice radar signatures from ERS-1 SAR during late summer and fall in the Beaufort and Chukchi Seas. *First ERS-1 Symposium held in Cannes, France, on 4-6 November 1992*, ESA-SP-359 (Paris: European Space Agency), pp. 339-342, 1992.
- Houghton, J.T., G.J. Jenkins, and J.J. Ephraums, *Climate Change - the IPCC scientific assessment*, Cambridge University Press, England, 1990.
- Hyypä, J. and M. Hallikainen, Classification of low-salinity sea ice types by ranging scatterometer, *International Journal of Remote Sensing*, vol. 13, no. 13, pp. 2399-2413, 1992.
- Iizuka, K., A.P. Freundorfer, K.H. Wu, H. Mori, H. Ogura, and V.K. Nguyen, Step-frequency radar, *Journal of Applied Physics*, vol. 56, no. 9, pp. 2572-2583, 1984.
- Jezek, K., P. Gogineni, L. Peters, J. Young, S. Beaven, E. Nassar, and I. Zabel, Microwave Scattering from Saline Ice Using Plane Wave Illumination, *Digest IGARSS'94*, pp. 493-495, Pasadena, CA, August 8-12, 1994.
- Keller, W.C., W.J. Plant, and D.E. Weissman, The dependence of X-band microwave sea return on atmospheric stability and sea state, *Journal of Geophysical Research*, vol. 90, no. C1, pp. 1019-1029, 1985.

- Kwok, R., J.C. Curlander, R. McConnell, and S.S. Pang, An ice-motion tracking system at the Alaska SAR Facility, *IEEE Journal of Oceanic Engineering*, vol. OE-15, no. 1, pp. 44-54, 1990.
- Kwok, R., E. Rignot, B. Holt, and R.G. Onstott, Identification of sea ice type in spaceborne SAR data, *Journal of Geophysical Research*, 97(C2), 2391-2402, 1992a.
- Kwok, R., G. Cunningham, and B. Holt, An Approach to Identification of Sea Ice Types from Spaceborne SAR Data, in *Microwave Remote Sensing of Sea Ice*, edited by F.D. Carsey (Washington D.C.:American Geophysical Union), Geophysical Monograph, vol. 68, pp. 355-360, 1992b.
- Laur, Henri, ERS-1 SAR Calibration: Derivation of Backscattering Coefficient σ^0 in ERS-1.SAR.PRI Products. European Space Agency, ESRIN. (Issue 1 Rev. 0), October 1992.
- Li, Shusun, Development and Applications of an algorithm for a two-way transformation between the geographical coordinates and the ASF SAR image coordinates, technical memorandum, Geophysical Institute/UAF, Fairbanks, Alaska, 1994.
- Livingstone, C.E., K.P. Singh, and A.L. Gray, Seasonal and regional variations of active/passive microwave signatures of sea ice, *IEEE Transactions on Geoscience and Remote Sensing*, vol. GE-25, pp. 159-173, 1987.
- Loshchilov, V.S. and V.A. Voyevodin, Determining elements of drift of the ice cover and movement of the ice edge by the aid of the Toros aircraft lateral scan radar station, *Problemy Arktiki i Antarktiki*, vol. 40, pp. 23-30, 1972.
- Lytle, V.I., K.C. Jezek, A.R. Hosseinmostafa, and S.P. Gogineni, Laboratory Backscatter Measurements Over Urea Ice with a Snow Cover at Ku Band,

- IEEE Transactions on Geoscience and Remote Sensing*, vol. 31, no. 5, pp. 1009-1016, 1993.
- Maykut, G.A., Energy exchange over young sea ice in the Central Arctic, *J. Geophys. Research*, vol. 83, pp. 3646-3658, 1978.
- Moore, R.K., J.P. Claasen, and Y.H. Lin, Scanning Spaceborne Synthetic Aperture Radar with Integrated Radiometer, *IEEE Transactions on Aerospace and Electronic Systems*, vol. AES-15, pp. 697-708, 1981.
- Moore, R.K., V. Hesany, R. Lawner, and S. Gogineni, Intermediate results of the NORDSEE experiment, *RSL Technical Report 419-3*, November 1984.
- NSIDC Special Report-1, *DMSP SSM/I Brightness Temperature and Sea Ice Concentration Grids for Polar Regions on CD ROM: User's Guide*, National Snow and Ice Data Center, Special Report - 1, Cooperative Institute for Research in Environmental Sciences, University of Colorado, Boulder, CO, January, 1992.
- Onstott, R.G. and S.P. Gogineni, Active microwave measurements of Arctic sea ice under summer conditions, *Journal of Geophysical Research*, vol. 90, no. C3, pp. 5035-5044, 1985.
- Onstott, R.G., T.C. Grenfell, C. Mätzler, C.A. Luther, and E.A. Svendsen, Evolution of microwave sea ice signatures during early summer and midsummer in the marginal ice zone, *Journal of Geophysical Research*, vol. 92, no. C7, pp. 6825-6835, 1987.
- Onstott, R.G. and R.A. Shuchman, Comparison of SAR and scatterometer data collected during CEAREX, *Proceedings of the IGARSS'90 Symposium*, pp. 1513-1516, College Park, Maryland, 1990.

- Onstott, R.G., SAR and Scatterometer Signatures of Sea Ice, in *Microwave Remote Sensing of Sea Ice*, edited by F.D. Carsey (Washington D.C.:American Geophysical Union), Geophysical Monograph, vol. 68, 73-104 1992.
- Onstott, R.G., Examination of the Physical, Electrical, and Microwave Evolution of Sea Water into Young Ice, *Proceedings of the IGARSS'92 Symposium*, vol. II, pp. 1259-1261, 1992b.
- Parashar, S.K., R.M. Haralick, R.K. Moore, and A.W. Biggs, Radar scatterometer discrimination of sea ice types, *IEEE Transactions on Geoscience and Electronics*, Vol. GE-15, pp. 83-87, 1977.
- Parkinson, C.L., J.C. Comiso, H.J. Zwally, D.J. Cavalieri, P. Gloerson, and W.J. Campbell, *Arctic Sea Ice, 1973-1976: Satellite Passive-Microwave Observations*, NASA SP-489, Washington DC: NASA Scientific and Technical Information Branch, 1987.
- Preller, R.H., J.E. Walsh, and J.A. Maslanik, The use of Satellite Observations in Ice Cover Simulations, in *Microwave Remote Sensing of Sea Ice*, edited by F.D. Carsey (Washington D.C.:American Geophysical Union), Geophysical Monograph, vol. 68, 385-404, 1992.
- Racette, P.E., R.R. Forster, and R.K. Moore, Limitations of the Luneburg Lens as a Calibration Target for a Dual-Antenna Radar System, *IEEE Transactions on Geoscience and Remote Sensing*, vol. 29, no. 1, pp. 179-180, 1991.
- Rothrock, D.A., and D.R. Thomas, Ice Modeling and Data Assimilation with the Kalman Smoother, in *Microwave Remote Sensing of Sea Ice*, edited by F.D. Carsey (Washington D.C.: American Geophysical Union), Geophysical Monograph, vol. 68, pp. 405-418, 1992.
- Rouse, J.W., Arctic ice type identification by radar, *Proceeding of the IEEE*, vol. 57, no. 4, pp. 605-611, 1969.

- Saunders, W.K., CW and FM Radar, in *Radar Handbook*, edited by M. Skolnik (New York:McGraw-Hill), 14.1-14.45, 1990.
- Schwartz, K., M.O. Jeffries, and S. Li, Using ERS-1 SAR Data to Monitor the State of the Arctic Ocean Sea Ice Surface Between Spring and Autumn, 1992, *Digest IGARSS '94*, pp. 1759-1762, 8-12 August, Pasadena, CA, 1994.
- Sethmann, R., B.A. Burns, and G.C. Heygster, Spatial Resolution Improvement of SSM/I Data with Image Restoration Techniques, *IEEE Transactions on Geoscience and Remote Sensing*, vol. 32, no. 6, 1994.
- Skolnik, M.I., Introduction to Radar Systems, New York:McGraw-Hill, pp. 81-92, 1980.
- Steffen, K., and A. Schweiger, NASA Team Algorithm for Sea Ice Concentration Retrieval from Defense Meteorological Satellite Program Special Sensor Microwave Imager: Comparison With Landsat Satellite Imagery, *Journal of Geophysical Research*, vol. 96, no. C12, pp. 21,971-21,987, 1991.
- Swift, C.T., K. St. Germain, K. Jezek, S.P. Gogineni, A. Gow, D. Perovich, T. Grenfell, and R. Onstott, Laboratory Investigations of the Electromagnetic Properties of Artificial Sea Ice, in *Microwave Remote Sensing of Sea Ice*, edited by F.D. Carsey (Washington D.C.:American Geophysical Union), Geophysical Monograph, vol. 68, 177-200, 1992.
- Thomas, D.R., Arctic Sea Ice Signatures for Passive Microwave Algorithms, *Journal of Geophysical Research*, vol. 98, no. C6, pp. 10,037-10,052, 1993.
- Thorndike, A.S., A toy model linking atmospheric thermal radiation and sea ice growth, *Journal of Geophysical Research*, vol. 97, pp. 9401-9410, 1992.
- Tjuatja, S, A.K. Fung, and J. Bredow, A Scattering Model for Snow-covered Sea Ice, *IEEE Transactions on Geoscience and Electronics*, Vol. GE-30, pp. 804-810, 1992.

- Tjuatja, S., A.K. Fung, and M.S. Dawson, An Analysis of Scattering and Emission from Sea Ice, *Remote Sensing Reviews*, vol. 7, pp. 83-106, 1993.
- Tucker, W.B. III, Grenfell, T.C., Onstott, R.G., Perovich, D.K., Gow, A.J., Shuchman, R.A., and Sutherland, L.L., Microwave and physical properties of sea ice in the winter marginal ice zone. *Journal of Geophysical Research*, vol. 96, 4573-4587, 1991.
- Twomey, S., *Introduction to the Mathematics of Inversion in Remote Sensing and Indirect Measurements*, Elsevier Scientific Publishing Company, New York, 1977.
- Ulaby, F.T., R.K. Moore, and A.K. Fung, *Microwave Remote Sensing: Active and Passive*, vol. I, Artech House, Norwood, MA, 1982.
- Ulaby, F.T., R.K. Moore, and A.K. Fung, *Microwave Remote Sensing: Active and Passive*, vol. III, Artech House, Norwood, MA, 1986.
- Ulaby, F.T. and C. Elachi, Radar polarimetry for geoscience applications, Norwood, MA: Artech House, 1990.
- Ulander, L.M.H., and A. Carlström, C-band backscatter signatures of old ice in the central Arctic, *Digest IGARSS'92*, 958-960, 1992.
- Ulander, L.M.H., Askne, J., And Johannessen, B.O., 1992, Calibrated ERS-1 SAR signatures and video underflights over Arctic ice. *Proceedings IGARSS'92*, vol. 2, (Piscataway, New Jersey : IEEE Press), 1536-1538, 1992.
- Vass, P., and B. Battrick, (editors), ERS-1 System, ESA SP-1146, Noordwijk, The Netherlands: ESA Publications Division, ISBN 92-9092-021-1, 1992.
- Vesecky, J.F., R. Samandi, M.P. Smith, J.M. Daida, and R.M. Bracewell, Observation of sea-ice dynamics using synthetic aperture radar images: automated analysis, *IEEE Transactions on Geoscience and Remote Sensing*, vol. GE-26, no. 1, pp. 38-48, 1988.

- Waltz, E., and J. Llinas, *Multisensor Data Fusion*, Artech House, Inc., Norwood, MA, 1990.
- Winebrenner, D.P., B. Holt, and E.D. Nelson, Observing Seasonal Transitions on Sea Ice in the Arctic Using the ERS-1 SAR, pp. 1763, 8-12 August, Pasadena, CA, 1994a.
- Winebrenner, D.P., E.D. Nelson, R. Colony, and R.D. West, Observation of melt onset on multiyear Arctic sea ice using the ERS-1 synthetic aperture radar, *Journal of Geophysical Research*, vol. 99, no. C11, pp. 22,425-22,441, November, 1994b
- Zebker, HA., J.J. van Zyl, S.L. Durden, and L. Norikane, Calibrated imaging radar polarimetry: Technique examples and applications, *IEEE Transactions on Geoscience and Remote Sensing*, vol. 29, pp 942-961, 1991.
- Zwally, H.J., J.C. Comiso, C.L. Parkinson, W.J. Campbell, F.D. Carsey, and P. Gloersen, *Antarctic Sea Ice, 1973-1976: Satellite Passive-Microwave Observations*, NASA SP-459, Washington DC: NASA Scientific and Technical Information Branch, 1987.

APPENDIX A

IAOE Information and Physical Properties Measurements

Table A-1. IAOE'91 RSL Scatterometer Data Summary

Julian Date	Position	Time (UTC)	Angles	Coincident Data
234	84.3°N 35.1°E	08:00	20-65°	S, I
236	84.5°N 34.4°E	15:00	35-70°	S, I
237	84.9°N 38.4°E	18:00	20-65°	x
239	84.8°N 40.1°E	12:15	20-60°	S, I
241 a	84.3°N 44.9°E	09:00	20-65°	S, R
241 b	84.3°N 45.2°E	14:00	35°	x
242	84.0°N 46.6°E	18:00	20-55°	S, R
243	83.7°N 47.1°E	13:00	20-65°	S
244 a	83.3°N 46.7°E	00:30	20-65°	x
244 b	83.0°N 48.2°E	15:30	20-65°	S
245 a	82.7°N 48.0°E	01:00	20-65°	x
245 b	82.3°N 49.2°E	11:00	15-65°	S, R
S=snow properties; I=ice properties; R=surface roughness profiles; x=none				

Table A-2. In situ snow measurements

Station (Julian Date)	Depth (cm)	Density (Mg/m ³)	Wetness (% by vol)	Grain Size (mm)	Permittiv ity
231	0.5	0.265	1.8	1-5	1.84
236	1.0	0.229	1.3	5	1.47
239	1.0	0.249	0.9	5-10	1.55
241 a	4.5	0.267	x	1-3	1.30
242	3	0.263	x	1-5	1.37
243	12	0.181	0.15	1-5	1.29
244 b	10	0.163	0.2	1-3	1.31
245 b	4	0.218	0.3	1-2	1.40
x = wetness was measured to be 0 %					

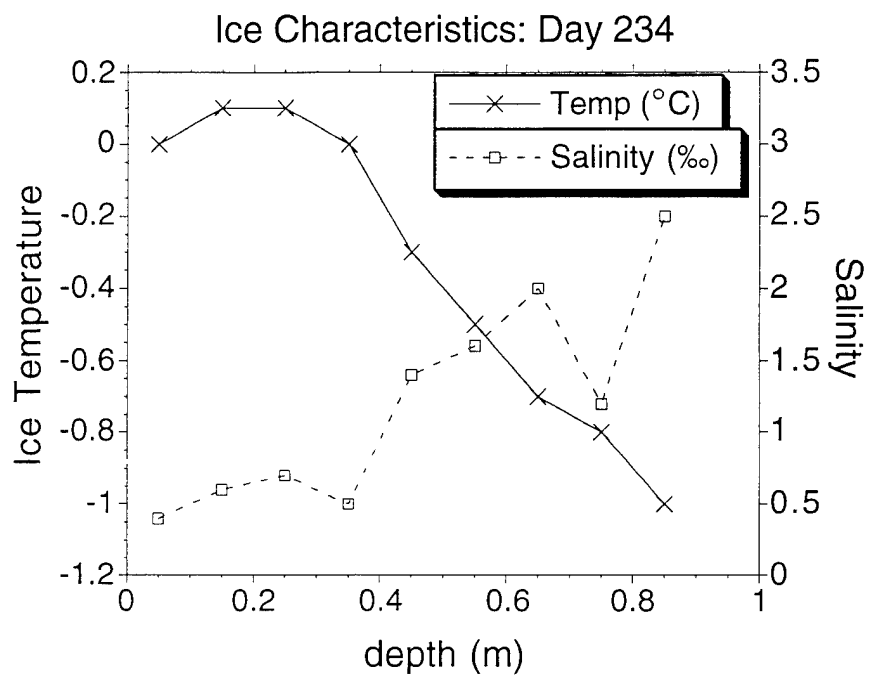


Figure A.1 Sea ice salinity and temperature profiles, taken coincidentally with the second-year sea ice station data of day 234, 1991.

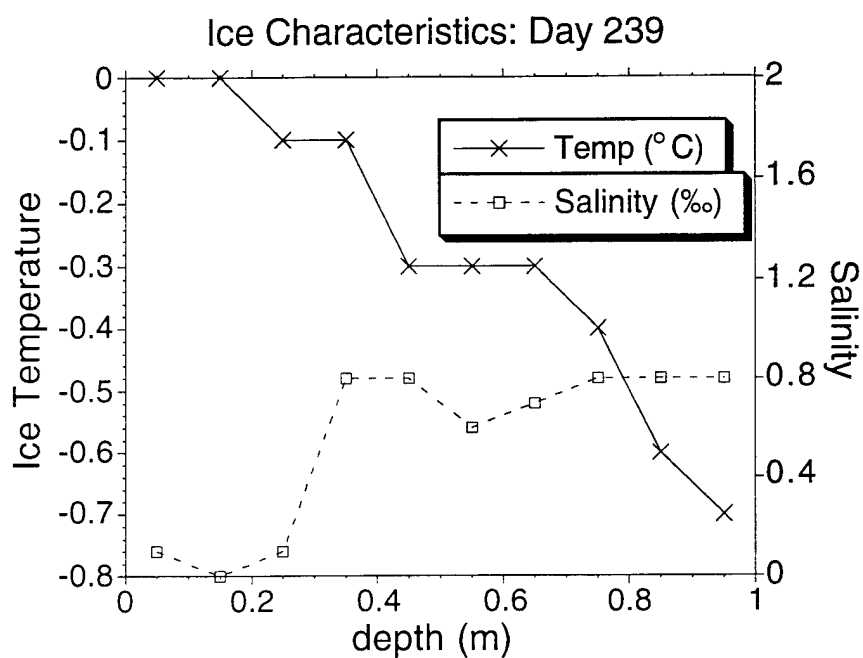


Figure A.2 Sea ice salinity and temperature profiles, taken coincidentally with the multiyear sea ice station data of day 239, 1991.

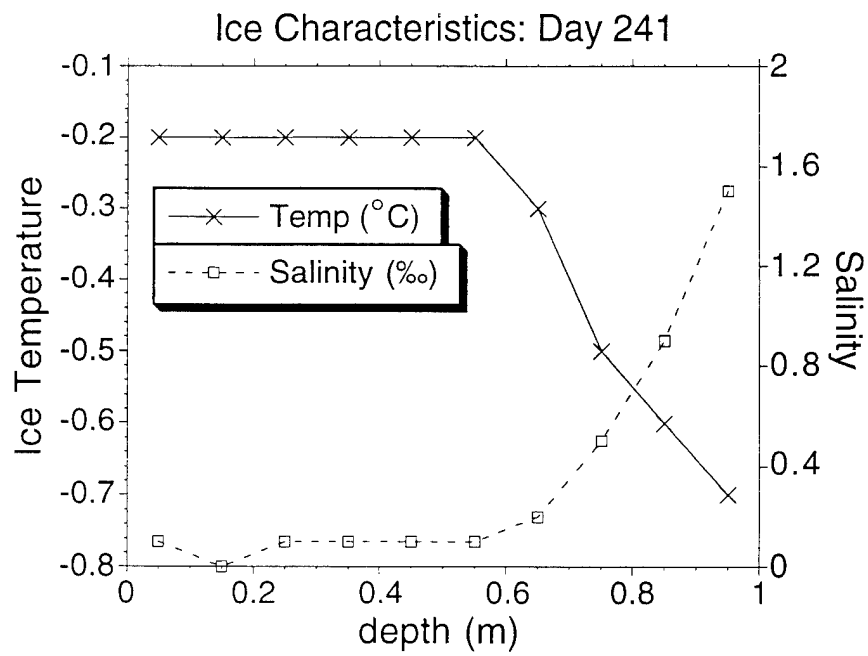


Figure A.3 Sea ice salinity and temperature profiles, taken coincidentally with the multiyear sea ice station data of day 241, 1991.

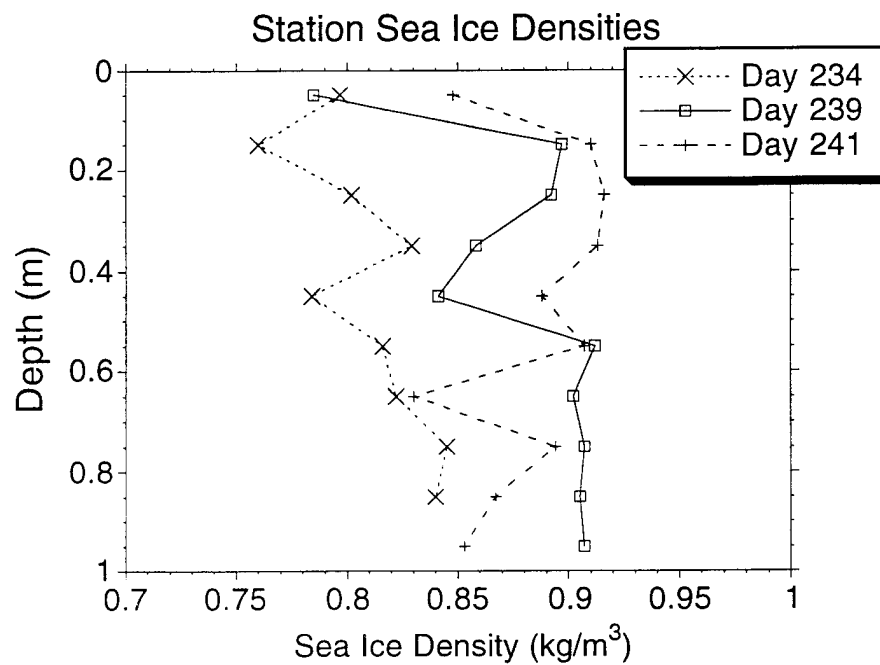


Figure A.4 Sea ice density profiles for the three sea ice stations in which both ice information and backscatter measurements were performed.

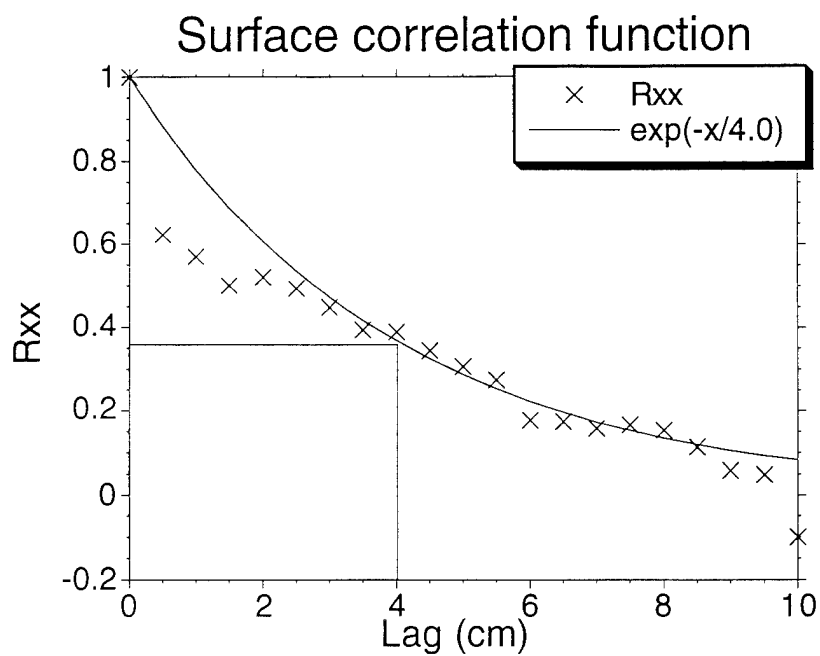


Figure A.5 Surface roughness autocorrelation sequence, computed from surface profile measurements from day 242. The correlation length was determined to be 4.0 cm. The rms surface height from this measurement is 4.2 mm.

APPENDIX B

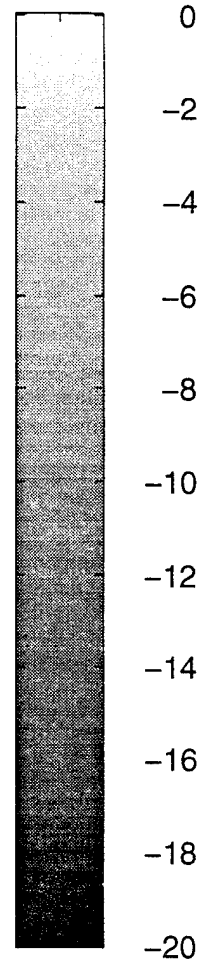
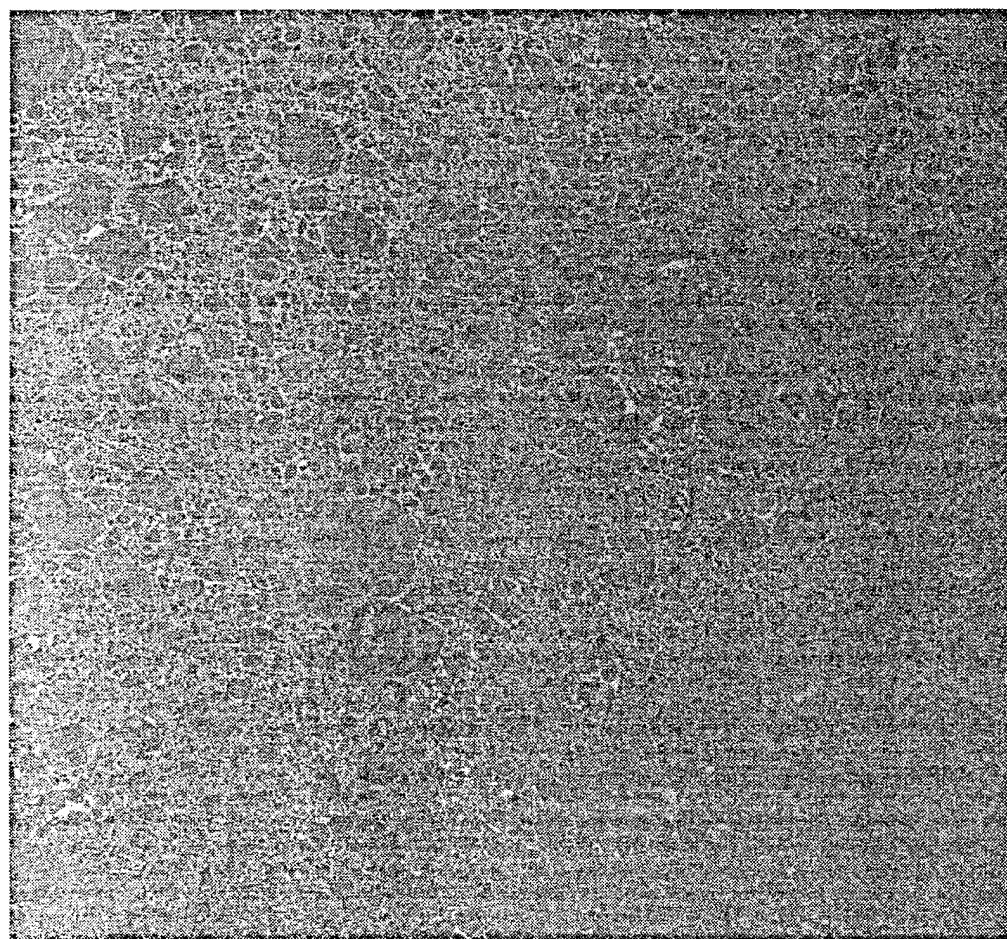
ERS-1 SAR Images and Information

- All ERS-1 SAR σ^0 images used in this study
- Ancillary information for ERS-1 SAR frames: image locations, times, identification numbers

Table B-1 ERS-1 SAR frame information					
Image date (1991)	Local time	Orbit #	Frame #	Center Latitude	Center Longitude
21 Aug	12:55	508	1827	84.01	39.38
23 Aug	11:49	536	1863	83.36	49.97
25 Aug	14:02	566	1791	84.18	39.72
26 Aug	13:29	580	1809	84.16	39.65
27 Aug	16:15	596	1701	82.48	43.40
28 Aug	14:02	609	1791	84.18	40.14
29 Aug	13:28	623	1791	84.18	48.51
29 Aug	13:29	623	1809	84.16	39.66
29 Aug	15:09	624	1755	83.82	40.35
30 Aug	16:15	639	1701	82.49	43.41
3 Sept	15:42	696	1719	83.01	46.05
6 Sept	12:22	737	1827	84.01	47.78
6 Sept	15:42	739	1719	83.01	46.04
7 Sept	13:29	752	1809	84.16	39.65
8 Sept	16:15	768	1701	82.48	43.41
12 Sept	15:42	825	1719	82.98	46.46
14 Sept		854	1701	82.48	43.45
22 Sept		968	1737	83.47	47.81

21 August Frame 1827

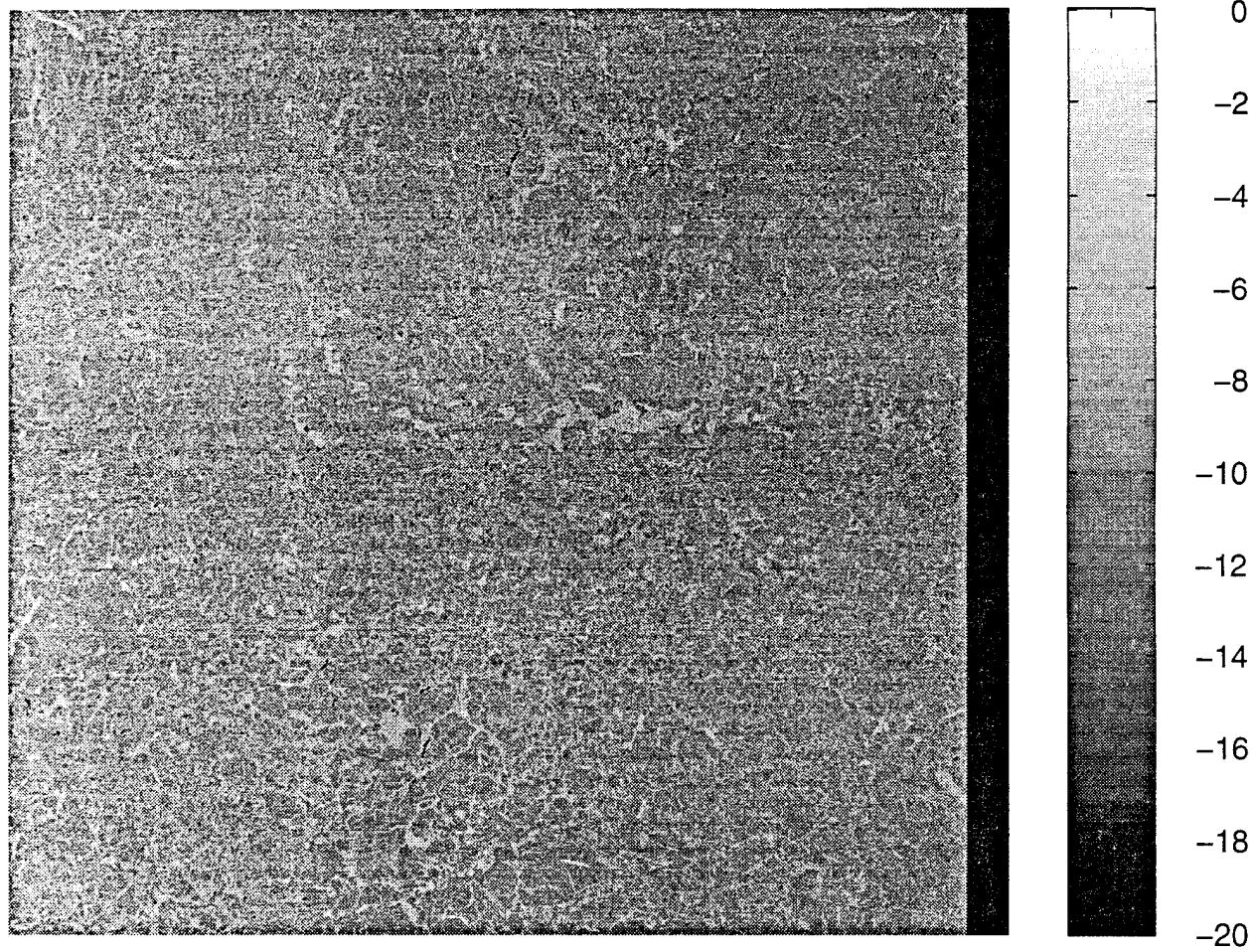
sigma nought



Copyright ESA, 1991

23 August Frame 1863

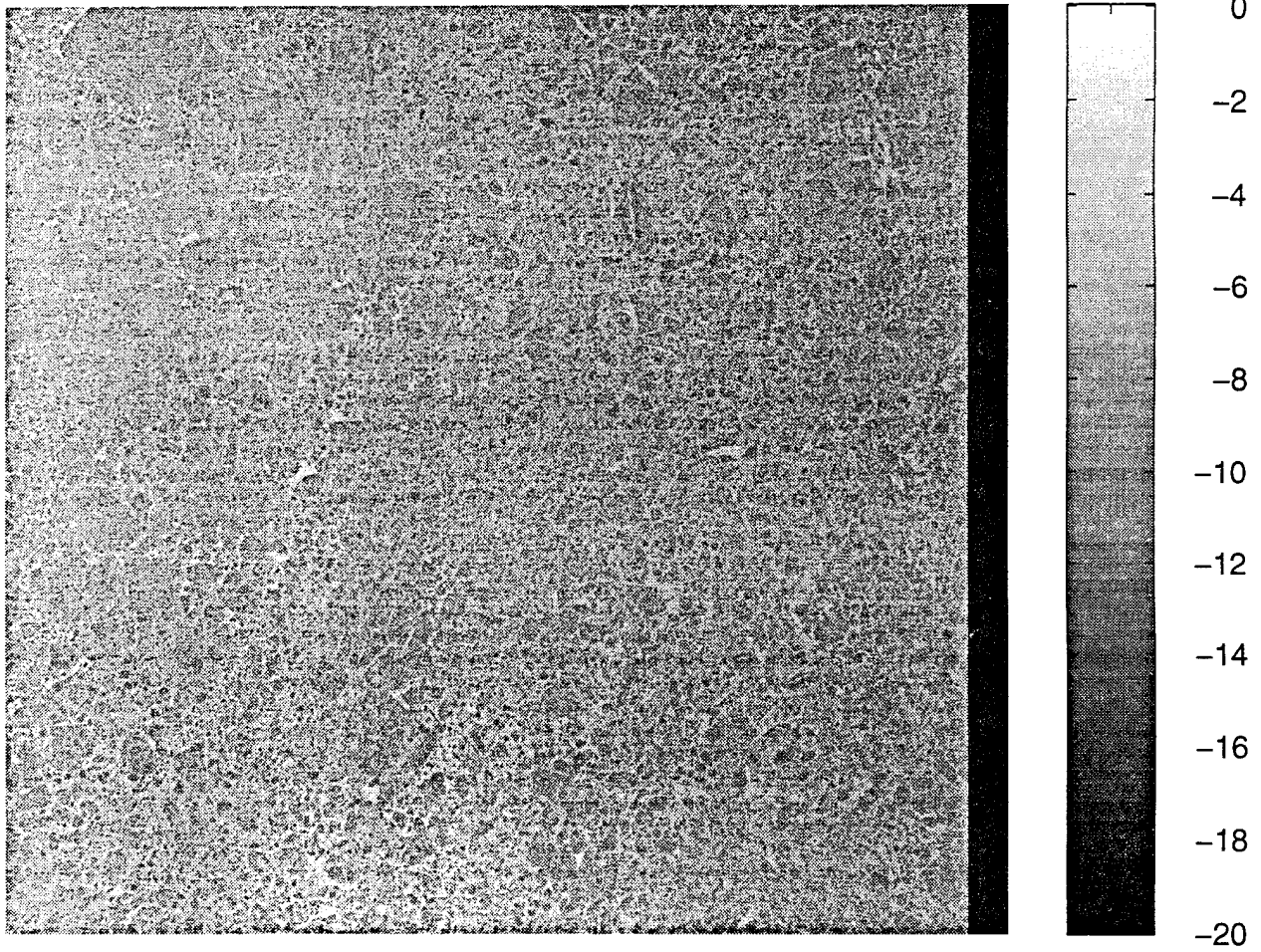
sigma nought (dB)



Copyright ESA, 1991

25 August Frame 1791

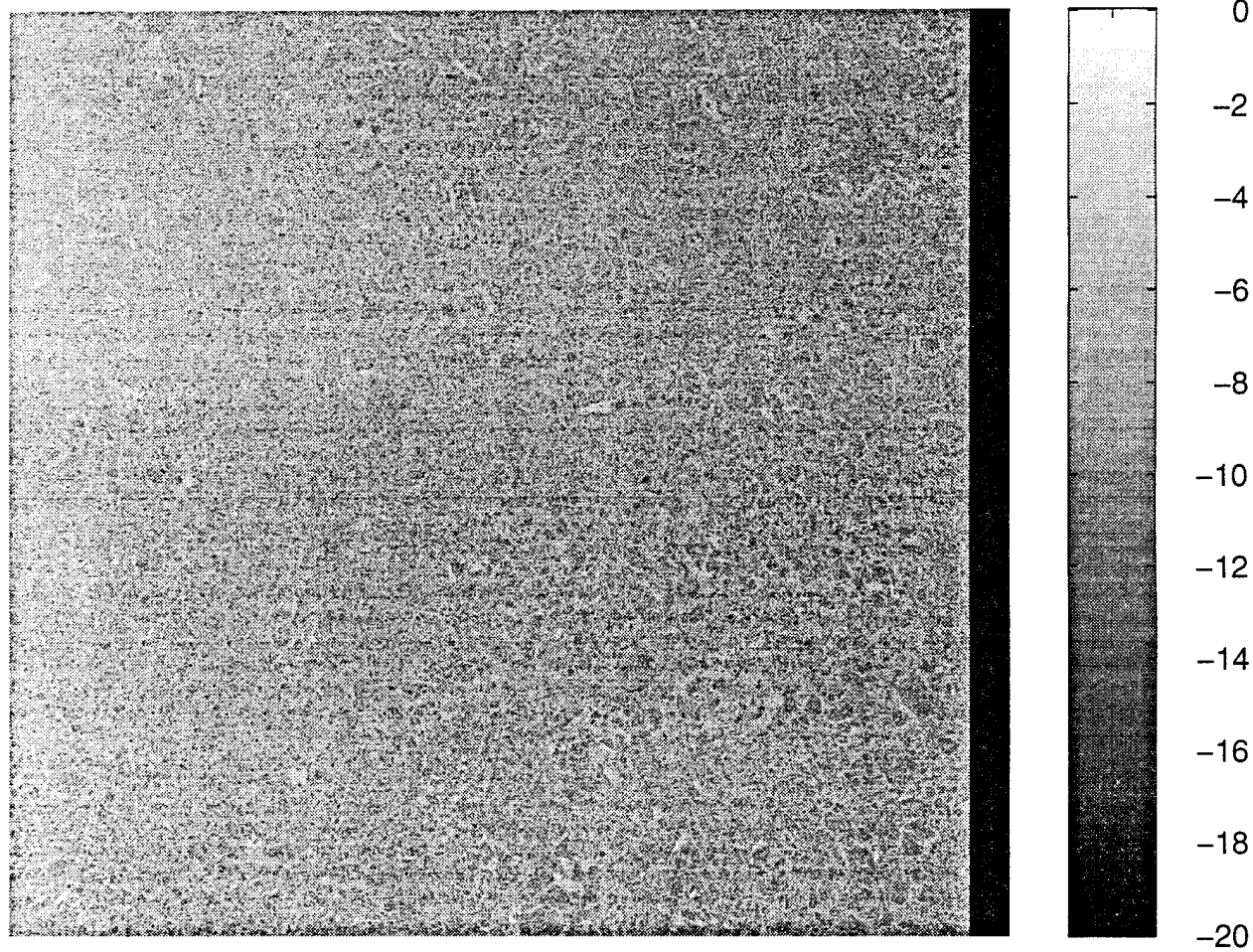
sigma nought (dB)



Copyright ESA, 1991

26 August Frame 1809

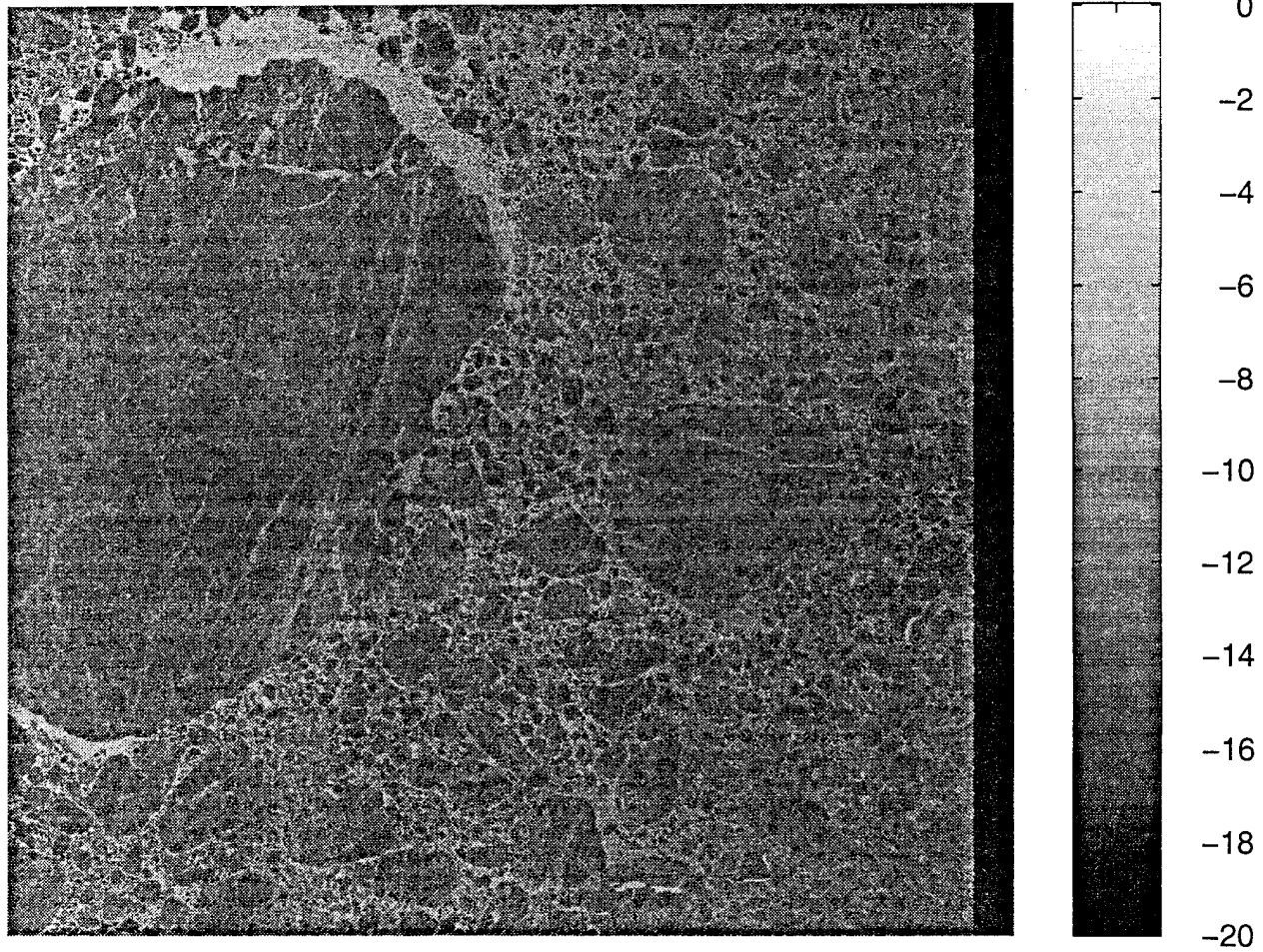
sigma nought (dB)



Copyright ESA, 1991

27 August Frame 1701

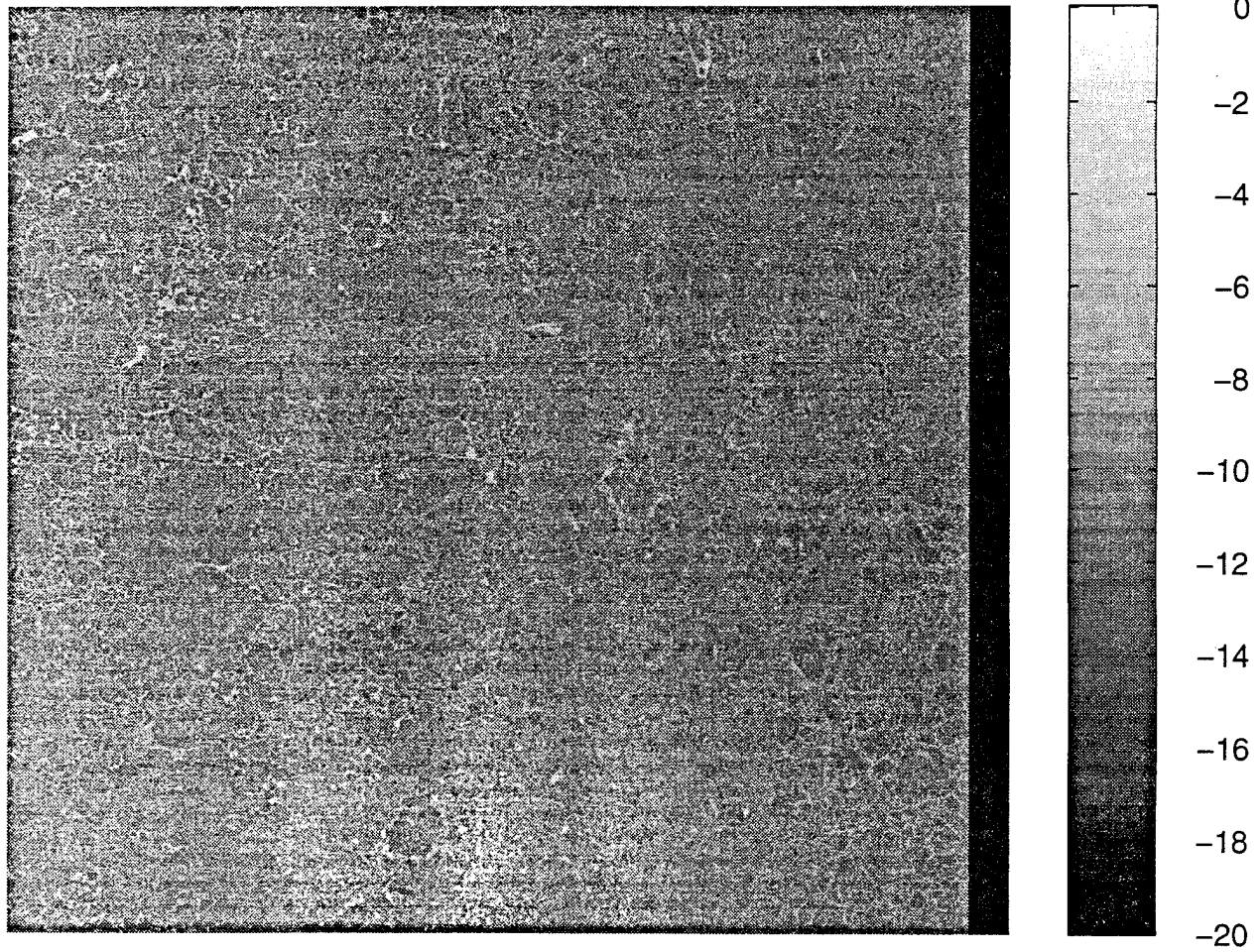
sigma nought (dB)



Copyright ESA, 1991

28 August Frame 1791

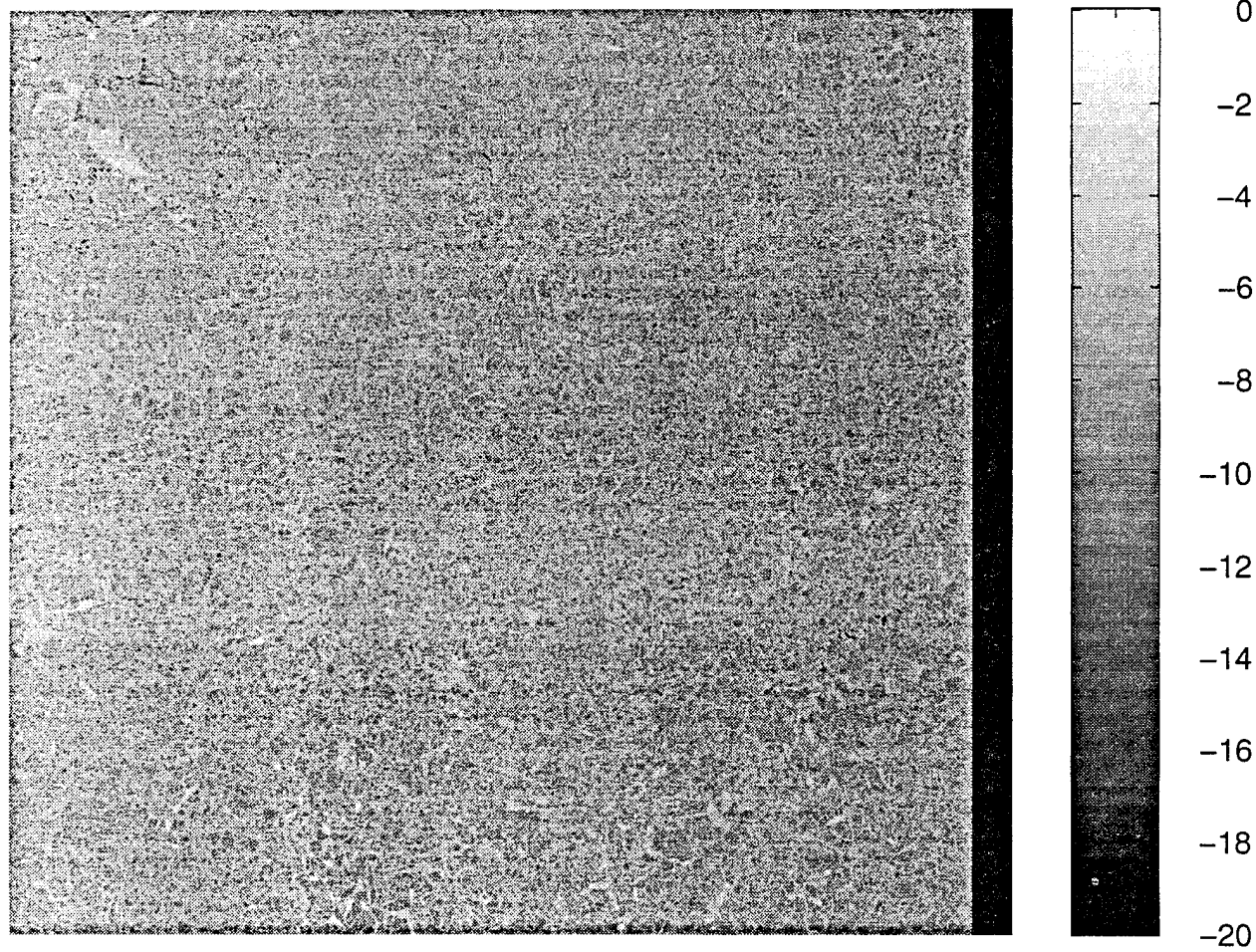
sigma nought (dB)



Copyright ESA, 1991

29 August Frame 1755

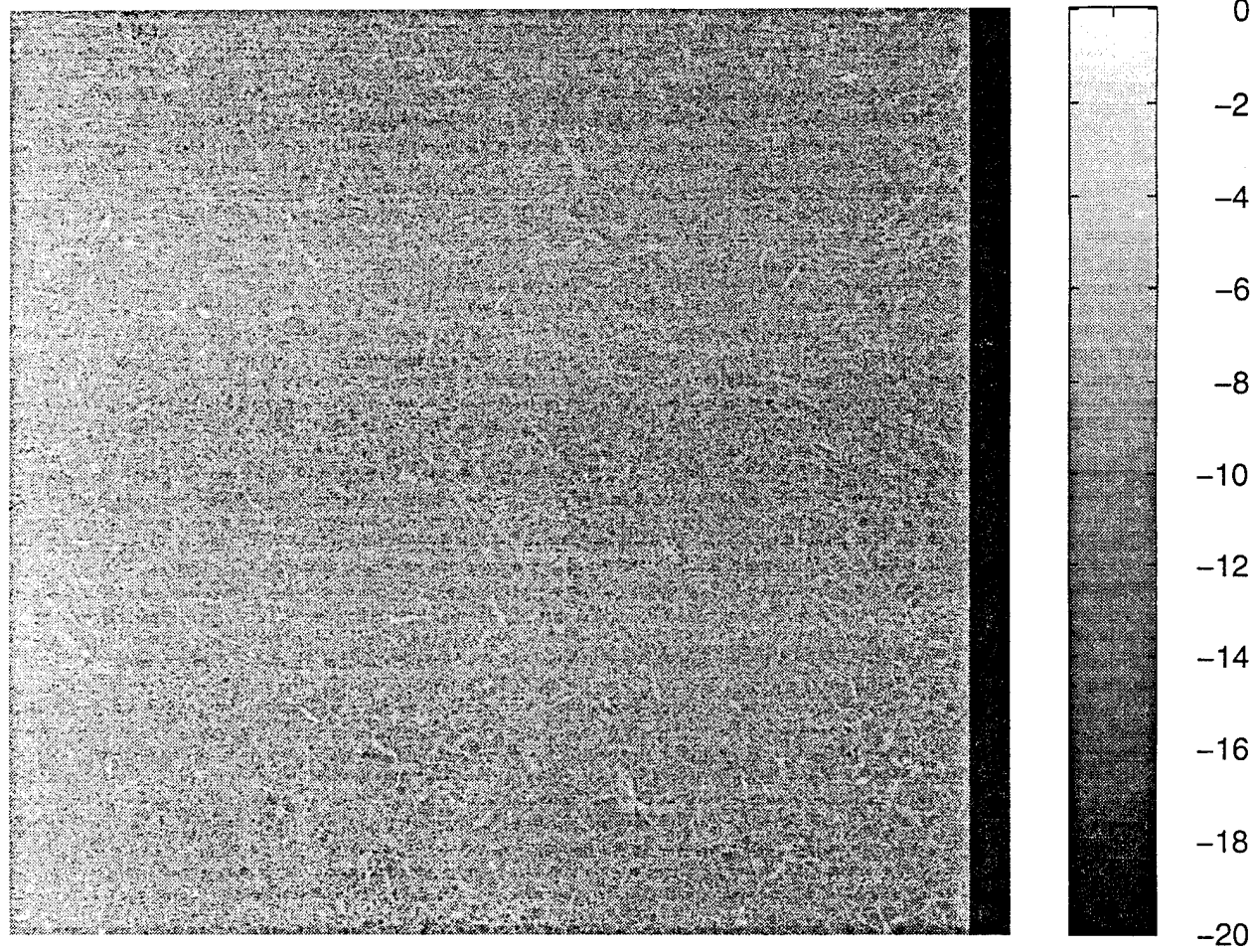
sigma nought (dB)



Copyright ESA, 1991

29 August Frame 1791

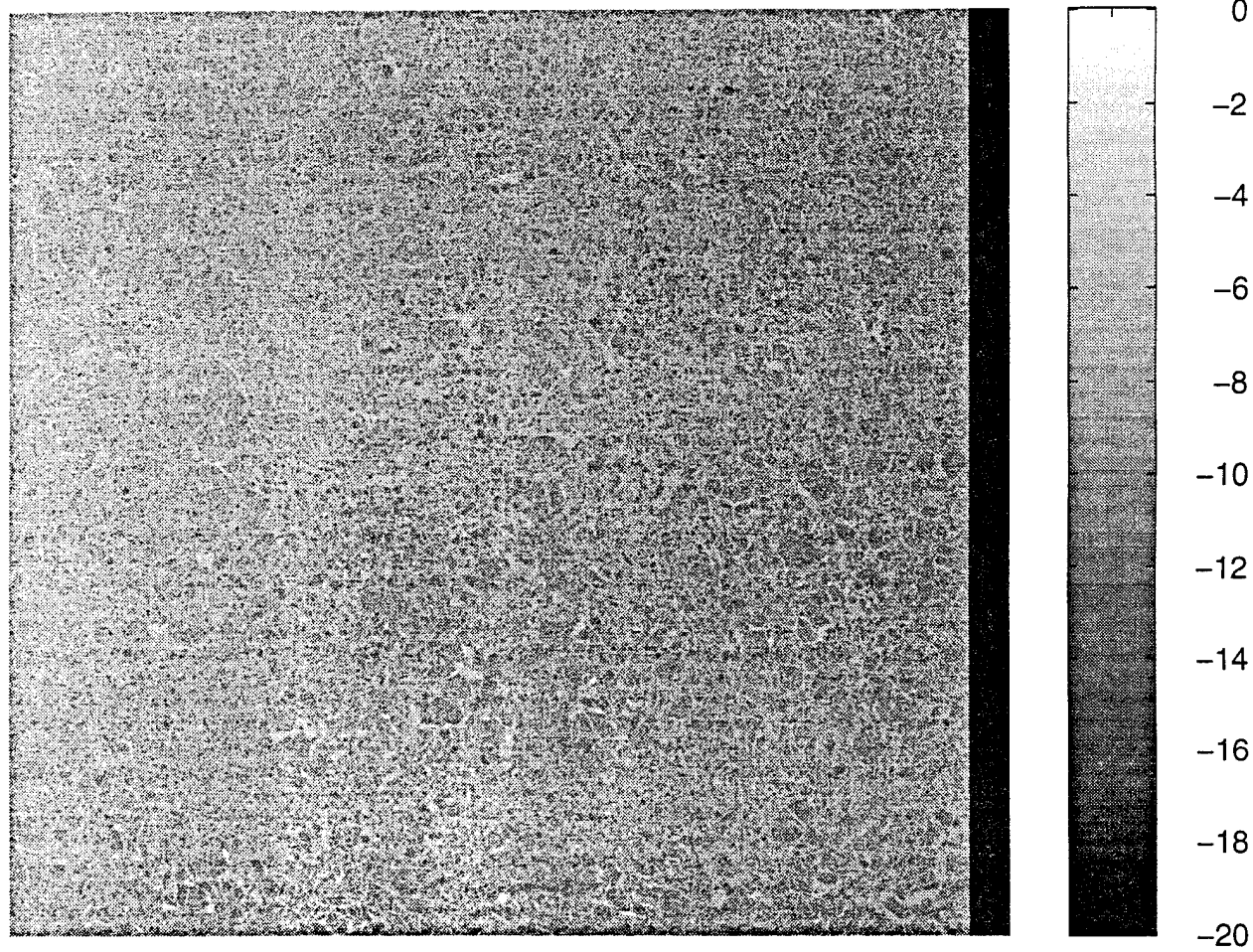
sigma nought (dB)



Copyright ESA, 1991

29 August Frame 1809

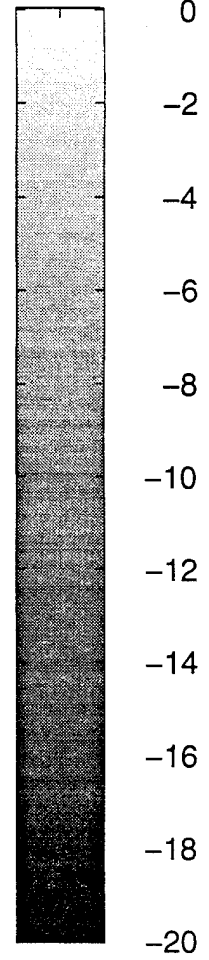
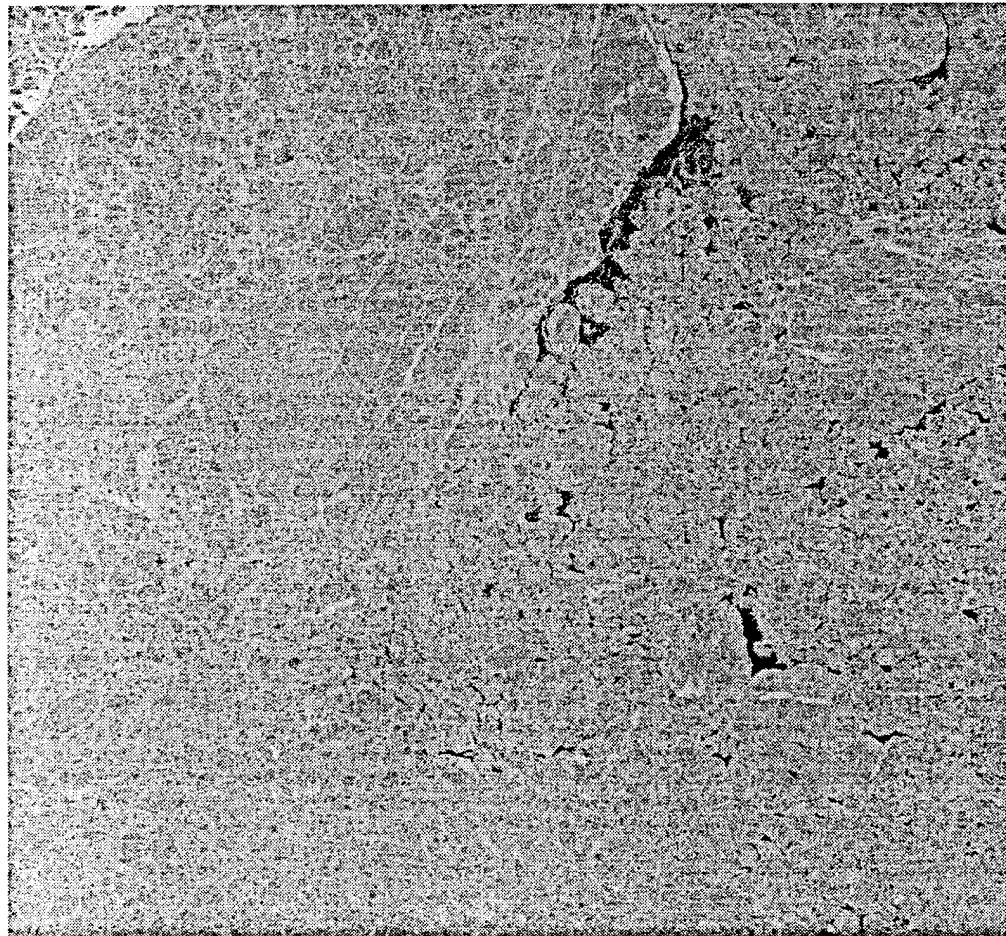
sigma nought (dB)



Copyright ESA, 1991

30 August Frame 1701

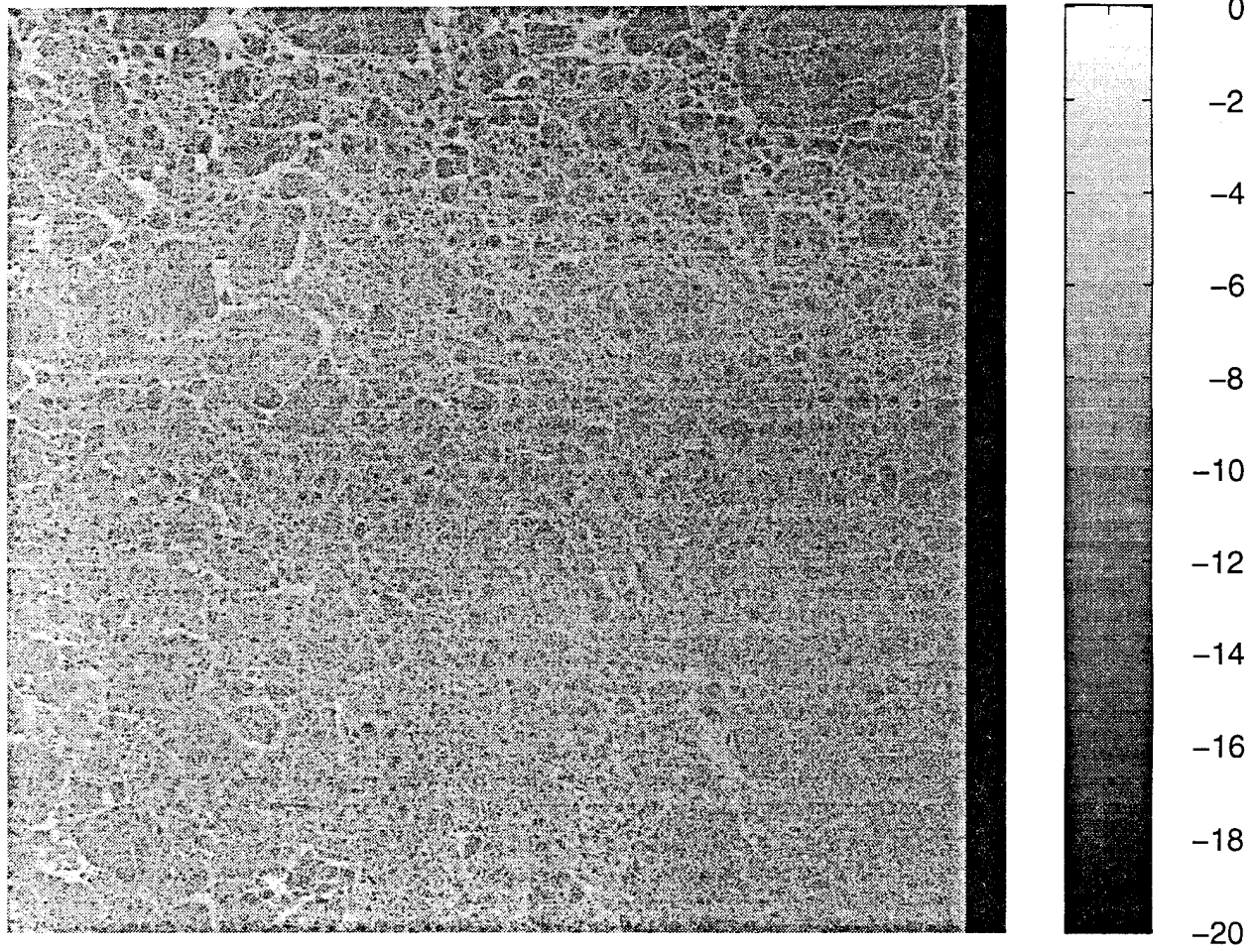
sigma nought (dB)



Copyright ESA, 1991

3 September Frame 1719

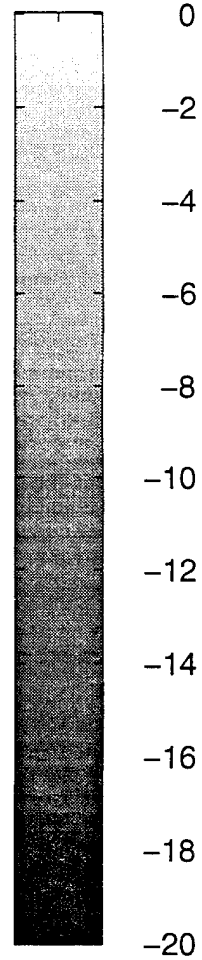
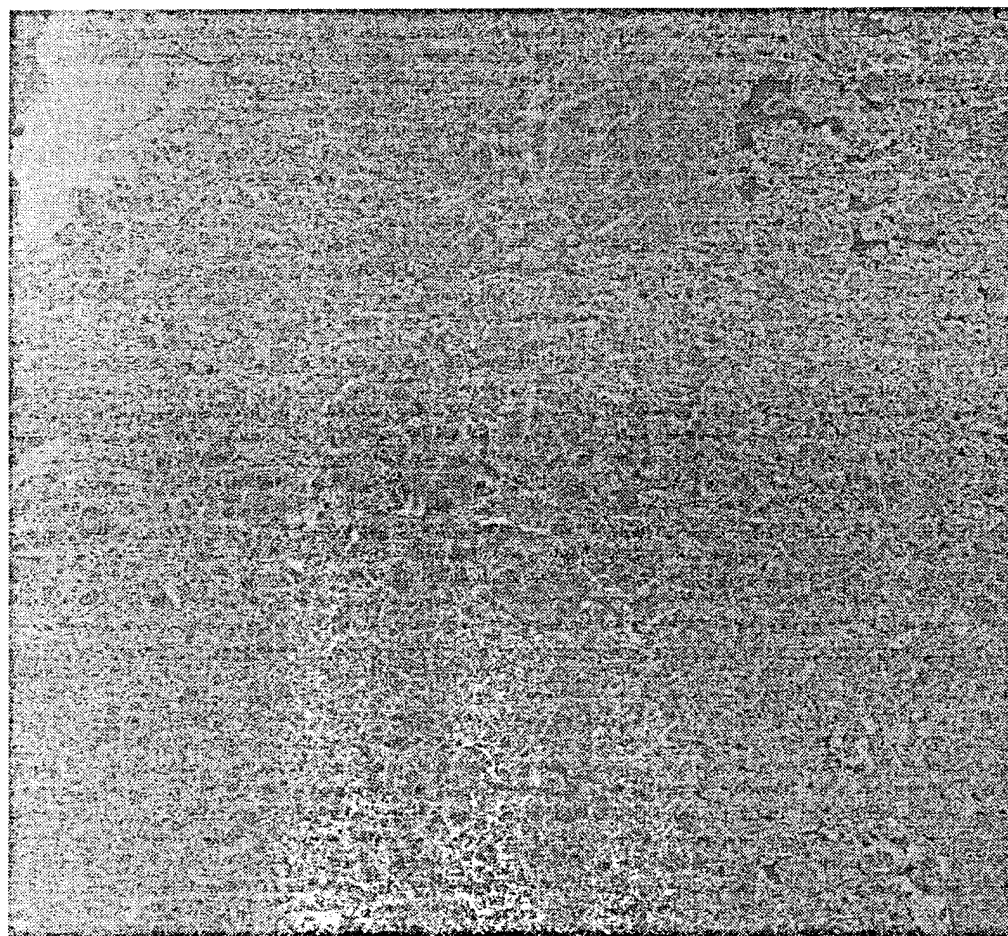
sigma nought (dB)



Copyright ESA, 1991

6 September Frame 1719

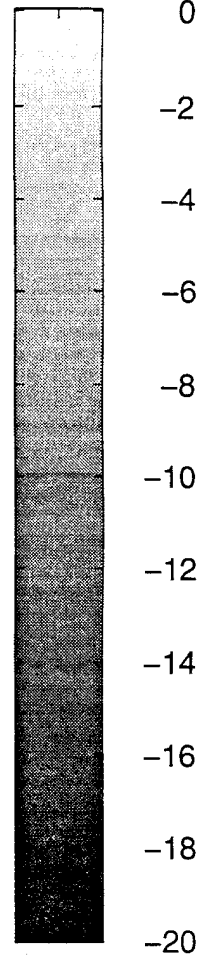
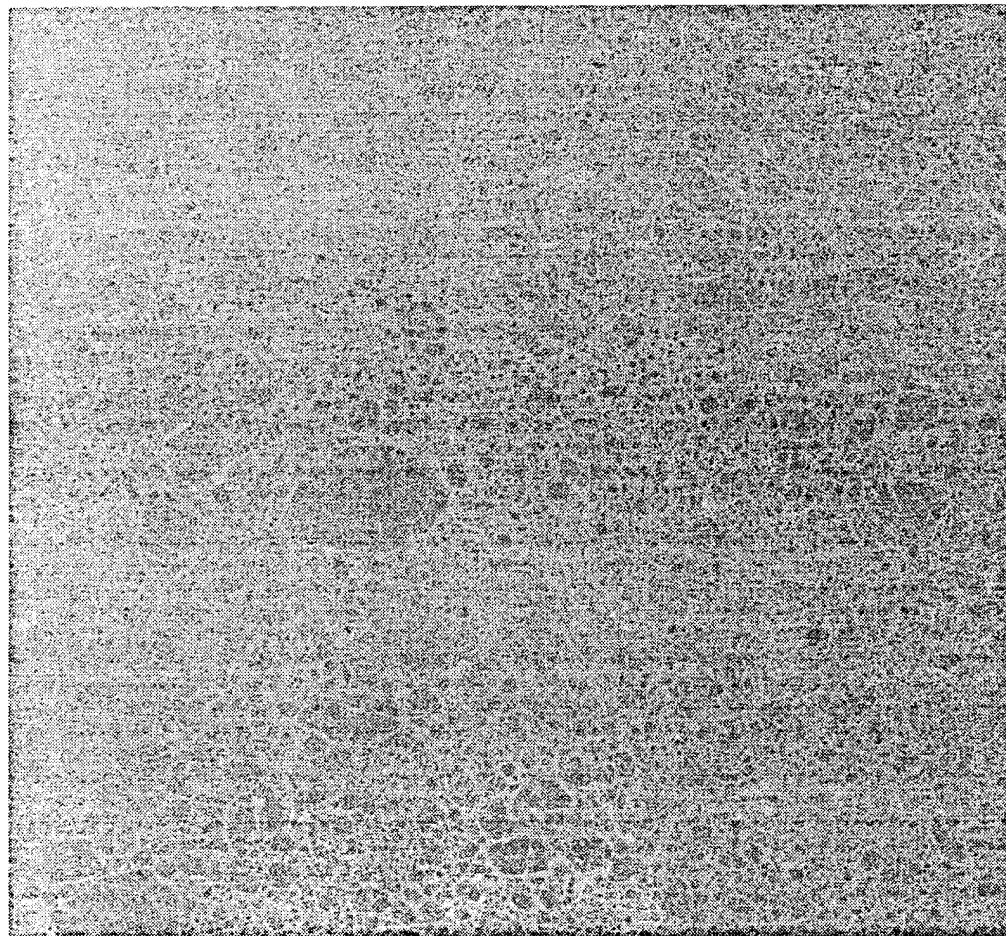
sigma nought (dB)



Copyright ESA, 1991

6 September Frame 1827

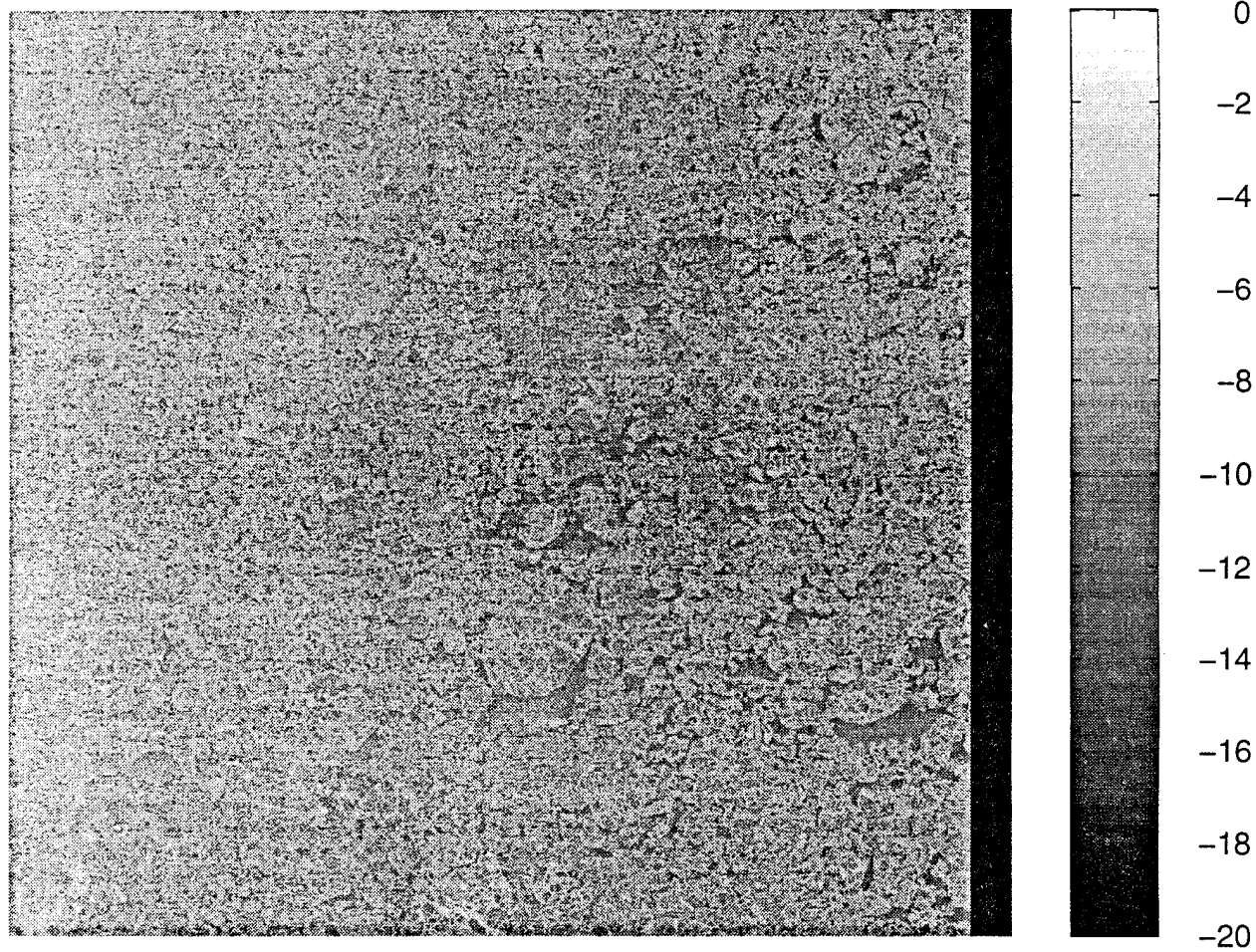
sigma nought (dB)



Copyright ESA, 1991

7 September Frame 1809

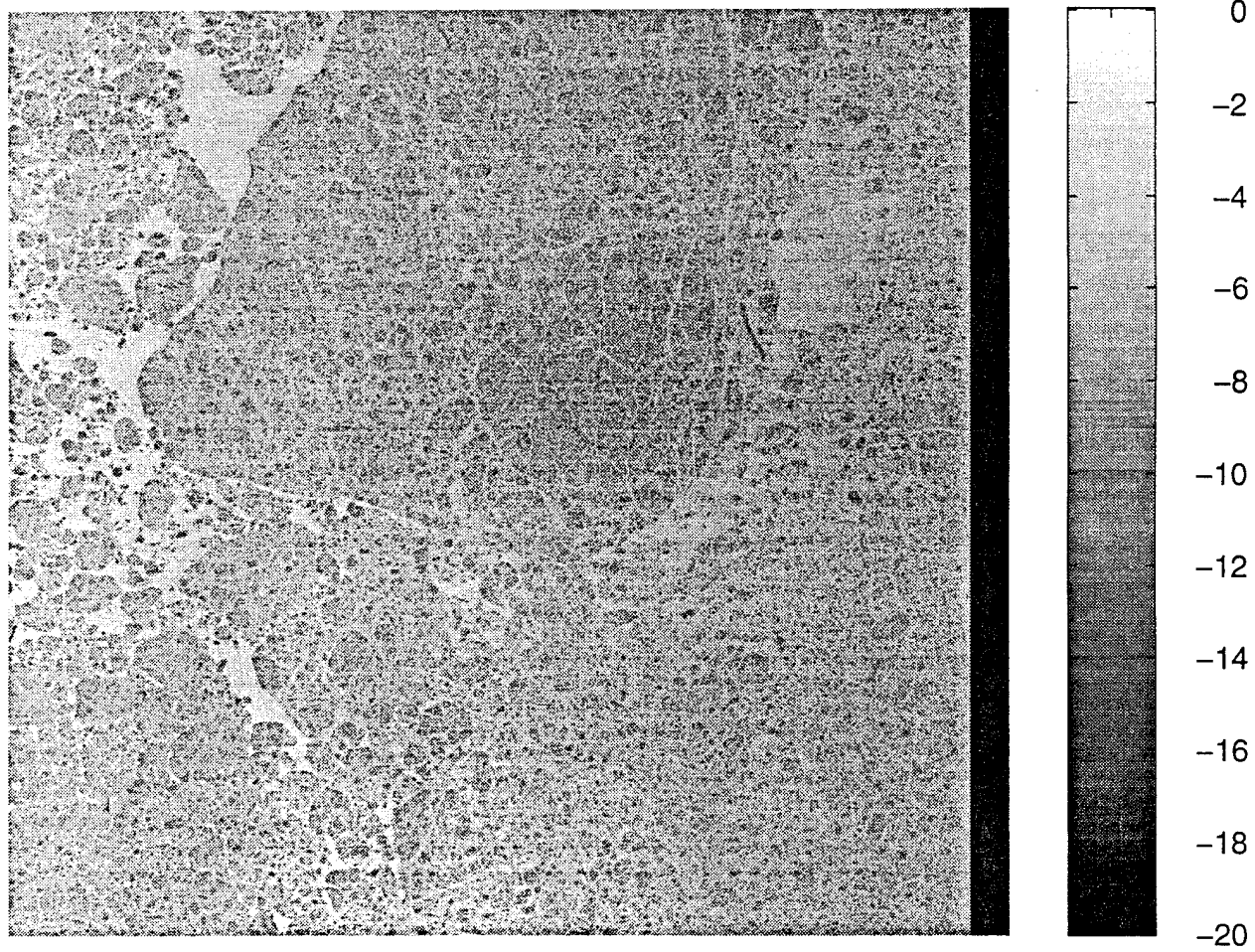
sigma nought (dB)



Copyright ESA, 1991

8 September Frame 1701

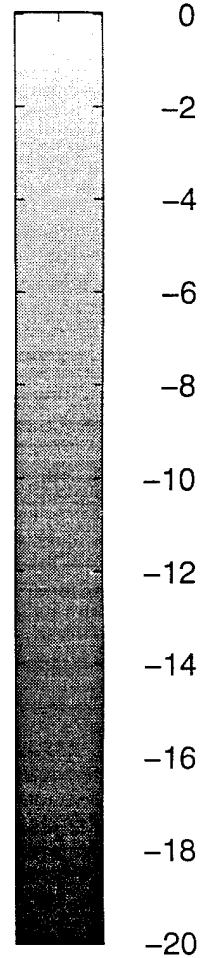
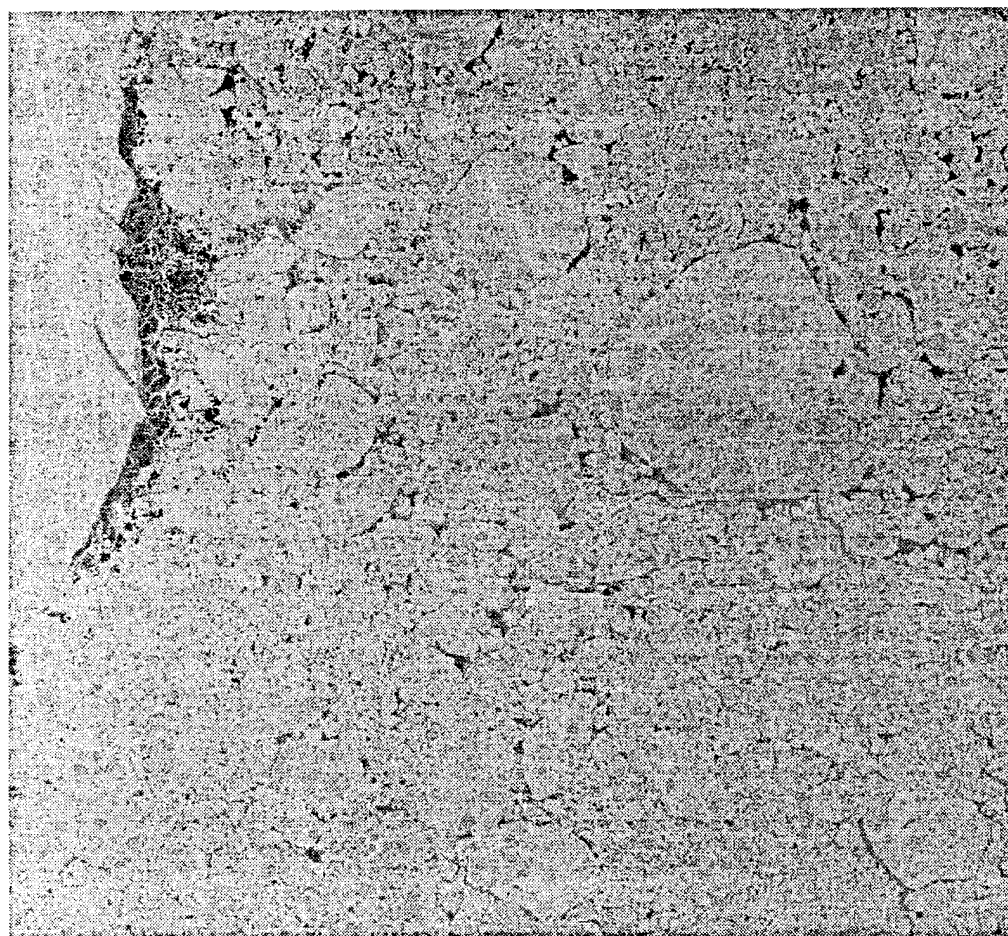
sigma nought (dB)



Copyright ESA, 1991

12 September Frame 1719

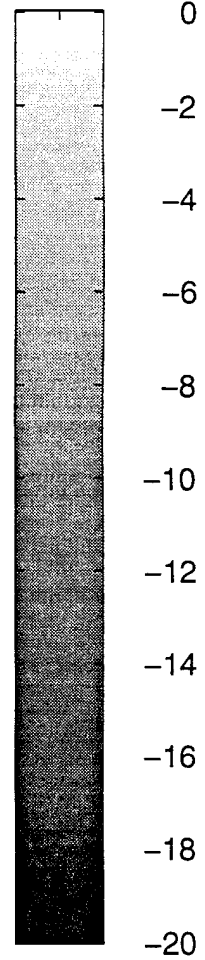
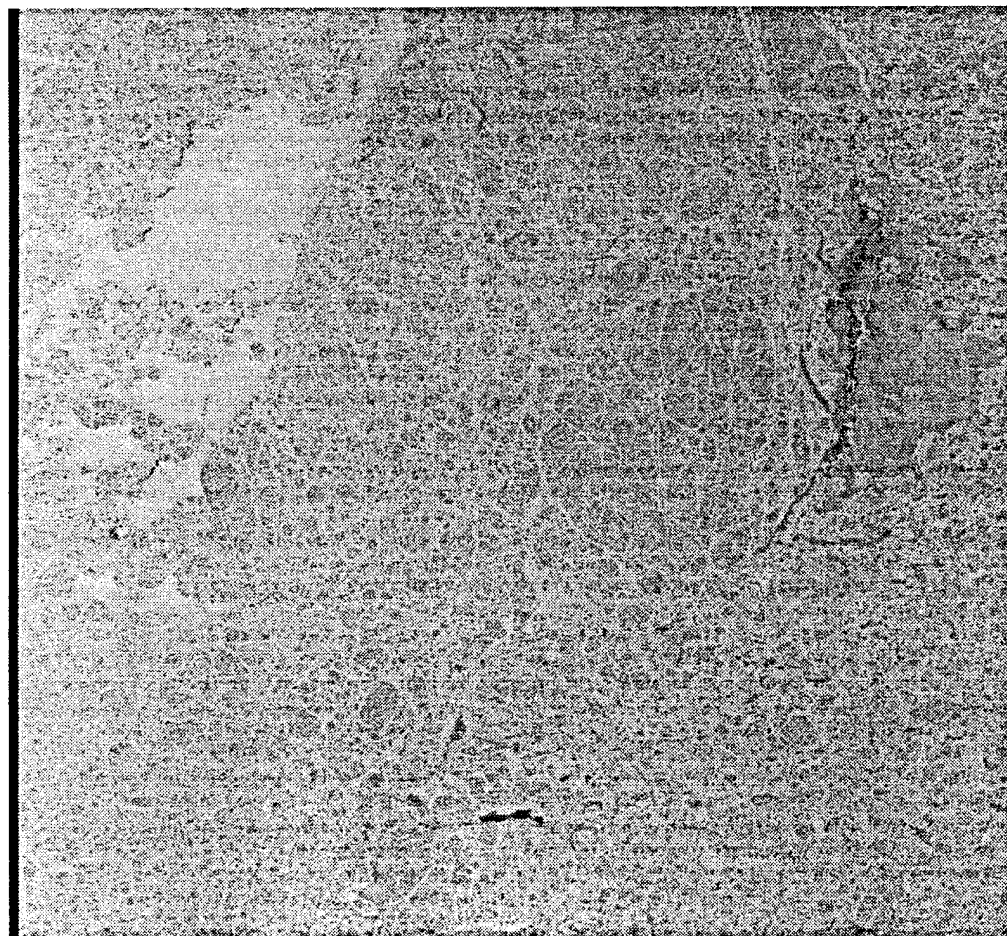
sigma nought (dB)



Copyright ESA, 1991

14 September Frame 1701

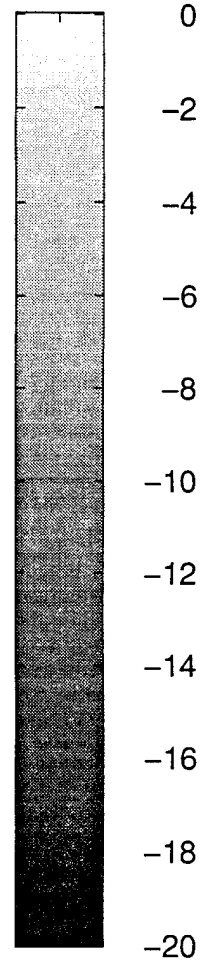
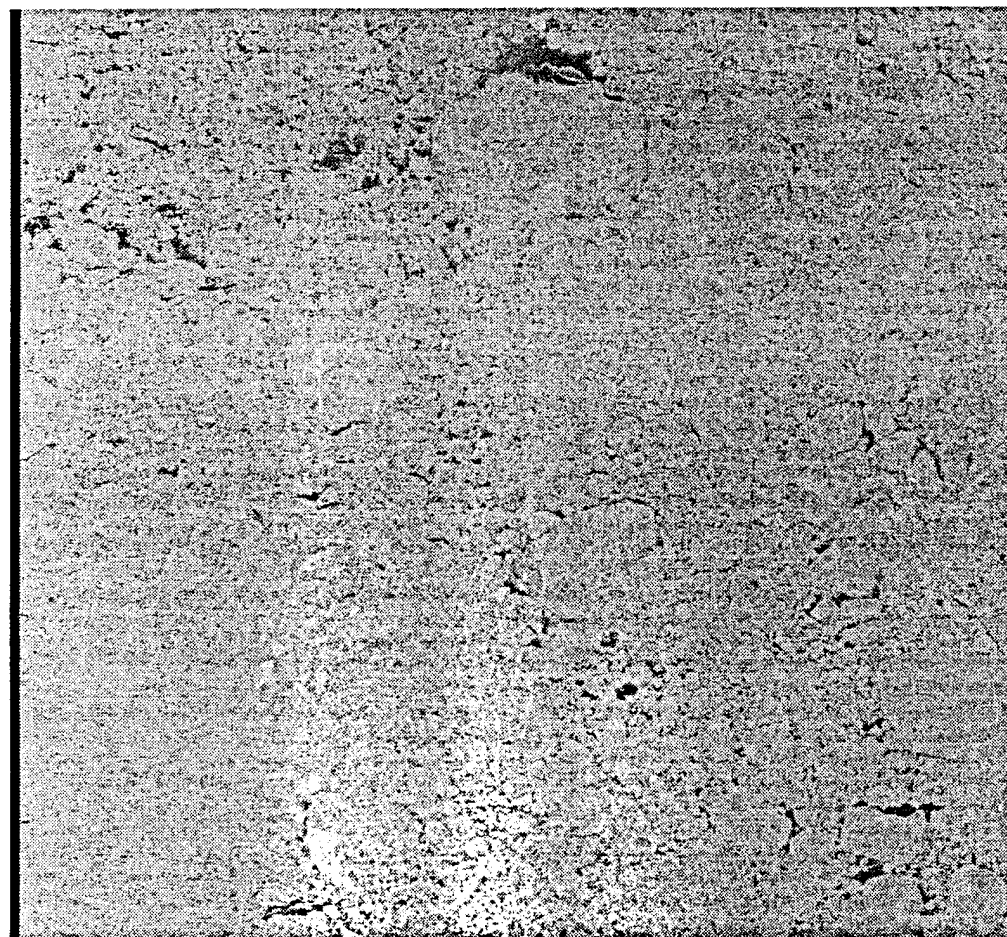
sigma nought (dB)



Copyright ESA, 1991

22 September Frame 1737

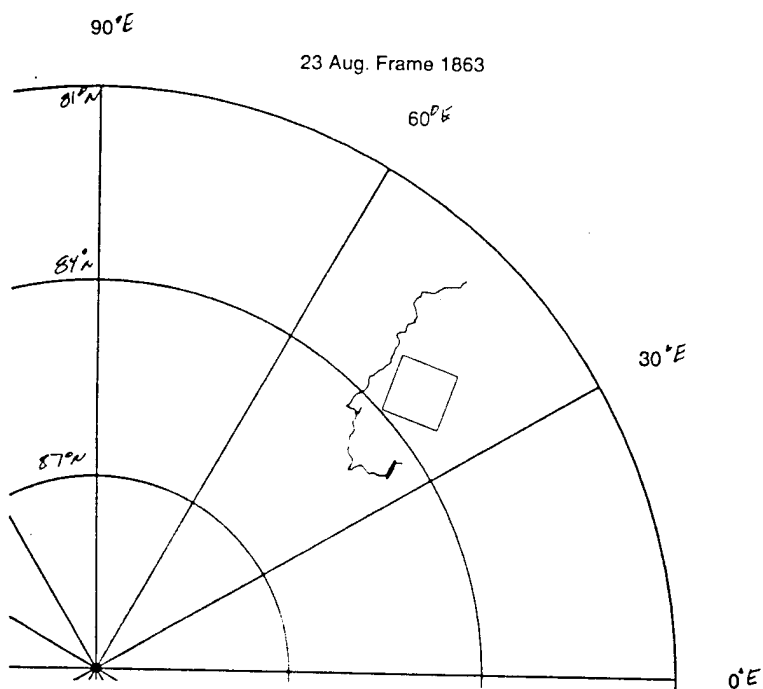
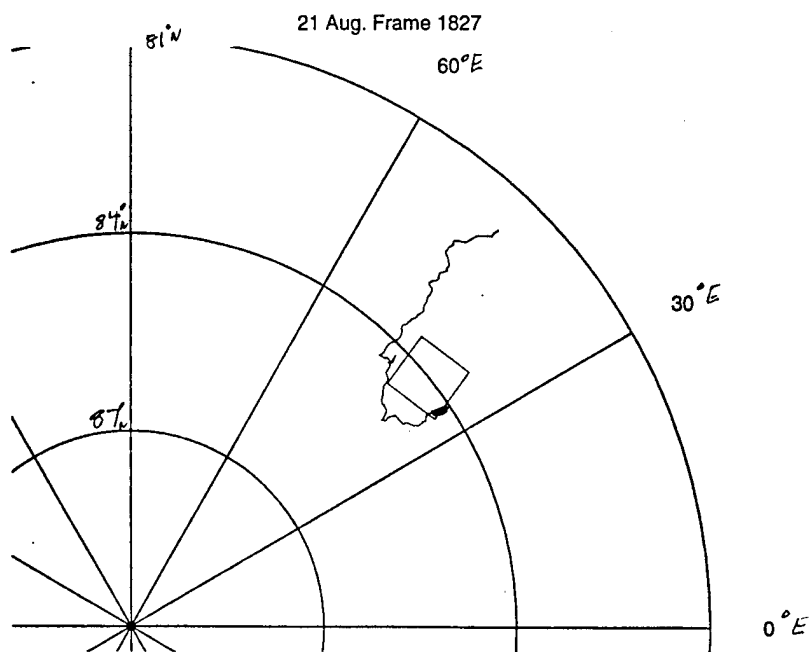
sigma nought (dB)

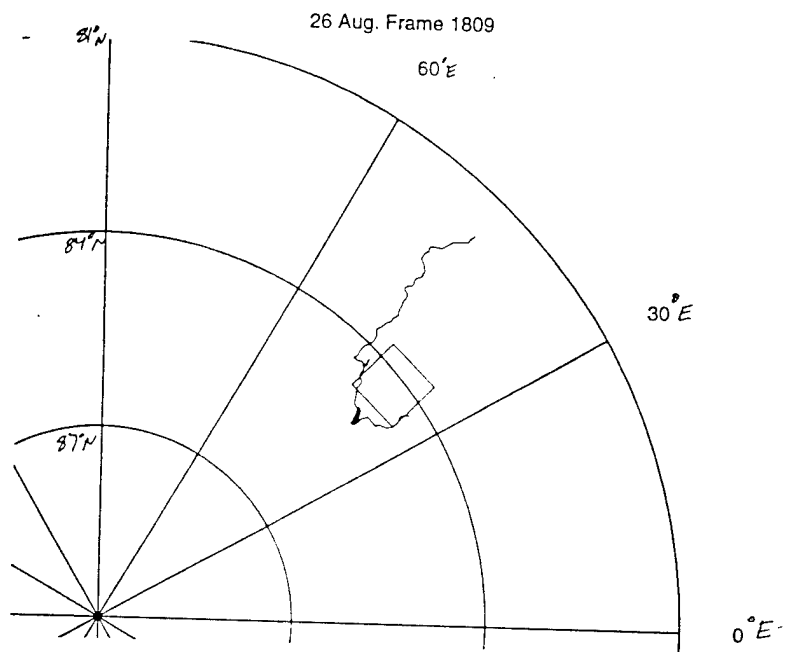
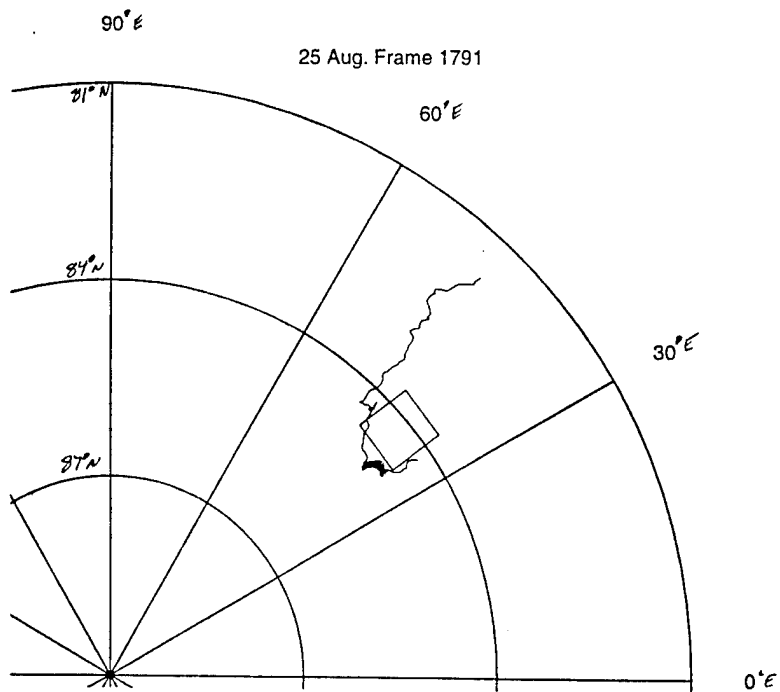


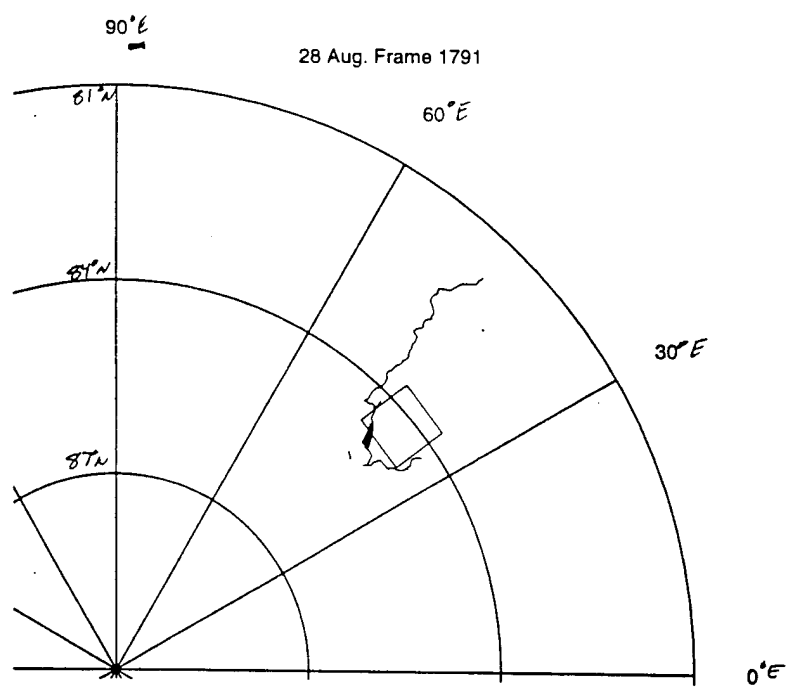
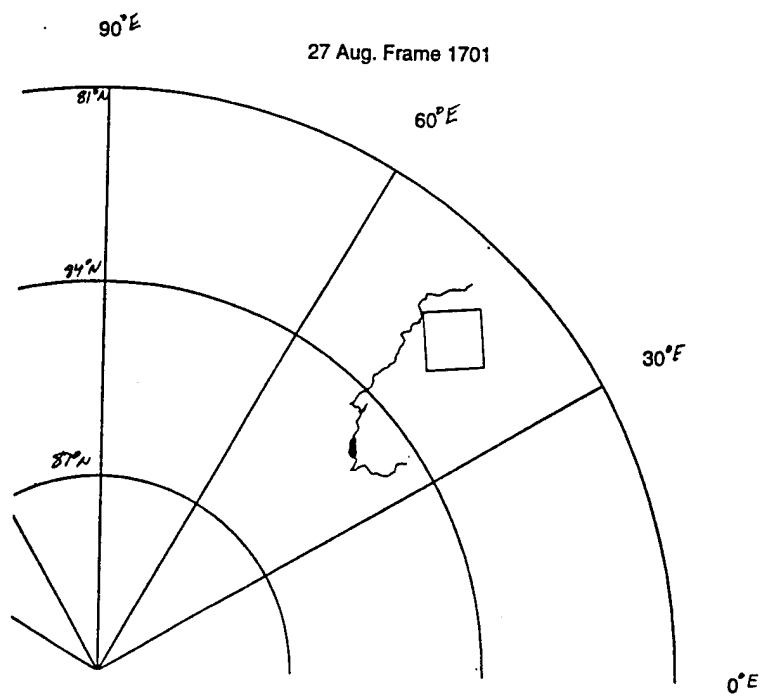
Copyright ESA, 1991

APPENDIX C

ERS-1 SAR Frame Locations mapped to IAOE cruise track

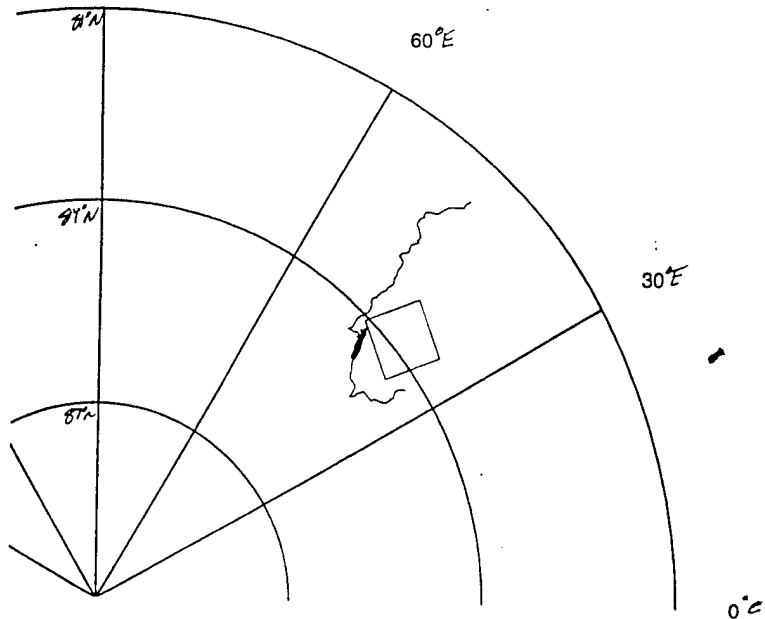






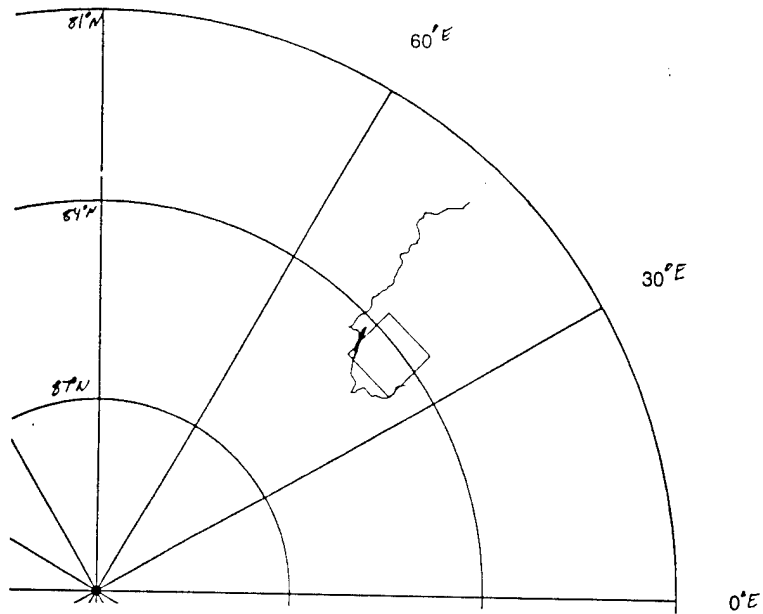
90°E

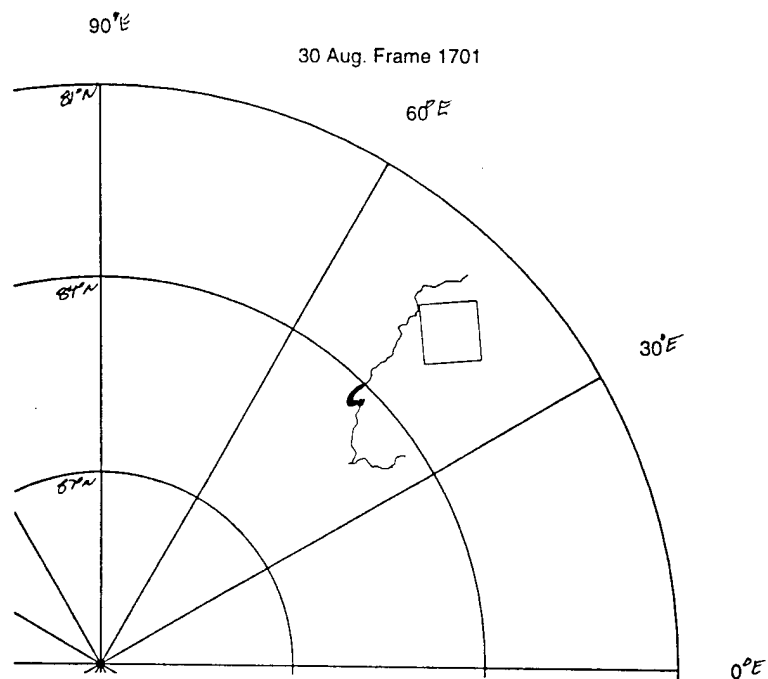
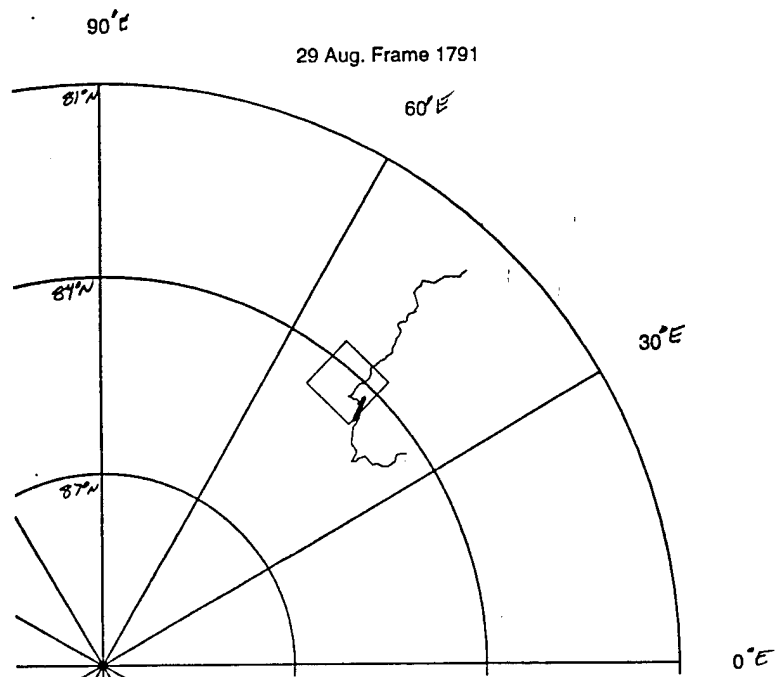
29 Aug. Frame 1755

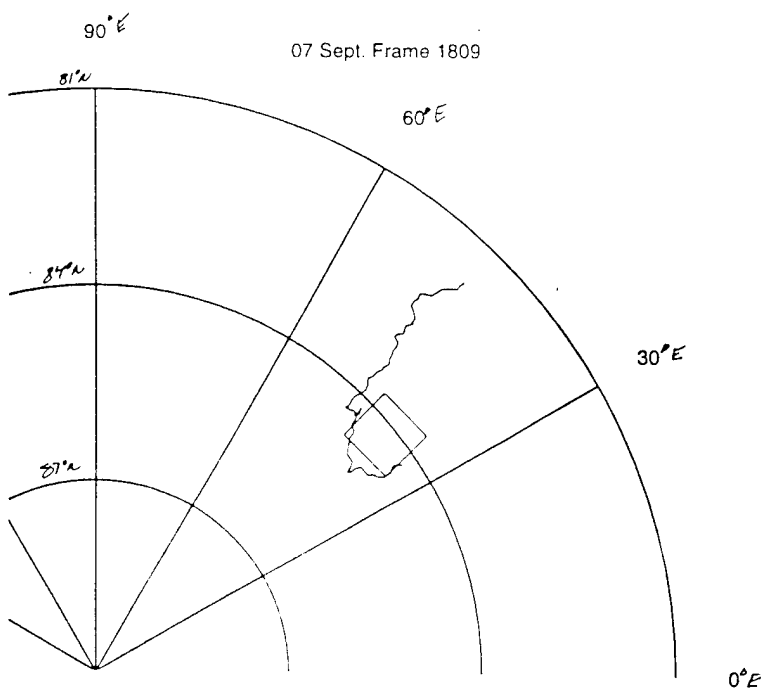
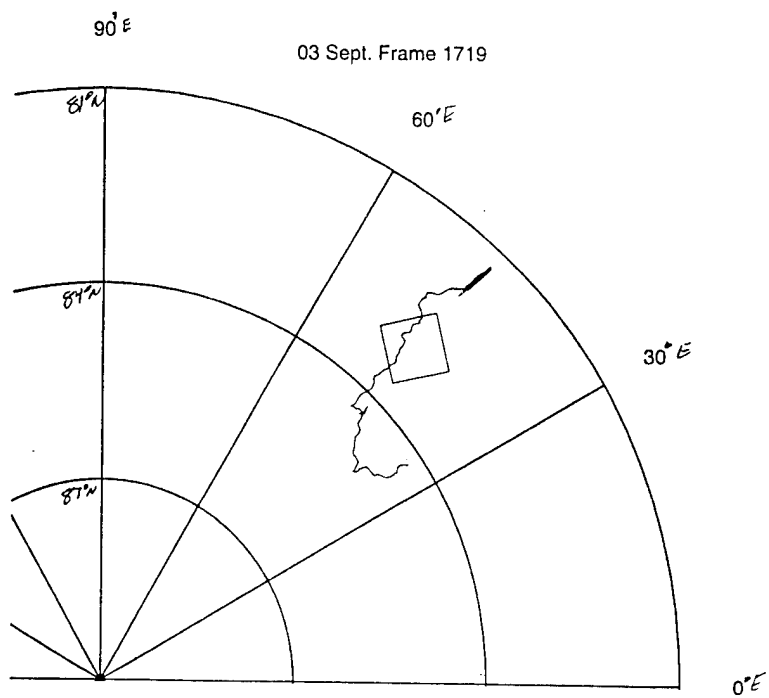


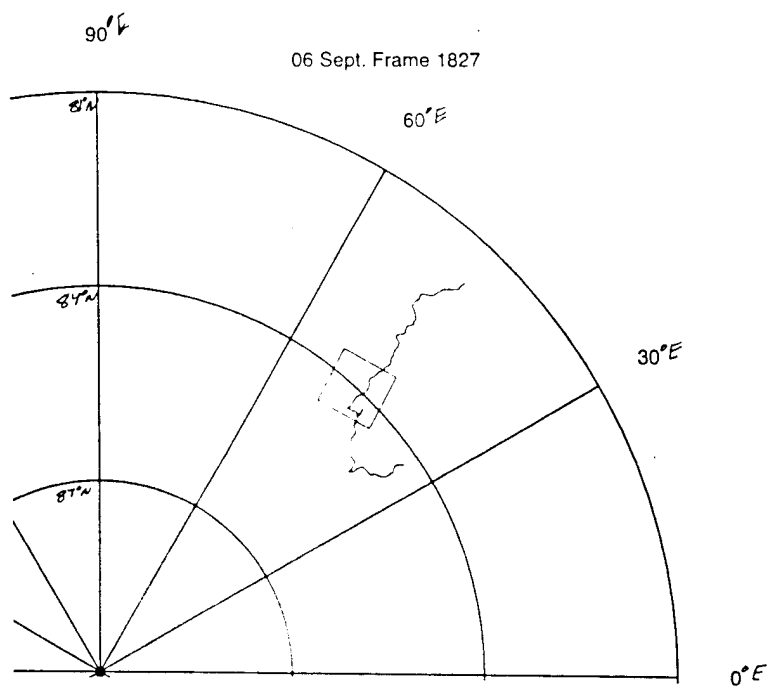
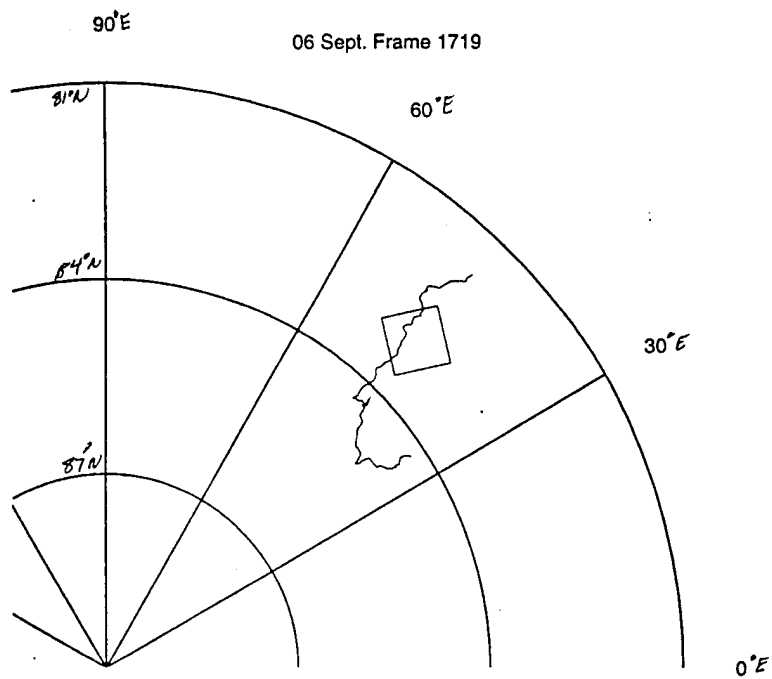
90°E

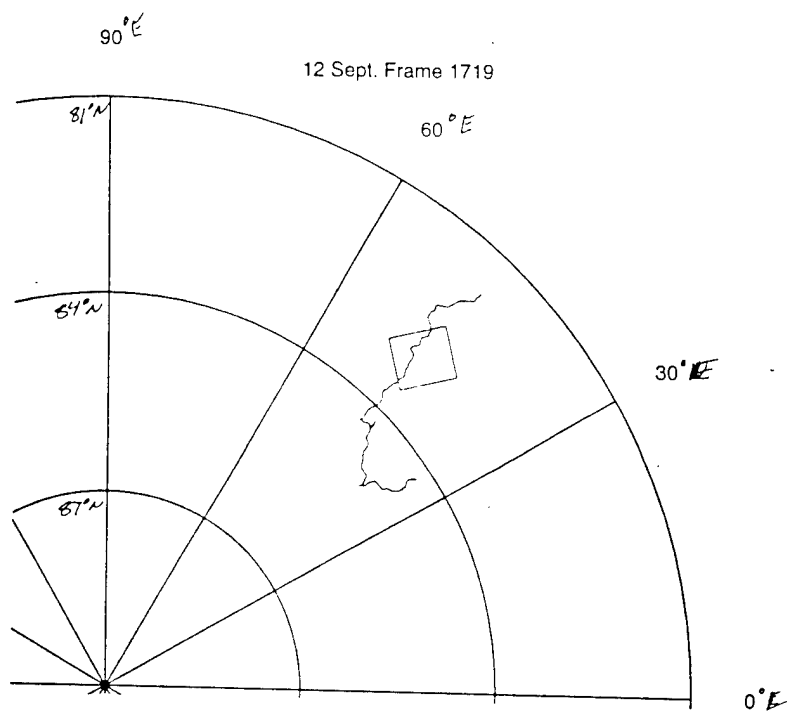
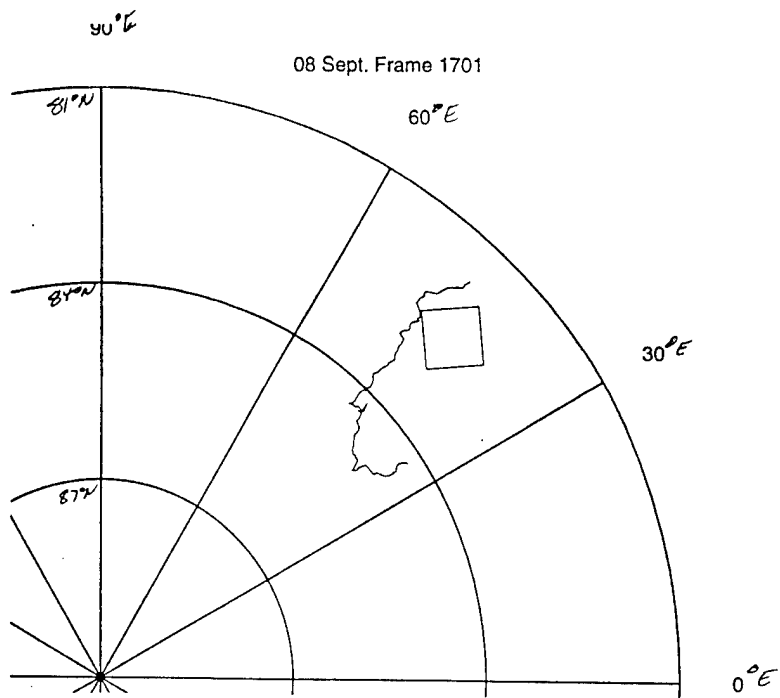
29 Aug. Frame 1809

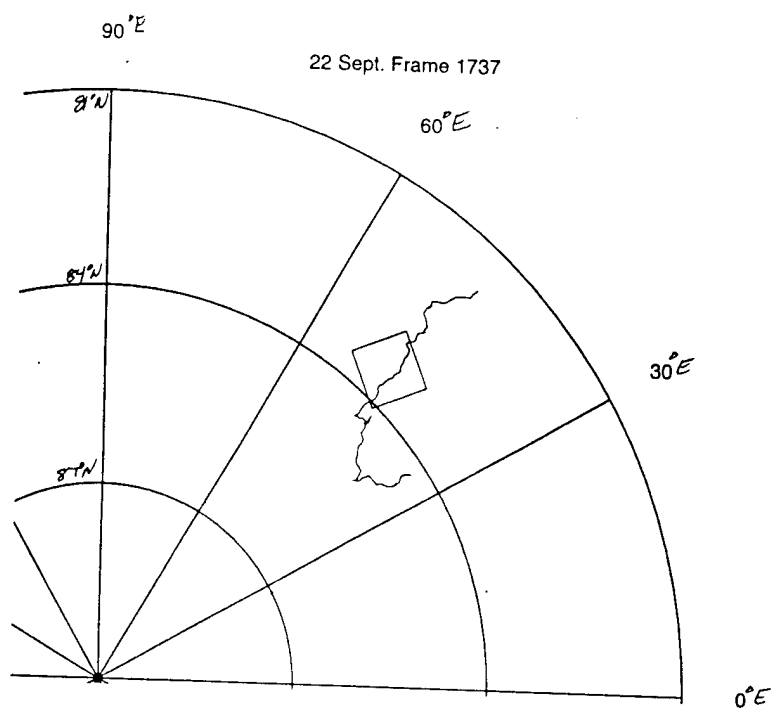
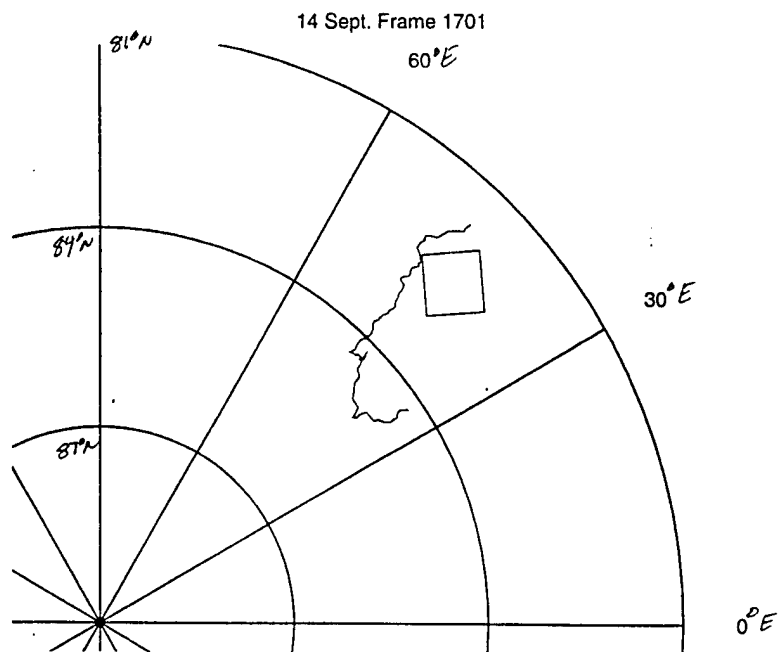




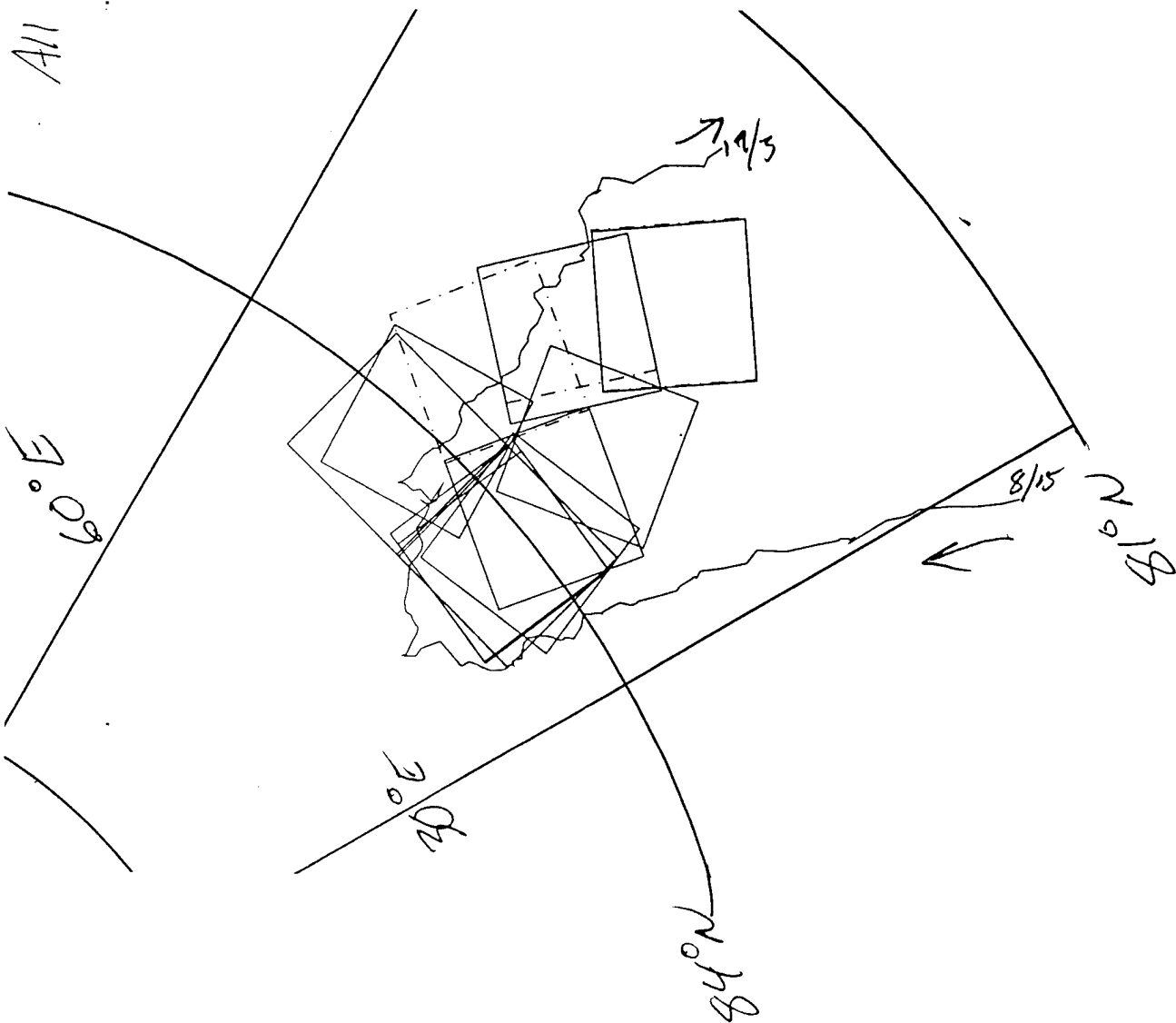








ALL SAR FRAMES



APPENDIX D

NASA Team Algorithm for Ice Classification

NASA Team Algorithm for ice type concentration

Results from SSM/I data, resampled to ERS-1 SAR frames

NASA Team Algorithm for ice classification

The brightness temperature measured by spaceborne microwave radiometers is determined by the combination of radiation from the surface, atmosphere, and space and can be expressed as,

$$T_B = T_s \exp(-\tau) + T_{UP} + (1 - \epsilon_s) T_{DN} \exp(-\tau) + (1 - \epsilon_s) T_{SP} \exp(-2\tau), \quad (D-1)$$

where T_s is the surface component, τ is the atmospheric opacity, T_{UP} is the upwelling atmospheric radiation component, T_{DN} is atmospheric downwelling radiation component, ϵ_s is the surface emissivity, and T_{SP} is the space component. The space component contribution is negligible in most terrestrial applications and is ignored. The two atmospheric terms can be expressed in terms of an atmospheric mean brightness temperature as,

$$T_{UP} = T_{DN} = T_A, \quad (D-2)$$

where T_A is the equivalent atmospheric mean brightness temperature.

If the atmospheric opacity is assumed to be small by retaining only the first-order terms of an expansion in terms of τ , equation (D-1) becomes,

$$T_B = T_s + \tau[(2 - \epsilon_s)T_A - T_s]. \quad (D-3)$$

In the NT algorithm, the atmospheric opacity is assumed to be negligible in the polar regions. This assumption may be invalid in some cases in which weather-induced effects must be considered. This is handled with a "weather filter" introduced into the algorithm [Gloersen and Cavalieri, 1986]. With the above assumptions, the brightness temperature measured with the SSM/I is assumed to be solely due to surface microwave emission in the main lobe of the antenna.

With the above underlying assumptions, the brightness temperature measured by the satellite radiometer is assumed to be solely due to the surface emission. It is also

assumed that the surface consists of only first-year ice, multiyear ice and open water. The brightness temperature from a mixture of these surfaces is given by,

$$T_B = T_W C_W + T_{FY} C_{FY} + T_{MY} C_{MY}, \quad (D-4)$$

where T_W , T_{FY} , and T_{MY} are the brightness temperatures of the ocean, first-year, and multiyear ice surfaces, respectively. Likewise, C_W , C_{FY} , and C_{MY} are the concentrations of each of the different surface types. The representative brightness temperatures depend on the frequency and polarization, so the above equation can be applied to each of the channels of the SSM/I. Furthermore, since only three surface types are assumed to be present, the open water concentration can be expressed in terms of the ice type concentrations as,

$$C_W = 1 - (C_{MY} + C_{FY}). \quad (D-5)$$

Equation (D-4) can be solved for the first-year and multiyear ice concentration with two independent variables, assuming that the brightness temperatures for each of the constituents (FY, MY and open water) are known. The representative brightness temperatures for each type and each channel are called tie points. The two variables used in the NT algorithm are the polarization ratio (PR) and the gradient ratio (GR).

The PR and GR for the SSM/I NT algorithm are given as,

$$PR = \frac{T_B(19, v) - T_B(19, h)}{T_B(19, v) + T_B(19, h)}, \quad (D-6)$$

and

$$GR = \frac{T_B(37, v) - T_B(19, v)}{T_B(37, v) + T_B(19, v)}, \quad (D-7)$$

where 37 and 19 denote the 37 GHz and 19 GHz channels of the SSM/I, and v and h denote the vertical and horizontal polarizations. These variables are used because they have been shown to be orthogonal in terms of the three surface types. Variations in PR are primarily caused by changes in ice concentration and GR is highly dependent on ice type [Cavalieri, et al., 1990]. The GR has also been shown to be

less affected by atmospheric effects than individual brightness temperature channels [Gloersen and Cavalieri, 1986].

Equation (D-4) is used for the 19v, 37v and 19h channels of the SSM/I and the relations for PR and GR are substituted into them to obtain two equations. These two equations are solved simultaneously to obtain estimates of C_{MY} and C_{FY} . These solutions are given below, along with a table of the hemispheric tie points used in this study for the three surface types (open water, first-year and multiyear ice). The open water and total ice concentration can be computed from the first-year and multiyear ice estimates, assuming that the total ice concentration is the sum of first-year and multiyear ice concentrations.

The tie points in the algorithm are representative values for PR and GR for each of the three surface types. These tie points form a triangle as shown in figure D.1. This figure demonstrates that the GR is primarily dependent on the first-year and multiyear ice concentrations, and the PR is primarily dependent on the difference between ice and open water. SSM/I pixels are generally assumed to contain a mixture of surface types, as described above. The resulting location of a particular pixel within the tie-point triangle determines the concentrations that are estimated with the NT algorithm.

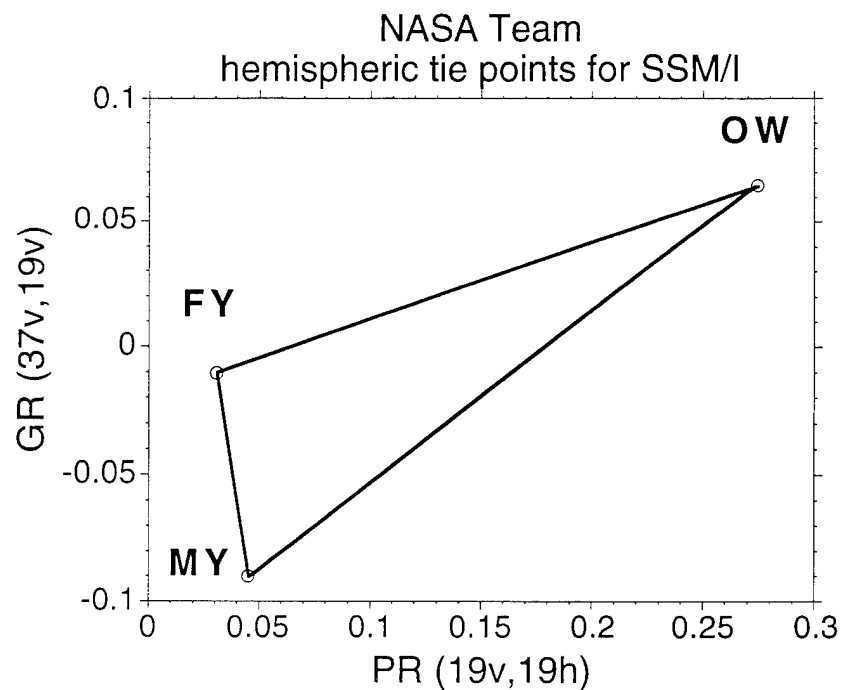


Figure D.1 Hemispheric tie points for the NASA Team algorithm on a PR-GR plot. The GR is more sensitive to the difference between first-year and multiyear ice and the PR is more sensitive to the difference between ice and open water.

As mentioned previously, atmospheric effects may create some problems with the NT algorithm. Gloersen and Cavalieri, [1986] developed a weather filter to reduce the effect of weather on the algorithm. This filter is simply an upper bound on allowed values of GR. When the computed GR exceeds 0.05, the ice concentrations are not computed for that given cell and its pixel value is set to some predetermined flag. This results in a reduction of misclassification of ice and open water, particularly in the marginal ice zone.

Concentrations of first-year and multiyear sea ice with the NASA Team algorithm are computed as follows. The multiyear concentration (C_M) and the first-year concentration (C_F) are given by,

$$C_M = \frac{1}{A_1 B_2 - B_1 A_2} \{A_1 [DW_2 - GR \cdot SW_2] - B_1 [DW_1 - PR \cdot SW_1]\}, \quad (D-8)$$

and

$$C_F = \frac{1}{A_1 B_2 - B_1 A_2} \{B_2 [DW_1 - PR \cdot SW_1] - A_2 [DW_2 - GR \cdot SW_2]\}. \quad (D-9)$$

In the above equations A_1 , A_2 , B_1 , and B_2 are given by

$$A_1 = PR [SF_1 - SW_1] - [DF_1 - DW_1], \quad (D-10)$$

$$A_2 = PR [SM_1 - SW_1] - [DM_1 - DW_1], \quad (D-11)$$

$$B_1 = GR [SF_2 - SW_2] - [DF_2 - DW_2], \quad (D-12)$$

and

$$B_2 = GR [SM_2 - SW_2] - [DM_2 - DW_2], \quad (D-13)$$

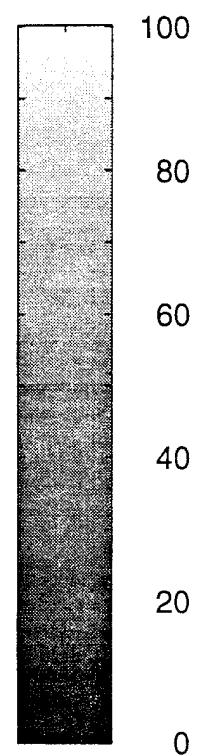
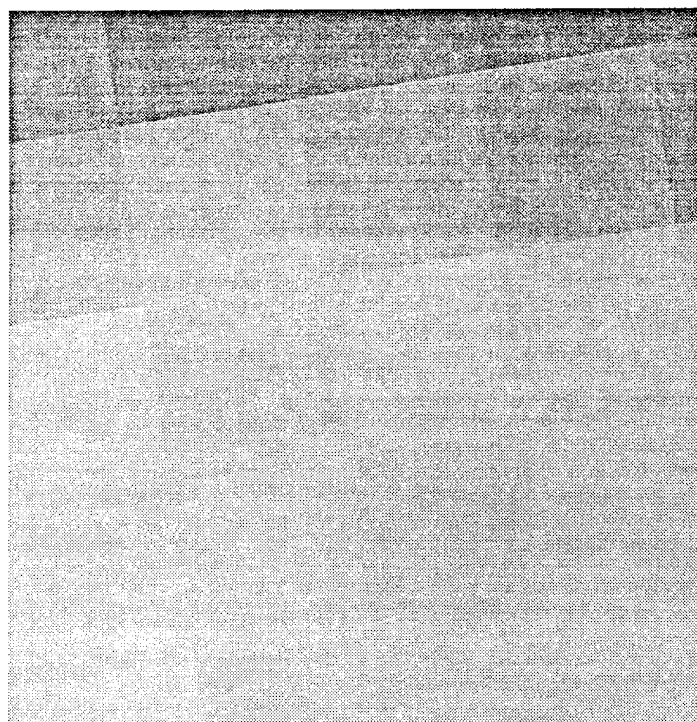
where

$$\begin{aligned} DW_1 &= T_{BW}(19, v) - T_{BW}(19, h) & DW_2 &= T_{BW}(37, v) - T_{BW}(19, v) \\ DF_1 &= T_{BF}(19, v) - T_{BF}(19, h) & DF_2 &= T_{BF}(37, v) - T_{BF}(19, v) \\ DM_1 &= T_{BM}(19, v) - T_{BM}(19, h) & DM_2 &= T_{BM}(37, v) - T_{BM}(19, v) \\ SW_1 &= T_{BW}(19, v) + T_{BW}(19, h) & SW_2 &= T_{BW}(37, v) + T_{BW}(19, v) \\ SF_1 &= T_{BF}(19, v) + T_{BF}(19, h) & SF_2 &= T_{BF}(37, v) + T_{BF}(19, v) \\ SM_1 &= T_{BM}(19, v) + T_{BM}(19, h) & SM_2 &= T_{BM}(37, v) + T_{BM}(19, v) \end{aligned}$$

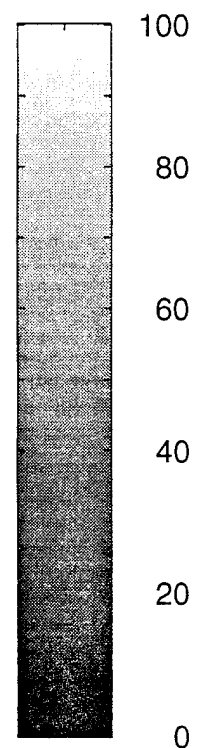
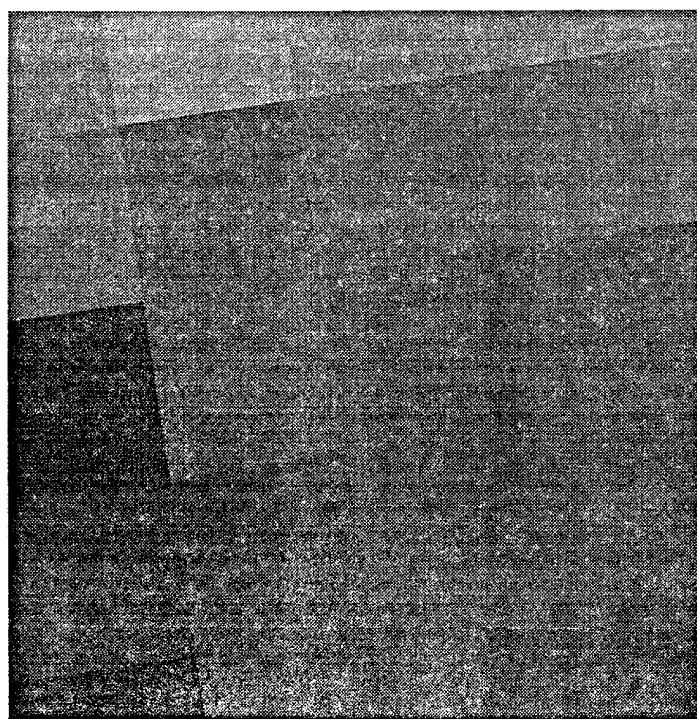
The tie points are the brightness temperature values as observed with SSM/I, through the polar atmosphere from first-year ice (T_{BF}), multiyear ice (T_{BM}) and open water (T_{BW}). The tie point values vary with polarization and frequency. The polarization is noted as v or h and the frequency is noted as 37 GHz or 19 GHz. The polarization ratio (PR) and gradient ratio (GR) are defined in equations (D-6) and (D-7).

Table D-1 Hemispheric tie points for NT algorithm for Northern Polar grid			
Channel	Open Water	First-Year	Multiyear
19 H	100.8	242.8	203.9
19 V	177.1	258.2	223.2
37 V	201.7	252.8	186.3

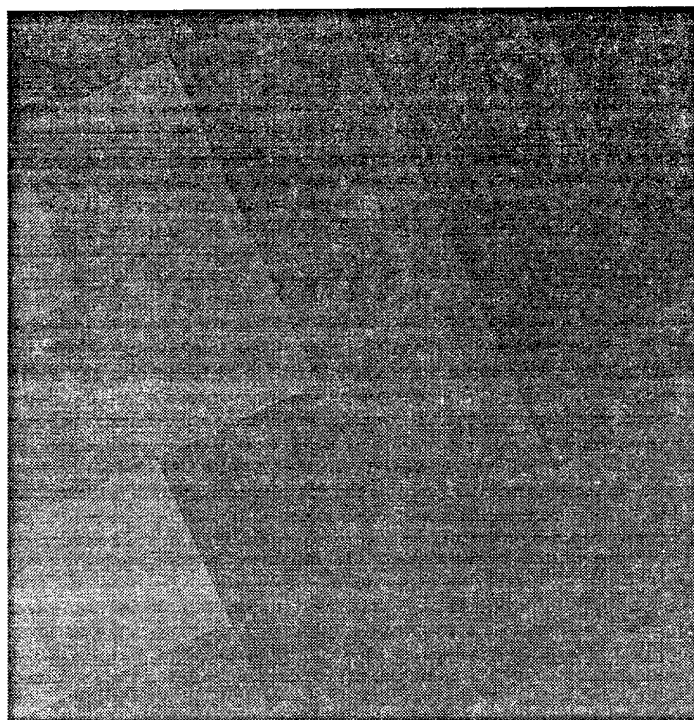
21 August FYC from NT algorithm : mapped to Frame 1827



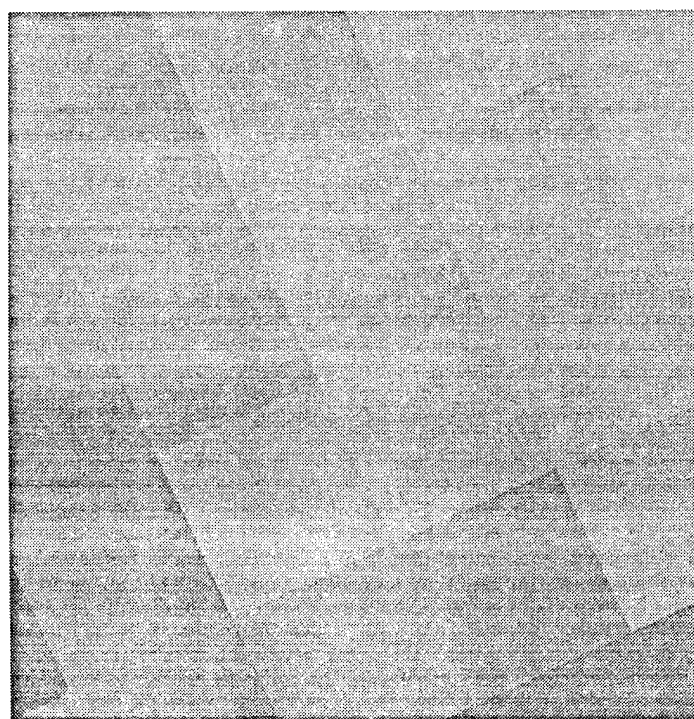
21 August MYC from NT algorithm : mapped to Frame 1827



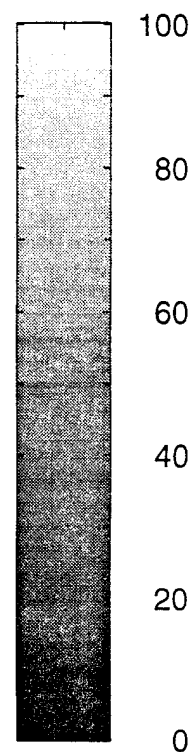
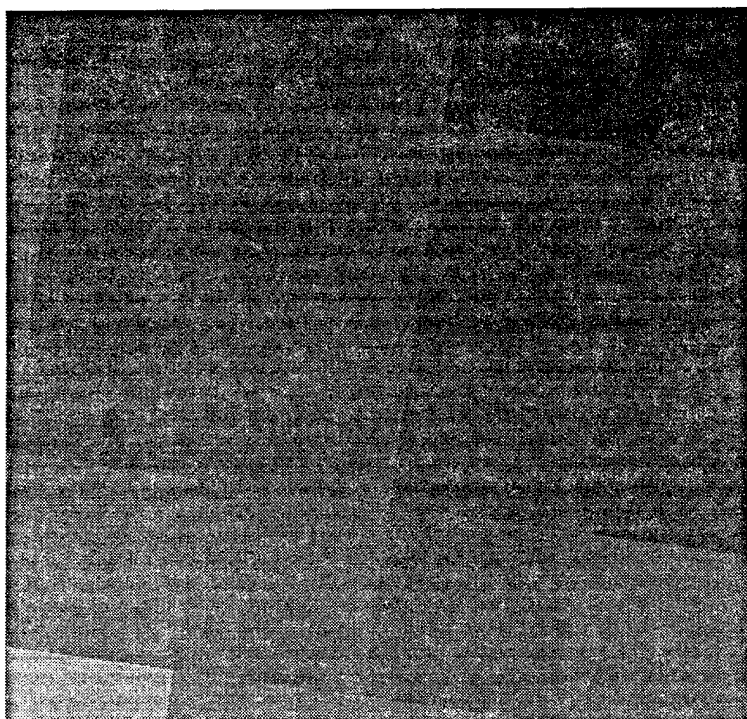
23 August FYC from NT algorithm : mapped to Frame 1863



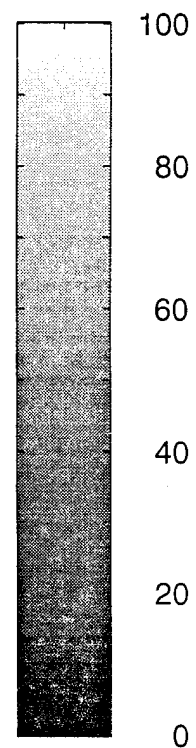
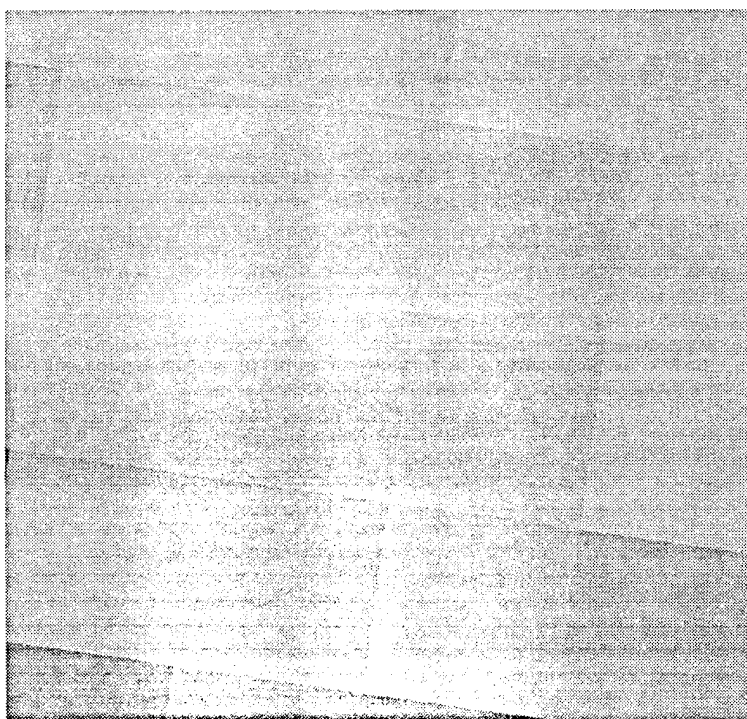
23 August MYC from NT algorithm : mapped to Frame 1863



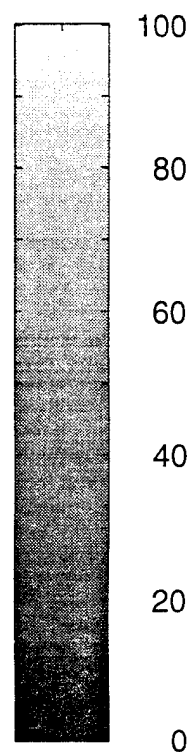
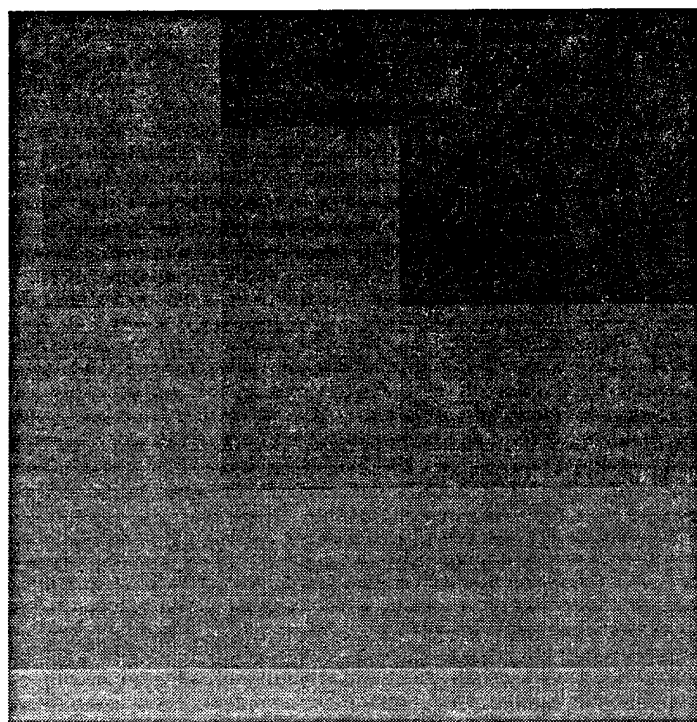
25 August FYC from NT algorithm : mapped to Frame 1791



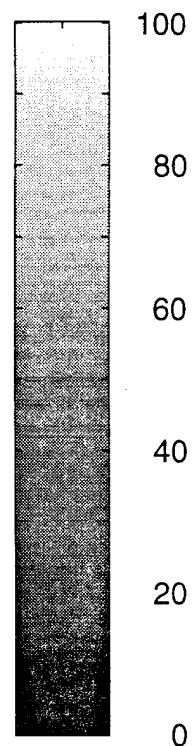
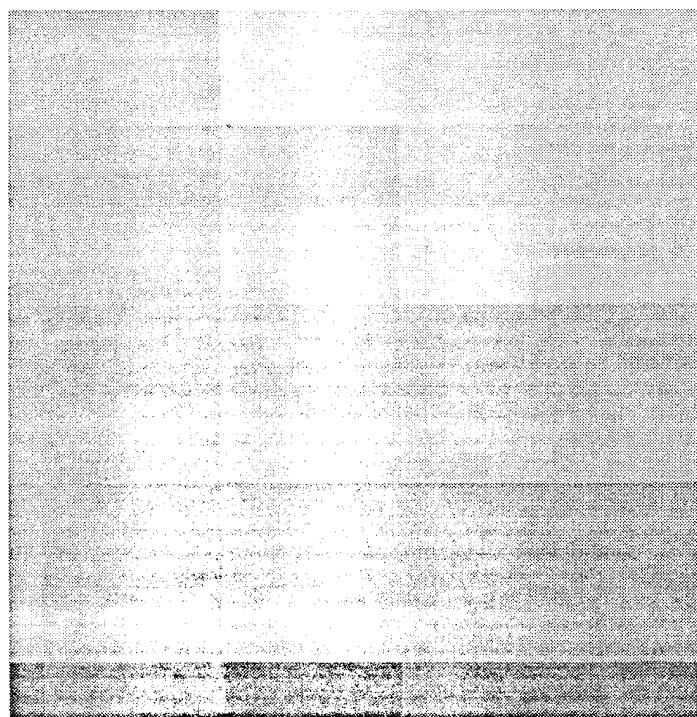
25 August MYC from NT algorithm : mapped to Frame 1791



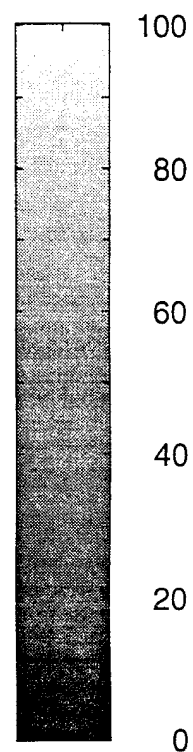
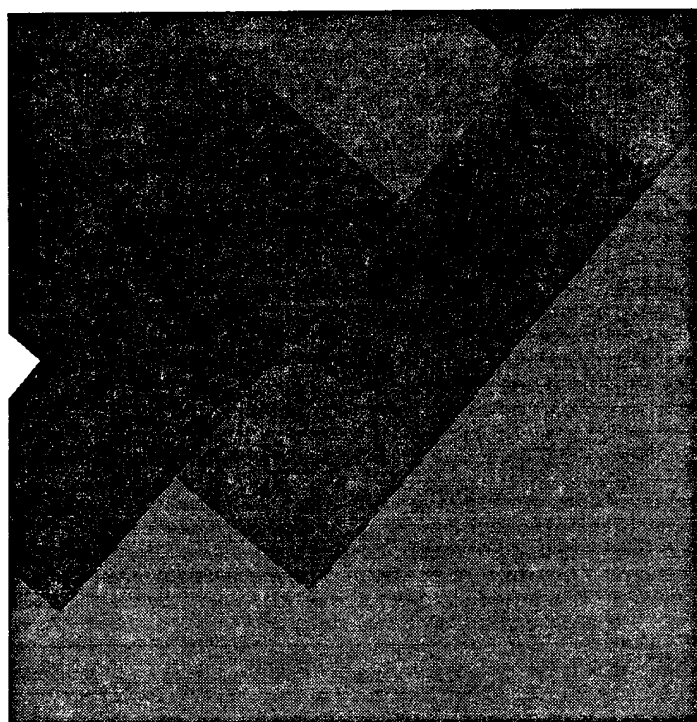
26 August FYC from NT algorithm : mapped to Frame 1809



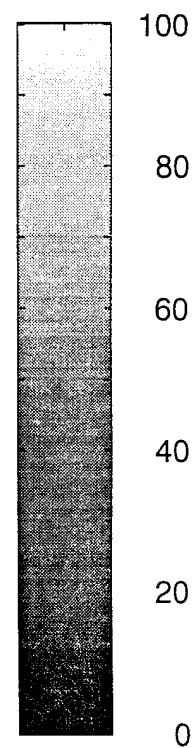
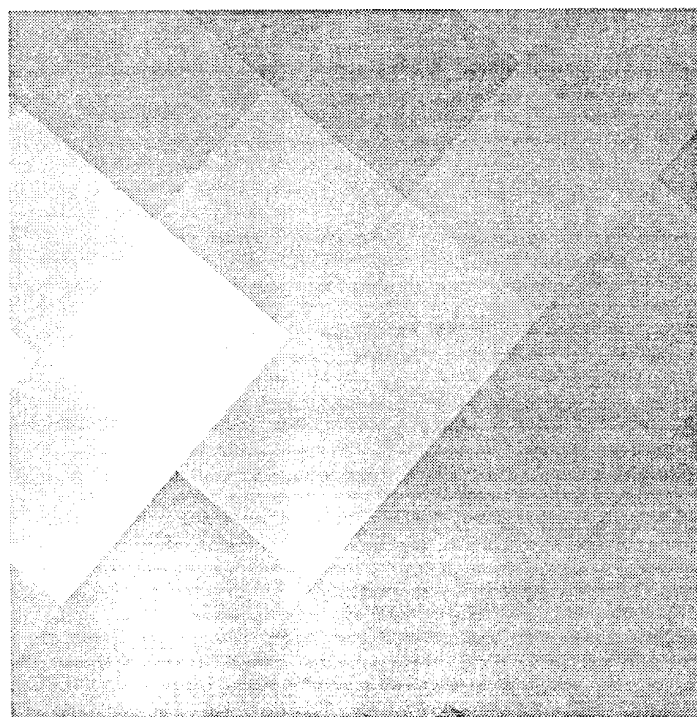
26 August MYC from NT algorithm : mapped to Frame 1809



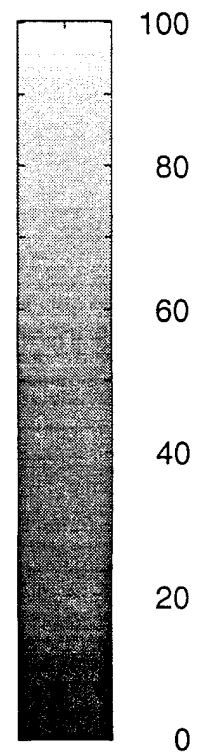
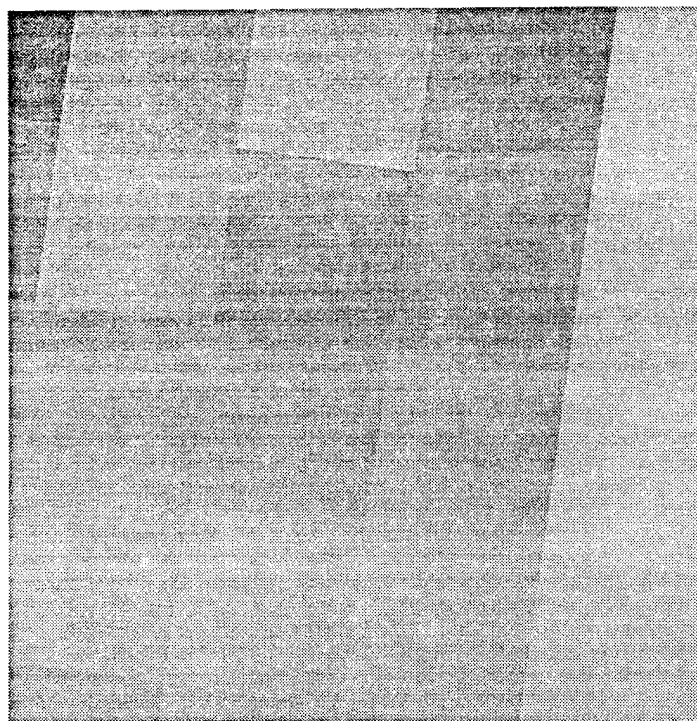
27 August FYC from NT algorithm : mapped to Frame 1701



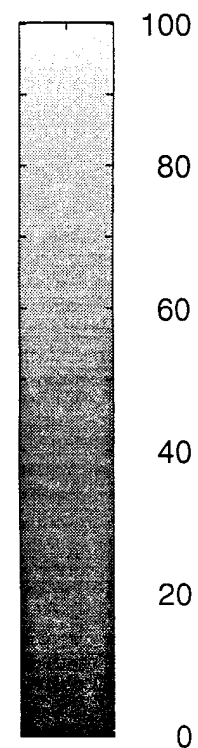
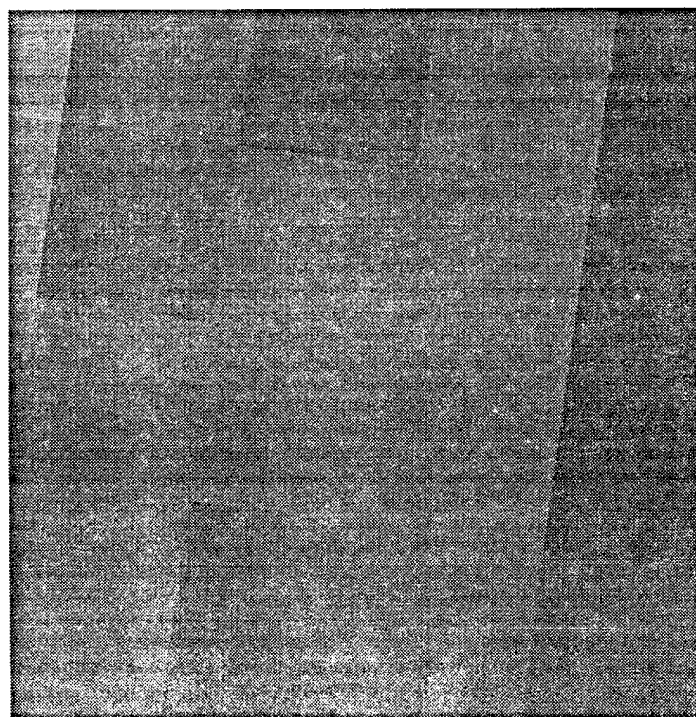
27 August MYC from NT algorithm : mapped to Frame 1701



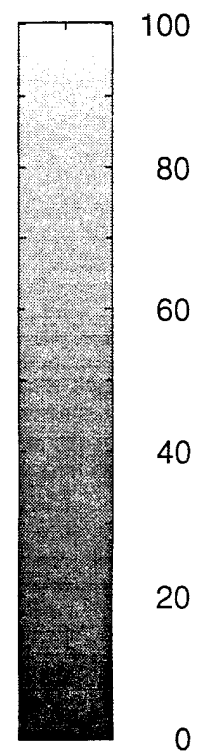
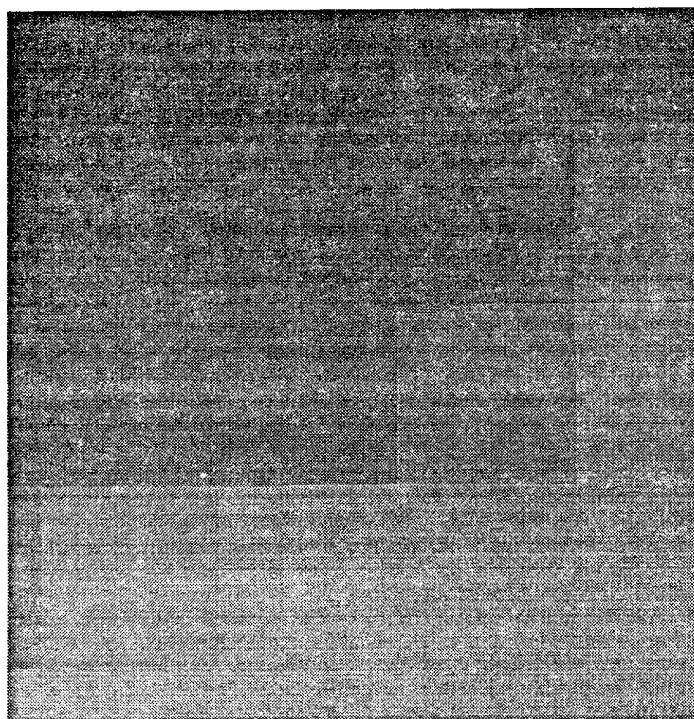
28 August FYC from NT algorithm : mapped to Frame 1791



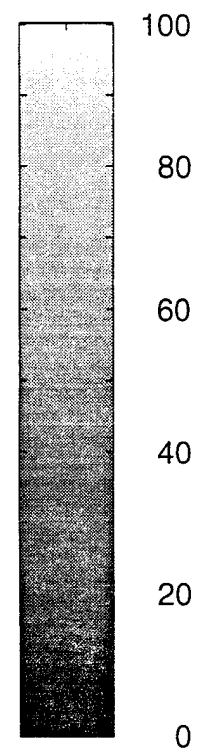
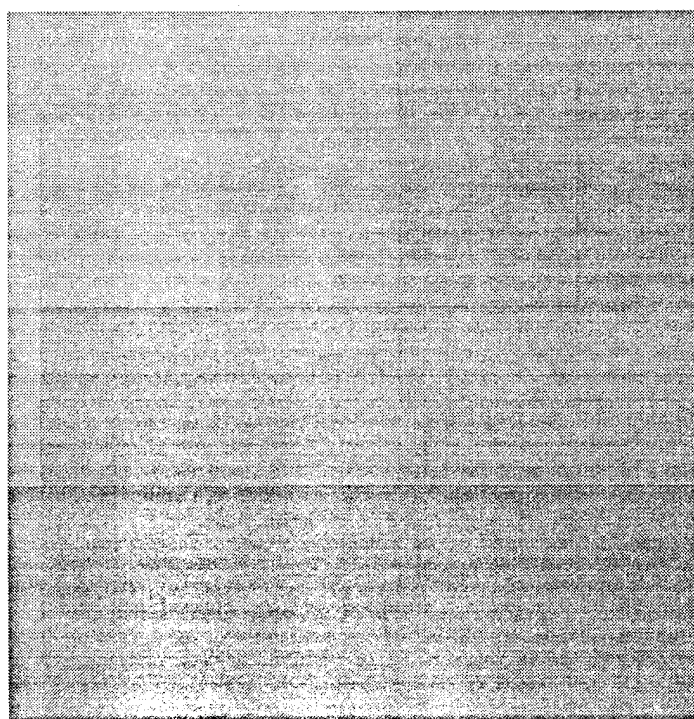
28 August MYC from NT algorithm : mapped to Frame 1791



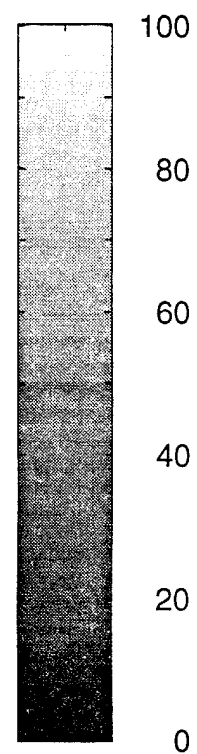
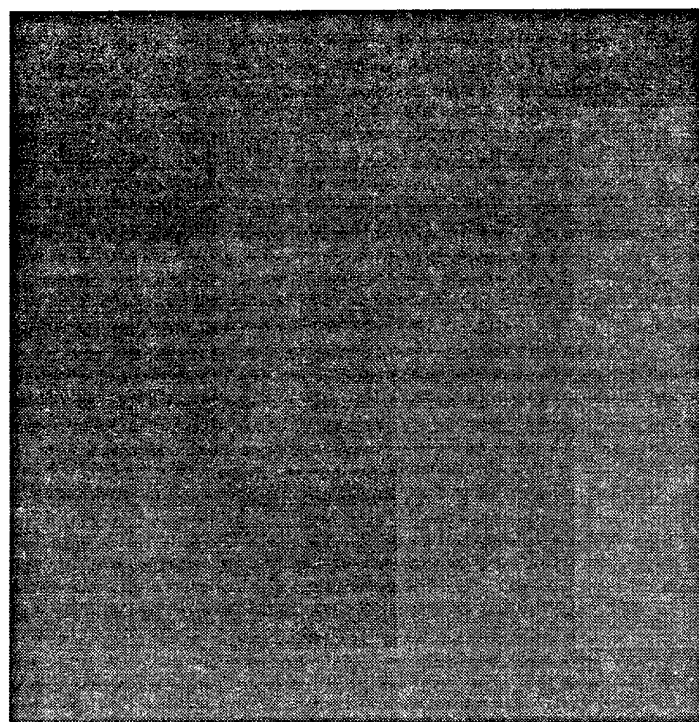
29 August FYC from NT algorithm : mapped to Frame 1809



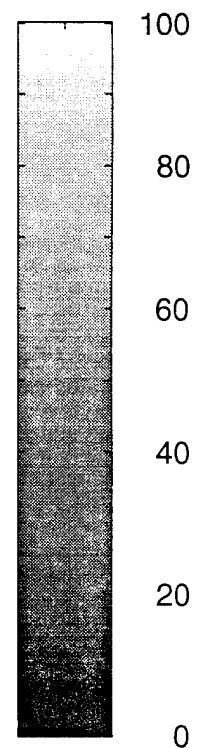
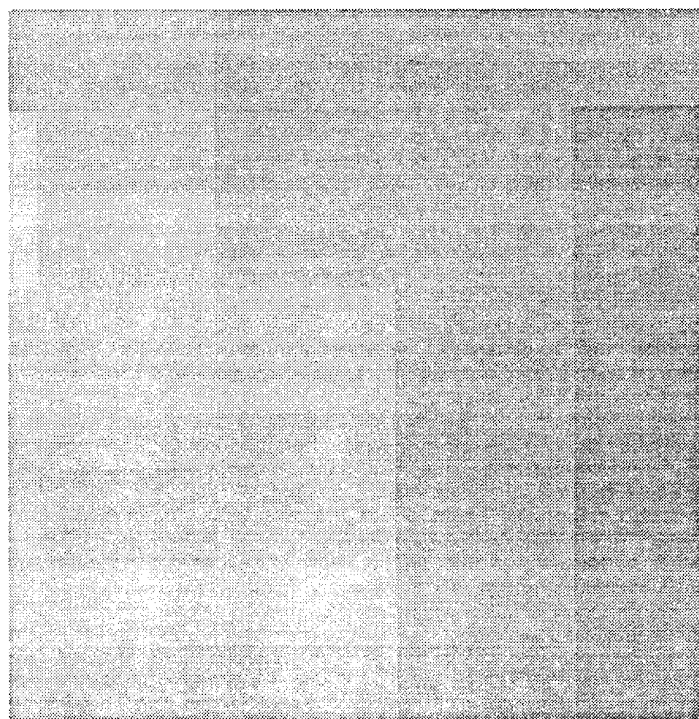
29 August MYC from NT algorithm : mapped to Frame 1809



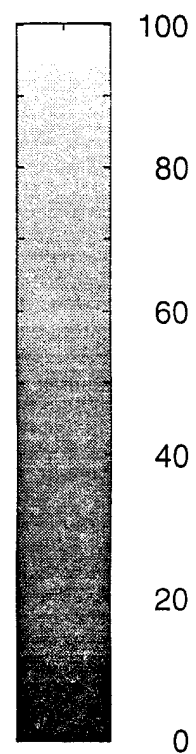
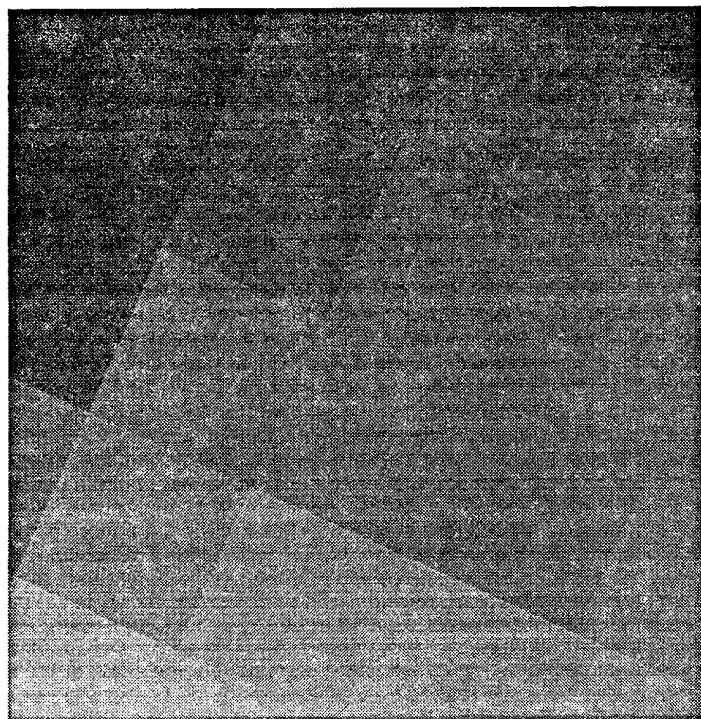
29 August FYC from NT algorithm : mapped to Frame 1791



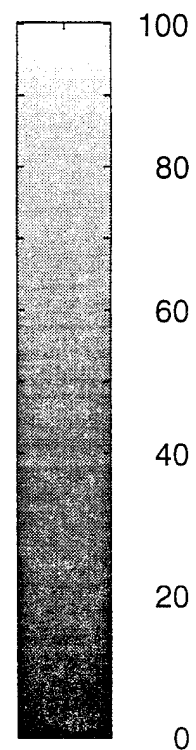
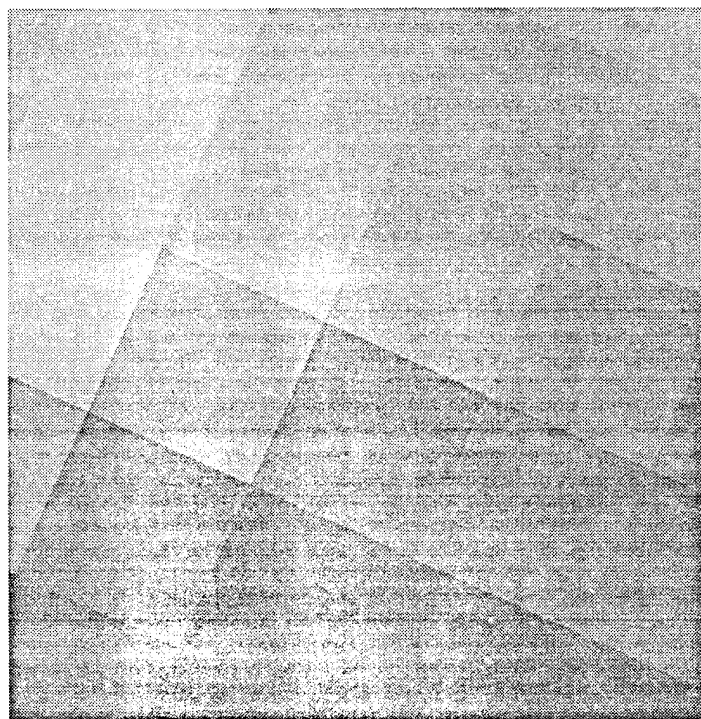
29 August MYC from NT algorithm : mapped to Frame 1791



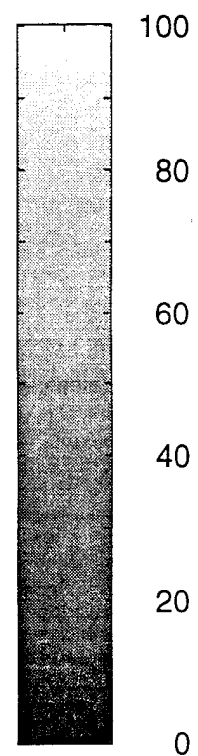
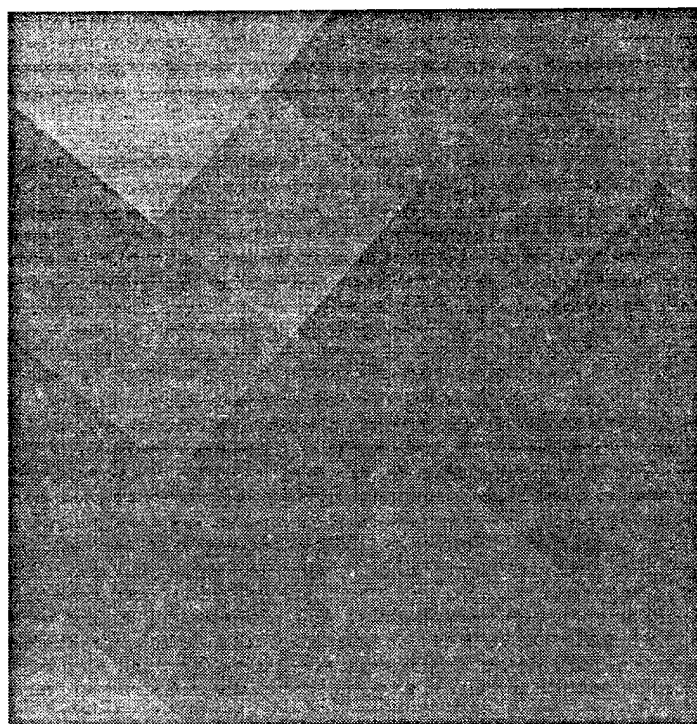
29 August FYC from NT algorithm : mapped to Frame 1755



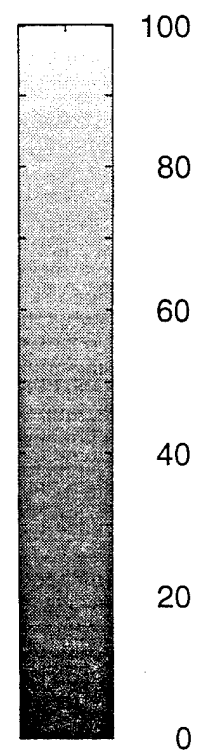
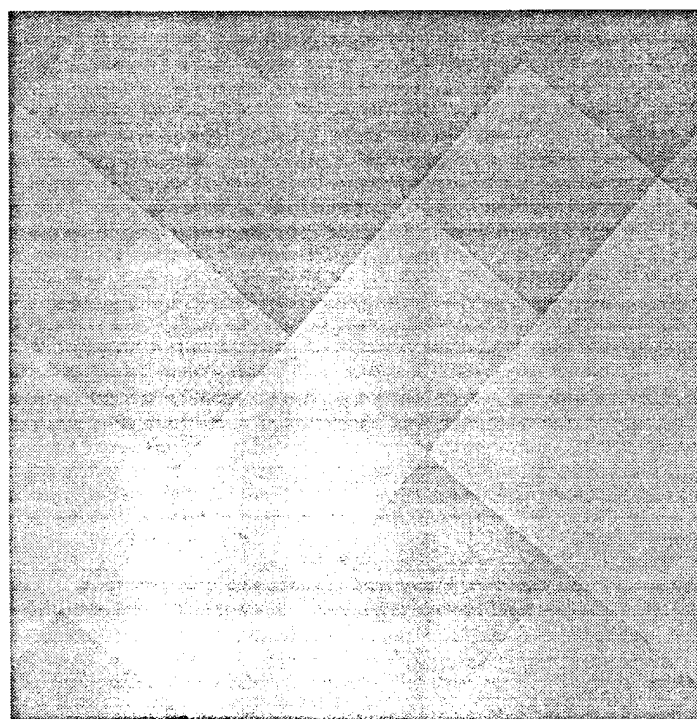
29 August MYC from NT algorithm : mapped to Frame 1755



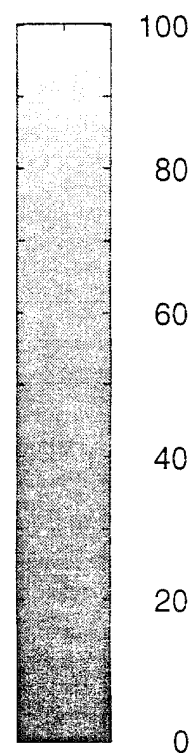
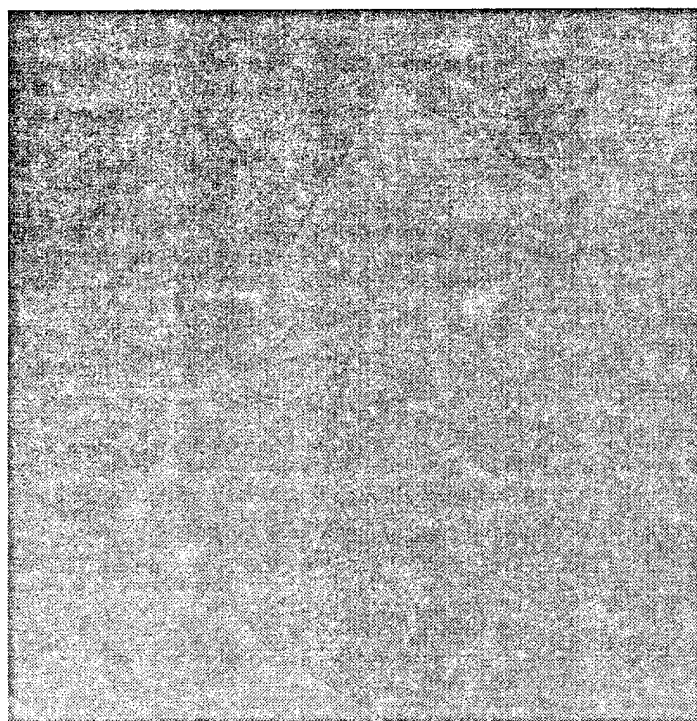
30 August FYC from NT algorithm : mapped to Frame 1701



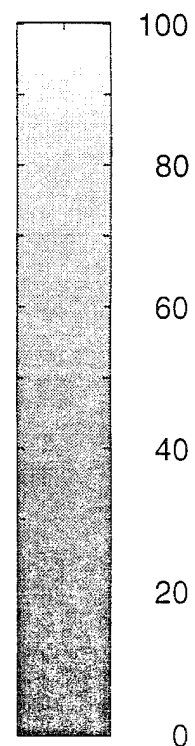
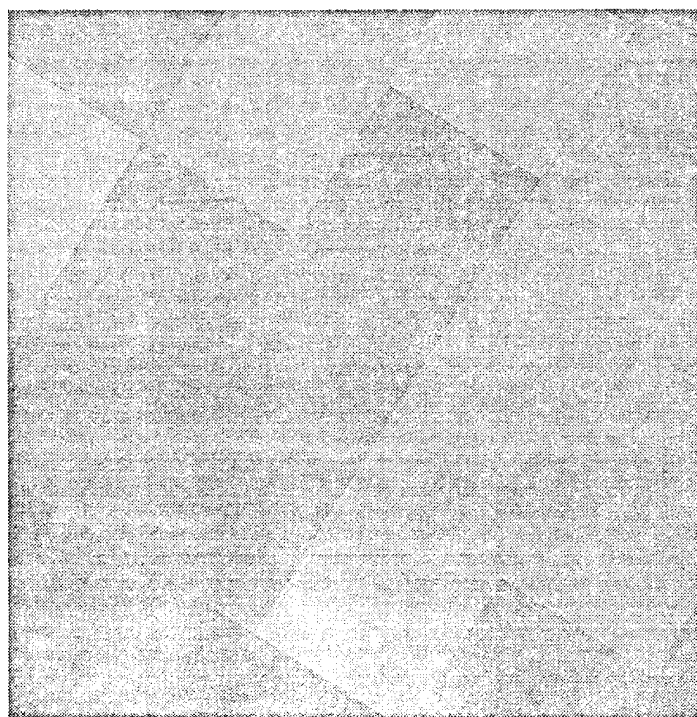
30 August MYC from NT algorithm : mapped to Frame 1701



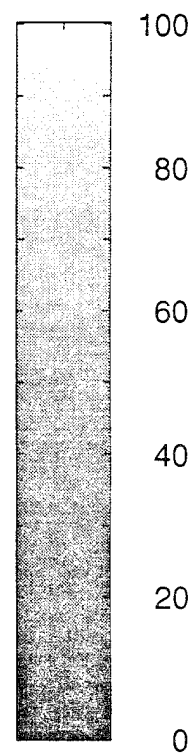
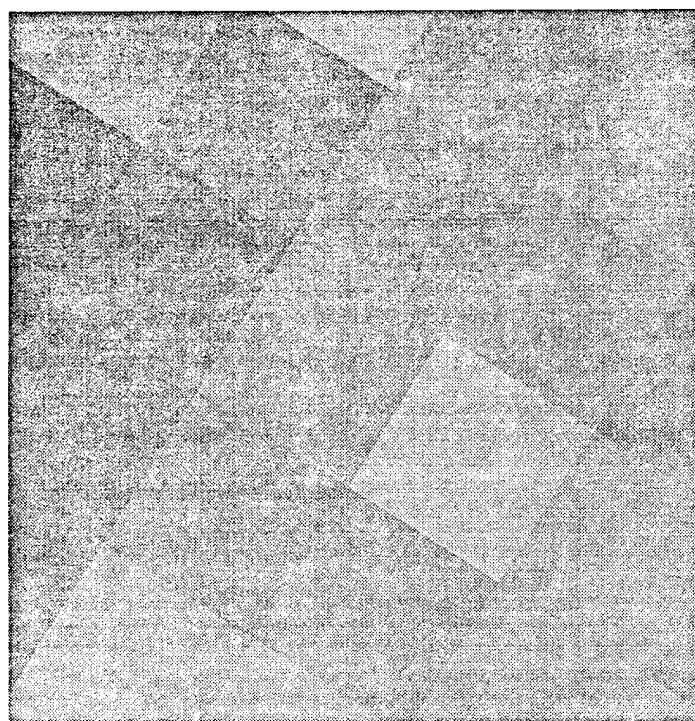
03 Sept FYC from NT algorithm : mapped to Frame 1719



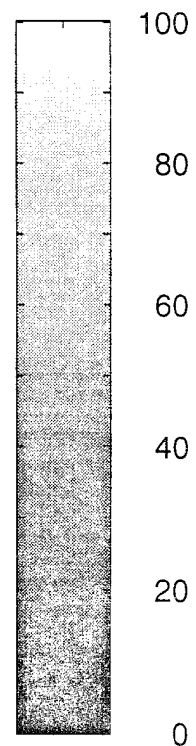
03 Sept MYC from NT algorithm : mapped to Frame 1719



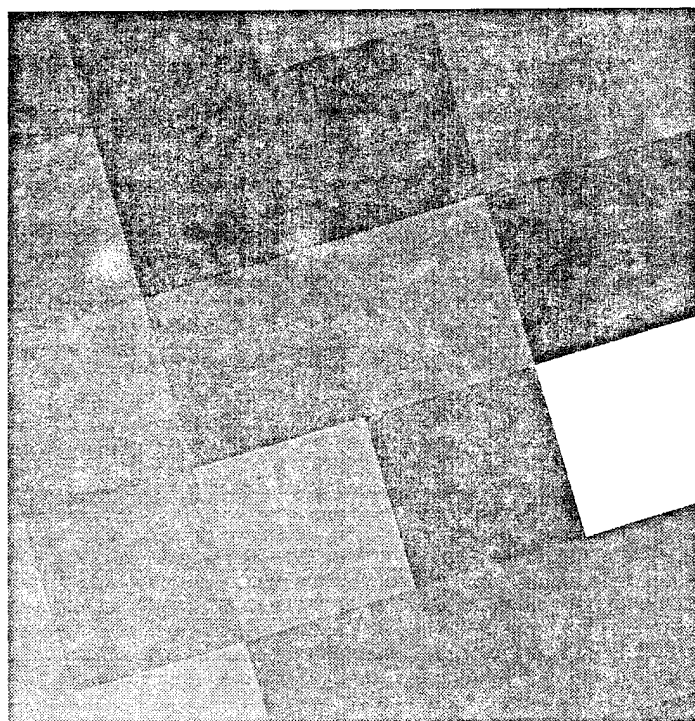
06 Sept FYC from NT algorithm : mapped to Frame 1719



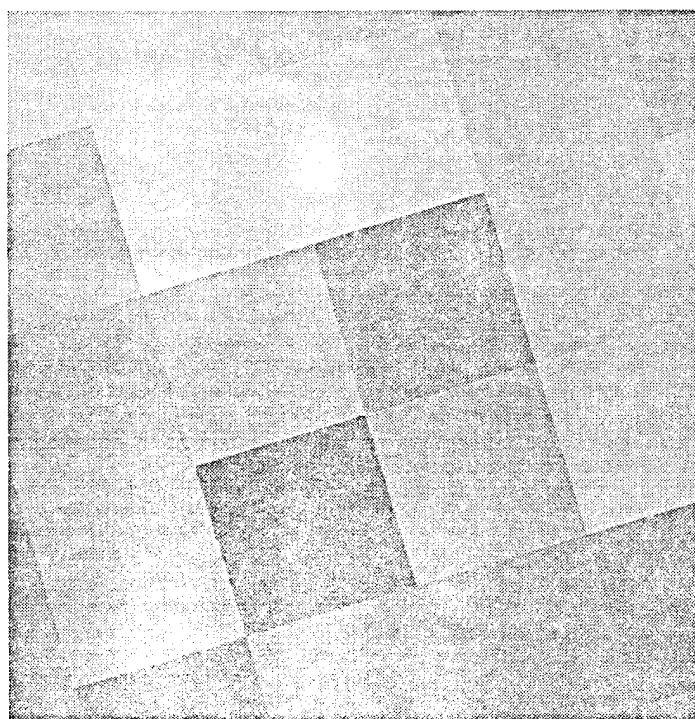
06 Sept MYC from NT algorithm : mapped to Frame 1719



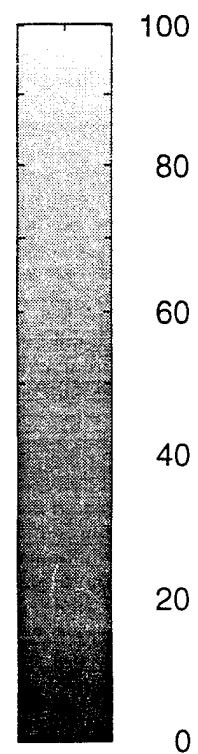
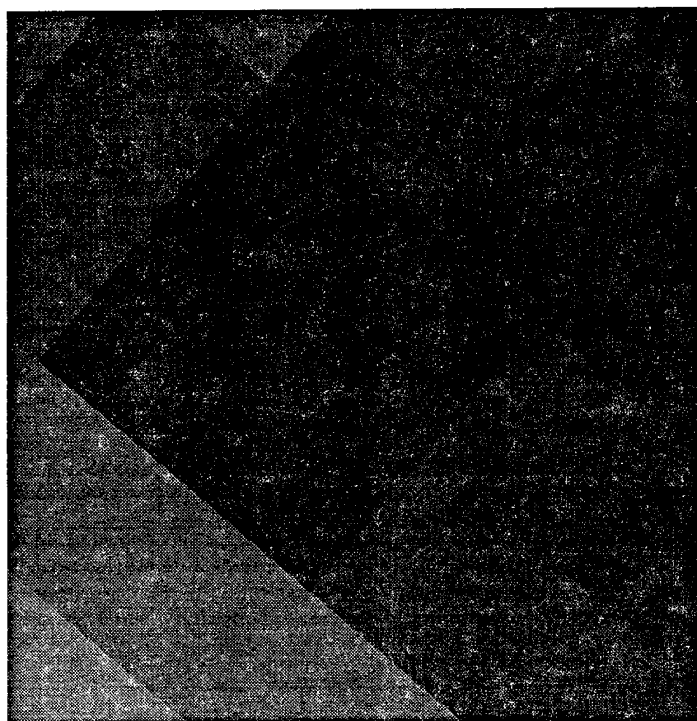
06 Sept FYC from NT algorithm : mapped to Frame 1827



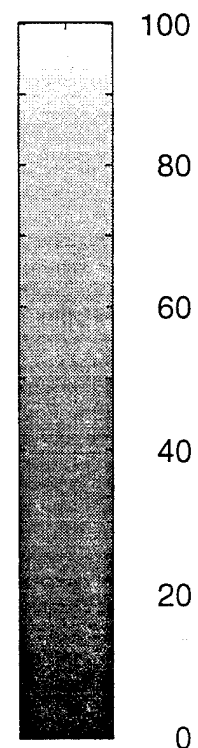
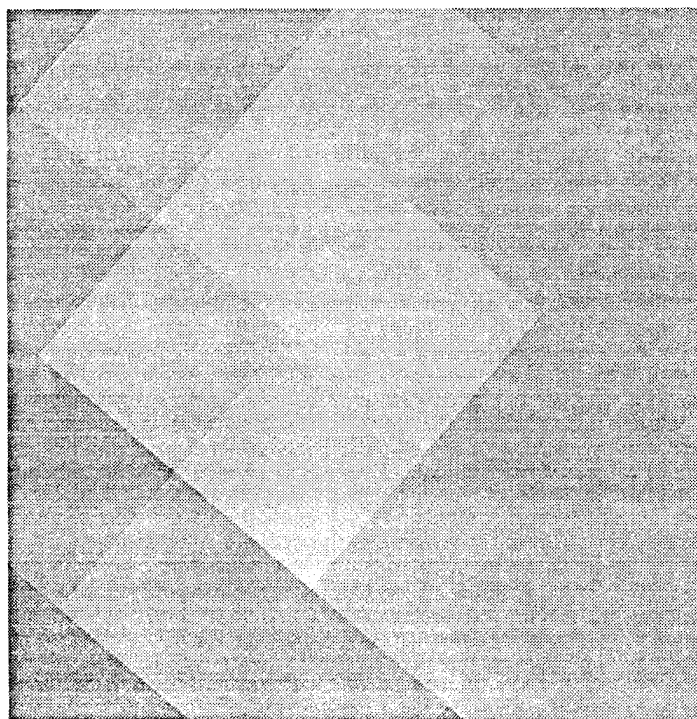
06 Sept MYC from NT algorithm : mapped to Frame 1827



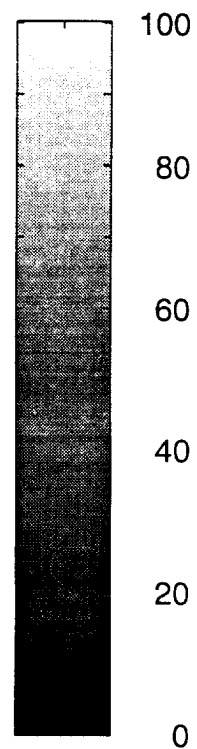
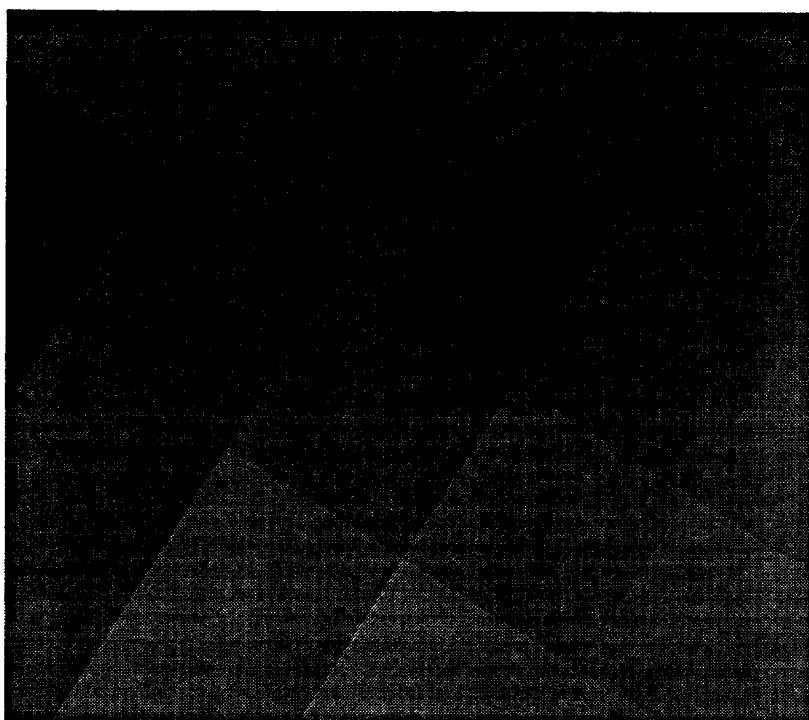
08 Sept FYC from NT algorithm : mapped to Frame 1701



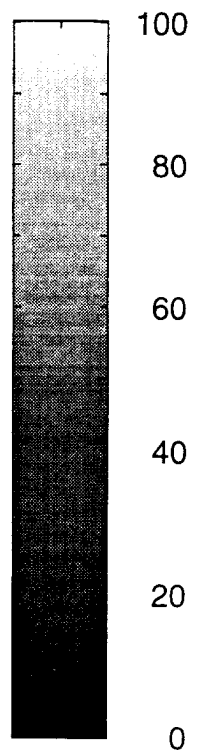
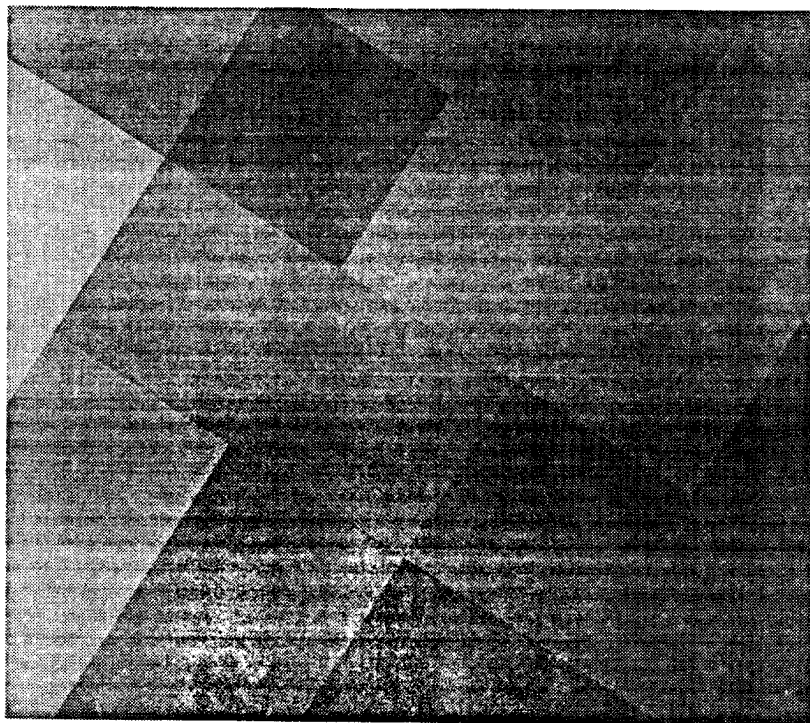
08 Sept MYC from NT algorithm : mapped to Frame 1701



12 Sept FYC from NT algorithm : mapped to Frame 1719



12 Sept MYC from NT algorithm : mapped to Frame 1719



Inter-Office Memorandum

10 OCT 1995

IN REPLY
REFER TO

DTIC-RSI (R. Delorie/767-8180/clh)

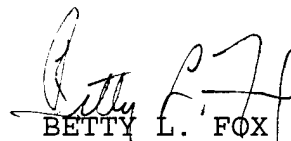
SUBJECT: Technical Library Survey

TO: SEE DISTRIBUTION

1. The DTIC Library is conducting a survey. The enclosed survey is to determine if our users needs are being satisfied and to identify ways in which services can be improved.

2. Please complete the enclosed survey, no names please, and return it to Ms. Rusty Delorie in the Technical Library, Rm 1816 within five days of receipt. Any questions may be directed to Ms. Delorie on 767-8180.

1 Encl



BETTY L. FOX

Director of Administration
and Resource Management

DISTRIBUTION:

E

USER'S SURVEY OF THE DTIC TECHNICAL LIBRARY

1. Are you aware of the various services available from the Library?

☐ Yes ☐ No

If you answered "no" to the above question, check all that apply:

☐ Did not know that there is a library at DTIC
☐ Have no reason to use the library
☐ Library collections do not meet my needs
☐ Other _____

2. How often do you use the Technical Library or any of its services?

☐ Several times a week
☐ Weekly
☐ Monthly
☐ Several times a year
☐ Never

3. What best describes your reasons for not using the Technical Library more often? (Check as many as are applicable.)

☐ I use the library only as often as I need to
☐ I use the library only as often as time allow
☐ My work does not require use of the library
☐ Library too crowed and/or noisy
☐ Library too far from my work station
☐ Library does not provide the services I need
☐ Other reasons: _____

4. Which of the following library resources and services do you use? Please enter the appropriate number:

1=Often 2=Regularly 3=Seldom 4=Never

Resources:

- ___ Books
- ___ Periodicals/journals
- ___ Reference works (a book, or work, compiled to be referred to rather than for continued reading)

Services:

- ___ Borrow books
- ___ Request books/materials
- ___ Order books/materials
- ___ Receive periodicals routed from the library
- ___ Reference request (requiring specific facts, responses or referrals)
- ___ Request Online database searches
- ___ Inter-library loan requests (books or articles not held by DTIC library may be borrowed from other libraries)
- ___ Other _____

CD-Roms:

- ___ Books in Print
- ___ Personnet
- ___ PhoneDisc

5. List any additional services the Library might provide that can be of benefit to you:

6. Which of the following library services and resources would you like to see improved, expanded or started.

Please respond by indicating the degree of importance you attach to such improvements based on the following scale:

1	2	3	4	5
very	moderate	somewhat	marginal	no opinion

___ Reference services
___ Inter-library loan services
___ Routing of selected periodicals/materials
___ Database searches
___ Expansion of periodical/magazine titles. If regarded as of importance, please give the names of some periodicals that you would like to see:

Please respond by indicating the degree of importance you attach to such improvements based on the following scale:

1	2	3	4	5
very	moderate	somewhat	marginal	no opinion

___ Improvement in the book collection. Please indicate also the subject areas that pertain to your work or speciality:

7. Are requested materials and/or services received within an adequate time-frame?

1	2	3	4	5	6	7	8	9	10
poor				satisfactory					excellent

8. Did materials provided meet your reference or information needs?

1 2 3 4 5 6 7 8 9 10
poor satisfactory excellent

9. Have you seen the notices of books, periodicals, and publications received by the library in the DTIC NewsLine?

___ Yes

___ No

10. Please provide either:

a) your job classification series number: _____

or

b) your general job title (systems manager, administrator, clerk, information technician, etc.):

11. Are you aware of the capability to query the library collection from your PC?

___ Yes

___ No

12. Are you aware of the procedures for ordering requests for periodicals and books for the library?

___ Yes

___ No

13. If you have any comments or suggestions that have not been covered in this survey please write them below. Your views and cooperation are appreciated.